Graphene Based Thermal Emitters

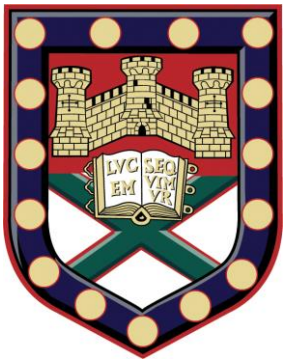

Submitted by Nathan Howard Mahlmeister, to the University of Exeter

as a thesis for the degree of

Doctor of Philosophy in Engineering,

July 2016

I certify that all material in this thesis which is not my own work has been identified and that no material has previously been submitted and approved for the award of a degree by this or any other University.

Signature .....

Abstract

Mid-Infrared thermal emission sources based on graphene were investigated both experimentally and simulated using the finite element method modelling software package COMSOL. Devices were fabricated by transferring graphene onto various substrates. The thermal emission of few-layer and single graphene on SiO_2/Si, under a pulsed square wave drive current, was characterised using spatially resolved thermal emission measurements. It was determined that the devices with single-layer graphene maintained characteristic properties of graphene, while few-layer graphene displayed properties typical of a semi-metal. The effect of thermal management on the emission was investigated by comparing simulations to the emission from these devices and a hexagonal boron nitride encapsulated few-layer graphene device. Limiting the vertical heat dissipation was shown to improve device modulation speed.

The emission from the graphene devices was determined to be grey-body in nature. Metamaterial structures, including ring resonators and split ring resonators, were integrated with the encapsulated devices in order to narrow the emission spectra. The emission and reflectance of the devices was characterised using Fourier transform infrared spectroscopy. A tuneable electromagnetically induced transparency like spectral response was observed for devices with metamaterial structures. The resonance peaks were shifted by altering the unit cell parameters.

Finally, gallium nitride nano-rod arrays were investigated for the potential to incorporate both spectral control and thermal management into the underlying

substrate, in addition to the possibility of the optical generation of graphene plasmons. It was determined that the conventional wet transfer technique was inadequate to transfer the graphene onto the nano-rods. Therefore, a modified transfer technique was utilised, with a significant improvement in the graphene coverage observed. Optical characterisation of the nano-rods using Fourier transform infrared reflectance spectroscopy indicated the excitation of localised surface phonon polaritons, while no evidence was observed in the graphene reflectance spectra of the generation of graphene plasmons.

Acknowledgements

There are many people to whom I would like to thank for aiding me throughout the course of my study. First, and most importantly, is my supervisor Professor Geoffrey R. Nash. It is no exaggeration for me to say that I cannot imagine having gotten to this point without him. The qualities that make him a fantastic supervisor are many: He is knowledgeable, enthusiastic, a great motivator, permanently positive and perhaps, most importantly for me, understanding. There were times during the course of my PhD that I got discouraged, for both professional and personal reasons, and I always knew I could confide in him. It is because of this that I not only consider him a great supervisor but a close friend, and it was a great pleasure to have him as my supervisor these last four years.

I would also like to thank the post-docs and PhD students in our group that I have worked alongside these last few years, both directly and indirectly. All of the post-docs were integral in making this a great learning experience. Particular thanks goes out to Dr. Lorreta Lawton. She assisted me greatly in navigating the cleanroom and fabricating samples during the first half of my PhD. I'm also extremely grateful for the help and patience of Dr. Isaac Luxmoore. His aid with using the FTIR and answering my many questions to help my understanding was invaluable. While I did not work directly with Dr. Penglei Li or Dr. Choon How Gan, they were always more than willing to answer any questions I had, no matter how insignificant. Additionally, my fellow PhD students, Tim Poole, Dr. Lokeshwar Bandhu, Kishan Menghrajani, Cheng Shi, Benjamin Ash, and Oliver Higbee, have been wonderfully supportive colleagues. I would like to particularly thank Kishan Menghrajani for helping me with the Raman measurements and Cheng Shi for

performing the simulations on the metamaterial structures presented in Chapter 6 and for our many prolonged theory discussions.

Outside of my research group, I would like to thank my many friends and family. Firstly, a significant thank you goes out to my partner Melissa Wix. I can say without a doubt that I would not be here right now without her because she literally found the advertisement for this PhD position, encouraged me to apply and unwaveringly supported me at all points along the way, even when I did not make it easy for her to do so. She also did me the great service of proofreading this thesis, finding the many grammatical errors I overlooked. Additionally, the many friends I have made while studying in Exeter have made this city that is 3000 miles from home into my new home. In no particular order I would like to thank my European family: Andrea Gori, Deniz Çizmeci, Callan Davies, Tom Fallows, Wessel Woldman, Silvia Barrett and Ed James. I am also so grateful to my family back in the US. Their support, both emotional and financial, has allowed me to achieve a landmark I never would have thought possible growing up in the small, unknown town of Sidney, NY. Their encouragement has motivated me for the past 26 years and I am truly blessed to have them in my life. Finally, I would like to say thank you to everyone who I have not named directly. If I were to list you all I fear this section would be longer than the body of this work

"I like the scientific spirit – the holding off, the being sure but not too sure, the willingness to surrender ideas when the evidence is against them: this is ultimately fine – it always keeps the way beyond open – always gives, life, thought, affection, the whole man, a chance to try over again after a mistake – after a wrong guess." Walt Whitman.

Contents

List of Tables

List of Figures

1 Introduction

1.1 Motivation

There is a current requirement for the development of a new generation of infrared emitters for the use as emission sources for portable nondispersive infrared (NDIR) gas sensors that are safe, fast and low-cost. Applications of portable gas sensors include the monitoring of CO_2 [1] in the brewing industry, methane [2,3] in mining and engine emissions [4] in the automotive industry. Currently, there are three main types of infrared (IR) sources suitable for the use in NDIR gas sensors. Incandescent micro-bulbs, the most frequently used source currently available, micro-machined thin membrane incandescent emitters [5] and IR light emitting diodes (LED) [6]. However, each type has significant disadvantages that include, slow response times, limited wavelength range, expensive to fabricate, low radiative efficiency and short life times. Therefore, there is a continuing need for the development of an IR source that can overcome these limitations. For example, higher modulation speeds allow for the utilisation of advanced signal processing techniques and improved sensor response, while the spectral efficiency, the percentage of the emittance spectra that is within the absorption band of the target gas, can be improved by tuning the peak in the emission spectra to the peak wavelength of the target gas.

Since its discovery in 2004, graphene [7], a two-dimensional allotrope of carbon that consists of a planar sheet (or sheets) of sp^2 hybridised carbon atoms arranged in a hexagonal crystal lattice, has attracted substantial interest, due to

its remarkable electronic [8], thermal [9] and mechanical properties [10]. Several of these outstanding properties make graphene an interesting prospect for a new type of incandescent light source for use in gas sensing or as a visible light source, as demonstrated by Kim *et al.* [11]. These include; excellent in-plane thermal conductivity, due to the covalent bonding of the carbon atoms; poor out of plane thermal conductivity, due to weak interlayer Van der Waals forces; the ability to sustain large current densities (orders of magnitude larger than tungsten filaments), with Lee *et al.* demonstrating a breakdown current density of 4×10^7 A/cm^2 for CVD multilayer graphene wires [12]; an extremely low thermal mass (orders of magnitude lower than any other incandescent source), due to its 2D nature, potentially allowing for much higher modulations speeds than other incandescent sources.

In addition to the potential gas sensing applications, devices presented in this work offer a test bed to examine the impact of thermal management on device operation. They also allow for the examination of the effect of integrated metamaterial structures on the spectral response of the graphene based devices and if patterned substrates can be utilised to incorporate aspects of thermal management and spectral control into the devices substrate. Finally, while thermal emission has predominantly been utilised to investigate the electronic structure of much smaller, exfoliated single-layer graphene transistor devices under bias [13–15] it can also be used to characterise the electronic structure of the much large CVD single and multilayer graphene devices presented in this work [16,17].

1.2 Overview

The results presented in this thesis are among the first in the study of chemical vapour deposition (CVD) graphene based infrared (IR) emitters. Investigations performed on the CVD graphene IR emitters include: the spatial variation of the thermal emission along with the gate dependence, frequency dependence of the emission intensity and spectral measurements (both emission and reflectance) from device with flat substrates, patterned substrates and graphene encapsulated devices with an integrated metamaterial structure on top. Simulations are also performed utilising the finite element software, COMSOL. This work demonstrates the potential application of graphene IR emitters, in areas such as gas sensing, with aspects being adapted for publication in various journals including; Thermal emission from large area chemical vapor deposited graphene devices, Applied Physics Letters **103**, 131906 (2013); Prospective for graphene based thermal mid-infrared light emitting devices, AIP Advances **4**, 087139 (2014); Modulation characteristics of graphene-based thermal emitters, Applied Physics Express **9**, 12105 (2016) and Boron nitride encapsulated graphene infrared emitters, Applied Physics Letters **108**, 131110 (2016). This thesis is structured as follows:

Background information on infrared thermal emission is presented in Chapter 2. The first section provides information on blackbody radiation, including details on the emittance spectra of blackbodies, Planck's law, grey-bodies and Joule heating. This is followed by a discussion of 2D materials, including the electrical and thermal properties of graphene and hexagonal boron nitride principally. Finally, the last section discusses modelling, including background information

on the finite element method, meshing and the software chiefly utilised for the simulation results presented in this thesis, COMSOL.

Chapter 3 provides details on the methodology involved in the fabrication of the graphene based IR emitter devices. First, background information on the preparation of graphene and the characterisation process of h-BN and graphene is discussed. This is followed by information on the electron beam fabrication technique utilised, along with a description of the processes used for the transfer of CVD graphene/h-BN to various substrates. Additionally, the fabrication of metal contacts and metamaterial structures are discussed, alongside the bonding and packaging of devices into conventional 20 pin chip carriers. Finally, the last section which summarises the multistage fabrication processes involved in the fabrication of single and multilayer graphene devices on SiO_2/Si and h-BN encapsulated few-layer graphene devices.

Chapter 4 presents information on the experimental methodology involved in the measurement of the devices detailed in this work. The electronic characterisation of the devices, utilising current vs. voltage measurements and field effect characteristics measurements, is discussed first. This is followed by the discussion of the set-up for the spatially resolved thermal emission and reflectance measurements of the graphene devices, with details on cadmium mercury telluride detectors and lock-in amplifiers provided. A description of the grating spectroscopy measurement system, including background information on grating spectrometers, utilised in the measurement of device spectra is provided next. Finally, the set-up of the Fourier transform infrared spectroscopy (FTIR) measurement system for both emittance and reflectance spectroscopy

measurements of the devices is discussed, with background information of on FTIR spectrometers provided.

Chapter 5 investigates the spatial variation of the thermal emission from both single-layer graphene (SLG) and few-layer graphene (FLG) infrared emitters. The emission from the SLG devices is also investigated as a function of back gate voltage. It was observed that the location of maximum emission could be moved along the length of the channel of the graphene device by applying different back gate voltages, mirroring what was observed for exfoliated graphene devices [15]. This confirmed that the much larger CVD SLG devices retain characteristic electronic transport properties of graphene [16], while the results from the FLG device suggest that they can be thought of like a classic filament bulb with uniform channel resistance. Results from devices similar to the ones discussed in this part of the chapter are published in Thermal emission from large area chemical vapor deposited graphene devices, Applied Physics Letters **103**, 131906 (2013). Chapter 5 also investigates the modulation characteristics of both the SLG and FLG devices, In addition to an h-BN encapsulated FLG device. All three could be driven with drive current frequencies up to 100 kHz, with a significant drop off in emission intensity observed in each of the different devices. At higher frequencies the greatest normalised emission intensity was observed for the encapsulated device. Comparing the measured results to COMSOL simulations suggests that heat dissipation into the substrate limits the performance of the devices at high drive frequencies. Adapted forms of this part of the chapter are published in both Modulation characteristics of graphene-based thermal emitters, Applied Physics Express **9**, 12105 (2016) and Boron nitride encapsulated graphene infrared emitters, Applied Physics Letters **108**, 131110 (2016).

The possibility to narrow emission spectra from the graphene devices is investigated in Chapter 6. From obtained measurements of the emission spectra of the SLG and FLG on SiO_2/Si, it was determined that devices emit grey-body emission. An adapted form of this part of the chapter is published in Prospective for graphene based thermal mid-infrared light emitting devices, AIP Advances **4**, 087139 (2014). Simulations suggest that spectral narrowing can be achieved, with controllable peaks in the calculated spectra, by incorporating metamaterial structures, ring resonators and split ring resonators, on top of the h-BN encapsulated few-layer graphene devices. FTIR reflectance spectra of devices with six different ring resonator unit cell designs, along with emission measurements from four of the six confirm that the ring resonators predictably tune showing good qualitative agreement with the simulations. Additionally, preliminary results from devices with split ring resonators replacing the ring resonators on top of the encapsulated graphene emitters are presented and discussed. This chapter is currently being adapted with the aim of publication.

Chapter 7 investigates graphene transferred on top of patterned substrates, gallium nitride (GaN) nano-rods (NR) specifically. Patterned substrates are investigated for the possibility of altering the spectral response of the graphene emitters, in addition to reducing the heat dissipation into the substrate. Finite difference time domain simulations by a collaborator, Mr. Bofeng Zhu, suggest the possibility of exciting plasmon modes and using them to characterising the CVD graphene transferred on-top of the GaN NRs. Two different GaN NR arrays were provided by collaborators at the University of Bath for utilisation as patterned substrates. To facilitate the transfer of continuous graphene on top of the NR arrays the standard CVD transfer process was modified, with the quality of the transfer characterised with scanning electron microscopy. To characterise the

spectral response of the NR arrays their reflectance spectra was normalised to that of an Au mirror. In each sample two minima were observed at wavelengths within the Reststrahlen band, which are attributed to localised surface phonon polariton resonance modes. Finally, the effect of the graphene on the spectral response of the samples was examined by normalising the measured reflectance spectra from NR array with graphene on to bare NR arrays. No minima in the spectral response of the graphene could be attributed to the excitation of the plasmon modes. This suggests that the quality of the graphene is comparable to CVD graphene transferred to unpatterned substrates.

Chapter 8 provides a brief summary of the results presented in this thesis in addition to suggestions of future research to be performed.

1.3 Applications

1.3.1 Gas Sensing Sources

Many important polyatomic gases have unique absorption bands in the mid-IR region (2.5-25 μm) of the electromagnetic spectrum. For example, CO_2 has a characteristic intense absorption band at ~4.3 μm [18]. One of the most common gas sensing techniques utilised in industry is broadband, non-dispersive IR gas sensing (NDIR), due in large part to the compact design (optical path length of 3-20 cm) and simplicity of the measurement systems [19]. They generally consist of a filter, a broadband mid-IR detector, and a broadband mid-IR emission source. Common applications that utilise NDIR include, the monitoring of atmospheric

CO_2 levels in industries such as brewing, patient monitoring in the health care industry, methane detection in mining and air conditioning control. Properties of an ideal gas sensing sources for NDIR gas sensing include; sufficient optical power for the detection of the specified target gas; high modulation frequency, for a better signal to noise ratio and suitability for use with various detectors and lock-in amplifiers; low cost; steady emission output; and long lifetime.

1.3.2 Existing technology

There are currently a variety of mid-IR light sources available for NDIR gas sensing systems. This includes incandescent micro-bulbs, incandescent thin film structures based on microelectromechanical systems (MEMS) technology, semiconductor light emitting diodes (LEDs) and mid-IR lasers. The advantages, and disadvantages of each are summarised in table 1.1, in addition to graphene based IR emitters, and they are discussed in more detail in the following sections.

Table 1.1 Summary of advantages and disadvantages of various MIR sources.

Mid-IR Source	Advantages	Disadvantages
Micro-bulbs	• Inexpensive ($1-2) • Relatively high spectral emission	• Slow modulation speed (1-3 Hz) • Poor spectral efficiency • Requires inert atmosphere • High power consumption • Short device lifetime
Thin Film MEMS	• Faster modulation than micro-bulbs (up to 100 Hz) • Can be operated in atmosphere • Improved spectral efficiency compared to micro-bulbs • Improved device lifetimes	• More expensive than micro-bulbs • Generally lower total emitted power • Not fast enough modulation speed
LEDs	• Can be modulated at significantly higher drive frequencies • High spectral efficiency • Relatively high power efficiency • Longer lifetimes than thermal sources	• Low output power (typically less than 1 mW) • Centre wavelength of LED Emission is typically temperature sensitive • May require temperature control or compensation • Better suited for use with semiconductor detectors rather than thermal detectors (more expensive) • Commercial unavailable for longer IR wavelengths
Lasers	• High signal to noise ratio • High output power • A high degree of specificity to the target gas • Fast operation (MHz or above)	• Very expensive (thousands of dollars) • Interference effects limit detection sensitivity • Use semiconductor detectors rather than thermal detectors (more expensive)
Graphene	• Inexpensive • Highest modulation speed of thermal sources • Improved spectral efficiency • Can be operated in atmosphere • Suitable for integration with metamaterial structures	• Low emissivity • Relatively low output power • Thermal path plays significant role in the emission characteristics

1.3.2.1 Incandescent micro-bulbs

The most common mid-IR light sources in NDIR gas sensing systems on the market today are incandescent micro-bulbs. Micro-bulbs primarily utilise a tungsten coiled wire filament, due to the high melting point of tungsten. These IR sources operate on the Joule heating principle discussed in more detail in section 2.2.4. The primary advantages of the micro-bulb sources are their low cost ($1-2 [20]) and relatively high spectral emission [20]. However, their usability as an IR source for gas sensing is limited by multiple drawbacks. Tungsten's emissivity is dependent on both temperature and wavelength, with the average emissivity of tungsten at 2441 K measured to range from ~0.37 at λ = 1 μm to ~0.12 at λ = 5.2 μm [21], a 67% decrease. The operating temperature is extremely high (up to 3000 K), resulting in poor spectral efficiency, as the majority of the spectral emission occurs in the near-infrared region [22], away from the targeted absorption bands of most gases. Additionally, Puton *et al.* suggest that emission in the near-IR can be a source of erroneous components in the IR detector signal [23]. The high operating temperature also necessitates the operation of the devices in an inert atmosphere to prevent oxidation of the filament. This requires the devices to be placed in glass enclosures, with the glass envelope having negligible transmittance at wavelengths longer than 5-6 μm. The life time of a typical micro-bulb source is limited compared to the other existing technologies, with a lifetime as short as 5000 hrs for devices driven by high amperage drive currents. Finally, the electronic modulation frequency of the micro-bulbs is generally less than 10 Hz (frequencies at which 1/*f* noise can be an issue in infrared detection), due to the relatively high thermal mass of the filament, while the power consumption is relatively high, typically on the order of hundreds of

milliwatts to watts. The primary focus of recent research into mid-IR gas sources has been on developing new sources with improved modulation speed and spectral efficiency in comparison to the incandescent micro-bulbs.

1.3.2.2 Incandescent Thin Film MEMS

Incandescent thin film sources based on microelectromechanical systems (MEMS) technology operate on the same Joule heating principle as the tungsten coil micro-bulbs, discussed in the previous section. They can be thought of essentially as thin film versions of the conventional micro-bulbs. They are often silicon based, offering the advantage of being complementary metal-oxide-semiconductor (CMOS) compatible. Standard micromachining processing techniques are applied to fabricate the thin films which can be divided into two categories, suspended-membrane, (suspended by micro bars) [24] or closed-membrane [25]. The emission spectra from these mid-IR sources are primarily that of a grey-body, discussed in more detail in section 2.2.3. These sources overcome some of the micro-bulb shortcomings. Operating temperatures are typically much lower, 600-1400 K, allowing for operation in atmosphere, longer life times and higher spectral efficiency. Additionally, as a result of the micro-machining process, the thermal mass of the thin films are generally much lower compared to the coils of the micro-bulbs. The modulation frequency of the thin film MEMS sources are therefore consistently higher, ranging from 20-100 Hz [5,24,26–28]. However, to achieve the higher modulation frequencies, smaller device dimensions are typically utilised in order to further lower the thermal mass. This results in a reduction in total emitted power compared to the larger, slower, thin membrane emitters [27] and while the response times are improved

compared to the micro-bulbs, they are not fast enough to allow for more advanced signal processing techniques.

1.3.2.3 Semiconductor LEDs and Lasers

As opposed to the broadband thermal sources discussed in the previous sections the mid-IR semiconductor light emitting diodes (LED) are designed to emit at wavelengths that cover the specific absorption band of the designated target gas. This results in improved spectral efficiency compared to both the micro-bulbs and membrane sources, due to better matching between the specific absorption band and the LED emission spectra [29]. Mid-IR LEDs have been shown to operate in both forward bias (electroluminescence) [30,31] and reverse bias (negative luminescence) [32] modes. Recently, results have been presented for mid-IR LEDs based on interband cascade [33,34] and optical pumping [35] mechanisms. In addition to superior spectral efficiency, LED sources can be modulated at significantly higher drive frequencies [36]. A disadvantage of the LED sources is their relatively low output power, typically less than a milliwatt [30,33,37–39]. For adequate gas sensing of low concentration gases Smith *et al.* suggest a mid-IR continuous wave operating power of at least 1 mW [36], suggesting that LED sources are not ideal for the detection of gases at low concentrations due to their low output power. Improvements to the emitted power could be achieved with a pulsed drive current [19], with square wave drive currents (50% duty cycle) having demonstrated the largest signal to noise ratios [40]. Weik *et al.* have demonstrated a mid-IR optically pumped LED source with a continuous wave operating power of 2 mW [35]. Additionally, there are also sustainability issues with MIR LEDs, as they typically include elements such as Indium or Gallium. In

addition to LEDs, MIR lasers are also used as MIR sources for gas detection applications. However, they are not suitable for NDIR gas detection, for various reasons, but for a different technique called tuneable diode laser spectroscopy (TDLS). More information on TDLS can be found in a review paper on optical gas sensing by Hodgkinson *et al*. [19], however, going into detail on TDLS is outside the scope of this thesis.

2 Infrared Thermal Emission

2.1 Overview

A body at a temperature greater than absolute zero emits electromagnetic radiation that is generated by the thermal motion of charged particles; this phenomenon is termed thermal radiation/emission. Lattice vibrations and rotations in a solid results in localised oscillations in the electron density. Dipole-oscillations arise, resulting in the generation of coupled electric and magnetic fields. Electromagnetic energy is then radiated away from the body in the form of photons. A similar effect is produced in liquids and gases as a result of the random thermal motion of their particles. The first scientific studies of thermal radiation came at the beginning of the 17th century when Sir Francis Bacon proved the existence of “invisible heat rays” that could be focused by using mirrors. The emission often lies within the infrared (IR) region of the electromagnetic spectrum, first discovered by William Herschel in 1800 when he passed sunlight through a prism and placed a thermometer just beyond the red part of the spectrum. Max Planck later discovered in 1900, when studying blackbody radiation, that in order to explain his experimental data theoretically, he had to assume that the energy of vibrating molecules was quantised. In 1905, based on Planck’s work, Einstein developed the concept of the photon, the quanta of electromagnetic radiation. In the far field there are four principle properties that characterise thermal radiation: The thermal radiation spectrum from a body is composed of a wide range of frequencies, given by Planck’s law; as the temperature of the body increases the frequency range shifts to higher

frequencies, determined by Weins displacement law; the total radiated power scales with the temperature to the fourth power, determined by the Stefan-Boltzmann law; the emissivity of a body has to equal the absorptivity at each wavelength to maintain thermal equilibrium, which is given by Kirchhoff's Law $\varepsilon_\lambda = \alpha_\lambda$.

2.2 Blackbody Radiation

A blackbody is an object that absorbs 100% of the radiation that is incident on its surface, regardless of frequency or incidence angle. It is therefore an ideal absorber, and anything that is an ideal absorber is also an ideal radiator. The emissivity of blackbody is unity where emissivity is a dimensionless quantity, between 0 and 1, a ratio of the rate of radiation from a surface to the rate of radiation from an ideal radiator. The name blackbody is used because under illumination it would appear totally black, reflecting no light. At thermal equilibrium a blackbody emits a continuous-spectrum of electromagnetic radiation (EM), equal to its absorption spectrum, termed blackbody radiation. Blackbodies are termed ideal emitters because at each frequency of the blackbody radiation spectra the emitted energy is greater than any other real physical body, at the same temperature. Additionally, they also function as diffusive emitters [41], meaning the emission is independent of direction (isotropic).

2.2.1 Spectrum

A plot of measured blackbody radiation spectra at three different temperatures is shown in Figure 2.1 [42]. The measured spectral emittance varies both with wavelength and the temperature of the blackbody with the total emitted intensity also changing with temperature. The total intensity, I_T , at a specific temperature, T , is given by the Stefan–Boltzmann law

$$I_T = \sigma T^4 \tag{2.1}$$

where σ , the Stefan-Boltzmann constant, is equal to 5.67×10^{-8} $Wm^{-2}K^{-4}$. Additionally, the wavelength corresponding to the maximum in spectral emittance shifts to shorter wavelengths as the temperature increases. This shift is a constant given by Wiens displacement law

$$\lambda_m T = 2.9 \times 10^{-3}\mathrm{mk} \tag{2.2}$$

where λ_m is the peak in spectral emittance and T is the temperature of the blackbody. While the peak in the intensity shifts with increasing temperature the shape of the spectral emittance is the same for all temperatures. Finally, the total radiated power from the blackbody is equal to the area under the curve and can be calculated by taking their integral with

$$P = \int_0^\infty I(\lambda)\, d\lambda \tag{2.3}$$

where P is the total radiated power $I(\lambda)$ is the intensity per wavelength interval.

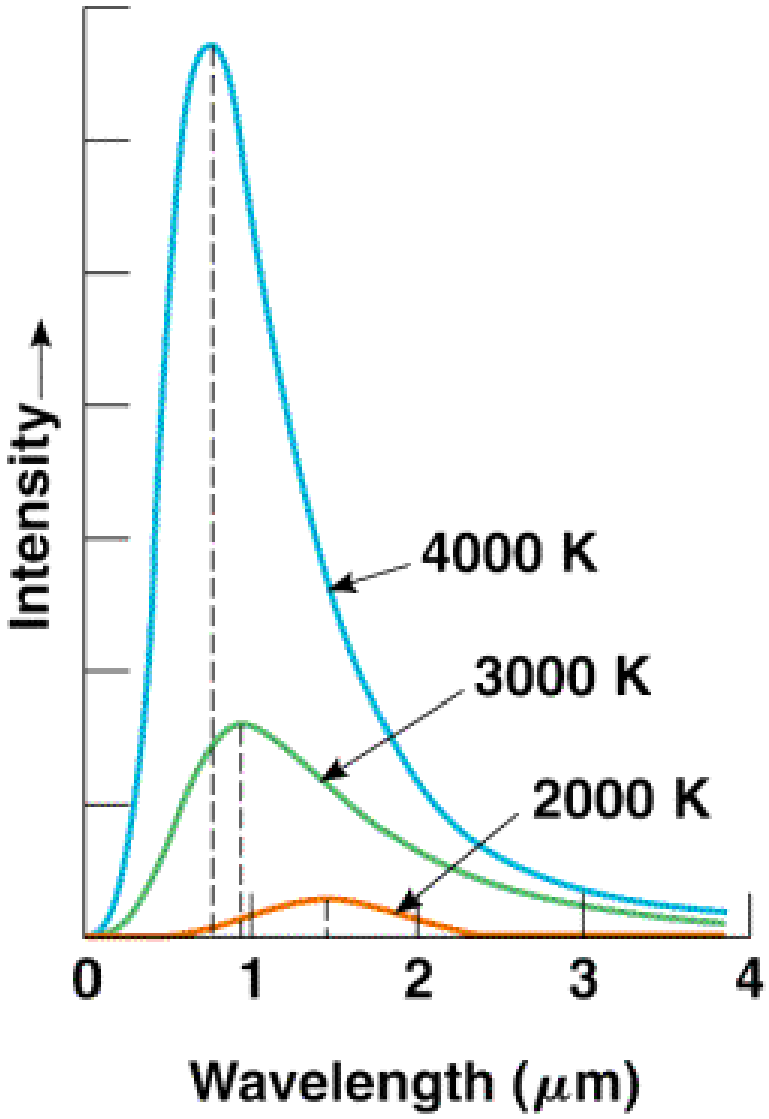

Figure 2.1 Blackbody spectra at three different temperatures (illustration taken from [42].)

2.2.2 Planck's Law

Classical theories are unable to explain the experimental results presented in Figure 2.1, with the theory deviating from the measured results at short wavelengths (the "ultraviolet catastrophe"). In 1900 Planck developed a model, Planck's radiation law, which agrees very well with experimental spectral

emittance. Planck's radiation law states the spectral emittance of a blackbody, B_λ, is given as

$$B_\lambda(\lambda, T) = \frac{2hc^2}{\lambda^5} \frac{1}{e^{\frac{hc}{k_B T \lambda}} - 1} \tag{2.4}$$

where k_B = 1.38 × 10^{-23}, Boltzmann's constant, h = 6.63 × 10^{-34}, Planck's constant, T is the temperature of the blackbody, c is the speed of light and λ is the wavelength. Figure 5.2 shows the blackbody spectral emittance calculated by Planck's radiation law compared to the measured spectra from a blackbody source at the same temperature. It can be observed that there is very good agreement between the experimental results and Planck's radiation law.

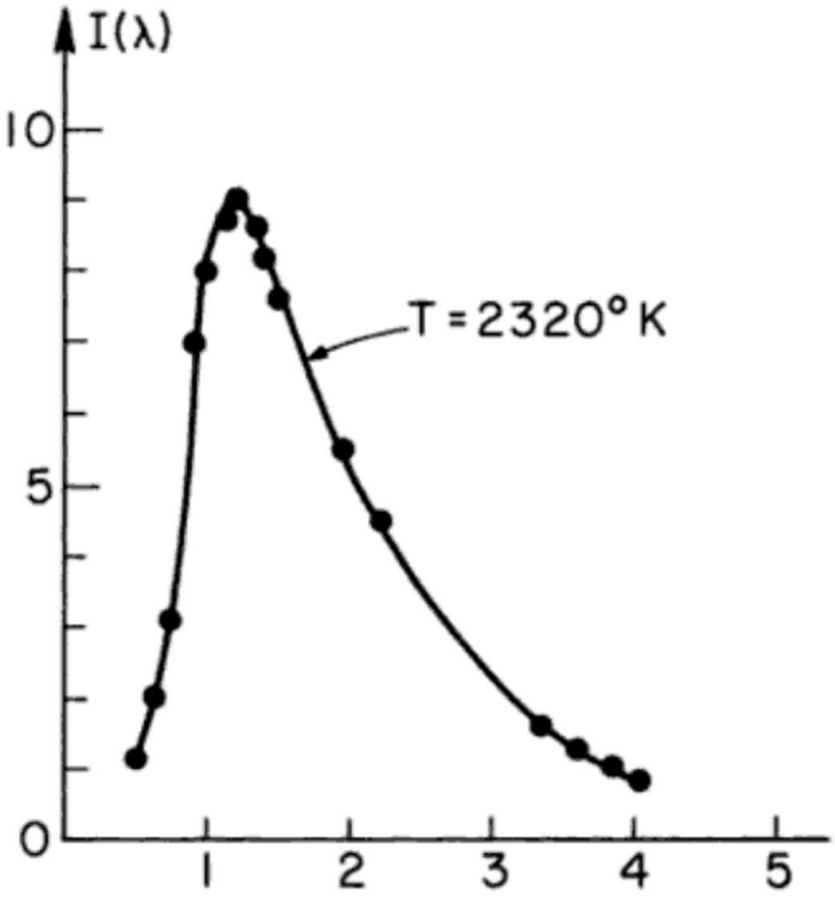

Figure 2.2 Measured (black circles) and calculated (black line) blackbody spectrum from a 2320 K source (illustration taken from [43]).

2.2.3 Grey-bodies

The majority of radiation sources are not blackbodies. Instead of absorbing 100% of the incident light, some is reflected/transmitted. For these systems the emissivity, the ratio of the spectral emittance of such a source to the spectral emittance of a perfect blackbody, is less than unity. These systems can be broken down into two categories, selective radiators and grey-bodies. The emissivity, and therefore the spectral emittance, of a selective radiator varies with frequency, and temperature, as shown in Figure 2.3. Alternatively, the emissivity of a grey-body does not depend on frequency, therefore the spectral emittance from a grey-

body is simply proportional to that of a black body, at the same temperature, as displayed in Figure 2.3. Thermal emission experiments of exfoliated graphene have shown it to behave as a grey-body source [15]. The spectral energy of a grey-body, at a specific wavelength and temperature, can be calculated by using a modified version of Planck's law which includes the dimensionless emissivity quantity. This modified Planck's law is given as

$$\mu_\lambda(\lambda, T) = \frac{2hc^2}{\lambda^5} \frac{\varepsilon}{e^{\frac{hc}{k_B T \lambda}} - 1} \tag{2.5}$$

where ε is the emissivity. The emissivity of single-layer graphene has previously been measured as $\varepsilon = (1.6 \pm 0.8) \times 10^{-2}$ [15] similar to the measured absorptivity $\alpha = 2.3 \times 10^{-2}$ [44,45] as would be expected of a grey-body. The optical absorption of graphene, and therefore the emissivity, was also shown to be proportional to the number of layers [46]. As the reflectance of single-layer graphene is $< 1.0 \times 10^{-3}$ of incident light in the visible region [44], rising to $\sim 2.0 \times 10^{-2}$ for ten layers [47], the transparency can be estimated as 97.7×10^{-2}.

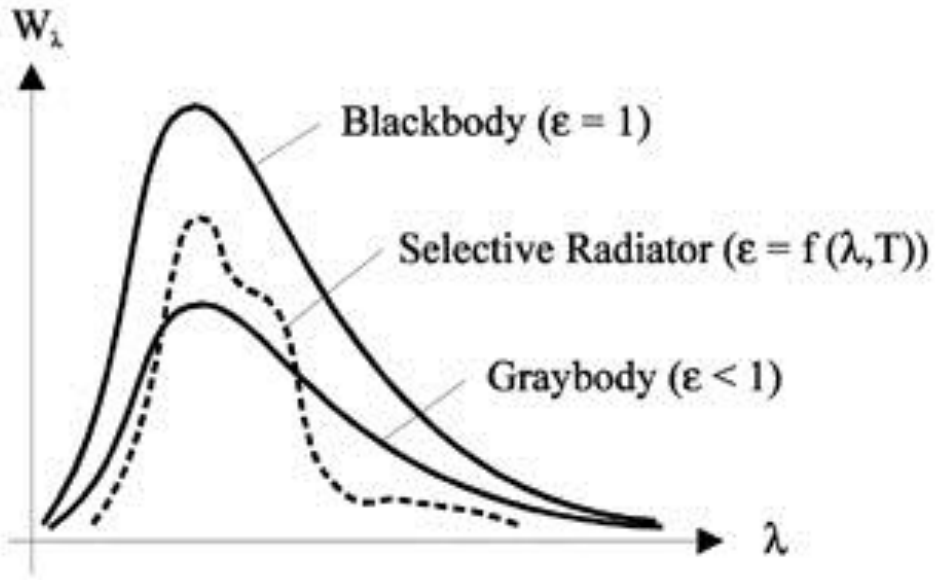

Figure 2.3 Calculated blackbody spectra (black line) at 673 K compared to a calculated grey-body spectra at 673 K with an emissivity of 0.9 (illustration taken from [48]).

2.2.4 Joule Heating

An electric current flowing through a material with some resistance generates heat, termed Joule heating (sometimes resistive heating), as a result of retarding forces and charge carrier collisions. It is the heat that corresponds to the work done by the charge carriers in travelling from higher to lower potentials [49]. Joule heating in semiconductor devices is a result of energy loss by the carriers to the lattice. Hence, the spatial distribution of Joule heating is determined by the local current density and electric field strength (***J*·*E***), with regions of large local electric fields and current densities experiencing greater Joule heating [50]. The heat generated as a result of Joule heating can either be an unwanted consequence, resulting in resistive losses, as for power transmittance lines [51] and interconnects [52], or it may be intended by design, as in annealing [53],

nanostructure fabrication [54] and light sources [11]. The power generated by Joule heating is given by Ohm's law

$$P = I^2R \tag{2.6}$$

for a DC drive current, while the instantaneous power for an AC drive current is given by

$$P(t) = I(t)^2R \tag{2.7}$$

with the average power (P_{avg}) determined by replacing $I(t)$ with I_{rms}, the root mean square current. The heat generated, H, is therefore proportional to the current squared for a constant resistance.

2.3 2D Materials for Thermal Emission

2.3.1 Overview

Since the discovery of graphene in 2004 [7] a variety of different 2D materials have been isolated, including transition metal dichalcogenides such as molybdenum disulfide (MoS_2) [55] and tungsten diselenide (WSe_2) [56], hexagonal boron nitride (h-BN) [57] and phosphorene [58], to name a few. The 2D materials can be metallic [59], semi-metallic [60], semiconducting [61] and dielectric [62]. The following sections focus primarily on the properties of graphene and h-BN as they are the two 2D materials examined in this work.

2.3.2 Electrical Properties

2.3.2.1 Electric Field Effect

Graphene is a 2D allotrope of graphite, with sp^2 bonded carbon atoms arranged in a trigonal planar orientation, leading to a honey-comb lattice structure. The unit cell is composed of two carbon atoms, A and B, as displayed in Figure 2.4(a). Of the four valance electrons in carbon, three are utilised in the formation of strong σ bonds with nearest neighbour carbon atoms (they do not participate in electron transport). The fourth valance electron forms a $2p_z$ orbital that overlaps with the $2p_z$ orbital of the nearest neighbour carbon atom, due to short length of the σ bonds, forming delocalised π (valance) and π* (conduction) bands. Electronic properties of graphene can be assessed by examining the π-band structure, calculated using the tight-binding method as displayed in Figure 2.4(b). It can be observed that the valance and conduction bands “meet”, as opposed to slightly overlapping as in graphite. Therefore graphene is commonly referred to as a zero band gap semiconductor, or more accurately a semi-metal [8]. The points where the valance and conduction bands “meet” are termed the Dirac points and near these points the bands are conically shaped. It is this unique shape of the energy bands near the Dirac point that results in graphene’s unique electronic properties. In undoped, pristine graphene, the Fermi level is situated at the points where the valence and conductions bands meet, resulting in an empty conduction band and a completely filled valance band.

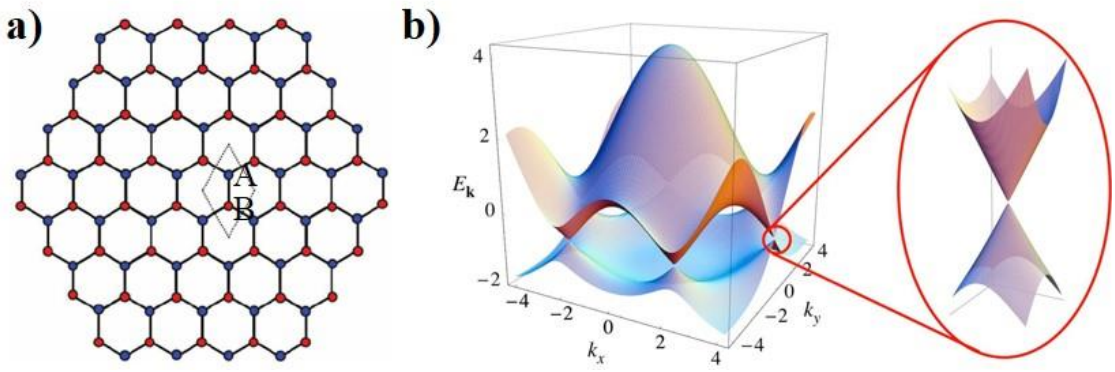

Figure 2.4 a) Illustration of graphene honey-comb lattice structure including the unit cell with carbon atoms A and B. b) Electron energy bands of graphene calculated using the tight-binding method (illustration taken from [8]).

In a semiconductor a gate voltage, V_g, can be used to change the carrier concentration along the conductive channel through the effect of the electric field. In semiconductors the relatively small carrier density, compared to metals, allows for the penetration of the electric field into the material. This alters the conductivity near the surface of the semiconductor and is called the field effect. Figure 2.5 shows a schematic of a graphene field effect transistor with the typical Hall bar geometry used to examine this effect in graphene devices. For these measurements a source contact is used to apply a source current, I_{xx}, and it is passed to the drain through the graphene. A voltage drop, V_{xx}, can then be measured longitudinally in order to calculate the resistivity/conductivity of the graphene. Using the back gate (or top gate) charge carriers can be induced as shown in figure 2.5(b). For a typical field effect transistor a plot of current as a function of voltage would show the current increasing linearly with applied voltage until it would level off (saturate) above a certain applied voltage. At this point the only way to further increase the current would be by applying a gate voltage and inducing more charge carriers. In this example the SiO_2 acts as a dielectric and the Si is heavily p-doped, improving it's conductivity, and is used as the back

gate. Electron and hole charge carriers can be induced in the graphene by applying a positive or negative gate bias respectively. It is then possible to calculate the charge density using the gate capacitance. For typical SiO_2/Si substrates with 300 nm oxide layer, like the SiO_2/Si substrates used for some of the fabricated devices presented in this work, the capacitance is known as 1.15 × 10^{-4} Fm^{-2}.

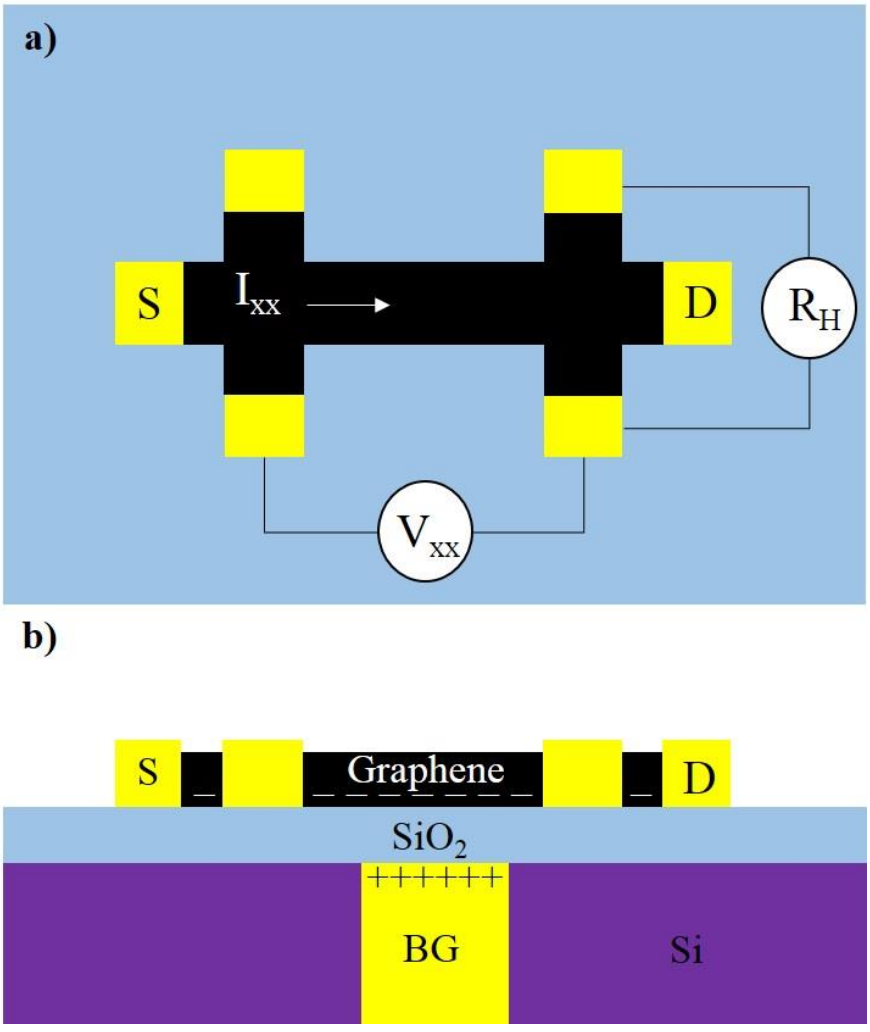

Figure 2.5 a) Planar diagram of a typical Hall-bar geometry used for field effect measurements, where the source (S) contact passes a current, I_{xx}, to the drain (D) contacts and the voltage drop, V_{xx}, is measured longitudinally and the Hall coefficient R_H, is measured transversally. b) Cross-section diagram of a typical back gated device.

Measurements of resistivity, as a function of gate voltage for single-layer graphene on SiO_2/Si, have revealed a sharp peak in resistivity at a specific gate voltage [7], V_0 (Dirac voltage), as illustrated in Figure 2.6. The peak at V_0 is located at the point where the Fermi level crosses the charge neutrality point (CNP) or Dirac point. At the CNP (Dirac point) the effective carrier density is zero, resulting in a maximum in the resistivity at the Dirac voltage. Near this point the conductivity, σ, is linear with changing gate voltage. The field effect mobility, μ, can then be calculated as

$$\mu = \frac{d\sigma}{dV}\frac{1}{C} \tag{2.8}$$

where C is the gate capacitance.

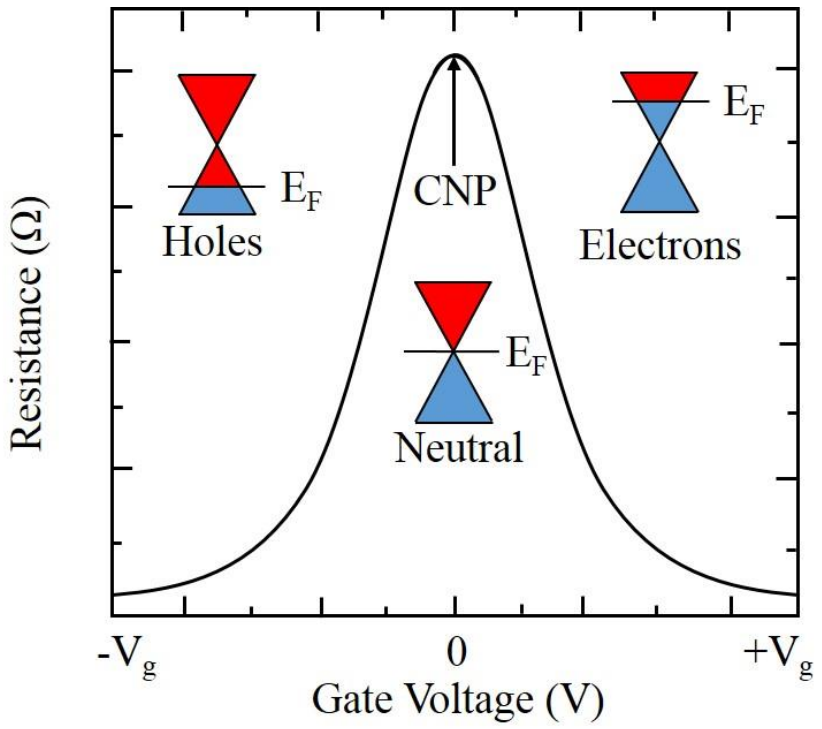

Figure 2.6 An example of a typical transfer curve; resistivity of graphene as a function of gate voltage (V_g) showing the ambipolar nature of graphene. The insets indicate how the Fermi level shifts by inducing charge carriers through an applied gate voltage.

The value of the Dirac voltage is indicative of the amount of dopants present in the graphene. In undoped, pristine graphene, the Dirac point is located at $V_0 = 0$ V. Dopants introduced in the transfer process, like absorbed water molecules, can shift the Dirac voltage away from $V_0 = 0$ V. The location of these absorbed water molecules determines whether the dopant is p-doping (surface of the graphene) or n-doping (between the graphene and the substrate) [63]. Additionally other sources of doping include the exposure to $FeCl_3$ [64] or NH_3 [65] which can lead to p- or n-doping respectively, with p-doping causing V_0 to shift to positive gate voltages and n-doping causing a negative shift in V_0 [66]. Finally the absorption of dipolar molecules like water and ammonia can also lead

to hysteretic behaviour in the field effect measurements, due to flipping of the molecular dipoles [67].

Hexagonal boron nitride is extremely similar to graphene structurally. It has the same honey-comb lattice, with alternating sp^2 bonded boron and nitrogen atoms, and the same layered structure of graphene/graphite. However, h-BN is different from graphene as it is an insulator, with a bandgap of 5.97 eV [68]. H-BN is also an excellent dielectric with a similar lattice constant to graphite. The dielectric constant of h-BN has been shown to be~2-4 while the break down electric field has been shown to range from 1.5-2.5 $MVcm^{-1}$ respectively [69]. The use of h-BN as a dielectric layer in graphene devices has been shown to improve the mobility of those devices in comparison to graphene on SiO_2/Si by an order of magnitude [70]. Dean *et al.* also demonstrated reduced roughness, intrinsic doping and chemical reactivity for the graphene on h-BN devices compared to graphene on SiO_2/Si [70]. This makes h-BN an extremely exciting material as a dielectric layer in 2D Heterostructures.

2.3.2.2 Joule Heating Hot Spot

Due to graphene's unique band structure, it exhibits novel transport effects including a minimum conductivity and ambipolar charge transport, where both holes and electrons act as charge carriers along the graphene channel, that are not found in other "conventional" materials [71]. As with "traditional" semiconductors, under an applied source-drain bias the carrier density of graphene varies along the length of a graphene channel. In semiconductor devices, and graphene under unipolar charge transport, a "hot spot " (localised

temperature maximum) will form when under an applied current bias, either at the source or the drain depending on the direction of the current bias and the type of charge carriers [16]. In graphene devices, it was confirmed that the “hot spot” is electrostatic in nature and is the effect of a localised increase in the heat generated due to Joule heating [14]. The “hot spot” marks the physical location of the lowest carrier-density, and therefore the location of highest resistivity. In exfoliated graphene devices it was shown that under the right bias conditions, both holes and electrons can act as charge carriers, due to graphene’s ambipolar nature, resulting in the “hot spot” moving away from the source/drain and into the middle of the channel. The specific location could then be moved by changing the carrier concentration with the applied gate voltage, as is shown in Figure 2.7. Additionally, not all “hot spots” observed in graphene devices are due to the varying carrier density along the channel. Freitag *et al.* [15] found stationary “hot spots” that do not move with changing gate voltage and “hot spots” that turn into “cool spots” when the carrier type is changed. These were attributed to defects in the graphene and trapped charges in the oxide respectively.

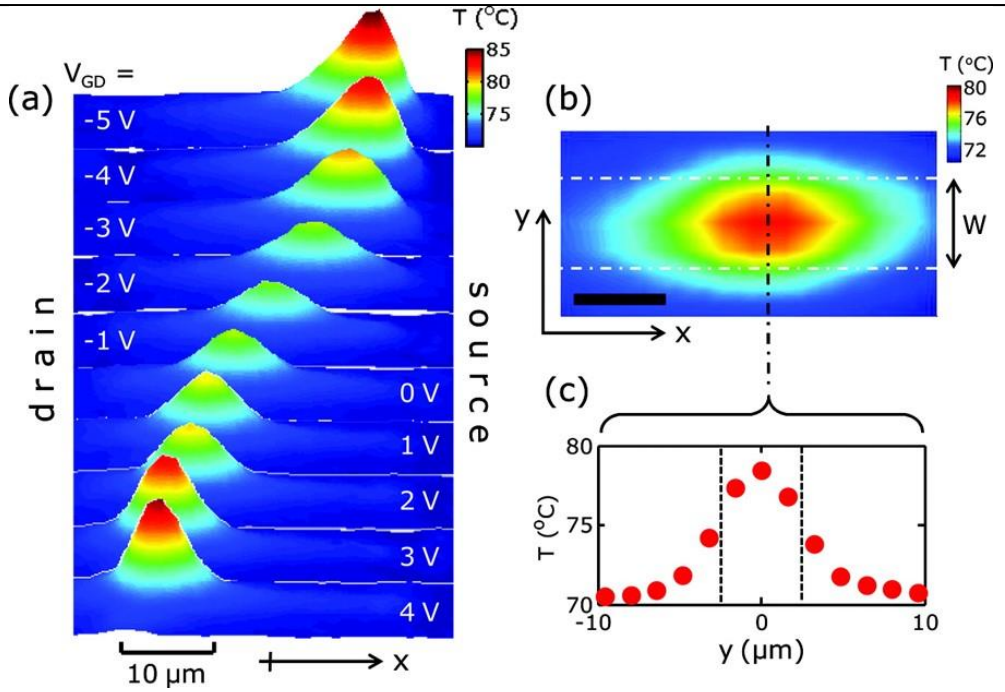

Figure 2.7 a) Spatially resolved thermal emission mapping along graphene field effect transistor devices as a function of the applied gate-drain voltage, V_{GD}. b) "Hot spot" top down view with V_{GD} = -2V. c) Cross-sectional temperature profile taken along the dashed line shown in b) (illustration taken from [14]).

2.3.3 Thermal Properties

The atomic structure of a material largely determines its thermal properties. Theoretical studies of two-dimensional crystalline materials have shown significant changes in thermal properties, like thermal conductivity, when compared to their bulk counterparts [72,73]. The successful exfoliation and discovery of graphene [7] allowed for the first experimental studies of the thermal properties of 2D materials [74]. This sparked interest in the measurement of the thermal properties of other 2D materials, like h-BN [75], however the amount of work published on the thermal properties of 2D h-BN is relatively little compared to graphene.

2.3.3.1 Phonon Dispersion

The phonon characteristics of crystalline materials, such as graphene/h-BN and their corresponding bulk crystals, are fundamentally important in determining a materials thermal properties. For example, the phonon dispersion and the phonon density of states allow for the determination (either directly or indirectly) of properties such as the specific heat and the thermal conductivity [76]. Therefore, inspection of the phonon dispersion of 2D materials is an important first step in understanding the thermal properties of the material in question. Figure 2.8(a) displays a schematic of the atomic arrangement of three layer graphene, with the dashed line in the bottom layer indicating the rhombic unit cell of graphene. The total number of atoms contained within the unit cell (UC), N, is two, as it contains two carbon atoms within the UC. The total number of optical (O) phonon modes is given by $3N - 3$. Therefore, there are a total of three optical phonon modes, while the total number of acoustic (A) phonon modes for any $N \geq 2$ UC is also three. The dispersions [77–79] of the six total phonon modes are shown in Figure 2.8(b). The three acoustic and three optical phonon modes are broken down into transverse (T), longitudinal (L) and flexural (Z). The L modes correspond to the movement of atoms along the direction of the propagation wave, T modes to the in-plane atomic displacement, perpendicular to the direction of the propagation wave and Z modes to the out-of-plane displacement unique to 2D materials like graphene. It can be observed in Figure 2.8(b) that the LA and TA dispersions are linear, for low values of q, while the ZA dispersion is quadratic. The existence of the ZA modes accounts for some of the unusual thermal properties of graphene. The graphene phonon distribution allows for the

calculation of the graphene thermal conductivity, for various temperatures, using the phonon Boltzmann transport equation (BTE) [80],

$$k = \frac{1}{4\delta}\sum_{p}\int_{\omega=0}^{\omega_{max}} v_p^2\,\tau_p D_p(\omega)\hbar\omega\frac{d\langle n\rangle}{dT}\,d\omega \tag{2.9}$$

where δ is the spacing between layers, p is the phonon polarization, v_p is the group velocity, τ_p is the relaxation time, $D_p(\omega)$ is the phonon density of states, and $\langle n\rangle$ is the Bose−Einstein distribution. $D_p(\omega)$ and v_p are calculated from the phonon dispersion.

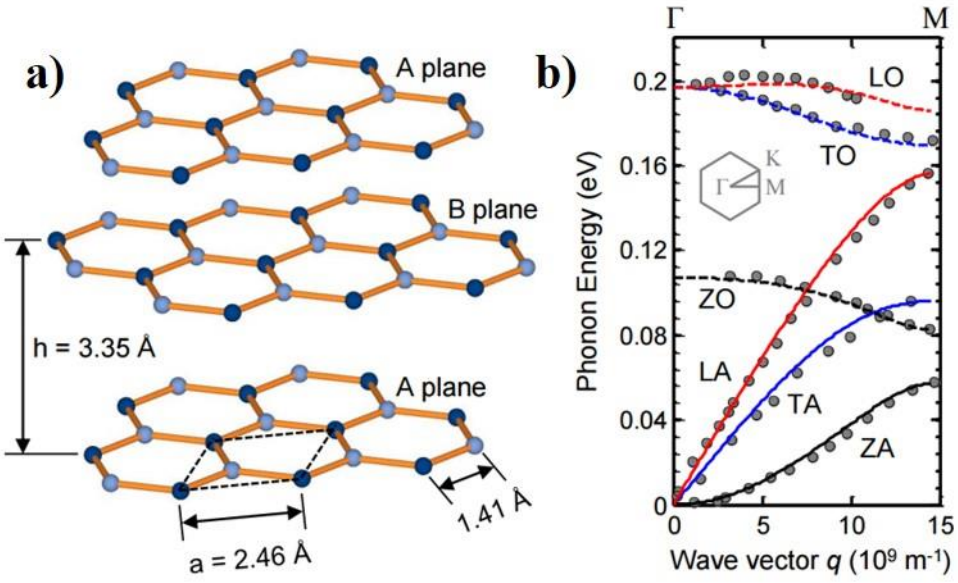

Figure 2.8 a) Illustration of atomic arrangement of graphene layers with the dashed line in the bottom layer representing the graphene unit cell. b) Phonon dispersion of single-layer graphene (illustration taken from [9])

The lattice structure of two-dimensional h-BN is isostructural to graphene, with alternating boron and nitrogen atoms replacing the carbon atoms, with the exception of the stacking order for the few-layer, as shown in Figure 2.9(a). While few-layer graphene is generally AB stacking, like graphite, h-BN favours the same

AA´ stacking of bulk h-BN [81]. Similarly to graphene there are two atoms in the crystal lattices, resulting in three optical (LO, TO and ZO) and three acoustic (LA, TA, ZA) phonon modes as shown in Figure 2.9(b). As with graphene the phonon distribution can be utilised to calculate the polarisation-specific phonon group velocity and the density of states, which in turn can be used in equation 2.9 to calculate the theoretical thermal conductivity of h-BN [75,82].

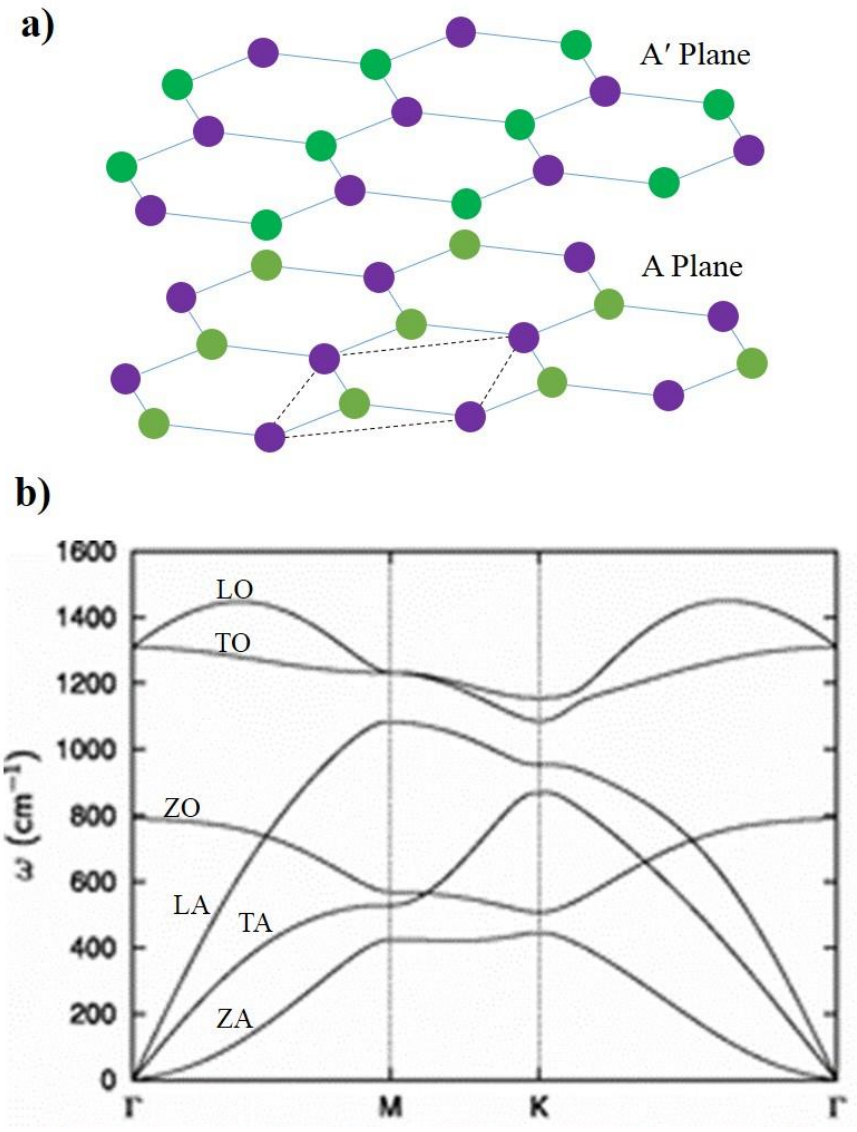

Figure 2.9 a) Schematic of atomic arrangement of bi-layer h-BN, with the dashed line in the bottom layer representing the h-BN unit cell. b) Calculated phonon dispersion of 2D h-BN (illustration taken from [83]).

2.3.3.2 Thermal Conductivity

The thermal conductivity, k, is a tensor that describes the ability of a material to conduct heat as the result of a temperature gradient. Materials with a high thermal conductivity are good thermal conductors, while materials with a low thermal conductivity are considered insulators. The heat flux per unit area, *Q″*, is related to the temperature gradient, ∇T by the thermal conductivity, $Q'' = -k\nabla T$. The thermal conductivity is negative to indicate the flow of heat from higher to lower temperatures. Under diffusive transport, the thermal conductivity is related to the specific heat by [84]

$$k \approx cv\lambda \tag{2.10}$$

where *v* is the average phonon group velocity and *λ* is the mean free path. The in-plane thermal conductivity of suspended, exfoliated, single-layer graphene has been measured optically to range from 2000-5000 $Wm^{-1}K^{-1}$ [74,85–87]. Similar values are obtained theoretically by solving the BTE for suspended SLG. The large range in measured thermal conductivities is due to variations in grain boundary size. It is expected that *k* will decrease further for samples with greater disorder, with some evidence suggesting that residues on the surface, a consequence of the fabrication process, will also result in a reduction in the thermal conductivity [80].

Optical measurements of the thermal conductivity of suspended, exfoliated, few-layer graphene (FLG) of various thickness show *k* decreases as the number of atomic layers' increases [88]. For bilayer graphene the thermal conductivity was measured as 2800 $Wm^{-1}K^{-1}$ with the value decreasing to 1300 $Wm^{-1}K^{-1}$ for a FLG

sample consisting of four atomic layers. For single-layer and bilayer graphene *k* is greater than highly ordered graphite, whilst at four layers the value of the thermal conductivity of FLG is situated between the measured values of bulk graphite and highly ordered bulk graphite. The decrease in *k* is attributed to cross-plane phonon coupling, with more layers resulting in greater coupling, and an increase in phonon scattering, reducing the thermal conductivity. In contrast to the high in-plane thermal conductivity the cross-plane thermal conductivity of graphite is ~6 $Wm^{-1}K^{-1}$ [89]. This is due to the weak van der Waals interactions between the layers.

Calculations and experiments of the thermal conductivity of h-BN as a function of the number of BN layers found that *k* of multilayer h-BN saturates at the value for bulk h-BN as the number of BN layers is increased above five layers [75,82]. Experiments of bulk h-BN have measured the room temperature, in-plane thermal conductivity to be between 600 $Wm^{-1}K^{-1}$ and the cross-plane thermal conductivity to be 30 $Wm^{-1}K^{-1}$ [90]. This large anisotropy is a result of the strong, covalent bonding between the boron and nitrogen atoms in-plane, compared to the weak van der Waals interactions between the BN layers, in the cross-plane.

2.3.3.3 Specific Heat

The amount of heat, *Q,* needed to change the temperature of a certain material is given by

$$Q = mc\Delta T \tag{2.11}$$

where m is the mass of the material ΔT is the temperature change and c is the specific heat, a quantity that depended on the material in question. The specific heat represents the amount of change in the heat for a one Kelvin change in temperature $c = dQ/(mdT)$. In addition to the amount of energy stored within an object the specific heat determines the thermal time constant τ, how efficiently an object heats up or cools down.

$$\tau = R_T cV \tag{2.12}$$

where R_T is the thermal resistance and V is the volume of the object. The thermal time constant of graphene on insulator devices was shown to be ~100 ns with a strong dependence on the substrate and capping layer [91].

There is no experimental data on the specific heat of graphene, with experimental data from graphite used instead. Phonons and free conduction electrons determine the specific heat, with phonons dominating the specific heat of graphene at temperatures greater than 1 K [92,93]. The specific heat contribution from the phonons, c_p, increases with increasing temperature, with $c_p \approx 0.7$ $Jg^{-1}K^{-1}$ at room temperature, [94] until it is nearly constant, $c_p \approx 2.1$ $Jg^{-1}K^{-1}$ at temperatures near the Debye temperature for graphene ($\Theta_D \approx 2100$ K) [95]. The Debye temperature is the temperature at which the highest frequency phonon mode (therefore every mode) is excited. It is expected that for suspended graphene the specific heat would be similar, with the specific heat of supported graphene possibly decreasing, as suggested by theoretical simulations of graphene on insulator devices [96].

The room temperature specific heat of single-layer h-BN was theoretically predicted, using atomistic simulations, to be 25.2 $Jmol^{-1}K^{-1}$, similar to the molar value of graphene, with the specific heat ranging from 24.8 – 28.2 $Jmol^{-1}K^{-1}$ over a temperature range of 200 – 3000 K. [97]. The room temperature specific heat of bulk h-BN is ~19.7 $Jmol^{-1}K^{-1}$ [98,99].The h-BN utilised in this work is approximately 13 nm thick, or ~38 layers, assuming the thickness of a single-layer of h-BN to be 0.34 nm. Some evidence suggests that the thermal properties of this many layers of h-BN approach the bulk values [75].

2.3.3.4 Role of Substrate

The substrate that graphene is supported on has been shown to impact the graphene, and therefore the performance of graphene emitters, in a number of ways. First, the high in-plane thermal conductivity measured for exfoliated graphene is greatly suppressed when the graphene is transferred on top of a substrate. As a result of the atomic thickness of the graphene, it likely that the phonon propagation is sensitive to any surface interactions. This decrease has been observed both experimentally and theoretically. The measured in-plane thermal conductivity, at room temperature, was ~600 $Wm^{-1}K^{-1}$ for exfoliated graphene on SiO_2/Si [100] and ~160 $Wm^{-1}K^{-1}$ for SiO_2 encapsulated [101]. The result of theoretical calculations are consistent with this significant decrease of in-plane thermal conductivity [102]. This reduction in thermal conductivity can be attributed to coupling and scattering of SLG phonon modes to the substrate vibrational modes [96,100,103], with Qui *et al.* [103] suggesting the use of substrates with better lattice matching and weaker coupling to the graphene to improve the thermal conductivity.

The ability for graphene to dissipate heat is important in determining the operating temperature of graphene devices [9]. The heat dissipation is generally limited by the substrate and contacts, with the impact of each depending on the length of the device. For sufficiently long devices the heat dissipation is dominated by the substrate, with numerical calculations suggesting the contacts only play a significant role in dissipating the heat from devices when the length, *l*, is less than three times the characteristic length, λ. The characteristic length defines the length scale of the in-plane heat flux into the contacts and is given by [104]

$$\lambda \approx \left(\frac{kA}{g}\right)^{1/2} \tag{2.13}$$

where *k* is the in-plane thermal conductivity, *A* is the cross sectional area, defined by *wh* (device width and graphene height respectively) and *g* is thermal conductance into the substrate per unit length. The typical value obtained for exfoliated SLG graphene on SiO_2/Si is λ = 0.1-0.2 μm [13], while encapsulating CVD few-layer graphene in hexagonal boron nitride was shown to result in a two orders of magnitude increase in the characteristic length [104,105]. A potential disadvantage, of heat dissipation in graphene based devices is that it limits the operating temperatures to temperatures that coincide with emission peak that are in the infrared range [13,15,16,105–109]. Additionally, the radiative efficiency of these devices has been shown to be poor, with only a small amount of the energy that is put into the system being converted to EM radiation, approximately 10^{-6} [15,106]. Heat dissipation into the substrate has been shown to be a primary factor in the origin of these drawbacks [110]. Suspended graphene is largely free of these negative impacts, for graphene emitters, that are a direct result of heat dissipation into the substrate [111].

2.4 Modelling

2.4.1 Finite Element Method Modelling

Finite element method (FEM) modelling, sometimes known as finite element analysis, is a numerical analysis technique utilised in determining the approximate solutions to boundary value problems for partial differential equations (PDE). In a boundary value problem the dependent variables (one or more) must satisfy the PDE/ODE (ordinary differential equation) within a known domain (field) of independent variables, in addition to conditions on the domain boundary (boundary conditions), with the field generally representing a physical structure. Examples of dependent variables (field variables) include properties such as temperature, heat flux, and current density. Within the domain, there are elements that enclose a smaller sub-domain of finite size, termed a finite element due to the element not being a differential element. For the 2D case, these elements are either triangular or quadrilateral shapes. An example of a triangular element inside a two dimensional domain is shown in Figure 2.10. The numbered vertices of this triangular element are specific points (nodes) at which the value of the dependant variables are explicitly calculated. The calculated values at these nodes are then used to approximate the values of the dependent variables at non-node points inside the triangular element. The nodes of this element are exterior nodes because they lie on the element boundary. Multiple elements are then used, connected at the exterior nodes, to approximate the entire domain geometry.

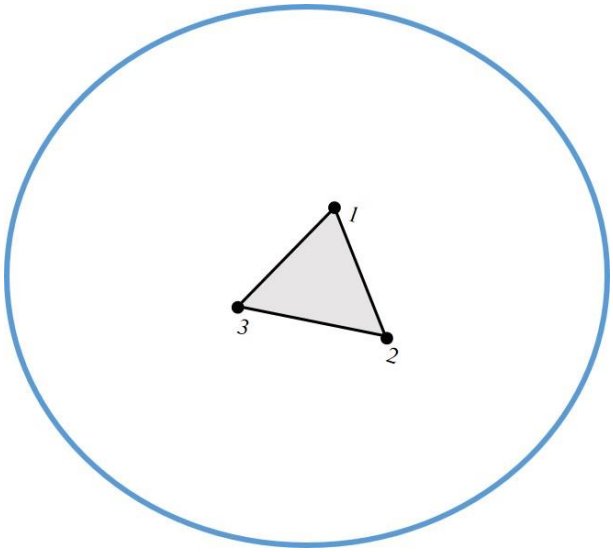

Figure 2.10. A 2D domain with a smaller three node subdomain within.

2.4.1.1 Meshing

The collection of multiple finite elements that approximate the entire domain geometry is known as the finite element mesh, while the process it-self is termed meshing. For a curved boundary, the mesh represents an approximation of the original domain geometry. Figure 2.11(a) shows a coarse mesh (less dense), while figure 2.11(b) shows a fine mesh (denser). As demonstrated by comparing Figure 2.11(b) to Figure 2.11(a); the denser the mesh the better it represents the geometry. The white area in Figure 2.11(a) would not be included in the model. The meshing process is arguably the most important step in FEM modelling. Due to its large implications on size of the resulting file, computation time, and accuracy of the numerical solution. For a coarse mesh the computation time is generally much shorter compared to the same analysis with a finer mesh, however, the numerical solution is often less accurate. A fine mesh generally results in a more accurate numerical solution but the computation time can be

exponentially longer and the file size prohibitively large. The size of the elements can also have a significant impact on the numerical solution. As the element size is reduced, and the computation rerun, the solution often changes incrementally. As the element size is further reduced the incremental change becomes smaller until there is little difference in the numerical solution for a reduction in element size (convergence). This systematic process of reducing the mesh element size and examining how it impacts the solution is known as mesh refinement.

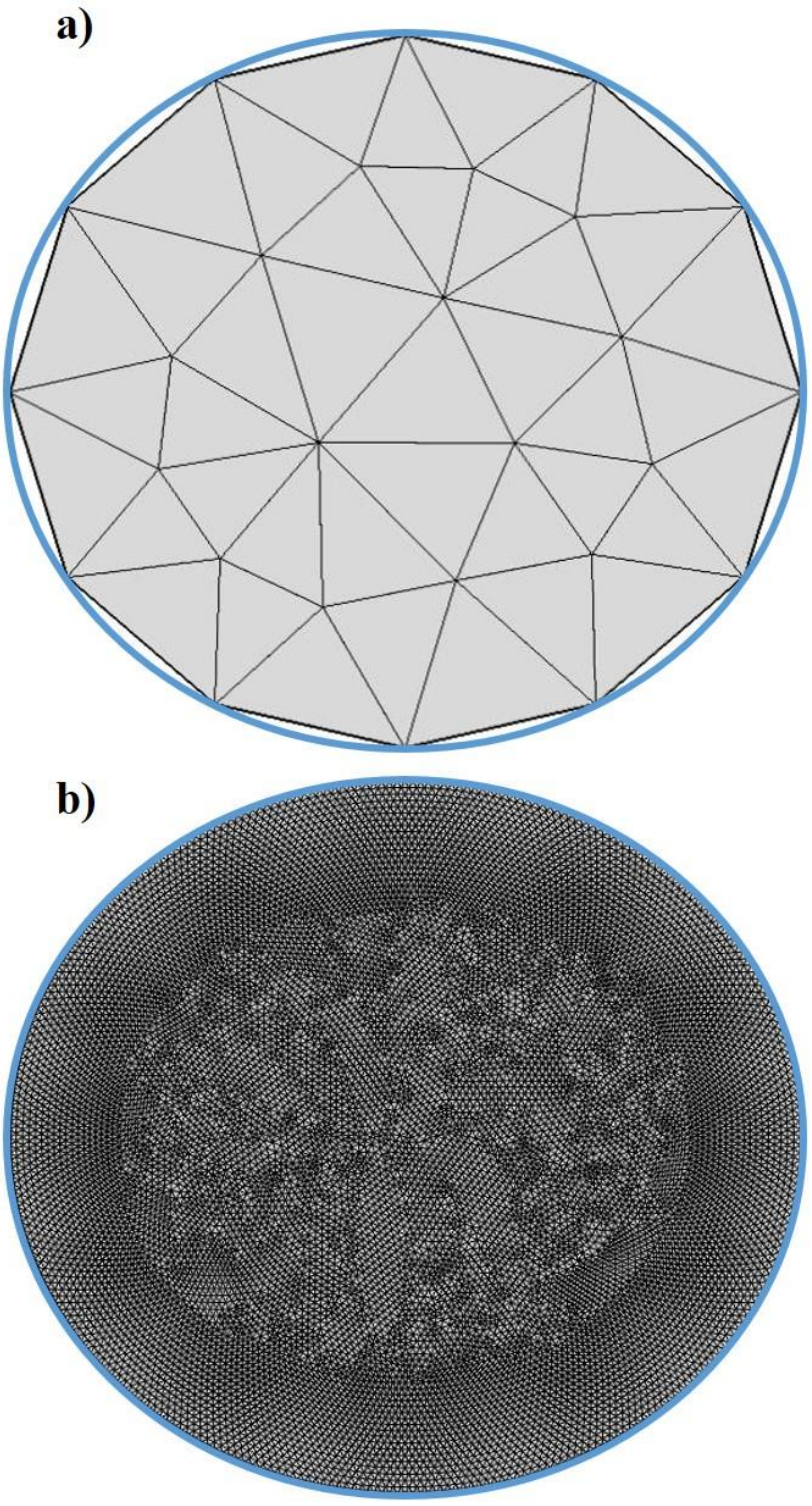

Figure 2.11 Circular boundary domain modelled using a a) coarse triangular mesh and a b) fine triangular mesh.

2.4.2 COMSOL

Finite element method modelling of the graphene based infrared (IR) emitters was performed utilising the COMSOL Multiphysics software package. COMSOL is a FEM software package that aids in the study of various physical phenomena with application specific modules: AC/DC module, acoustics module, heat transfer module, optics module and RF module, to name a few, which can be utilised on their own or in combination to simulate coupled physics phenomena. For example, the temperature distribution in graphene based infrared emitters (as a result of Joule heating in the graphene) is modelled in COMSOL by coupling the heat transfer in solids interface, part of the heat transfer module, with the electric current interface, part of the AC/DC module. This allows for the simulation of the electrical heat generation, as a result of an applied current bias to graphene contacts, and the resulting steady state temperature distribution.

Setting up a COMSOL model to simulate Joule heating in a graphene device involves multiple steps, as displayed in Figure 2.12. In the first step the dimension to be studied is selected (1D, 2D etc.). This is followed by the specification of the physics to be added to the simulation in the second step and a specification of the of study node for the third. The study contains all the information that defines how the model will be solved including the type of study and solver configuration utilised. The types of studies include the time dependant domain and the stationary domain among others. For the time dependant domain, the system of equations is solved at each time step *t*, and can be used to model Joule heating of the graphene devices under the application of a pulsed drive current. Alternatively, for the stationary domain the field variables do not vary with time

and can be utilised to model devices under a DC drive current. The solvers can be divided into two fundamental classes of algorithms, direct and iterative. Direct solvers arrive at the solution in one large computational step. The three direct solvers used in COMSOL are, MUMPS, PARADISO and SPOOLS. Each is based on lower upper decomposition, the factoring of a matrix as the product of a lower and upper triangular matrix, and primarily differ only in the time required to obtain a solution. The solution should be the same, regardless of the direct solver utilised, for a well-defined problem. As opposed to the direct solvers, iterative solvers arrive at solutions in a number of steps, *n*. Modules that employ iterative methods are considered converged when the relative error, which should reduce as *n* increases, is below the relative tolerance, typically 0.001. There are multiple types of iterative solvers in COMSOL, all of which are based on some variation of the conjugate gradient method. The main disadvantage of iterative solves, in comparison to direct solvers, is dependence of the type of iterative solver used on the system of equations being solved. The primary advantage of iterative solvers is a significant decrease in the amount of memory used, in comparison to direct solves. For all of the COMSOL results presented in this thesis the MUMPS direct solver is utilised in combination with iterative solvers.

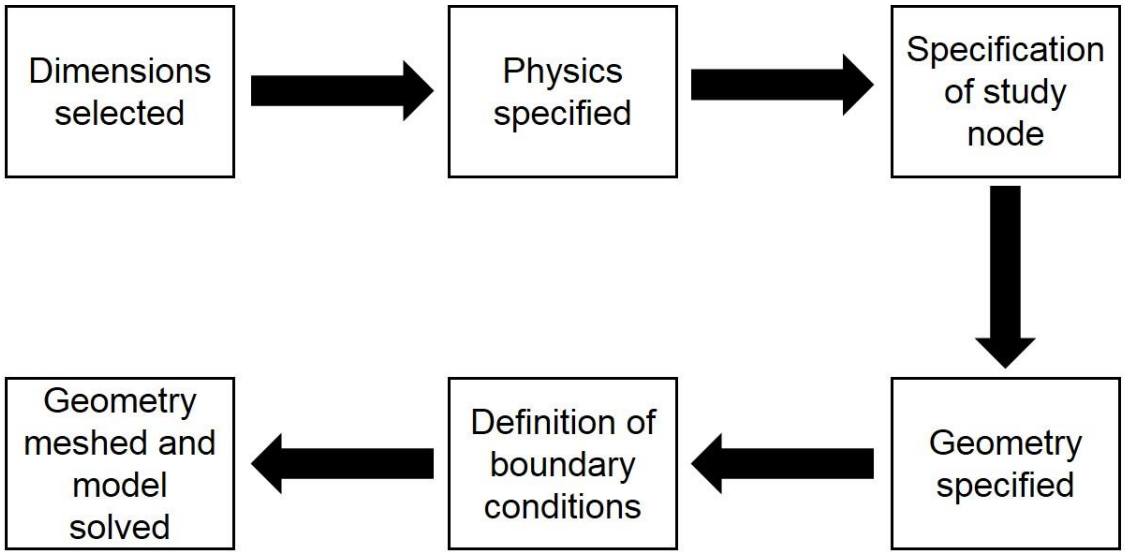

Figure 2.12 Flow chart of the steps involved in setting-up the COMSOL model.

The fourth step of setting up the COMSOL model includes the specification of the geometry and description of the subdomains. In this step, important properties like the graphene thermal conductivity, specific heat, and electrical conductivity are set. This is followed by the definition of the boundary conditions in the fifth step. Examples of the boundary conditions defined include: the boundary current, boundary temperatures, thermal boundary resistances and the specification of any thermal convection/radiation. After meshing in the final step, the simulations solve the current conservation equation based on Ohm's law using the scalar electric potential *V,* as the dependent variable and the temperature equation that corresponds to Fourier's law, including the heat generated by Joule heating $Q = \sigma|\nabla V|^2$, with the temperature *T* as the dependent variable, simultaneously for each element. These simulations can be performed in either the time dependant domain, where the system of equations is solved at each time step *t*, for an AC current bias, or in the stationary domain, for a DC current bias as field variables do not vary with time.

3 Device Fabrication

In this chapter, the specific steps involved in the fabrication of the three main types of graphene based devices used for the experimental results in this work are described. These included encapsulated and unencapsulated graphene devices on SiO_2/Si substrate in addition to graphene on GaN nano-rod substrates. The first section, section 3.1, addresses the preparation of graphene, specifically the exfoliation and chemical vapour deposition (CVD) methods. Section 3.2 illustrates the different Characterisation methods used, such as Raman spectroscopy, to determine the number of layers and to identify defects, in the form of polymethyl methacrylate (PMMA) residue and holes in the graphene. The transfer of CVD graphene and hexagonal boron nitride (h-BN) onto flat substrates, such as SiO_2/Si, using the standard PMMA wet transfer process and suspended on patterned substrates, such as gallium nitride (GaN) nano-rods, using a slightly altered transfer procedure, is discussed in section 3.3 and 3.4 respectively. Details on the patterning and metallisation with electron beam lithography (EBL) and thermal evaporation respectively are provided in section 3.5. In section 3.7, the stages involved in the fabrication of single and few-layer graphene devices on SiO_2/Si (3.6.1) and encapsulated few-layer graphene devices (3.6.2) are summarised. Following the device fabrication the samples are mounted in a standard, multi pin sample package and wire bonded with gold (Au) wires, as described in section 3.7. Finally, in section 3.8 a summary of all the fabricated devices used in the experiments presented in this work is provided.

3.1 Graphene Preparation

A large amount of time and research have gone into developing methods to consistently produce high quality, large area graphene. There are several different techniques, each with their own advantages and disadvantages. These include: mechanical exfoliation from highly orientated pyrolytic graphite (HOPG) [112], epitaxial growth on either transition metals or silicon carbide [113], intercalation of graphite layers [114], reduction of graphene oxide [115], chemical exfoliation [116] and the unzipping of carbon nanotubes [117]. Of these primary techniques it depends on the intended use of the graphene as to which production method is best. For fundamental research or applications where extremely high mobility is a requirement, exfoliated graphene is the more attractive option. However, arguably the best technique for the reliable, large area, cost effect production of single and few-layer graphene is the epitaxial growth on transition metals. Both of these methods are examined in more detail in the following sections.

3.1.1 Mechanical Exfoliation

The first, and most famous, method used for the production, as well as discovery, of graphene was the mechanical exfoliation method. It is simple technique that is also sometimes referred to as the scotch tape method. This is due to the fact that the mechanical exfoliation of the graphite flakes is achieved through the use of adhesive tape followed by its transfer to an insulating substrate, typically silicon dioxide. More precisely it is multiple mechanical exfoliations of HOPG crystals

resulting in the cleavage of graphite layers of various thicknesses, including single-layer, bilayer and few-layer graphene. This mosaic of different graphite layers is then pressed onto an arbitrary substrate, like SiO_2/Si, and the adhesive tape slowly peeled back. This leaves behind many of the exfoliated flakes, due to the Van der Waals forces between the target substrate (SiO_2 in this case) and the bottom layer of the flakes being greater than the inter-layer forces within the graphite, which can then be observed using optical microscopy (if the substrate is SiO_2/Si) to find the graphene flakes with the desired number of layers. Often single-layer, though in some cases bilayer or few-layer. The main advantages of this method are: the consistent production of graphene, suitability for transferring graphene to a large number of different target substrates, no expensive equipment required and it results in relatively pristine graphene, with high mobility. However, it also has many disadvantages: the majority of flakes left behind after removing the tape are graphite and not graphene, necessitating a time-consuming process of finding the graphene flakes with an optical microscope, the tape utilised in the process leaves behind residues on the surface of sample, the size of the graphene flakes are relatively small, typically smaller than 100 μm and perhaps most significant is the inherent randomness involved. Important factors including the number of layers, position, size and shape of the graphene are entirely unpredictable.

3.1.2 Chemical Vapour Deposition

One of the methods that addresses some of the limitations of the mechanical exfoliation process discussed in the previous section, is the chemical vapour deposition (CVD) of hydrocarbons on transition metal substrates. It is notable for

the affordable, reliable growth of large-area graphene films on primarily copper (Cu) and nickel (Ni). The CVD growth is accomplished through the high temperature decomposition of a hydrocarbon source to carbon radicals at the metal surface where they then form either single or few-layer graphene. Often the grain size of the transition metal substrate is increased through thermal annealing, at ~1200-1300 K in an Ar/H_2 atmosphere, prior to being exposed to the carbon source, facilitating larger graphene domains. The deposition mechanism is determined by the metal substrate used. For example, the solubility of carbon in Ni is greater than Cu. After the decomposition of the hydrocarbon source the carbon radicals are dissolved into the Ni thin film, forming a Ni-C solid solution. However, the solubility of carbon in Ni is temperature dependent; as the Ni film is cooled in an Ar rich environment the solubility rapidly decreases. This results in the carbon atoms diffusing out of the solution, settling on the Ni surface and forming graphene. Due to the mechanics of this deposition mechanism, the cooling rate greatly affects the thickness and quality of the graphene films. Through optimization of the cooling rate, the growth of few layer graphene has been reliably achieved [118]. The graphene films are generally continuous, however, the number of graphene layers is usually inhomogeneous and polycrystalline, with areas ranging from single to few layer graphene across the surface of the film, possibly limited by the size of the Ni grain boundaries. Alternatively, graphene grown on Cu foil is predominantly single-layer due to the different deposition mechanism [119]. Rather than the precipitation process of the Ni growth the deposition mechanism for Cu is a surface catalysed process. The fact that this growth mechanism is a surface reaction results in the growth process being self-limiting, as the Cu surface is inaccessible after the deposition of the first graphene layer. An additional advantage of the CVD method is the ability to

easily transfer the graphene to an arbitrary substrate. This is done by first coating the graphene surface with a polymer support, typically polymethyl methacrylate (PMMA), followed by the removal of the underlying metal layer with the requisite metal etchant. This leaves the PMMA/graphene film floating on the surface. This is discussed in more detail in section 3.3.

3.2 Characterisation

For both CVD and exfoliated graphene, the most commonly used characterisation techniques are optical microscopy and Raman spectroscopy. Typically, optical microscopy is used for the initial identification of exfoliated graphene flakes amongst a sea of thicker graphitic ones or to examine the initial result of a CVD graphene transfer. In both cases this is followed by Raman spectroscopy as a non-destructive means of identifying the number of graphene layers present. For suspended samples scanning electron microscopy is an additional characterisation method that is useful for visualizing the graphene.

3.2.1 Optical Microscopy

Graphene transferred to a SiO_2 capped substrate is visible under an optical microscope due to sufficient transparency of the graphene allowing it to add to the optical path of the light that is reflected off the substrate [7]. This results in a small but visible change in contrast between areas with and without graphene, which varies linearly with the number of graphene layers. This allows for the identification of exfoliated graphene flakes and for an estimation of the number of

layers prior to confirmation with Raman spectroscopy (discussed in 3.2.2). The amount of contrast is largely dependent on the thickness, with a 5% change in thickness from a 300 nm SiO_2 layer resulting in no perceivable difference in contrast between single-layer graphene and the oxide layer [120]. Additionally, it is possible to enhance the contrast between the graphene and the SiO_2 by using a green light filter [121].

As well as the identification of graphene flakes, optical microscopy is useful characterisation technique for identifying the continuity of both transferred CVD graphene and h-BN film, in addition to the inspection of subsequent fabrication processes. By taking pictures at various stages of lithography, it is a useful way to make quick observations about the sample. Figure 3.1 (a) shows a typical optical micrograph of a completed single-layer graphene device. The dark region between the two contacts is the graphene, which is clearly visible compared to the lighter SiO_2 around it. It can be observed that the transfer is homogeneous with only small holes visible in the graphene, possibly brought about by the transfer process. Figure 3.1 (b) displays an optical micrograph of CVD transferred multilayer h-BN on a SiO_2/Si substrate. The multilayer h-BN is 13 nm thick on average and is the light blue region on the right hand side of the image, while the purple area on the left hand side is the SiO_2.

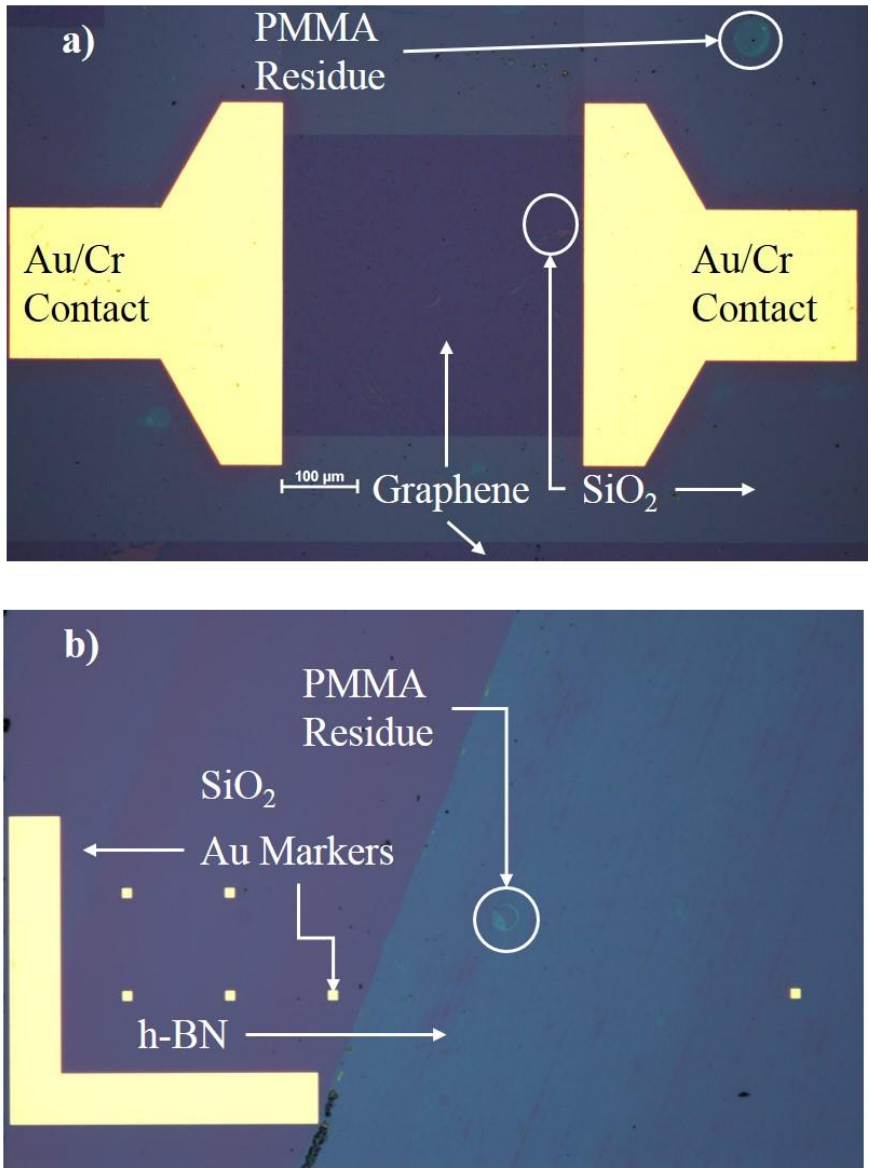

Figure 3.1 a) Optical micrograph of a typical 0.5 mm × 0.5 mm single-layer graphene device. b) Optical micrograph of multilayer h-BN on a SiO_2/Si substrate.

3.2.2 Raman Spectroscopy

Raman spectroscopy is an important tool in the characterisation of graphene due to its ability to reliably determine the number of graphene layers and give an indication of the quality and uniformity of the graphene transfer, through the novel capture of graphene's electronic spectrum via inelastic scattering of

monochromatic light. The light source utilised is typically near-infrared to near-ultraviolet wavelength laser. Electrons in the sample are excited to a higher energy state by the absorption of photons and emit light, at the same frequency of the incident beam, elastic scattering, or at higher/lower frequencies, inelastic scattering, upon relaxing to the ground state.

In graphene, the doubly degenerate (TO and LO) in-plane E_{2g} mode is the only first order Raman active mode, corresponding to the G band, with a laser excitation energy independent position of 1580 cm^{-1}. On the other hand, there are bands that are the result of second order scattering processes which exhibit dispersive behaviour and, therefore, their frequencies do depend on the laser excitation energy. These include the disorder induced D band, attributed to the A_{1g} zone edge mode, and the 2D (G´) band, due to second order double resonant scattering from the zone boundary; assuming an excitation energy of 2.41 eV, their positions are 1350 cm^{-1} and 2700 cm^{-1} respectively. Figure 3.2 shows a schematic of the first order Raman scattering process responsible for the G peak and the second order Raman scattering processes responsible for the D, D´ and 2D peaks. In pristine graphene, the D peak is not present while the ratio of the 2D peak to the G peak is ~3-4. As the number of layers increases from single-layer graphene to bulk graphite the intensity of the G peak stays relatively constant whereas the 2D peak intensity decreases until it is weaker than the G peak at bulk graphite [122]. The reason for the large intensity of the 2D peak in graphene can be explained by the double and triple resonance that connects the electronic band structure with the phonon modes. As Mallard *et al*. [123] explain, an electron around the K point absorbs a photon with energy equal to the laser excitation energy, $E_{laser.}$ The electron is then either in-elastically scattered, by a phonon, or elastically scattered, by a defect, to a point around the K' point. From

there the electron is inelastically scattered back to a location around the K point by a phonon, where it goes on to emit a photon by recombining with a hole. While the 2D, D and D´ peaks are all the result of double resonance processes, the D and D´ processes consist of only one inelastic scattering event. In comparison, the two inelastic scattering events are responsible for the 2D peak observed in the graphene Raman spectra. The 2D peak can be used to identify the number of graphene layers as there is significant band splitting that is dependent upon the number of layers, with the 2D peak evolving from no band splitting seen in single-layer graphene to resembling the graphite 2D peak with the number of layers increases [122].

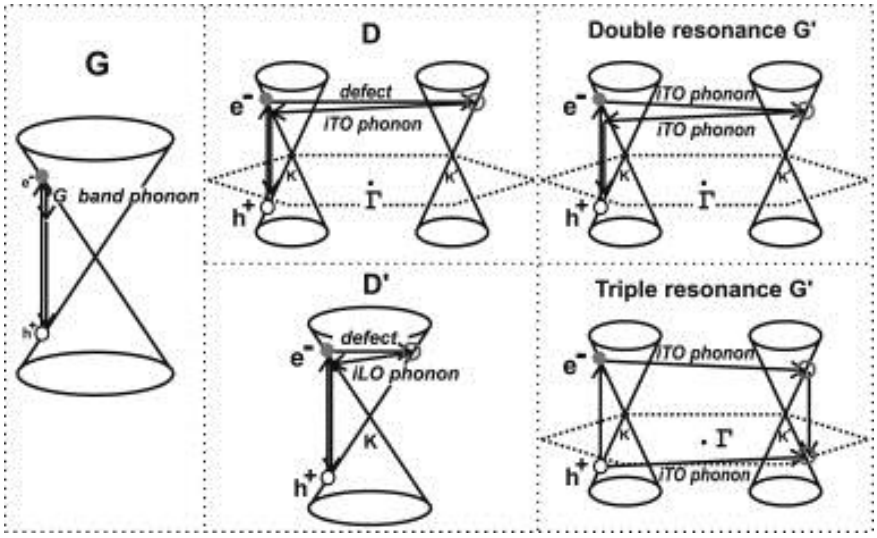

Figure 3.2 Schematic illustration showing (left) the First order G-band process, (centre) the second order one phonon D, D´ process and (right) the second order two phonon 2D (G´) process (Illustration taken from [123]).

In this work, the Raman spectroscopy measurements are performed using a 100 mW Renishaw continuous wave 532 nm laser source to excite the sample. A lens is used to collect the emitted light and pass it through a spectrophotometer where interference notch filters are used to separate the Raman signal from the much

stronger Rayleigh signal. An optical microscope is used to determine the location of the graphene and then multiple Raman spectra are taken at a number of different points on the sample. The average of the measured spectra for both a CVD single-layer and a CVD few-layer device is shown in Figure 3.3 with the spectral response observed between 1200-3000 cm^{-1}, the Raman active region of graphene.

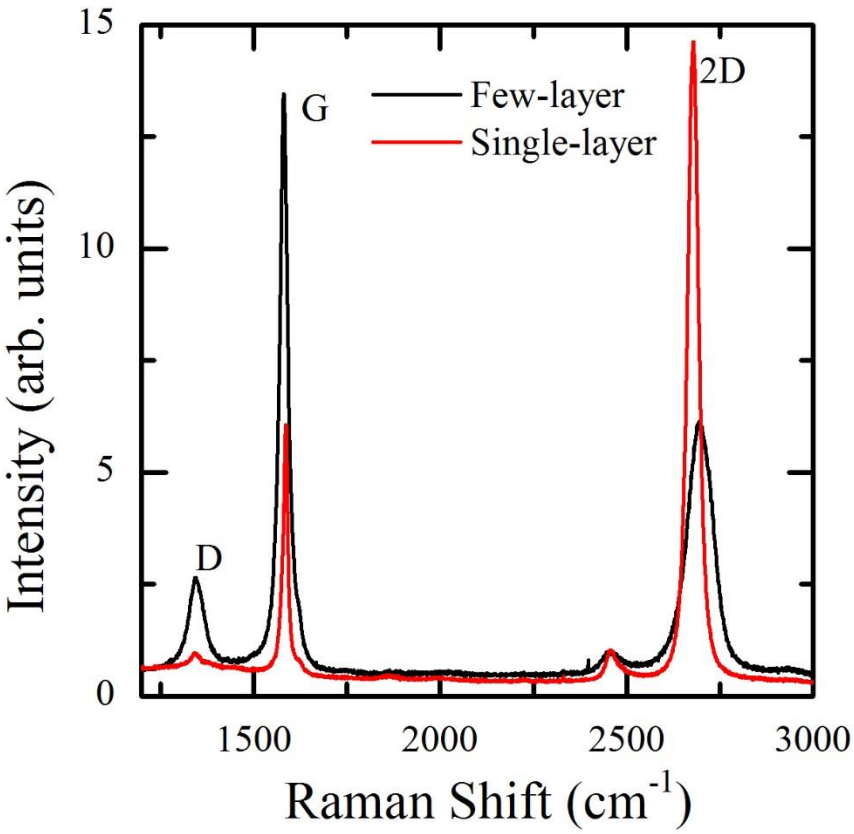

Figure 3.3 Average Raman Spectra for single-layer graphene (red line) and few-layer graphene (black line) on doped SiO_2/Si.

For the single-layer device the D peak is obtained at 1348 cm^{-1} the G peak at 1587 cm^{-1} and the 2D at 2678 cm^{-1}. The average ratio for the 2D/G peaks for this device is ~2.5. The symmetry and sharpness of the 2D peak along with the measured 2D/G ratio is indicative of single-layer graphene [122,124]. Additionally, the small D peak indicates that the transferred graphene is uniform with few defects. For the few-layer graphene, the D peak is obtained at 1346 cm^{-}

^{1}, the G peak at 1582 cm^{-1} and the 2D peak at 2694 cm^{-1}. The broadening seen in the 2D peak is typical of few-layer graphene and suggests that the number of graphene layers is between 3-6 [125]. The D peak of the few-layer graphene is 2.5 times greater than the D peak of the single-layer suggesting there possibly more defects, such as wrinkles and/or tears in the graphene. Finally, the slight shift in the location of the Raman peaks for both the single and few-layer graphene from their expected locations is possibly due to doping from the transfer process [126].

Raman spectroscopy is also a useful tool for the identification and characterisation of single and multilayer h-BN. Figure 3.4(a) shows typical Raman spectra for exfoliated h-BN samples which are single-layer, bi layer and multilayer in addition to bulk h-BN. Like graphene, the only first order Raman active mode of h-BN is the E_{2G} phonon mode, resulting in a characteristic Raman peak that is analogous to the G peak observed in the Raman spectra of graphene [127]. In bulk h-BN, the peak position corresponding to the E_{2g} mode occurs at ~1366 cm^{-1}. As the number of layers decreases from bulk to single-layer, the peak intensity also decreases. Additionally, the integrated intensity of the E_{2g} peak is linearly proportional to the number of layers, N, as shown in the inset of Figure 3.4(a). Figure 3.4(b) shows the measured peak position for various h-BN samples. Compared to the peak location of bulk h-BN, the E_{2g} peak position of single-layer h-BN is typically red shifted by ~2-4 μm while bi-layer h-BN is typically blue shifted by ~2-4 μm. This, along with the linear intensity of the E_{2G} peak with increasing h-BN layers, makes Raman spectroscopy a good characterisation method for determining the number of h-BN layers, as well as the uniformity.

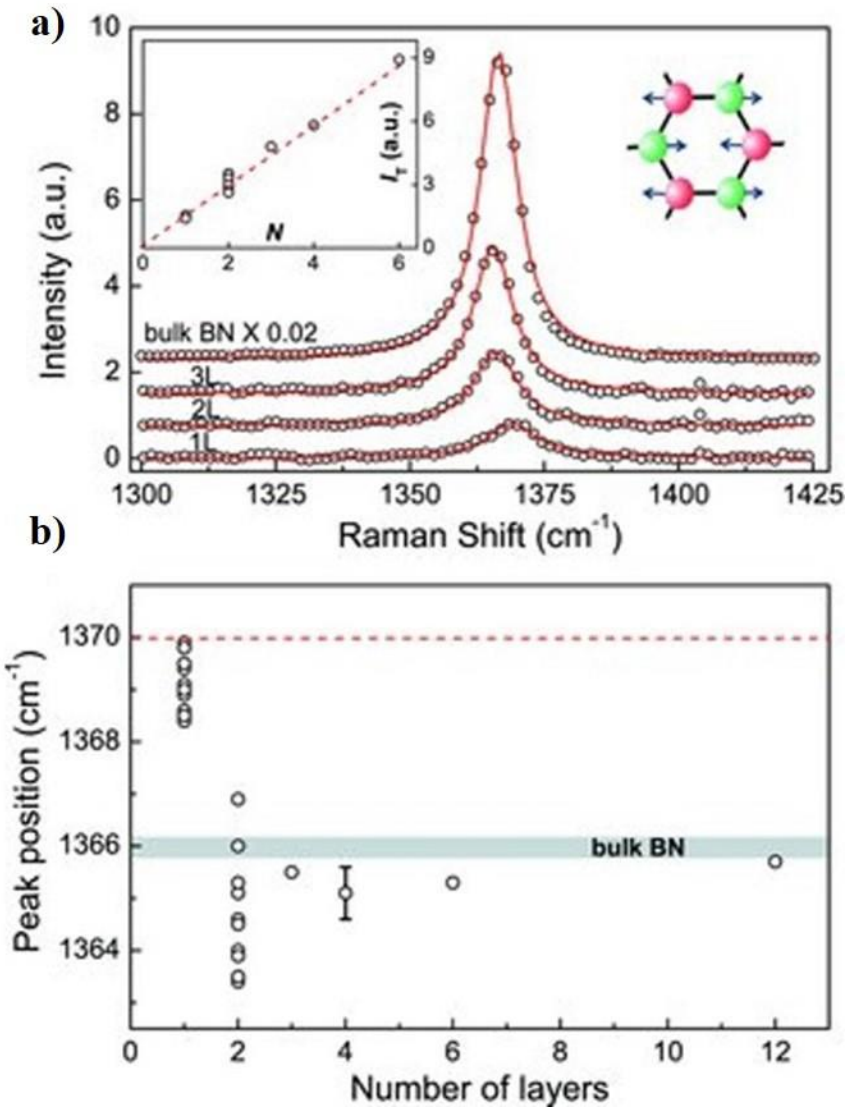

Figure 3.4 a) Atomically thin h-BN Raman spectra using a 514.5 nm green laser. The right inset shows an illustration of E_{2g} phonon mode that causes the peak at ~1366 cm^{-1} and the left inset plots integrated intensity, I_T as function of the number of h-BN layers, N. b) Raman peak position plotted against N. The dashed line is the theoretical single-layer h-BN peak position (illustration taken from [128]).

3.2.3 Scanning Electron Microscopy

A scanning electron microscope (SEM) generates an image (scanning electron micrograph) by scanning a focused electron beam over the surface of the sample. The electrons interact with the sample surface, generating various signals that can be used to obtain information about the sample including the surface morphology, chemical composition and crystal structure. The scanning electron micrograph that is generated by the SEM is typically a 2D image of these properties spatial variation. The signals produced by the electron/sample interactions include secondary electrons, backscattered electrons, diffracted backscattered electrons, photons and heat. Scanning electron micrographs of the sample surface are generated using either secondary or backscattered electrons. Secondary electrons are generated by the inelastic interaction of either electrons from the incident beam or high energy backscattered electrons with the valence electrons of atoms in the sample. Electrons are then emitted from the sample, due to ionisation, at energies that are typically less than 50 eV [129] and are termed secondary electrons. Due to their relatively low energies, only electrons close to the surface can escape the sample, with the maximum depth termed the escape depth, ε. For metals $\varepsilon \approx 5$nm while for insulators $\varepsilon \approx 50$ nm. The number of secondary electron generated by a sample is dependent on the elements that composes the sample. For example, the fraction of secondary electrons generated by carbon compared to the number of electrons in the incident beam (δ) is approximately 0.5, while for Au $\delta \approx 2.0$. Additionally, more electrons can leave the sample at the edges and inclined areas termed the edge effect. Brighter regions in scanning electron micrographs of the spatially resolved secondary electron signal correspond to areas where larger quantities of secondary electron

are emitted compared to other regions. All of the scanning electron micrographs presented in this work are morphology images generated using the secondary electron signal. The resolution of SEMs is approximately 10 nm, which is 20 times smaller than the maximum resolution of optical microscopes (200nm) due to the shorter wavelength of electrons compared to visible light.

3.3 Transfer Process of 2D Materials onto Substrates

3.3.1 CVD Graphene and Hexagonal Boron Nitride on Cu

Currently, the simplest and cheapest way to produce large area graphene and hexagonal boron nitride that can easily be transferred to an arbitrary substrate is through CVD on transition metal substrates. Both single-layer and few-layer graphene, as well as single and multilayer h-BN are commercially available through multiple outlets and are widely used for research purposes. For the experiments described in this work, both CVD single-layer graphene and multilayer hexagonal boron nitride grown on copper foil (from Graphene Supermarket) were used. For both, a standard PMMA transfer technique was used [130], an illustration of which is shown in Figure 3.5. PMMA is used on top of the graphene/h-BN to both protect it during the transfer process, as well as function as a mechanical support after the removal of the underlying Cu foil. The PMMA solution used for this is a 950K A4 solution, where 950K is the molecular weight and A4 describes the 2:1 ratio of PMMA to anisole, the solvent. A spinner is used to deposit the solution onto the graphene surface. The RPM, molecular weight of the PMMA and the total spin time determine the thickness of the PMMA

spun. Cu foil, with either CVD graphene or CVD h-BN on both the top and bottom, is cut to the necessary size for transfer, typically a few mm square, from a 2.0″ × 2.0″ sheet of graphene grown on Cu and placed on the sample holder in the spinner. The spin speed and time are set so the required parameters give 80 nm PMMA thickness with the 950K A4 solution, which are 3500 RPM and 50 s respectively. The 50 s time is broken down into 5 s for ramping up to the 3500 RPM and 45 where the RPM is held constant. After the spinning process is complete the sample is placed on a hot plate and baked at 150 °C for 8 minutes to remove the solvent. As the CVD process results in the growth of graphene on both the top and bottom of the Cu foil the graphene/h-BN is removed from the bottom of the Cu foil, with the PMMA protecting the graphene/h-BN on top, by etching in a reactive-ion etcher using O_2/Ar plasma. The etch recipe was as follows: RF power of 15W, oxygen flow of 10 sccm (standard cubic centimetre per minute), argon flow of 10 sccm, gas stabilisation time of 30 s and a process time of 30 s. This is repeated twice for single-layer graphene and ten times for the multilayer h-BN. The Cu foil was then floated on top of a 0.1 M solution of ammonia persulfate (APS), etched side down, and left overnight to allow the etchant to remove the Cu. After the Cu was sufficiently etched a transparent film of PMMA on graphene/h-BN remained floating on top of the solution. This is scooped out with a glass spoon and then rinsed in DI water six times, in order to remove any remaining etchant residue. This PMMA graphene/h-BN layer was then transferred to the desired substrate and then left to air dry overnight. The PMMA layer on top was removed with acetone.

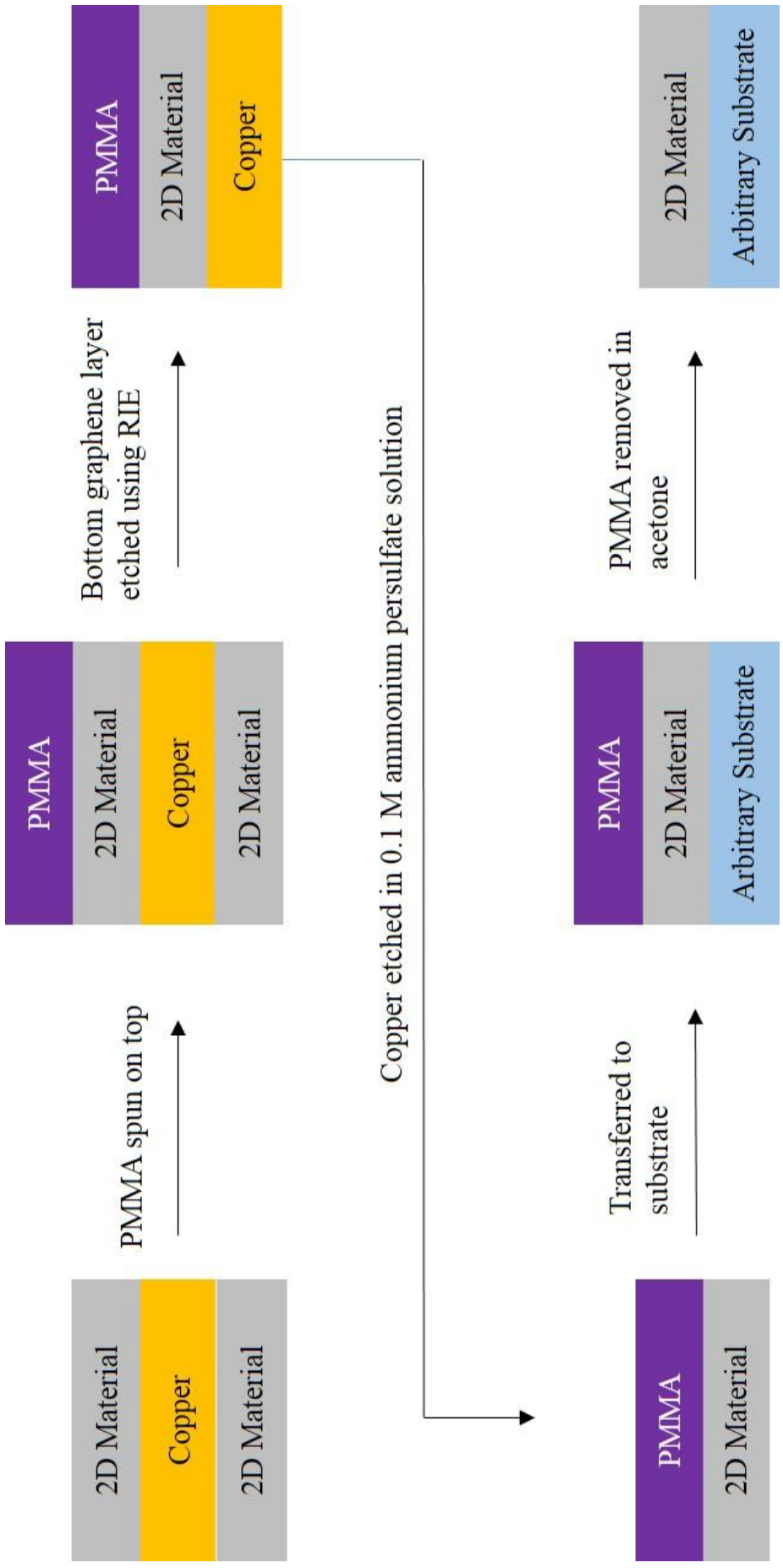

Figure 3.5 A schematic of the steps involved in the transfer of a 2D material from a copper film to an arbitrary flat substrate.

3.3.2 CVD Few-layer Trivial Transfer Graphene

For the fabrication of the encapsulated graphene devices described in this work few-layer graphene that has been pre-transferred to a polymer (supplied by ACS Materials) called Trivial Transfer Graphene (TTG) was used. The transfer process for TTG is a much simpler process than the transfer of single-layer graphene from Cu foil, and is illustrated schematically in Figure 3.6. The TTG is a 5 cm × 5 cm sheet of 6-8 layer few-layer graphene on polymer, with PMMA already spin coated on top of the graphene. To remove the graphene from the underling polymer, it was placed in DI water, PMMA side up. The PMMA/few-layer graphene film was released from the bottom polymer layer and floated on top of the water. The film was then transferred to filter paper where it was allowed to dry overnight and then cut down to approximately 3 mm × 3 mm squares. The process was then repeated with the stack of PMMA, few-layer graphene and filter paper placed in DI water. The few-layer graphene was released from the filter paper and the PMMA with graphene transferred to the desired substrate, specifically h-BN on SiO_2/Si. The substrates were allowed to dry in air over night and the PMMA removed in acetone.

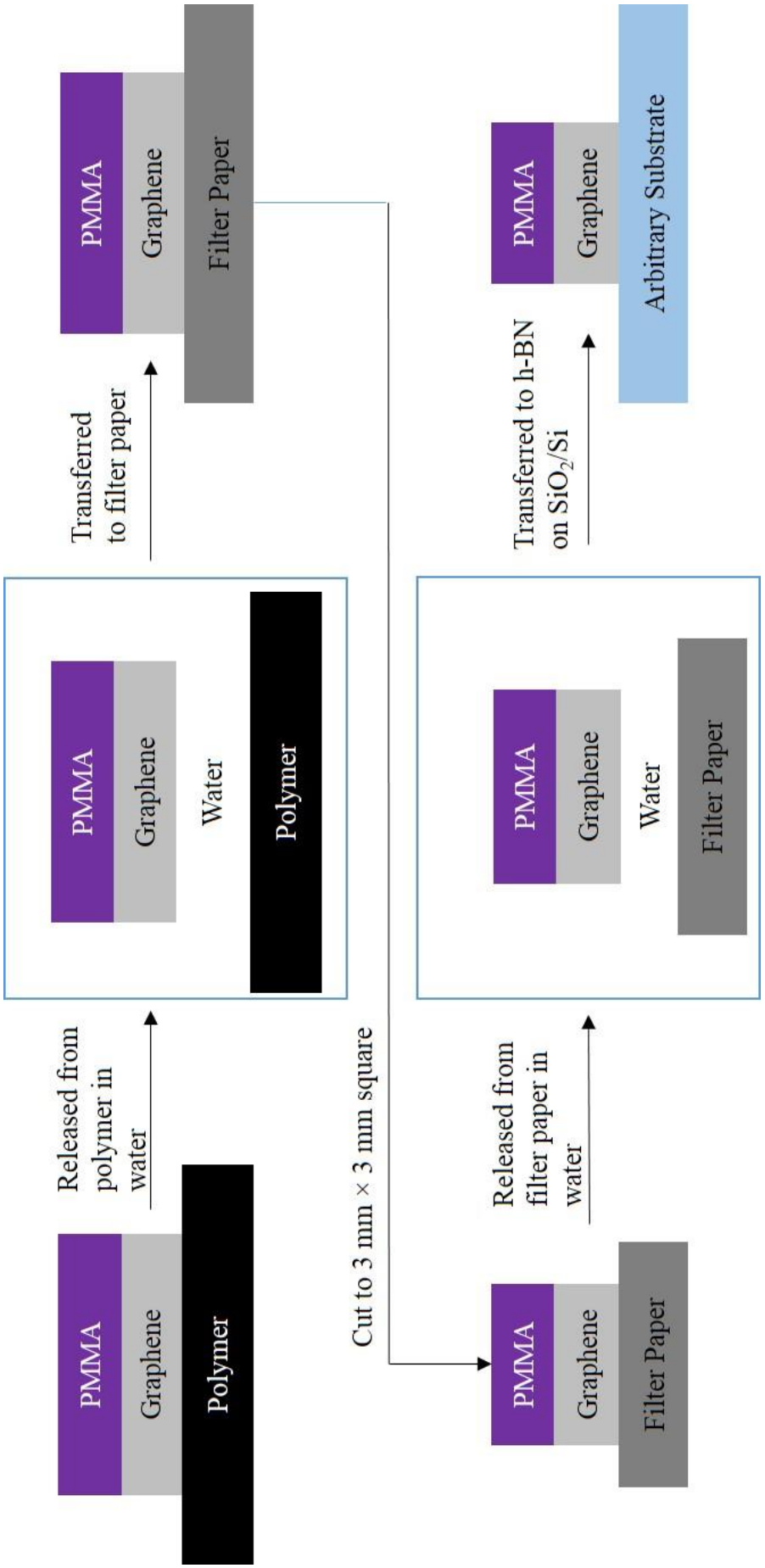

Figure 3.6 An illustration of the steps involved in the transfer of TTG to an oxidised arbitrary flat substrate.

3.4 Transfer of Graphene onto Patterned Substrates

3.4.1 Transfer of Graphene onto GaN Nano-Rods

Gallium Nitride (GaN) nano-rods (NR) were fabricated by collaborators at the University of Bath using inductively coupled plasma reactive ion etching (RIE) with the motivation of suspending graphene on top of the NRs. In addition to the potential benefits due to the thermal management aspect of the NR substrates, GaN based NRs have been shown to exhibit strong photonic crystal behaviour [131]. Using the standard PMMA assisted transfer technique (described in section 3.3.1) for the transfer of single-layer graphene grown on Cu film (from Graphene Supermarket) to a substrate of GaN nano-rods, resulted in substrates with very little to no graphene suspended on the GaN nano-rods when observed in the SEM. In contrast to the strong adhesion between single-layer graphene and SiO_2, 0.45 ± 0.02 J m^{-2} [132], the adhesion between graphene and GaN is poor [133,134] and it is common for the graphene to peel off of the GaN as shown in Figure 3.7. In order to overcome this the transfer process was altered slightly in an attempt to improve the overall transfer. Firstly, Suks *et al*. [130] have reported that a 30 minute post bake under atmospheric at 180 °C, after the transfer and before the removal of the PMMA, can be performed to achieve improved adhesion between the graphene and the substrate. This heats the PMMA to above the glass transition temperature and allows the PMMA to soften and to better conform to the substrate, reducing the gap between the graphene and the substrate, therefore, improving adhesion. After this post bake, the PMMA support was removed in acetone and the sample transferred to methanol and

dried with a critical point dryer (CPD). In critical point drying the chamber containing methanol, and the sample to be dried, is replaced with liquid CO_2, with a critical point of 31 °C and 1072 PSI. The chamber is then taken past the critical point (increasing the temperature and pressure above 31 °C and 1072 PSI) transitioning CO_2 from the liquid phase into supercritical fluid phase. The pressure is then reduced, while maintaining the temperature above 31 °C. This allows the CO_2 to transition from the supercritical fluid phase to the gas phase. This is a common technique for preserving the structure of suspended graphene [44,135,136] as the surface tension of the liquid used for the removal of the resist, acetone in the case of PMMA, can break the suspension during the standard drying procedure through capillary forces [137].

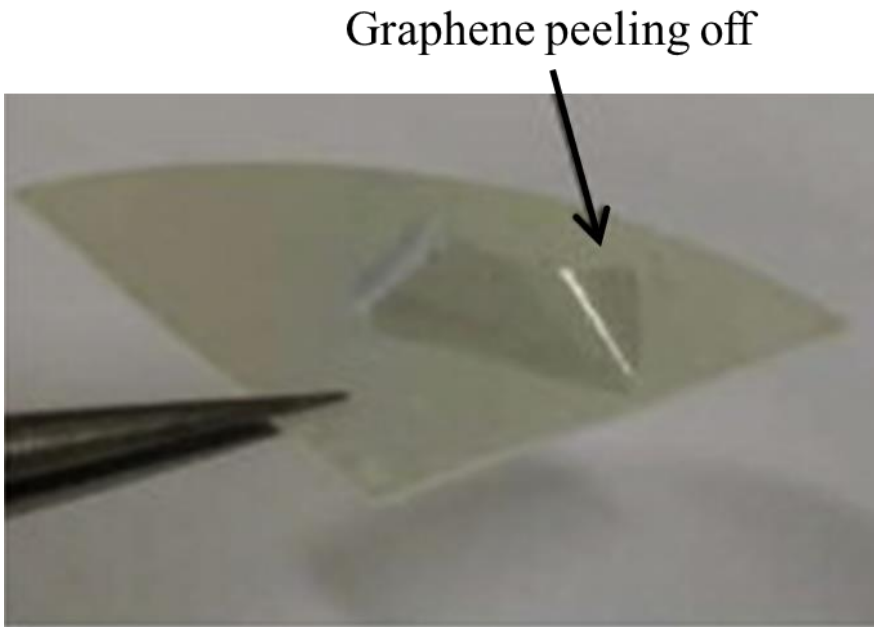

Figure 3.7 Micrograph of graphene transferred to GaN using PMMA assisted technique (illustration taken from [133]).

3.5 Patterning and Metallisation

3.5.1 Electron Beam Lithography

After the transfer of the 2D material, either graphene or h-BN, the area of the devices along with the metallic contact were defined using electron-beam lithography (EBL). This process is a nano-lithographic process that has a potential resolution of 5 nm. Electron-beam lithography, much like optical lithography, requires a resist to be deposited on the sample that is then exposed to an electron beam to write a pattern. By exposing sections of the resist to the electron-beam, the chemical structure of the resist is locally altered. After the pattern is written into the resist the sample is placed in a developer solution where either the exposed section (positive resist) or the unexposed section (negative resist) is removed. The developer solution used depends on the resist used and is unique to each different type of resist. This process is known as ‘developing’. After the developing processes the desired pattern remains on the substrate in the form areas with no resist on top of the substrate. The next step after developing depends which stage of lithography is being performed. If it is for the definition of the desired 2D layered structure, then the sample is placed in a reactive ion etcher with the remaining resist acting as an etch mask and the exposed area being removed by a plasma etching process. If it is for contacts, markers or resonators, then a thin layer metal is deposited on the resist and into the holes. A “lift-off” process is performed in order to remove unwanted metal on the resist. This lift-off is accomplished by using a solvent to dissolve the resist, leaving behind the desired metallic contacts. The two different stages of

lithography performed to fabricate devices used in the experiments performed in this work are as follows: A 400 nm layer of PMMA 950K A6, a positive resist, was spun onto the sample and baked at 150 °C for 10 minutes. The required etch pattern was designed using AutoCAD Design software. The AutoCAD file was then used to generate the pattern and dose file. The pattern file is a set of instructions the EBL machine can read to follow the design and the dose file determines electron beam dose, the number of electrons per unit area per second required to write the design. The sample was then loaded into the EBL machine exposed to a high energy electron beam that follows the designed pattern. After this was completed the sample was removed from the EBL machine and the developing solution prepared. For PMMA, the developing solution is a 3:1:0.06 ratio of isopropyl alcohol (IPA), methyl iso-butyl ketone (MIBK) and methyl ethyl ketone (MEK) respectively. The sample was placed in the developing solution for 30 seconds and then rinsed in IPA. The sample was then dried using N_2 gas. An optical microscope was used to ensure that the pattern was written and developed correctly. After being checked under the microscope, the sample was either loaded into the RIE machine, if defining the device area, or loaded into the thermal evaporator for metallization.

3.5.2 Reactive Ion Etching

Reactive ion etching is a dry etching technique commonly used in nanofabrication. RIE uses a chemically reactive plasma in order to etch certain materials. The etching process can be chemical, physical or ion induced depending on the process parameters. The sample is first loaded into a vacuum chamber which is then pumped down to low pressures. The chamber is then filled

with the chosen process gas or gases at the specified flow rate and the plasma is then initiated by applying a strong RF field to the wafer plate. The oscillating electric field removes electrons from the process gas molecules causing ionization and creating a plasma. The free electrons are then accelerated up and down in the vacuum chamber by the oscillating electric field and they strike the walls of the chamber, which is grounded, and wafer plate. At this time, the ions remain relatively unaffected by the RF electric field. The electrons striking the plate cause it to build up charge due to its DC isolation generating a large negative bias. The plasma, which is positively charged, due to the high concentration of cations, is then attracted to the negatively biased plate. The ions then collide with the sample on the plate where they react chemically with the material on the surface of the sample. The etch rate is contingent on the process parameters including, pressure, flow rate of the process gases, RF power and the material you are etching. In the fabrication of devices for this work, a JLS Designs RIE 80 Etching System was used for etching both graphene and h-BN at different points during the fabrication process. This was done either to remove the CVD graphene or h-BN from one side of a Cu film before etching away the Cu, as discussed in section 3.3 and 3.4, or to define the area of CVD graphene/h-BN after the transfer process. In the latter case, PMMA that has been patterned using electron beam lithography acted as an etch mask, protecting the desired area of graphene/h-BN whilst the exposed regions were removed by the etching process. The O_2/Ar plasma etch recipe used for this was the same as the one described in section 3.3.1, with the etch recipe being repeated ten times to etch few-layer graphene/h-BN or twice to etch single-layer graphene. This was done in order to ensure complete removal of either the graphene or h-BN.

3.5.3 Metallisation

A thermal evaporator was used to deposit both chromium (Cr) and Au at different points during the fabrication process. The sample, along with the desired metal, is placed into the thermal evaporator's vacuum chamber which is evacuated to < 2×10^{-6} mbar. The metals are placed in carrier boats where they are heated through a resistive heating process. This causes the evaporation of the metal, the rate of which is controlled by the amount of current applied to the boat, which then condenses on the much cooler sample and forms a metal thin film. The rate of deposition is kept constant at 0.5 $Å s^{-1}$ for both the Cr and Au deposition, which is monitored using a quartz crystal. For the two terminal metallic contacts typically 7 nm of Cr was deposited initially followed by 70 nm of Au. Alternatively, for the encapsulated graphene devices an initial 20 nm of Au was deposited on the graphene to lower the contact resistance followed by a deposition of 7 nm of Cr and then a further 70 nm of Au. For Au metamaterial structures, typically 5 nm of Cr followed by 100 nm of Au was deposited. In all of these cases metal was deposited on top of PMMA as well as into the holes in the PMMA. The unwanted metal and PMMA were removed by dissolving the PMMA in warm acetone at 50 °C and then rinsed in fresh acetone followed by IPA. An ultrasonicator was used to aid in the lift off of the metamaterial structures.

3.6 Fabricated Devices

3.6.1 Graphene on SiO_2/Si Devices

Pre-transferred single and few-layer graphene on SiO_2/Si substrates are available from multiple sources commercially. For the experiments discussed in this work involving single and few-layer graphene on a SiO_2/Si substrate, both were fabricated from pre-transferred single and few-layer graphene (from Graphene Supermarket) on a 300 nm thick insulating layer of SiO_2, with a highly p-doped Si substrate. The device fabrication is illustrated schematically in Figure 3.8: (a) Graphene Supermarket transferred graphene to a SiO_2 substrate using the PMMA assisted transfer method discussed in section 3.3.1 (b) a 400 nm resist layer of A6 950K PMMA was spun and baked at 150 °C for 8 minutes (c-d) the area of the graphene device was defined using E-beam lithography (discussed in section 3.5.1) followed by a RIE dry etch process (e) a second 400 nm resist layer of A6 950K PMMA was spun and baked (f) the second e-beam lithography stage was performed to define the contacts (g) contacts were deposited using the metallisation process described in section 3.5.3 (h) the PMMA and unwanted metal were removed with the lift off procedure described in section 3.5.3 (i) sample is bonded and packed following procedure discussed in section 3.7.1.

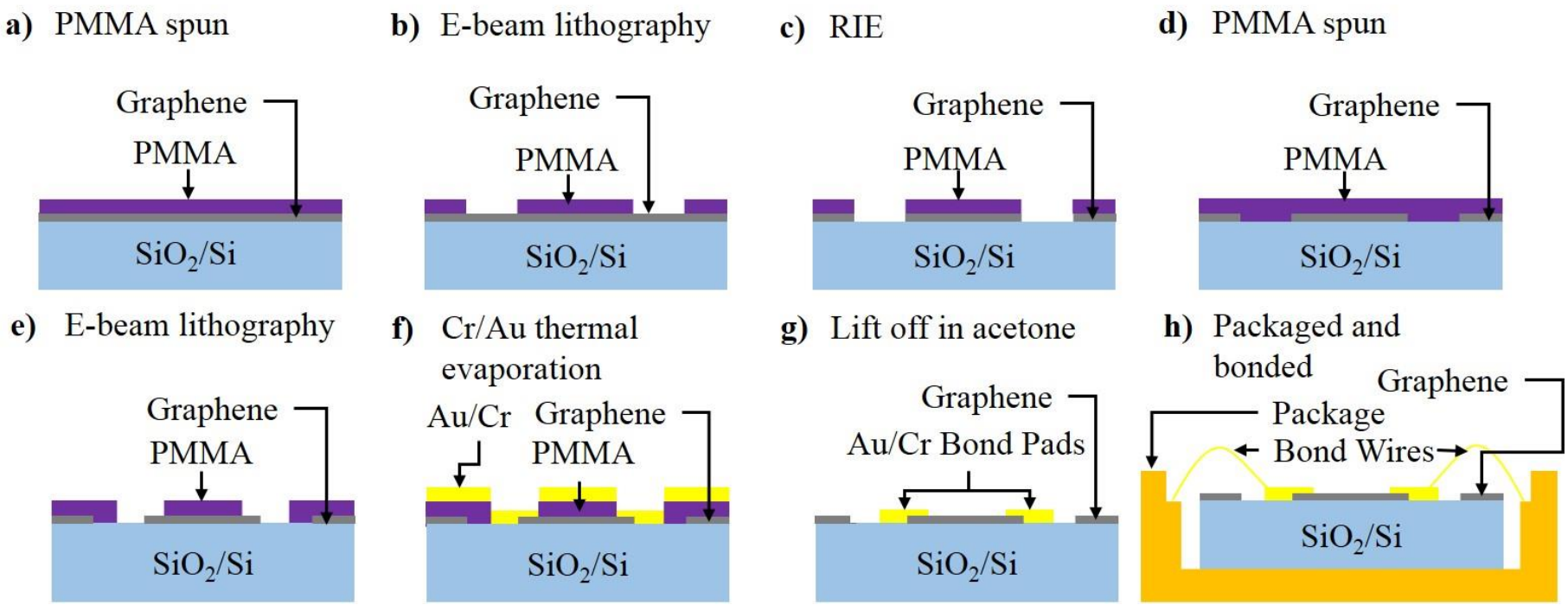

Figure 3.8 Schematic cross sectional diagram illustrating the single and multilayer graphene on oxidised silicon device fabrication: a) 400 nm of A6 950K PMMA resist layer spun and baked at 150 C for 8 minutes b) electron beam lithography performed to define etch mask c) reactive ion etching performed to define graphene area using O_2/Ar plasma d) PMMA spun and baked again e)

3.6.2 Encapsulated Graphene Devices

Using a multistage process, encapsulated graphene devices, consisting of 6-8 layer few-layer graphene between two layers of 13 nm multilayer h-BN, were fabricated. Both the multilayer h-BN and few-layer graphene were transferred onto a heavily doped silicon wafer with a 300 nm capping layer of SiO_2, using the transfer procedure described in more detail in section 3.3.1. A 80 nm layer of neat A6 950K PMMA was spun onto the h-BN, using a 4000 RPM spin speed for a total time of 50 seconds, prior to the removal of the underlying Cu foil using a 0.1 M APS etchant solution. After etching, the multilayer h-BN and PMMA layer was washed six times with fresh DI water. The seven (or eight if device required the fabrication of the metamaterial structure on top of the h-BN) stage fabrication process is illustrated schematically using a cross-section view in Figure 3.9 and a planar view in Figure 3.10: (a) the initial transfer of multilayer h-BN from Cu foil, followed by electron beam lithography and RIE (described in more detail in section 3.5.1 and 3.5.2 respectively), with an 80 nm A6 950 K PMMA resist, in order to define a 0.5 mm × 0.6 mm area of h-BN (b) the transfer, using the TTG transfer process described in section 3.3.1, and definition of an overlaying area of few-layer graphene, using the same lithography and etch process as for the multilayer h-BN (c) definition of a 0.5 mm × 0.6 mm area of 50 nm thick Au onto the outer edges of the few-layer graphene for improved contact resistance using electron beam lithography, with a 400 nm resist layer of A6 950K PMMA, by the metallisation process described in section 3.5.3 (d) definition of a 0.1 mm × 0.6 mm area of 7nm/70nm Cr/Au onto the Au and Si/SiO to ensure good contact with the final contact layer after encapsulation (e) the transfer and definition of the final encapsulating h-BN layer using the same 80 nm A6 950 K resist layer (f) definition

of final 7 nm/70 nm Cr/Au contacts over the prior 0.1 mm × 0.6 mm Cr/Au metallisation and extended over the substrate to provide 0.2 mm × 0.2 mm square bond pads (g) the optional stage for the definition of the metamaterial structure on top of the top h-BN layer (h) the sample is bonded and packed using the procedure discussed in section 3.7.1.

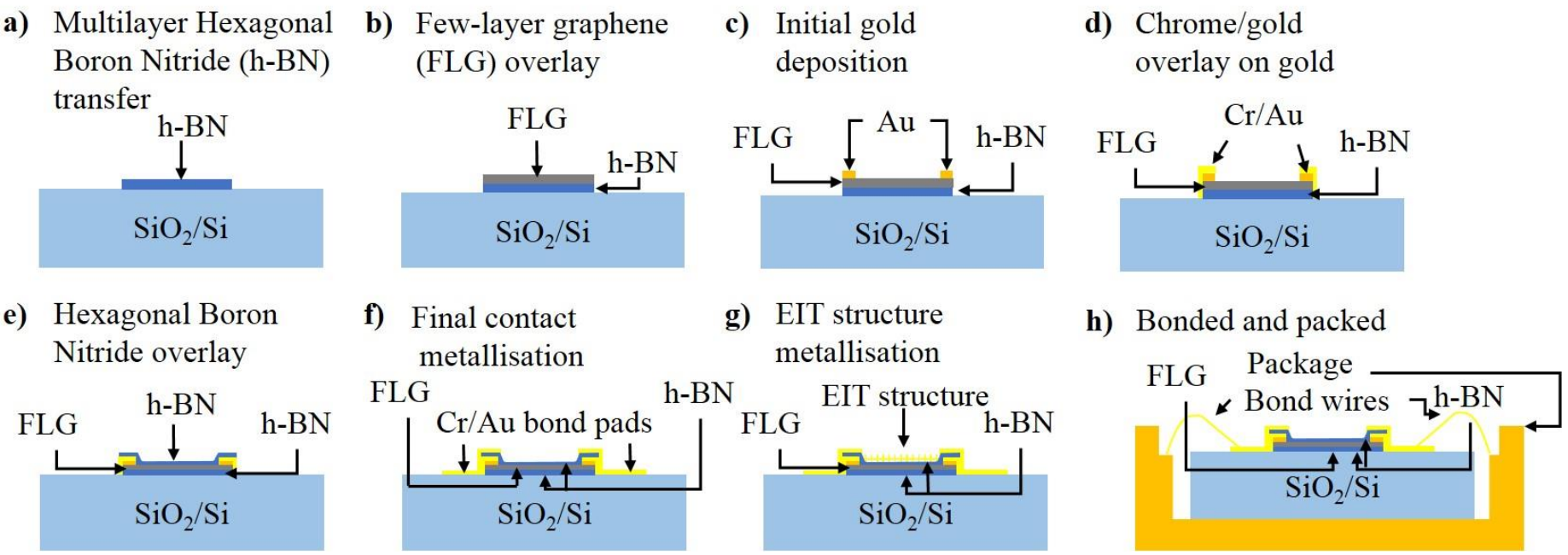

Figure 3.9 Schematic cross sectional diagram illustrating the encapsulated graphene device fabrication: a) transfer and definition of 1st multilayer h-BN layer onto SiO_2/Si b) multilayer graphene transferred on top and defined c) 50 nm wide by 20 nm thick of Au deposited on multilayer graphene d) 100 nm wide by 7/70 nm thick Cr/Au overlay on top of Au and SiO_2 e) encapsulation of multilayer graphene with transfer and definition of top multilayer h-BN layer f) final 7/70 nm thick Cr/Au contact

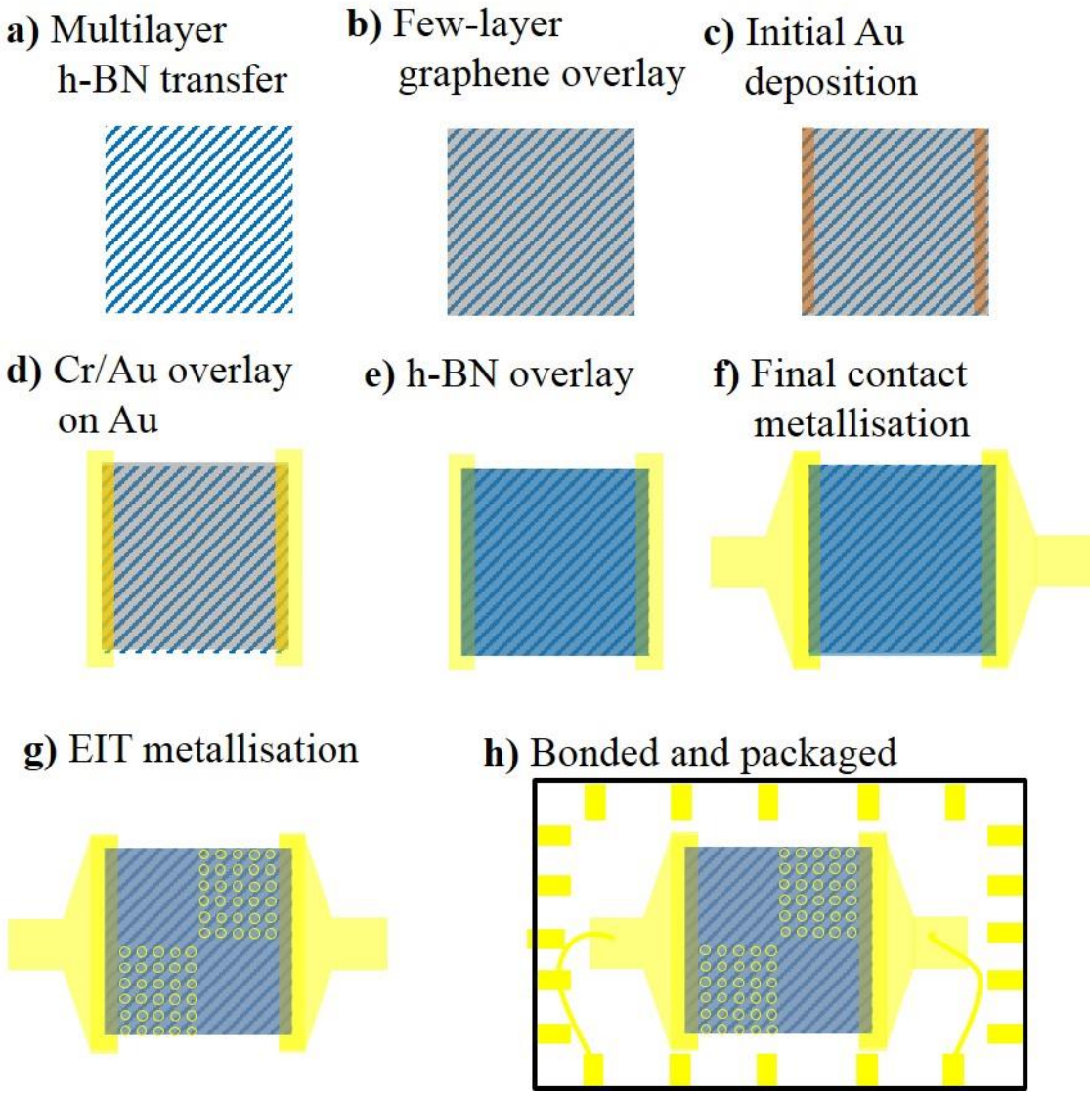

Figure 3.10 Schematic planar diagram illustrating the encapsulated graphene device fabrication: a) transfer and definition of 1st multilayer h-BN layer onto SiO_2/Si b) few-layer graphene transferred on top and defined c) 50 nm wide by 20 nm thick of Au deposited on few-layer graphene d) 100 nm wide by 7/70 nm thick Cr/Au overlay on top of Au and SiO_2 e) encapsulation of few-layer graphene with transfer and definition of top multilayer h-BN layer f) final 7/70 nm thick Cr/Au contact layer deposition g) optional deposition of metamaterial structure h) finished device is packaged and bonded for emission measurements.

3.7 Sample Mounting

3.7.1 Mounting and Sample Bonding

In order to perform emission measurements, the devices must be placed into a multi-pin sample package and the metallic contacts connected to the Au pins on the package and therefore be able to apply a bias current. Silver colloidal solution is used as a conducting adhesive to stick the sample to the package. After drying, the metallic contacts are connected to the pins of the sample package using a wire-bonding machine. The wire-bonder works by melting Au wire with an ultrasonic pulse, first bonding the wire to the pin followed by the contact. It is important that the bond is not made on contacts that are positions on top of graphene because the metal does not have good adhesion to the graphene and when a bond is attempted the contact is damaged. As a result, the bond pads are positioned away from the graphene. During the bonding process a bond is also made between one of the pins and the base of the package. This allows the highly doped silicon substrate to be used as a back gate for resistance modulation of the graphene.

3.8 Summary of Fabricated Devices

The results presented in the experimental chapters of this thesis are from devices that are the result of a multistage fabrication process in which many samples

were tested in order to refine the process. All of the devices used for the experiments presented in this work are listed in table 3.1 below.

Table 3.1 List of all of the devices measured and discussed in this work.

Sample	Substrate	Graphene	Area (mm)	Metamaterial Structure
SLG_D_1	SiO_2/Si	Single-layer	2.0 × 0.5	None
SLG_D_2	SiO_2/Si	Single-layer	0.5 × 0.5	None
FLG_D_1	SiO_2/Si	Few-layer	0.5 × 0.5	None
BN_D_1	SiO_2/Si	Encap. few-layer	0.5 × 0.5	None
RR_D_1	SiO_2/Si	Encap. few-layer	0.5 × 0.5	Rings
RR_D_2	SiO_2/Si	Encap. few-layer	0.5 × 0.5	Rings
RR_D_3	SiO_2/Si	Encap. few-layer	0.5 × 0.5	Rings
RR_D_4	SiO_2/Si	Encap. few-layer	0.5 × 0.5	Rings
RR_D_5	SiO_2/Si	Encap. few-layer	0.5 × 0.5	Rings
RR_D_6	SiO_2/Si	Encap. few-layer	0.5 × 0.5	Rings
SRR_D_1	SiO_2/Si	Encap. few-layer	0.5 × 0.5	Split rings
SRR_D_2	SiO_2/Si	Encap. few-layer	0.5 × 0.5	Split rings
SRR_D_3	SiO_2/Si	Encap. few-layer	0.5 × 0.5	Split rings
SLG_NR600	GaN/AlN/Si NRs	Single-layer		None
SLG_NR2000	GaN/AlN/Si NRs	Single-layer		None

4 Experimental Set-up

This chapter describes the different experimental systems used to characterise the fabricated graphene based devices. In the first section the electrical characterisation measurements are briefly discussed. IV characterisation measurements are covered in section 4.1.1, followed by the gate sweep measurements of single-layer graphene devices in section 4.1.2. In addition, the discussion of the spatially resolved thermal emission measurements using IR microscopy, with a description of CdHgTe photoconductive detector and lock-in amplifier, can be found in section 4.2. In section 4.3, the spectra measurements are discussed with an initial description of grating spectrometers in section 4.3.1, followed by a description of the experimental set-up for the measurement of the emission spectra using a Jobin-Yvon iHR550 grating spectrometer, with the same CdHgTe photoconductive detector (discussed in section 4.2.1) given in section 4.3.2. Details on the calibration of the grating spectrometer acquired emission spectra with a blackbody source are given in section 4.3.2.1. Section 4.3.3 describes Fourier transform infrared spectroscopy with details given in section 4.3.3.1 for the emission spectra measurement set-up utilising a Bruker Vertex V80 spectrometer. Finally, in section 4.3.3.2 the set-up for the reflectance measurements using the same Bruker spectrometer is discussed.

4.1 Electrical Characterisation

4.1.1 IV Characterisation

The initial characterisation measurement performed on the graphene based devices studied in this report were simple two terminal current-voltage measurements, as displayed in Figure 4.1. For these measurements a completed device, packaged and bonded following the procedure discussed in section 3.8.1, was mounted on ceramic chip holder and placed in a vacuum chamber. The chamber was evacuated to approximately 10^{-5} mbars. A Keithley 2400 source meter swept a low DC bias current, over the range of a few mA, while a Keithley 2182A nanovoltmeter measured the voltage drop across the terminals. The resistance values obtained for the devices discussed in this work were typically on the order of 1000 Ω, consistent with values obtained for CVD graphene [138].

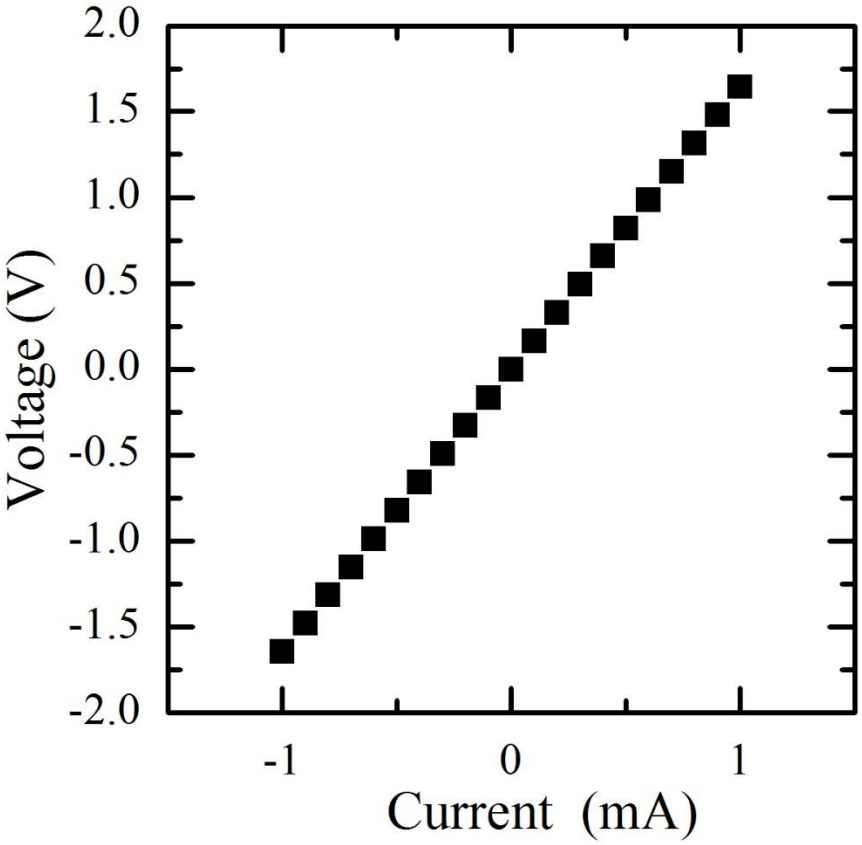

Figure 4.1 Typical IV curve obtained from a graphene on SiO_2/Si device.

4.1.2 Gate Sweeps

In addition to two terminal current-voltage measurements, the electronic properties of the single-layer graphene devices were characterised using field effect measurements. For these measurements a silicon back gate was used along with the two gold (Au) terminals. A 100 nA alternating current, I_D was applied to the graphene through the source drain contacts using a Keithley 6221 current source and the voltage drop across the device is measured, as a function of the back gate voltage, V_g, by a Signal Recovery 7265 DSP lock-in amplifier. The back gate voltage was applied by a Keithley 2400 source meter. The resistance was calculated, using Ohm's law, at each back gate voltage and plotted as a function of V_g. These measurements allowed for the determination

of the appropriate conditions for ambipolar charge transport measurements of the single-layer graphene devices, presented in Chapter 5.

4.2 Device Driving

For the experimental systems discussed in the following sections that require the application of a current bias across the contacts of the graphene devices, a Keithley 6221 current source was used. In each instant the applied current was a pulsed DC drive current, typically on the order of tens of milliamps. The waveform of the drive current was always a square waveform with a 50% duty cycle with the frequency typically set to 1 kHz, with the exception of the frequency dependent measurements (presented in section 5.3), in which the overall emission intensity of the graphene based devices was measured as a function of drive frequency. For these measurements the drive frequency was swept from 1 to 100 kHz.

The devices were placed inside a vacuum chamber for measurements with an applied drive current. The devices were first mounted on a ceramic chip holder and then placed inside a chamber with a polished 2 mm thick calcium fluoride (CaF_2) window for optical access. The transmittance range of the CaF_2 window is 0.15-12 µm. The cut off wavelength is dependent on the thickness of the CaF_2, with thinner CaF_2 having a longer cut-off wavelength. The vacuum chamber would typically be evacuated to ~10^{-5} mbar.

4.3 Spatially Resolved Emission/Reflectance Measurements

The spatially resolved emission measurements presented in this work were performed using an IR microscopy set-up. This consisted of a motorised xy-stage, reflecting objective, focusing lens and a Cadmium Mercury Telluride (CMT) photoconductive detector connected to a lock-in amplifier for phase sensitive measurements, as illustrated schematically in Figure 4.2. The devices were driven as described in section 4.2 with the back gate typically left floating, though it could be swept to measure the spatially resolved thermal emission as a function of the back gate voltage. The applied bias current caused Joule heating in the graphene and the resulting thermal emission was collected using either a 15X or 40X reflecting objective and focused, using a CaF_2 lens, onto the CMT detector. The reflecting objective was mounted on a motorised xy-stage in order to measure the thermal emission at various points across the surface of the sample. This allowed for the generation of a 2D surface map of the emission intensity as a function of position by systematically scanning the reflecting object over the sample and measuring the overall emission intensity at each point. The signal from the CMT detector was amplified by a low noise pre-amplifier, specific to the CMT detector, and finally passed to a lock-in amplifier, where the signal was compared to a reference signal from the current source, for phase sensitive measurements. The spatially resolved reflectance measurements were performed similarly, utilising the same IR microscopy set-up, however, an optical chopper was inserted between the detector and the device in order to pulse the signal and provide the reference for the lock-in. Additionally, the spectrum from a

mid-infrared (MIR) blackbody source was measured to calibrate and compare to the measured device emission. For these measurements the vacuum chamber was replaced by the blackbody source. More details on both the CMT detector and lock-in amplifier follow.

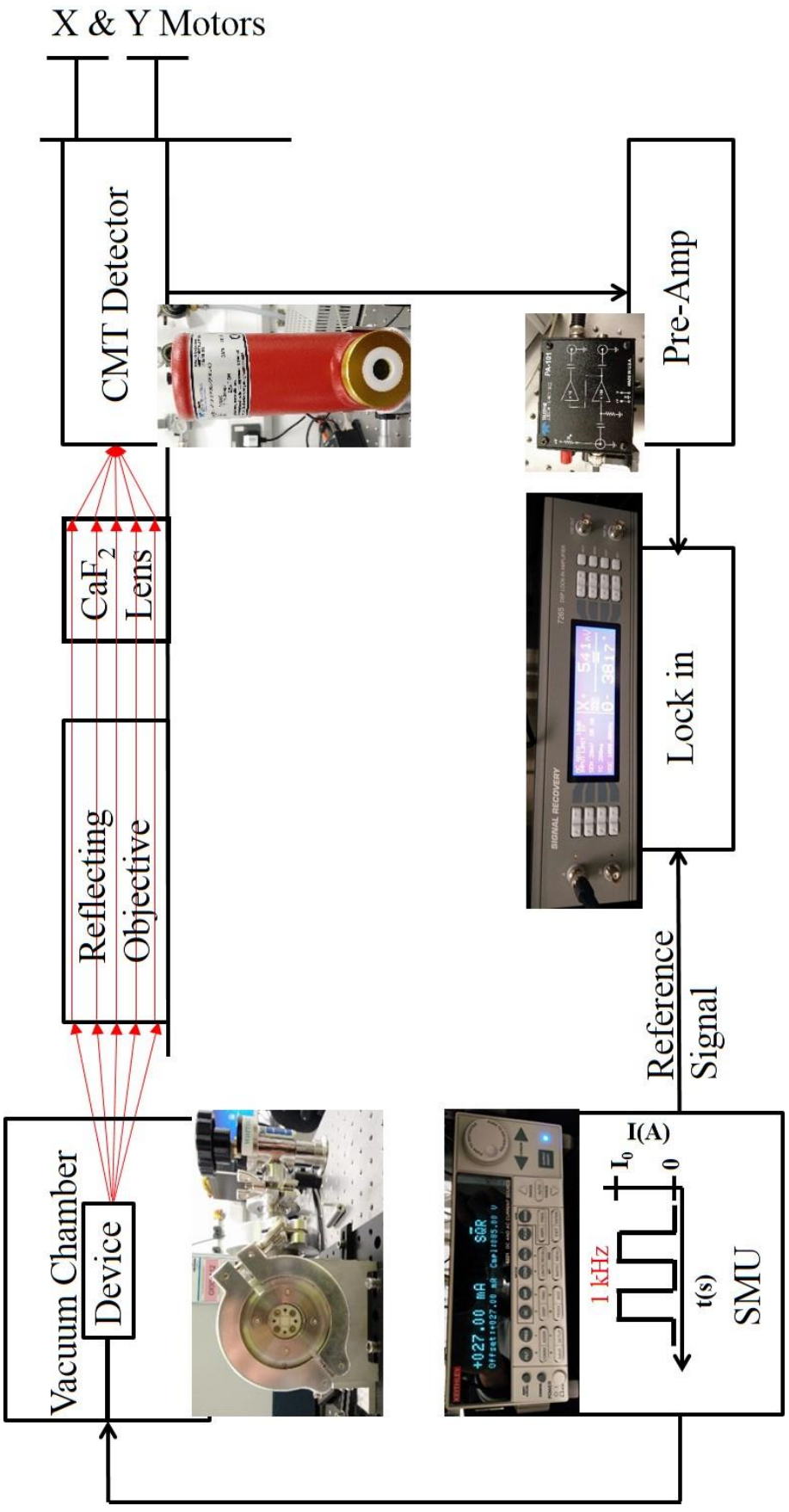

Figure 4.2 A schematic diagram illustrating the optical path and experimental set-up used for the spatially resolved thermal emission measurements.

In a CMT photoconductive detector the resistance of the photoconductive element, R_D, changes proportionally to the incident infrared (IR) radiation. The active region is a 10-20 µm layer of CdHgTe, a ternary semiconductor compound, between two metallic contacts, and the incident photons excite electrons from the valance band to the conduction band, if their energy is greater than the semiconductor band gap. This increases the conductivity of the semiconductor thus lowering the resistance. This change in resistance, ΔR_D, is converted to a change in voltage, ΔV, by applying a constant bias current, I_B. Therefore, the change in voltage is given by

$$\Delta V = I_B \Delta R_D \tag{4.1}$$

with the optimal bias current depending on characteristics of the detector such as size and spectral response. The band gap of CdHgTe can be tuned between the shortwave infrared (IR) through to the very longwave IR regions by altering the amount of Cd in the alloy. The composition of CdHgTe also determines both the cut-off wavelength and frequency of the CMT detector where the cut-off wavelength is defined as the wavelength at which the response is 20% that of the peak response. The cut-off frequency is the frequency at which the response of the detector decreases 3dB from the steady output level. Additionally, at low frequencies the noise increases as ~1/f below 1 kHz. It is therefore best to keep the operating frequency of the detector between the 1 kHz and the cut-off frequency. Finally, CMT detectors require a pre-amplifier with a low voltage noise due to their low impedance (10-150 Ω). Each pre-amplifier supplied with the detector is specific to that detector. The J15D12 detector has an active area of 4 mm^2 and is mounted in a metal dewar, to allow for liquid nitrogen cooling to its operating temperature of 77 K, with a ZnSe window for optical access. Cryogenic

cooling is required to overcome thermal noise and to increase the detectors sensitivity to small temperature variations. The optimum frequency range for the J15D12 is ~1-200 kHz with a time constant of 0.5 µs and a responsivity of ~100 V/W at the peak wavelength of 11 µm. The detector has an operating range of 2 – 12 µm with a peak response at 11 µm, as is displayed in Figure 4.3.

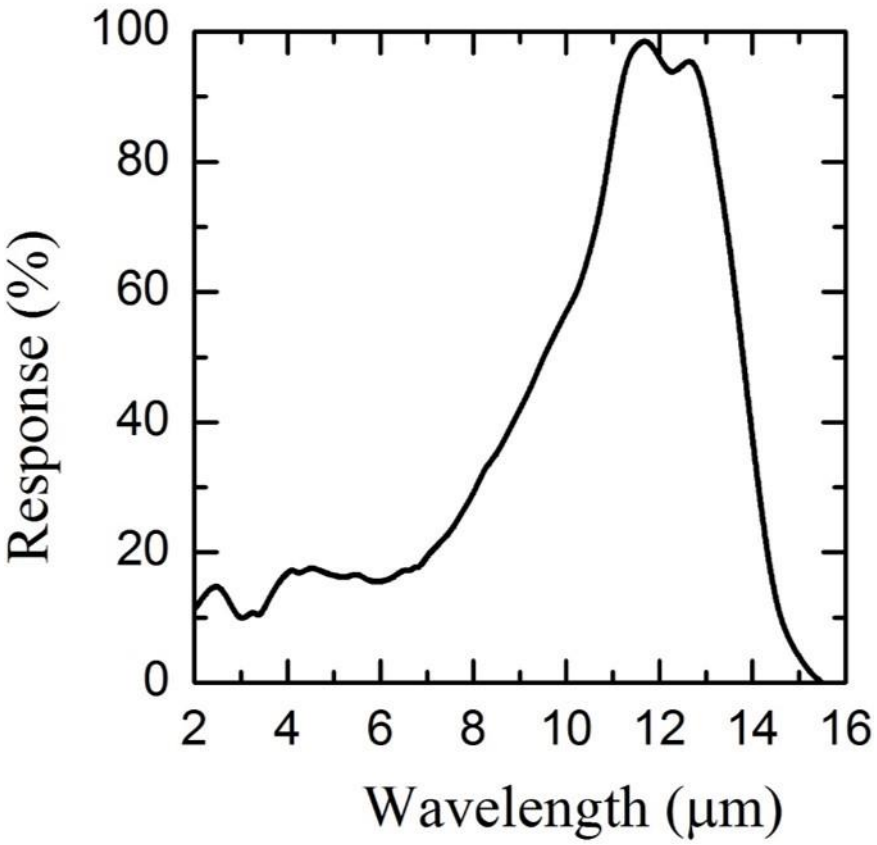

Figure 4.3 Spectral response of the J15D CMT detector at 10 kHz.

Due to the relatively large amount of noise and alternating nature of the signal the J15D CMT detector is paired with a lock-in amplifier for phase sensitive measurements. Lock-in amplifiers are typically used to measure very small AC signals, down to a few nanovolts, obscured by a large noise background. This is accomplished by using phase-sensitive detection to identify the component of the signal that has the same frequency and phase as a reference signal. Noise at frequencies different to the reference signal do not affect the measurements.

Typically, samples are excited at a fixed frequency, using an instrument like a function generator, and the lock-in detects the response from the sample at the reference frequency, which it would get in this example from the function generator. The signal is therefore a sinusoidal function represented by the equation, $V_s \sin(\omega_r t + \theta_s)$, where ω_r is the signal frequency, V_s is the singal amplitude and θ_s is the signal's phase. Lock-in amplifiers use a phase-locked-loop that is locked to the external reference from the signal generator in this case, to generate an internal reference. The internal reference is also sinusoidal and is given as, $V_l \sin(\omega_l t + \theta_r)$, where V_l is the internal lock-in reference amplitude, ω_l is the internal reference frequency and θ_r is the reference phase. The phase sensitive detector multiplies the signal by the internal reference with the output of the phase sensitive detector being

$$V_{psd} = ½V_s V_l \cos([\omega_r - \omega_l]t + \theta_s - \theta_r) - ½V_s V_L \cos([\omega_r + \omega_l]t + \theta_s - \theta_r) \quad (4.2)$$

with the PSD output being composed of two AC signals. This output is then passed through a low pass filter, removing the AC component. However, when $\omega_r = \omega_l$ the difference frequency component, $\omega_r - \omega_l$, is a DC signal and is therefore not filtered by the low pass filter. As a consequence, the lock-in only detects signals very close to the reference signal.

For all of the measurement systems that require phase sensitive measurements the J15D CMT detector is utilised in combination with a dual-phase Signal Recovery 7265 DSP lock-in amplifier. As the lock-in filters out all parts of the signal that are not the same frequency as the reference frequency, the only measurable signal is from areas of the sample that are able to heat up and cool down at the same frequency as the drive current. Additionally, this also allows for

the assumption that the measured emission spectra from the graphene devices corresponds to difference of two spectra, one at a higher temperature when the current is on, the “on” temperature and one at a lower temperature, the “off” temperature, when the current is off.

4.4 Grating Spectrometer Measurements

Spectrometers measure the intensity of light as a function of wavelength. There are multiple different configurations of spectrometers available to achieve this. This section will focus on plane grating systems (PGS), primarily the Czerny-Turner design, one of the most common spectrometers. This type of spectrometer was utilised to measure the emission spectra from the single and few-layer graphene on SiO_2/Si devices presented in this work. Figure 4.4 illustrates a top down view of a Czerny-Turner spectrometer including the optical path. In a Czerny-Turner spectrometer the broad spectra enter the instrument through the entrance slight where it reflects off the first mirror that is located at the necessary distance from the entrance slit to collimate the beam. The collimated beam is then diffracted from the diffraction grating and reflected by a second mirror, refocusing the now dispersed beam onto the exit slit. By rotating the grating on its axis the wavelength of light that is focused onto the exit slit changes. A detector is placed in front of the exit slit to measure the spectral intensity as a function of wavelength, in this example a CMT detector is utilised.

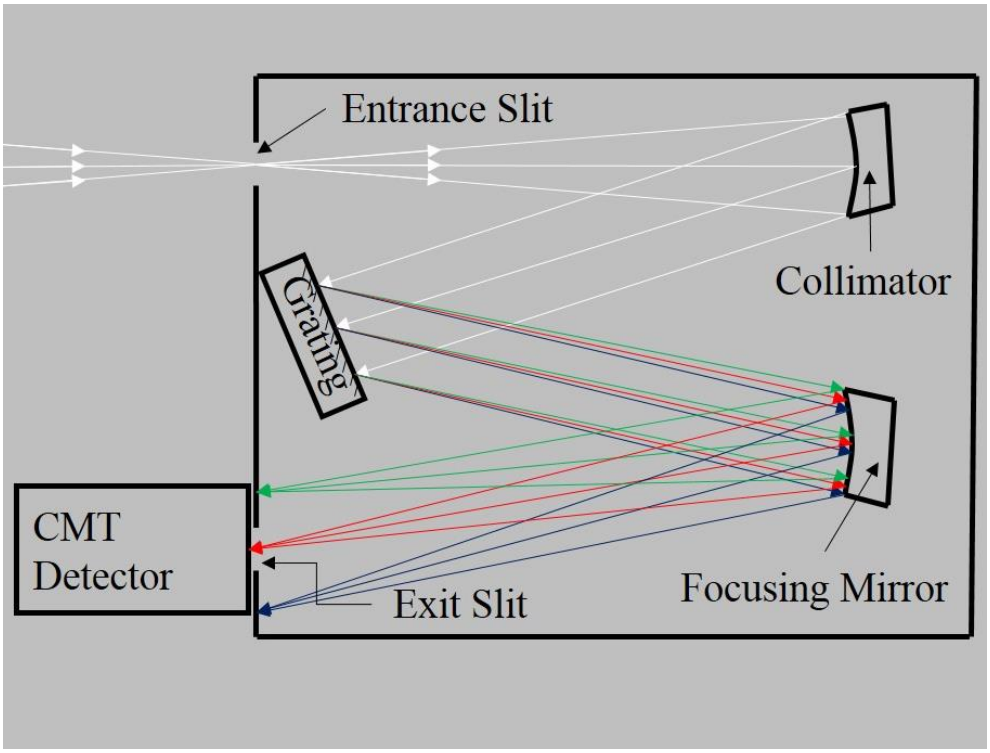

Figure 4.4 Diagram of the top down view of a Czerny-Turner spectrometer.

The diffraction gratings are either mechanically ruled, where grooves are etched into the surface of the grating using a diamond stylus, or they are holographically formed using the interference fringe field of two laser beams. Each has their own advantages and disadvantages with holographic grating often having lower scattering but also less aberrations. It is possible to calculate the resolution of different diffraction gratings. However, as the emission from the graphene based devices is that of a grey-body (discussed in Chapter 5), the resolution of the grating spectrometer is not a concern as the grating spectrometer is not used to resolve fine spectral detail. Alternatively, the efficiency of the diffraction gratings is an important consideration as the incident light can be diffracted into multiple orders. The efficiency of a grating is given as the fraction of light diffracted into any order, typically the first order. Diffraction gratings are not equally efficient at all wavelengths and can be tuned for a specific wavelength, maximizing the

efficiency at that wavelength, by a process known as blazing. This is done by changing the groove facet angle or blaze angle. The efficiency is generally given as the efficiency of the grating relative to a mirror coated in the same material. This relative efficiency equation is therefore

$$relative\ efficiency = \frac{grating\ efficiency}{mirror\ efficiency} \tag{4.3}$$

with the theoretical relative efficiency curves for the two blazed gratings utilised in the measurement of the device spectra, presented in Figure 4.5. They are both averages of the TE and TM efficiency. For a plane blazed grating, both the groove density and blaze angle determine the distribution of energy. The G300 grating is a 4 µm blazed grating with a blaze angle of 36°52’ and a groove density of 300 grooves per mm. The G150 is a 8 µm blazed grating with the same 36°52’ blaze angle and 150 grooves per mm. Combining the two gratings in spectral measurements gives a possible spectral range of ~2 -12 µm.

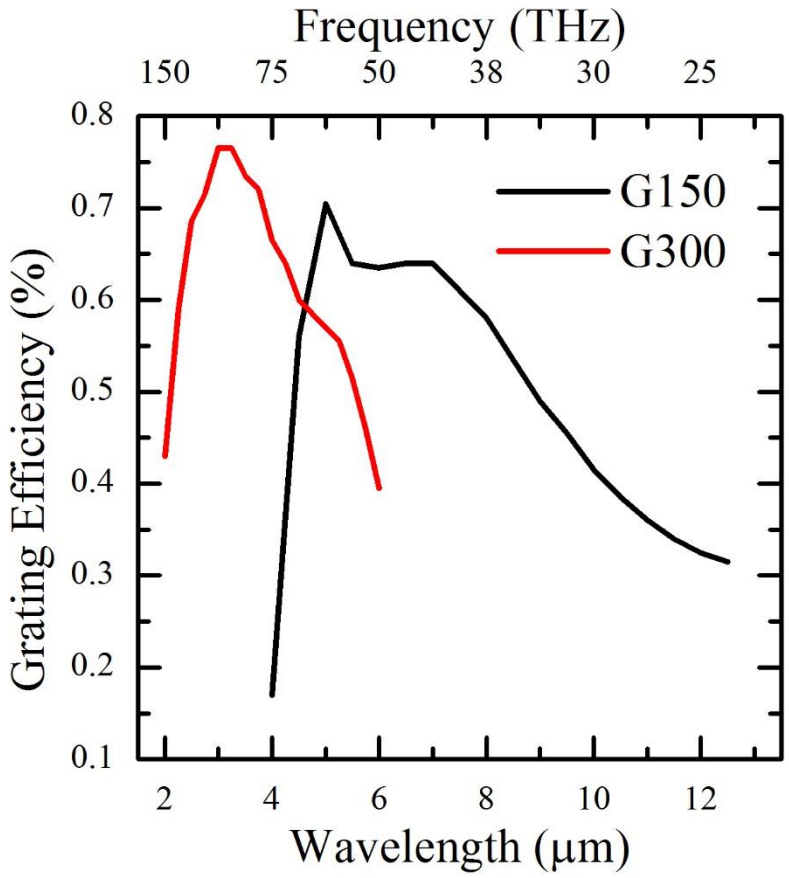

Figure 4.5 Spectra response of both the G150 (black line) and G300 (red line) blaze gratings.

A schematic illustration of the experimental system utilising a grating spectrometer to measure the emission spectra from both single and few-layer graphene based devices is displayed in Figure 4.6. The graphene devices were driven as described in section 4.2, with peak injection currents chosen to give similar power densities across the single and few-layer devices. The resulting emission was collimated and focused using two CaF_2 lenses. The 2nd CaF_2 lens focused the light on the entrance slit of a Jobin-Yvon iHR550 grating spectrometer. The light was diffracted from either the G300 or G150 grating and passed to the exit slit where it was collected by the CMT Detector. The spectra were primarily collected over 2–6 μm range by utilising just the G300 grating. The signal from the CMT detector was then sent to the lock-in amplifier for phase

sensitive measurements as discussed in the previous section. In addition to the two gratings the spectrometer also has an internal mirror, allowing for the measurement of the undispersed spectra. This was implemented in order to measure the overall emission intensity as a function of drive frequency.

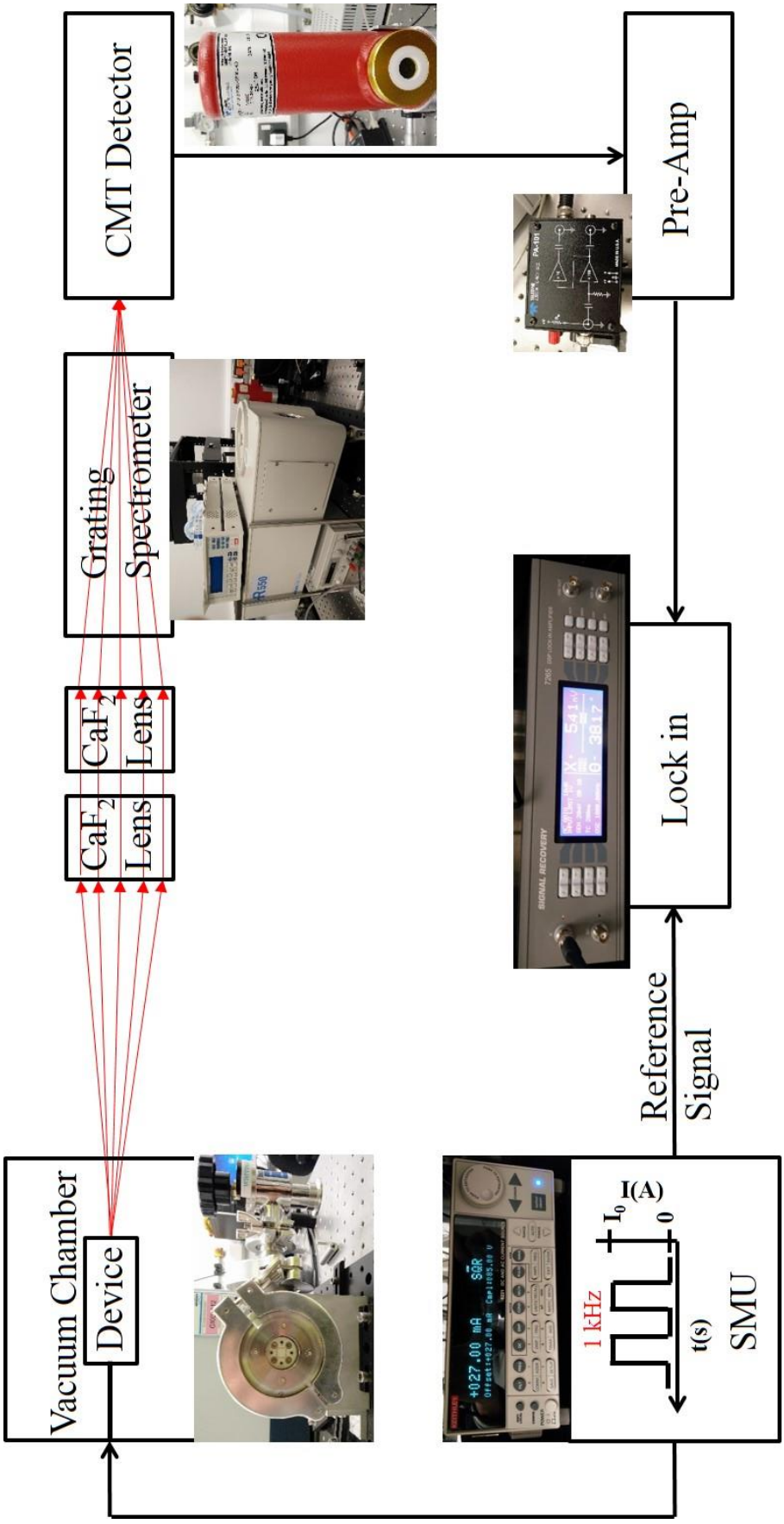

Figure 4.6 A schematic illustration of the experimental set-up, including the optical path, using a grating spectrometer to measure the overall emission spectra.

4.4.1 Calibration of Emission Spectra

In order to correct the measured emission spectra for atmospheric absorption, grating efficiency and detector response, an Omega BB703 blackbody calibration source was used. A schematic illustration of the experimental set-up involved in the measurement of the blackbody calibration source is shown below in Figure 4.7. To generate the calibration curve firstly the emission spectrum of the 0.95 emissivity blackbody source, set to a temperature of 673 K, was measured. To perform these measurements an optical chopper was inserted between the entrance slit of the grating spectrometer and blackbody source. In addition to modulating the signal from the blackbody source, the chopper provided the external reference signal for lock-in amplifier, at the frequency it is set to. The spectra were measured over 2-10 μm by using both of the gratings. The calibration spectra, C_s is given by

$$C_s = \frac{B_s}{T_s(T)} \tag{4.4}$$

where B_s is the measured blackbody spectra and $T_s(T)$ is the theoretical grey-body spectra, at 673 K given by

$$T_s(T) = \varepsilon B_\lambda(T) \tag{4.5}$$

where ε = 0.95 is the emissivity and $B_\lambda(T)$ is the blackbody spectra given by Planck's law provided in section 2.2.2. The calibration spectrum is then utilised to calibrate the measured device spectra, D_s, by dividing it on the device spectra giving

$$CD_s = \frac{D_s}{C_s} \tag{4.6}$$

where CD_s is the calibrated device spectra. The integral of the calibrated device spectra can then be taken to get the total emitted power.

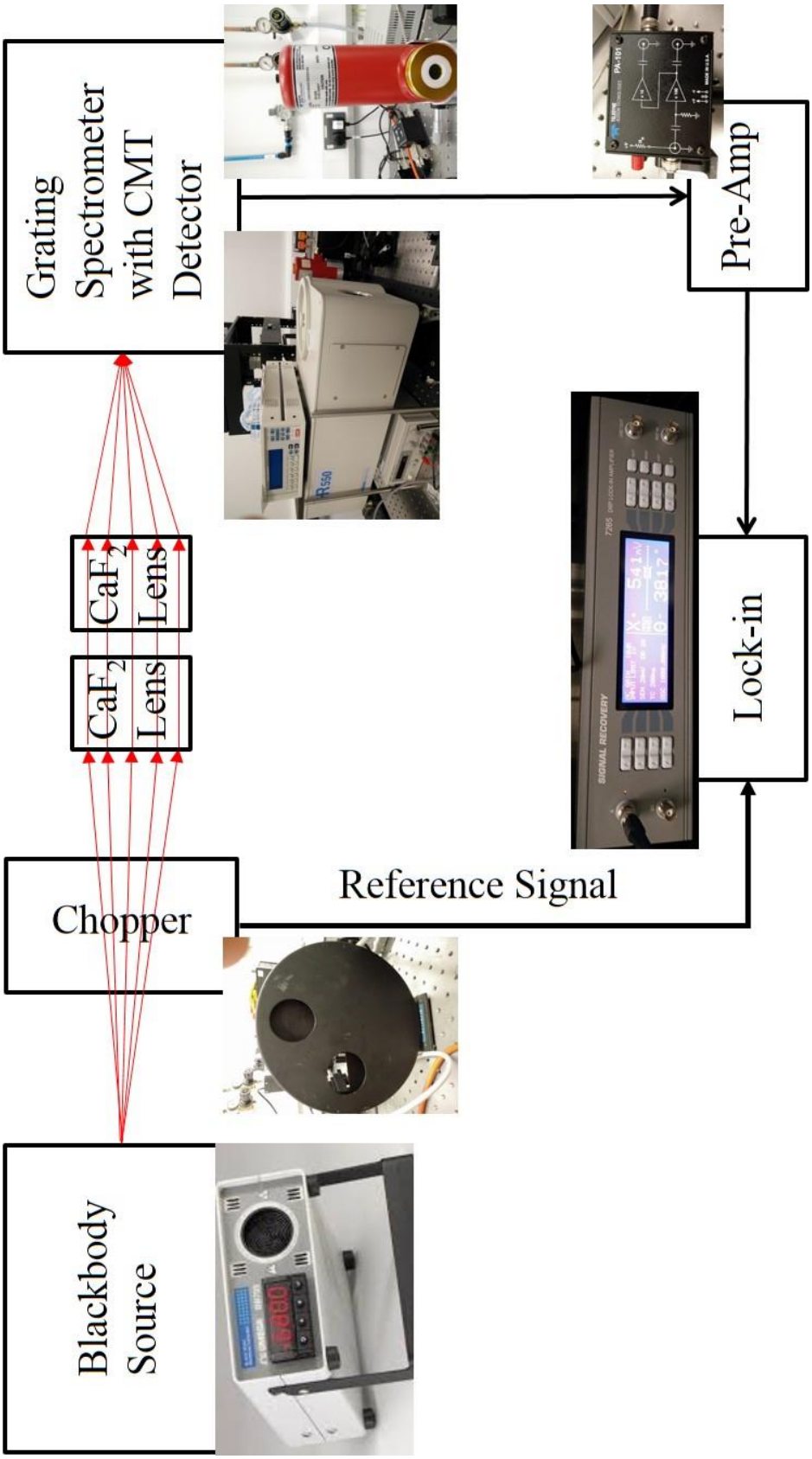

Figure 4.7 Schematic of the blackbody calibration measurement system.

4.5 FTIR Measurements

As opposed to diffraction spectroscopy, Fourier transform infrared spectroscopy (FTIR) obtains the infrared transmittance, reflectance or emission spectrum simultaneously over a wide spectral range. This allows for much quicker scan times in comparison to diffraction spectroscopy, a significant advantage. It also has a higher optical throughput, resulting in lower noise levels and is able to self-calibrate due to the internal HeNe laser. For reflectance and transmittance measurements an internal blackbody IR source is used to shine a broadband emission onto the sample. Prior to the reaching the sample the light passes through an aperture, which controls the beam size, and then through a Michelson interferometer. In the interferometer the light from the blackbody source is collimated and passed through a beamsplitter where 50% of the light is transmitted to a moving mirror and 50% of the light is refracted to a stationary mirror. As the one mirror moves it changes the optical path length in comparison to the light reflected from the station mirror. This difference is called the optical path difference (OPD) and results in periodic interference when the beams recombine at the beamsplitter. The light is then focused onto the sample where it is either transmitted or reflected and it is then focused onto a detector. An interferogram is obtained by varying the OPD and recording the signal from the detector. The interferogram is then converted to reflectance or transmittance spectra by taking the Fourier transform of the interferogram. For emission measurements the IR source is replaced by the IR emission from the sample. An example of an FTIR set-up for emission measurements and reflectance measurements is shown in Figure 4.8(a) and Figure 4.8(b) respectively. For these two set-ups the key difference is that instead of using the internal blackbody IR

source, as in the reflectance set-up, the emission set-up uses the broadband IR emission from the sample as the broadband IR source.

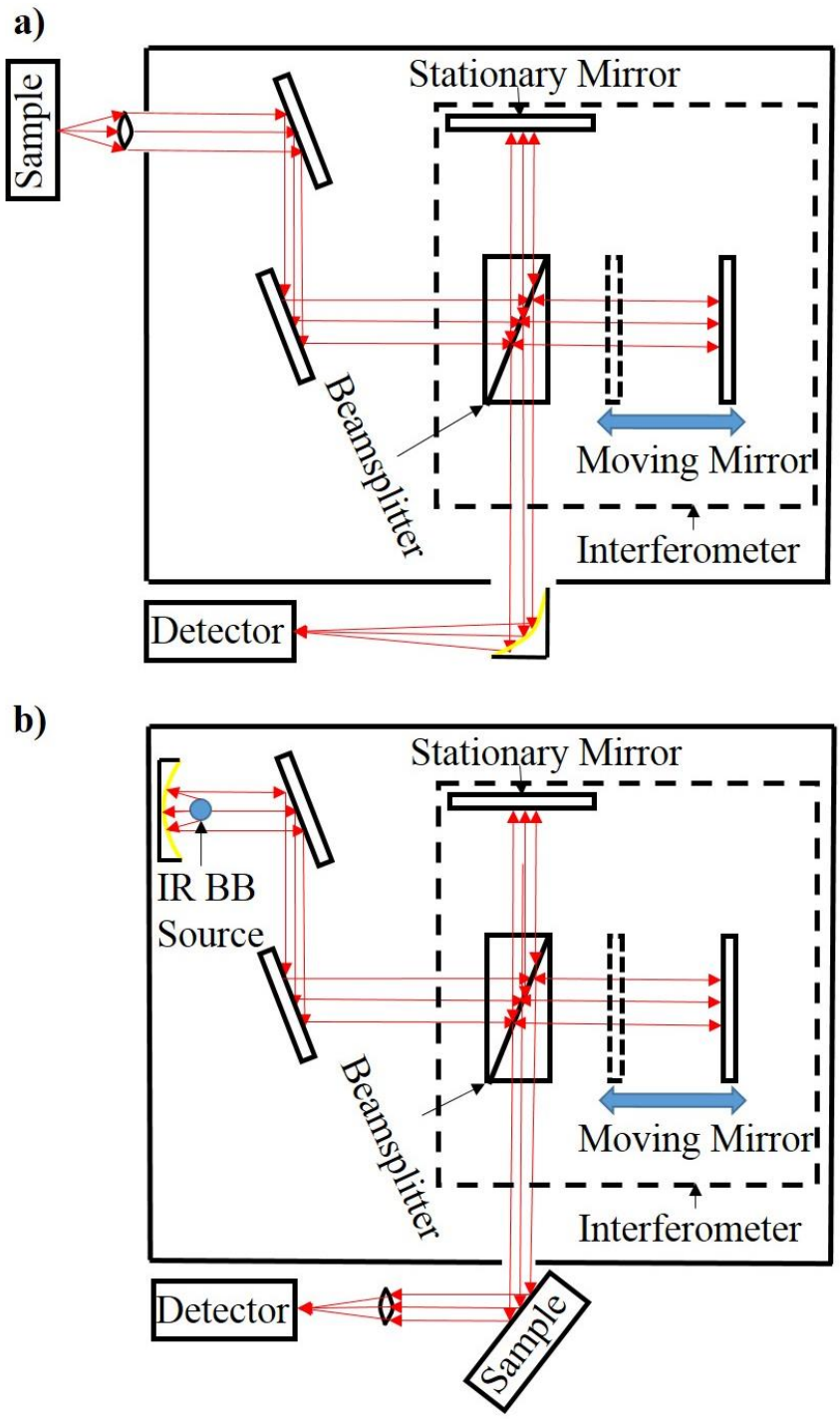

Figure 4.8 FTIR spectrometer set-up for a) emission measurements and b) reflectance measurements.

4.5.1 Emission Measurements

For the experimental emission results presented in Chapter 6, a Bruker Vertex 80 FTIR spectrometer was used, with a schematic illustration of the experimental system shown in Figure 4.9. The devices were driven as described in section 4.2 and the resulting thermal emission collected and collimated using a 40X reflecting object. The reflecting objective was mounted on a motorised xy-stage in order to perform spatially resolved thermal emission mapping experiments, discussed in section 4.3, and to determine the x and y positions to take spectral measurements from. Two flat mirrors were used to direct the collimated light into the FTIR spectrometer. The collimated beam was then passed through a KBr beamsplitter inside the interferometer section of the FTIR. The split beam was reflected off the stationary mirror and the moving mirror before recombining as it passed back through the beamsplitter. The recombined beam exits the spectrometer and was focused, using an Au parabolic mirror, onto the J15D12 CMT detector. The signal from the detector was then sent to the lock-in amplifier for phase sensitive measurements. The use of a lock-in amplifier necessitated the measurements be performed using the step scan measurement method. For step scans the interferometer mirror moves in discrete steps to each of the interferogram points and data is acquired at each point. The step scan was necessary because the lock-in needs time to measure and average the signal at each point (~5X the time constant). The disadvantage of this technique is that rather than performing tens of scans per second, as the rapid scanning method does, it takes minutes to perform one full scan. These measurements were performed on the encapsulated graphene devices integrated with metamaterials, presented in Chapter 6. For these devices, half of the active area is covered with a

metamaterial structure, such as ring resonators (RR), and the other half is bare hexagonal boron nitride encapsulated graphene. Five step scans each were performed at three different points on the two different sections of the encapsulated devices and then averaged. This helped to reduce noise and ensure that the average of the emission was obtained from each section. The spectra from the bare encapsulated area was utilised to normalise the measured spectra from the areas with the metamaterial structure. The normalised spectrum, *NS*, is given as

$$NS = \frac{S_{RR}}{S} \tag{4.7}$$

where *S* is the measured emission spectra from areas of the devices integrated with metamaterials and S_{RR} is the emission spectra from the bare encapsulated graphene regions.

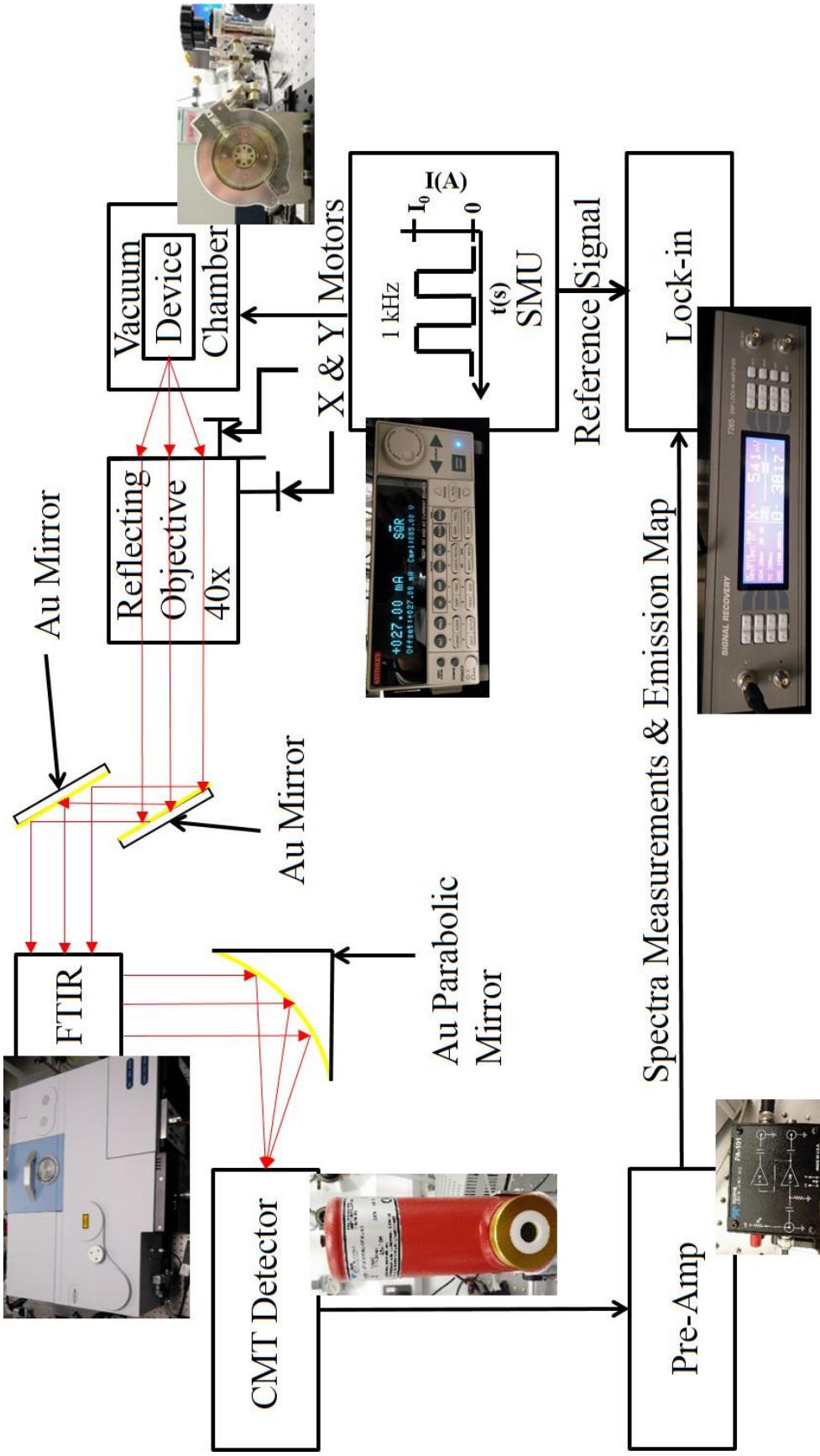

Figure 4.9 A diagram of the experimental set-up, including the optical path, using an FTIR spectrometer to measure the emission spectra from the metamaterial integrated graphene devices.

4.5.2 Reflectance Measurements

The same Bruker Vertex 80 FTIR was utilised for the IR reflectance measurement results presented in this work on both encapsulated graphene devices and graphene transferred on top of GaN nano-rod arrays in Chapters 6 and 7 respectively. A diagram illustrating the experimental set-up is shown in Figure 4.10. For these measurements the IR source was an internal mid-IR Globar source, with a spectra response that corresponds approximately to a blackbody radiator. The mid-IR beam was initially passed through the interferometer before exiting the spectrometer via the exit port. The collimated beam was then directed through a beamsplitter (using two Au parabolic mirrors to reduce the size of the collimated beam, ensuring maximum power is collected) followed by a 40X reflecting objective which focused the beam onto a sample mounted on a xy-stage. The focused beam was reflected off of the sample and was collimated by the reflecting objective collimated before again passing through the beamsplitter. The refracted portion of light from the beamsplitter was focused onto the J15D12 CMT detector using a third Au parabolic mirror. The signal from the IR detector was sent to the FTIR spectrometer where the interferogram was generated by the rapid scanning technique. This allowed for 256 scans to be performed and averaged, with a resolution of 8 cm^{-1} and an aperture size of 1 mm, in little more than a minute. Finally, the computer performed the Fourier transform on the interferogram to generate a plot of reflectance vs wavelength. The set-up also allowed for the measurement of the spatially resolved reflectance with the insertion of an optical chopper and lock-in amplifier, discussed in section 4.3. The spatial resolution of the reflection mapping was determined by characterising

samples with known feature sizes, with the minimum feature size that could be determined being approximately 10 µm.

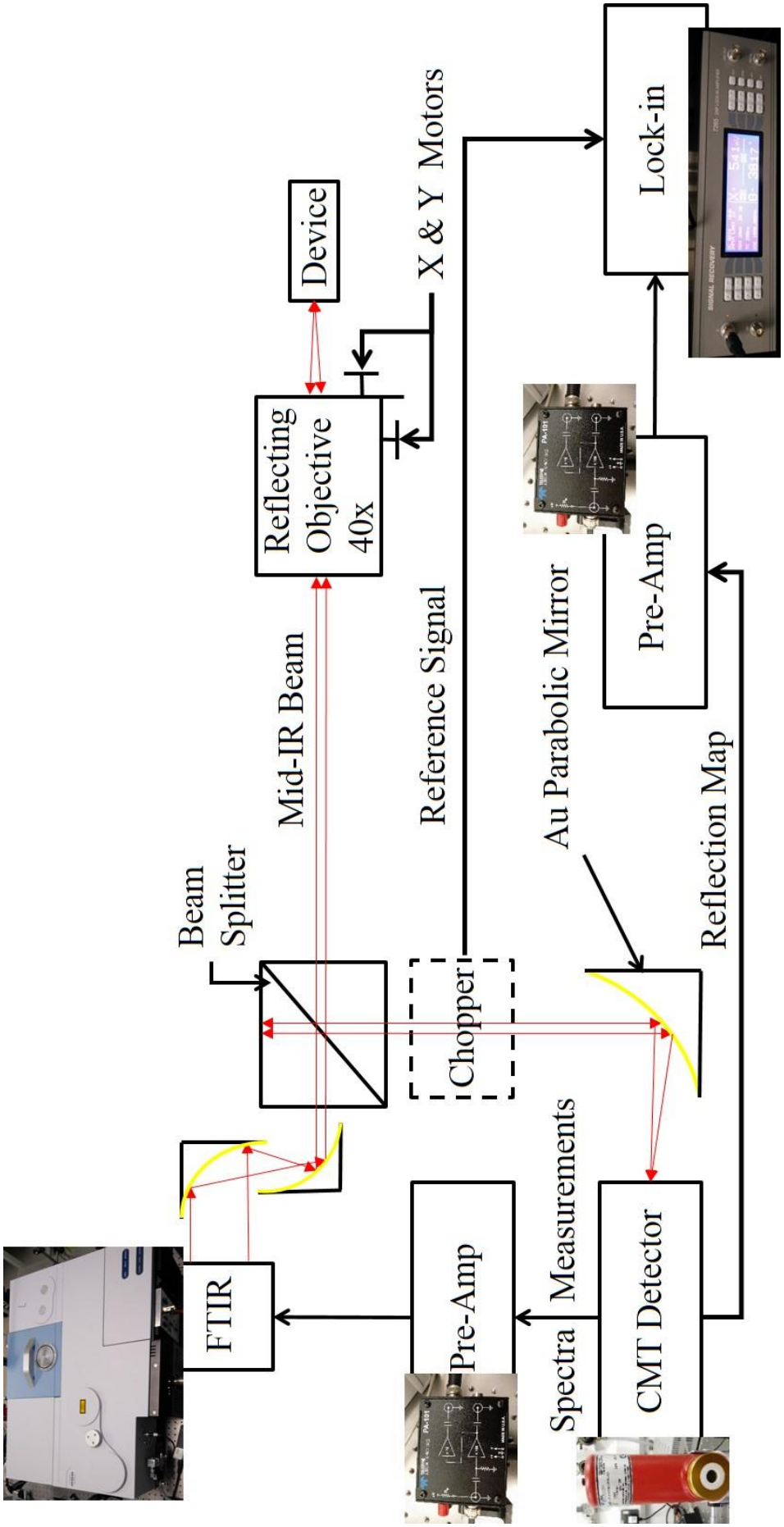

Figure 4.10 A diagram of the experimental set-up, including the optical path, using an FTIR spectrometer to measure the reflectance spectra.

5 Thermal Control

5.1 Introduction

The thermal emission from graphene is largely determined by its electrical properties, so it is important to understand the charge transport properties of graphene because the thermal emission is largely governed by the electrical properties. The charge transport properties of small area, monolayer exfoliated graphene transistor devices, have been investigated extensively in the last few years using thermal emission [14,15,139,140]. In the high electric field regime, the charge transport of single-layer exfoliated graphene can be ambipolar in nature, with an equal number of electron and hole charge carriers at a specific point along the channel. At this location, the charge neutral point (CNP), there is a maximum in the thermal emission or hot spot due to a localised resistance maxima [14,15,139]. However, little work has been done using the thermal emission to study the electrical transport properties of large area, CVD graphene devices. Here the thermal emission has been investigated as a function of position and frequency for both single and few-layer large area CVD graphene. Additionally the modulation characteristics of graphene based devices, including a third type of device where few-layer graphene is encapsulated between hexagonal Boron Nitride (h-BN), are investigated. One of the most important aspects to consider in the design of an infrared thermal emitter is the thermal management. For example heat dissipation into the underlying substrate has been shown to limit aspects like maximum operating temperature and radiative efficiency [141]. It is also of particular interest for devices that are intended to be

modulated at high frequencies [17]. Not only must devices heat up quickly, when the current is on, but they must also dissipate the heat quickly, when the current is off. The large surface area, high thermal conductivity [142] and low thermal mass of graphene make it an attractive option as a modulated thermal emitter. It has previously been shown that the heat dissipation of an exfoliated graphene device is dominated by the vertical heat sinking path; for devices that are longer than a few millimetres [143]. This suggests that the most effective way to achieve a large thermal modulation at high drive frequencies is to manage the vertical thermal path. COMSOL, a finite element software package, is utilised to create a 2D model in order to both better understand the experimental results and to investigate the impact of various changes on the thermal modulation.

In this chapter the experiments performed on the various graphene based devices are discussed. The spatially resolved thermal emission experiments are discussed in section 5.2, where the emission intensity is measured at specific points (in the xy plane) across the surface of the devices. The single-layer CVD graphene (SLG) device results are discussed in section 5.2.1 and few-layer CVD graphene (FLG) results in section 5.2.2. In section 5.2.3 the simulated normalised temperature profile along the surface of the 2D COMSOL model is compared to the measured intensity through the middle of the multilayer device. Section 5.3 discusses the modulation characteristic experiments where the emission intensity is measured as a function of drive frequency. Section 5.3.1 discusses the results of SLG and FLG based devices and section 5.3.2 discusses the h-BN encapsulated FLG device results that show an increase in the thermal emission as a function drive frequency compared to the standard FLG device. This is followed by a summary of the chapter in section 5.4. Parts of this chapter have been adapted for publication in; Thermal emission from large area chemical vapor

deposited graphene devices, Applied Physics Letters 103, 131906 (2013); Prospective for graphene based thermal mid-infrared light emitting devices, AIP Advances 4, 087139 (2014); Modulation characteristics of graphene-based thermal emitters, Applied Physics Express 9, 12105 (2016) and Boron nitride encapsulated graphene infrared emitters, Applied Physics Letters 108, 131110 (2016).

5.2 Spatially Resolved Thermal Emission

The spatial characteristics of the thermal emission from single and few-layer graphene based mid-IR emitters are investigated by measuring the spatial variation of the thermal emission from three different devices. The details of the experimental set-up utilised for these measurements are provided in section 4.3. The three devices investigated are: SLG_D_1, a single layer graphene device with an emitting area of 2 mm × 0.5 mm; SLG_D_2, a square 0.5 mm × 0.5 mm SLG device and FLG_D_1, a 0.5 mm × 0.5 mm few-layer graphene device. The substrates of all three devices are highly doped (p-doped) Si with a 300 nm thick oxide layer. The full fabrication process of these devices is described in section 3.7.1. For all three the contacts are large enough that the contact resistance can be assumed to be negligible [140]. A schematic of a typical device used in the experiments described in this chapter is shown in Figure 5.1.

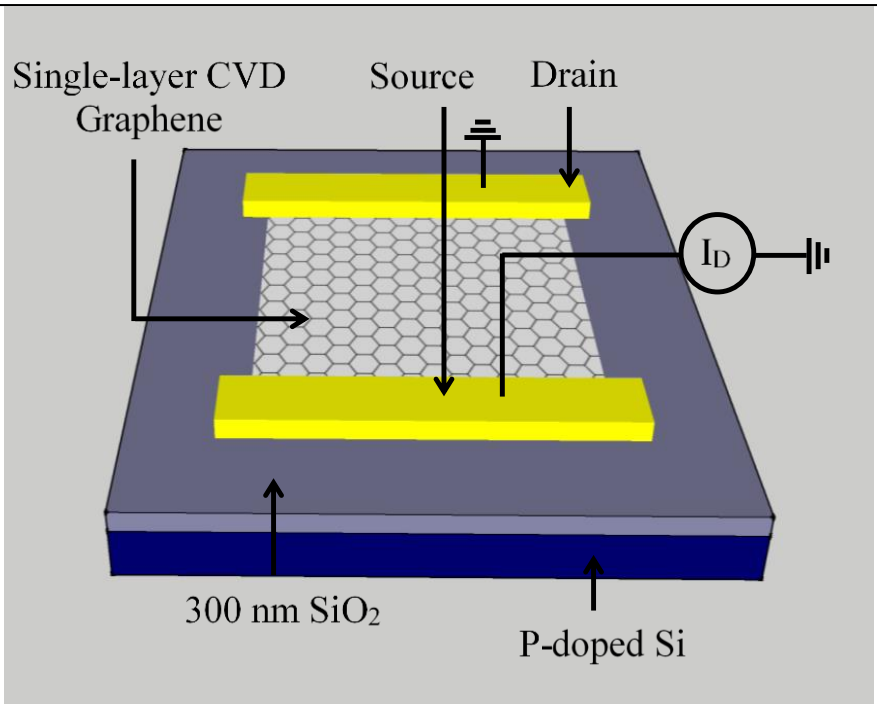

Figure 5.1 A schematic of a typical single-layer graphene device.

5.2.1 Single-layer Graphene Devices

In Figure 5.2(a-c) the spatial variation of the thermal emission from SLG_D_1, under a constant 1 kHz reverse bias drive current of 3.5 mA (V_{DS} ~35 V), is shown for three different gate voltages, V_{GD} = 40 V, V_{GD} = 60 V and V_{GD} = 80 V respectively. In all cases the emission is only observed from the 2 mm × 0.5 mm emitting area. This suggests that only the temperature of the graphene is changing on the time scale defined by the length (0.5 ms) and period (1 ms) of the current pulses, as the magnitude of the signal corresponds to the difference between the thermal emission when the current is on and when it is off described in more detail in section 4.3. In exfoliated, small area graphene devices at high lateral fields the electrostatic potential, and therefore the resistance, differs largely along the channel [139]. The applied gate voltage sets the electrostatic

potential at the drain, while the electrostatic potential at the source, $V_{GS,}$ is given by [14]

$$V_{GS} = V_{GD} - V_{DS} \tag{5.1}$$

where V_{DS} is the voltage bias between the drain and the source.

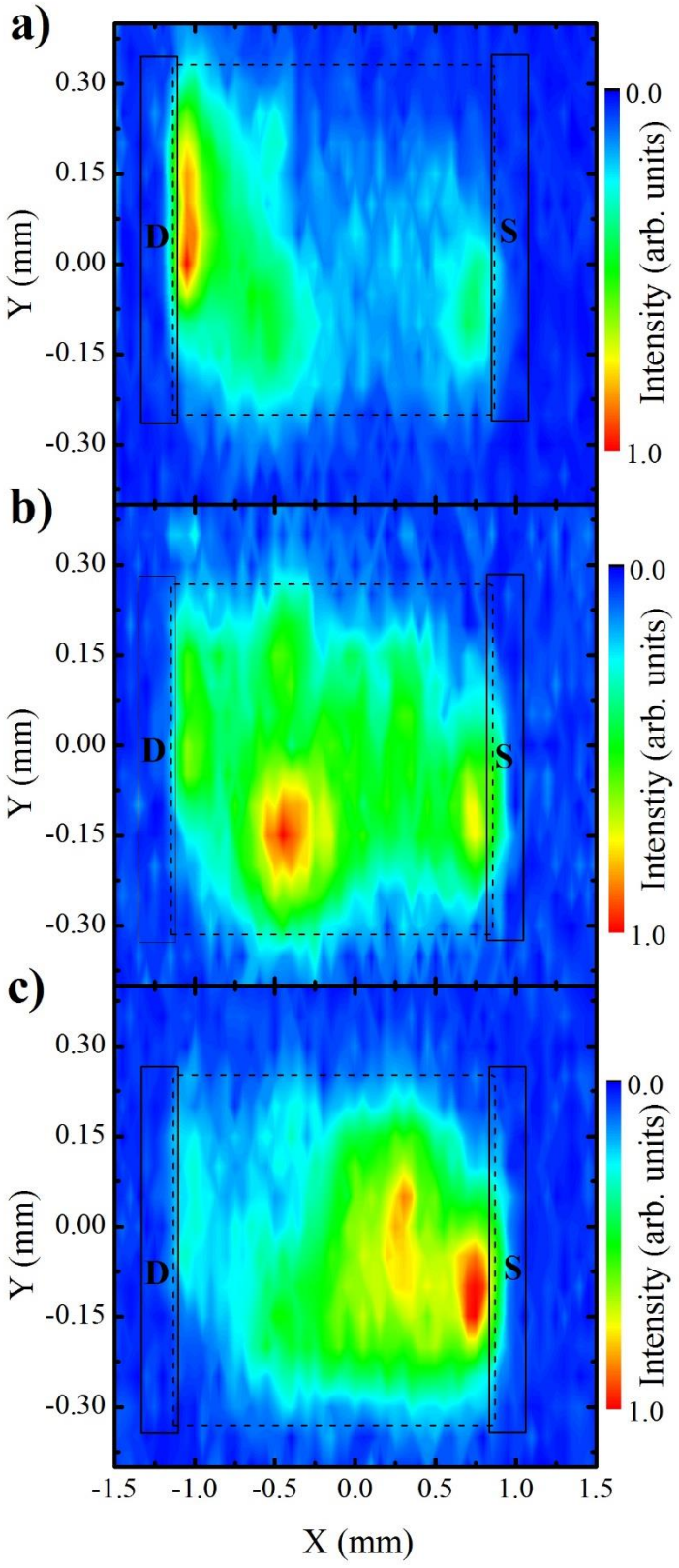

Figure 5.2 a-c) Spatially resolved thermal emission maps of SLG_D_1, the dashed line indicates the position of the single-layer graphene and the solid line the position of the Cr/Au contacts, with peak injection current of 35 mA and applied back gate voltages of a) V_{gd} = 40 V, b) V_{gd} = 60 V and c) V_{gd} = 80 V.

The Dirac voltage (V_0), defined as the backgate voltage at the point of maximum resistance, is measured by gate sweeping measurements, described in section 4.1.2, with V_0 ~35 V for SLG_D_1. For V_{GD} = 40 V the drain will be lightly electron doped ($V_{GD} > V_0$) and the source heavily hole doped as V_{GS} = 5 V ($V_{GS} << V_0$). The CNP is therefore located close to the drain and as can been seen in Figure 5.2(a) so is the maximum in the measured overall emission intensity (hotspot). The hotspot is located at X= -1.0 mm and is approximately 0.3 mm long by 0.2 mm wide. This is caused by a localised increase in Joule heating at the CNP. There is a second smaller “hot spot”, with approximately half the measured intensity compared to main one, located near the source. With the source being heavily hole doped this is not explained by the variation of the electrostatic potential along the channel. Increasing V_{GD} to 60 V the drain becomes more heavily electron doped ($V_{GD} > V_0$) and source becomes less hole doped as V_{GS} = 25 V. The CNP in this case would be expected to be located somewhere between the source and the drain. In Figure 5.2(b) there is a localised hotspot near the centre of the channel at X = 0.5 mm. Again there is a secondary hot spot located at the same location as the one observed in Figure 5.2(a). Finally by further increasing V_{GD} to 80 V and therefore V_{GS} to 45 V the drain becomes heavily electron doped and the source lightly electron doped, in this situation the charge transport is no longer ambipolar and has switched to unipolar. Therefore there is no longer a CNP along the channel but a location of minimum carrier density, which is located at the source. In Figure 5.2(c) it can be observed there is “hot spot” also located near the source, at X ~0.75 mm. It is likely that the secondary “hot spot” observed in the Figure 5.2(a,b) has combined with the primary “hot spot” caused by the variation in the electrostatic potential. A possible explanation for this secondary “hot spot” is it is the result of a localised defect in the graphene, as it does not

move as a function of V_{GD}. This confirms that large area, CVD SLG devices retain the characteristic nature of the much smaller exfoliated graphene devices [16].

The spatially resolved thermal emission of a second single-layer graphene device, SLG_D_2, with a square emitting area of 0.5 mm × 0.5 mm is also measured and is displayed in Figure 5.3. The applied forward bias for this device was 44 mA and the gate voltage was set to V_{gd} = 0 V. The emission from this device is dominated by a single hot spot located at X ~0 mm, the centre of the device. For this device, due to a large amount of gate leakage, the position of the hotspot was not able to be moved as a function of backgate voltage. Additionally, as with the previous device, the thermal emission extends approximately only over the 0.5 mm × 0.5 mm area of graphene.

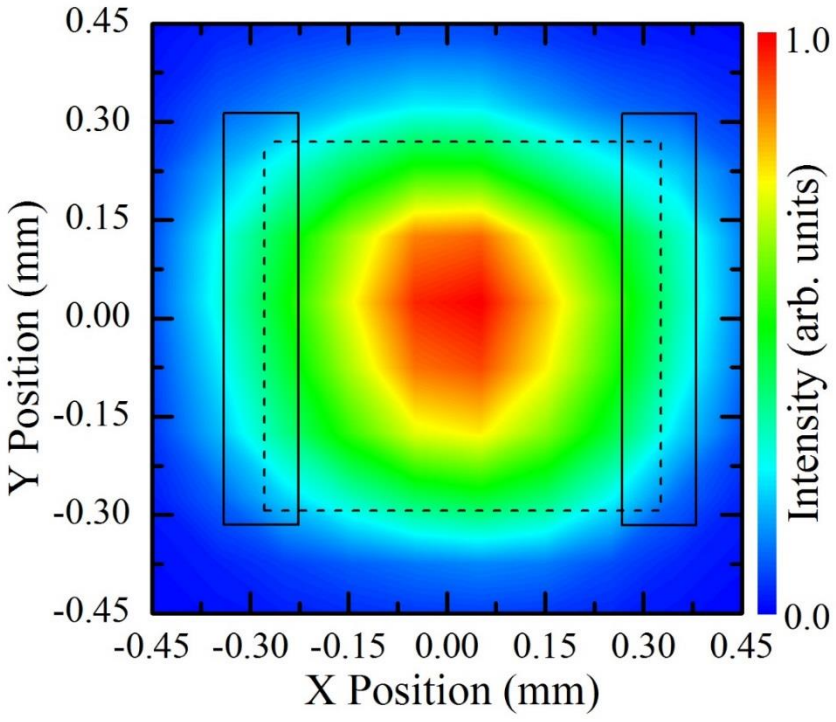

Figure 5.3 Spatially resolved thermal emission map from SLG_D_2 with a peak injection current of 44 mA. The black dashed line indicates the position of the single-layer graphene and the solid black lines indicate the position of the metal contacts.

5.2.2 Few-layer Graphene Devices

Spatially resolved thermal emission measurements are also used to characterise the thermal emission from large few-layer graphene based devices. The results from a typical FLG device, FLG_D_1, are presented in this section. The number of graphene layers were determined by taking multiple Raman spectra from a number of different points, with the average spectra shown in Figure 5.4. The number of layers was estimated as 3 – 6 through close examination of the 2D peak [125].

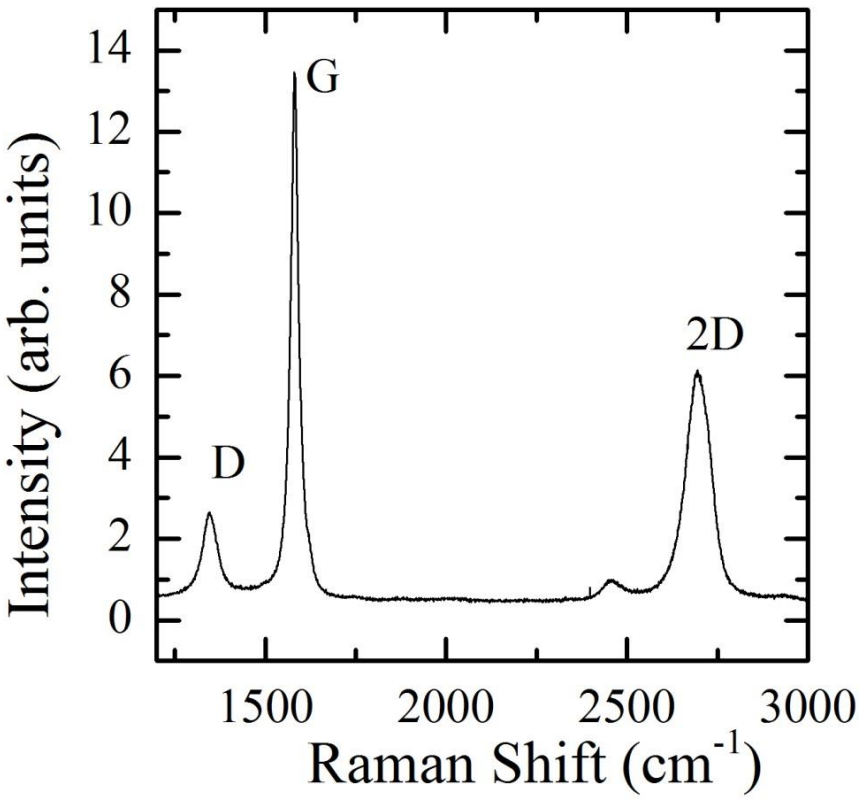

Figure 5.4 Average Raman spectra from FLG_D_1.

In Figure 5.5 the spatial variation of the thermal emission from FLG_D_1 is plotted for a peak injection current of 52 mA and V_{GD} = 0 V. As was seen for the single-layer devices, the emission from FLG_D_1 is primarily limited to the graphene

emitting area. However, in contrast to those devices, the emission from FLG_D_1 is more uniform with a maximum in intensity consistently located in the centre of the emitting area, regardless of the applied gate voltage. This is similar to what might be expected to be observed for a conventional semi-metal filament, with a uniform channel resistance and supported on both sides of the channel by two colder supports acting as heat sinks. This suggests that few-layer devices can be thought of this way.

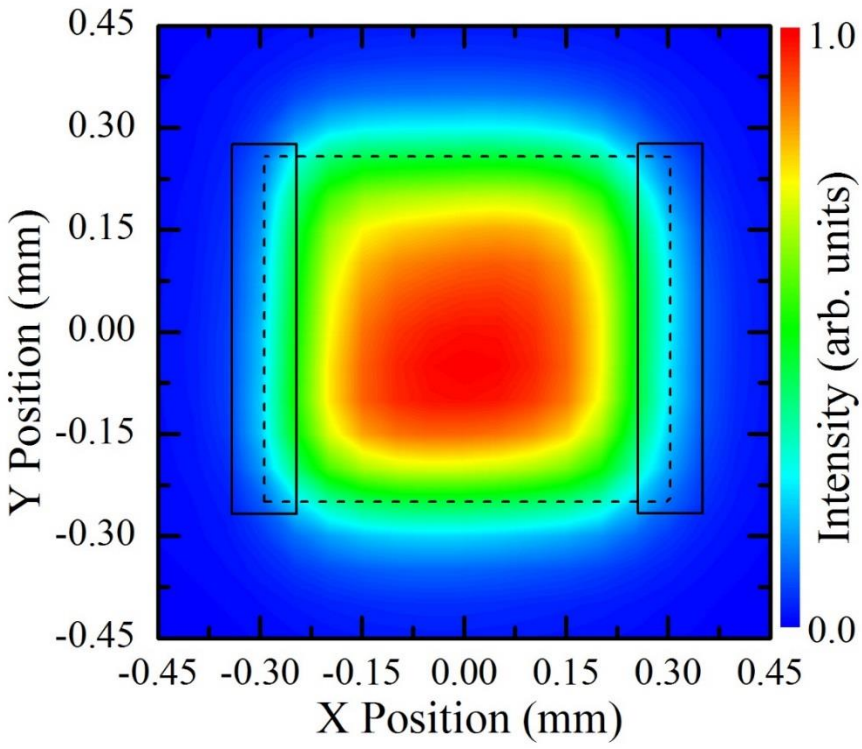

Figure 5.5 FLG_D_1 spatially resolved thermal emission map for peak inject current of 52 mA. The black dashed line indicates the position of the few-layer graphene and the solid black lines indicate the position of the metal contacts.

5.2.3 Verification of COMSOL Model

COMSOL has previously been utilised to simulate the heat transfer in suspended graphene flakes and graphene heat sink structures [144,145]. For this work a two dimensional (2D) time domain model is constructed in COMSOL, as schematically shown in Figure 5.6. A two dimensional model was chosen over a three dimensional model because it is far less computationally expensive and a two dimensional cross-section is sufficient for what is being studied. This model combines both the heat transfer in solids and electric currents modules. This allows for the simulation of Joule heating in different graphene based device architectures. Thin-graphite (approximately five layers) is used to represent that graphene, as the spatially resolved thermal emission measurements indicated FLG semi-metal characteristics. The resistance is set to be 1300 Ω, which equals the measured resistance for FLG_D_1. Additionally, the cross plane thermal conductivity of the FLG is set to the value for bulk graphite, 6 $Wm^{-1}K^{-1}$ [146], and the in plane thermal conductivity is taken to be 600 $W \cdot m^{-1} \cdot K^{-1}$ [147]. The thermal resistance of the graphite SiO_2 boundary, R_b, is set at 2×10^{-8} m^2KW^{-1}, a value that was previously extracted from exfoliated graphene devices [148]. The emissivity, ε, of the few-layer graphene is taken to be 6%, matching the estimated emissivity of FLG_D_1 from previous spectroscopy measurements [109]. All of the parameters are independent of temperature. Temperature dependent parameters were examined but it was determined they had no significant impact on the results. Boundary conditions of the electric currents module include a current source boundary condition for the top boundary of the left Au/Cr contact, a ground boundary condition for the top boundary of the right Au/Cr contact and electrical insulation boundary conditions for the rest of the boundaries. In the

multi-physics module all of the boundaries are defined as electromagnetic heat sources. Finally, the boundary conditions for the heat transfer in solids module include, a room temperature boundary condition for the base of the substrate, as it is assumed that the base of the substrate is kept at room temperature as it is thermally anchored to the sample holder, and the radiation boundary condition for the remaining boundaries.

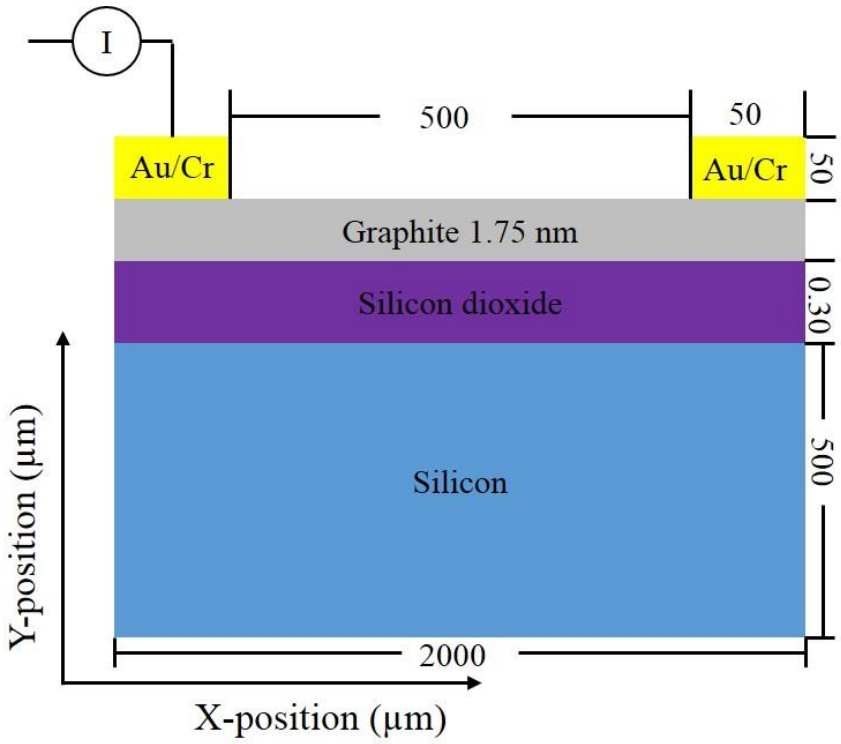

Figure 5.6 Example of geometry simulated using COMSOL.

The drive current of the COMSOL simulations is chosen to give similar on/off temperatures to those estimated for FLG_D_1 for a 1 kHz, 60 mA drive current. To estimate the on/off temperatures of FLG_D_1 the raw emission spectra is measured using a grating spectrometer, with the set-up for these measurements discussed in section 4.4.1. The measured raw emission spectra is then corrected using a 673 K blackbody source, described in more detail in section 4.4.2. The corrected spectrum from FLG_D_1, along with the calculated spectrum, is plotted in Figure 5.7. To estimate the temperature of the surface graphene the measured

spectra is assumed to correspond to the difference between two grey-body curves. A higher temperature grey-body, corresponding to the emission when the current is on, and a lower temperature grey-body, corresponding to the emission when the current is off (due to the signal measured on the lock-in amplifier being determined by the difference between the thermal emission when the current is on and the thermal emission when the current is off), as discussed in more detail in section 4.3. The calculated spectrum in Figure 5.7 is obtained by calculating the difference between these two grey-body curves, with the emissivity assumed to be 6%. The temperatures of the two grey-bodies (The on/off temperatures) are chosen to give the best qualitative fit to the corrected spectrum. The on/off temperatures of the calculated spectrum presented in Figure 5.7 are 620 K and 480 K respectively. COMSOL simulations are then run at various drive currents until similar on/off temperatures of the thin graphite surface are obtained.

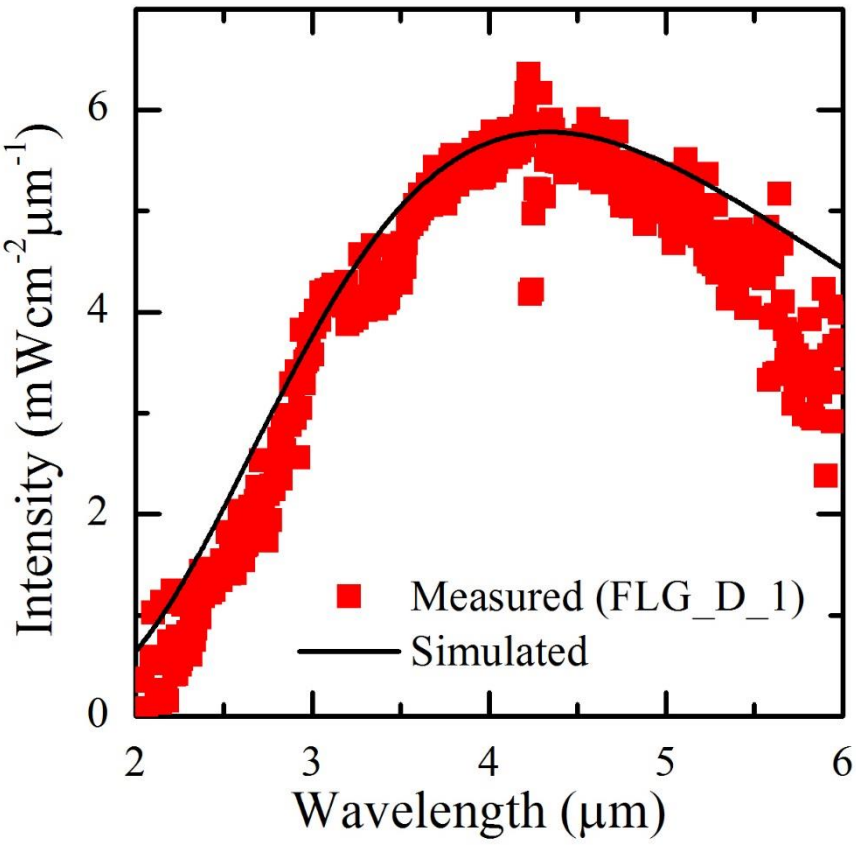

Figure 5.7 Corrected emission spectra FLG_D_1 and calculated spectra.

In order to test the validity of the model the measured emission intensities along the X-direction at Y = 0 mm from FLG_D_1 are compared to calculated emission intensities obtained from the COMSOL simulated temperature profile. The measured emission intensity as a function of position through the centre of the device, taken from the black line in Figure 5.8(a), is shown in Figure 5.8(b) along with the calculated normalised intensities. The simulated intensities are acquired by first extracting the temperature as a function of position across the thin graphite surface for when the current is on and when the current is off. The extracted temperature profile, along with the known spectral response of the CMT detector (see section 4.3), are used to calculate the emission intensity by assuming the emission is from a grey-body emitter with an emissivity of 6%. Both the calculated and measured intensities are normalised to the peak intensities. Overall there is good agreement between the calculated and measured intensity profiles, demonstrating the validity of the COMSOL model.

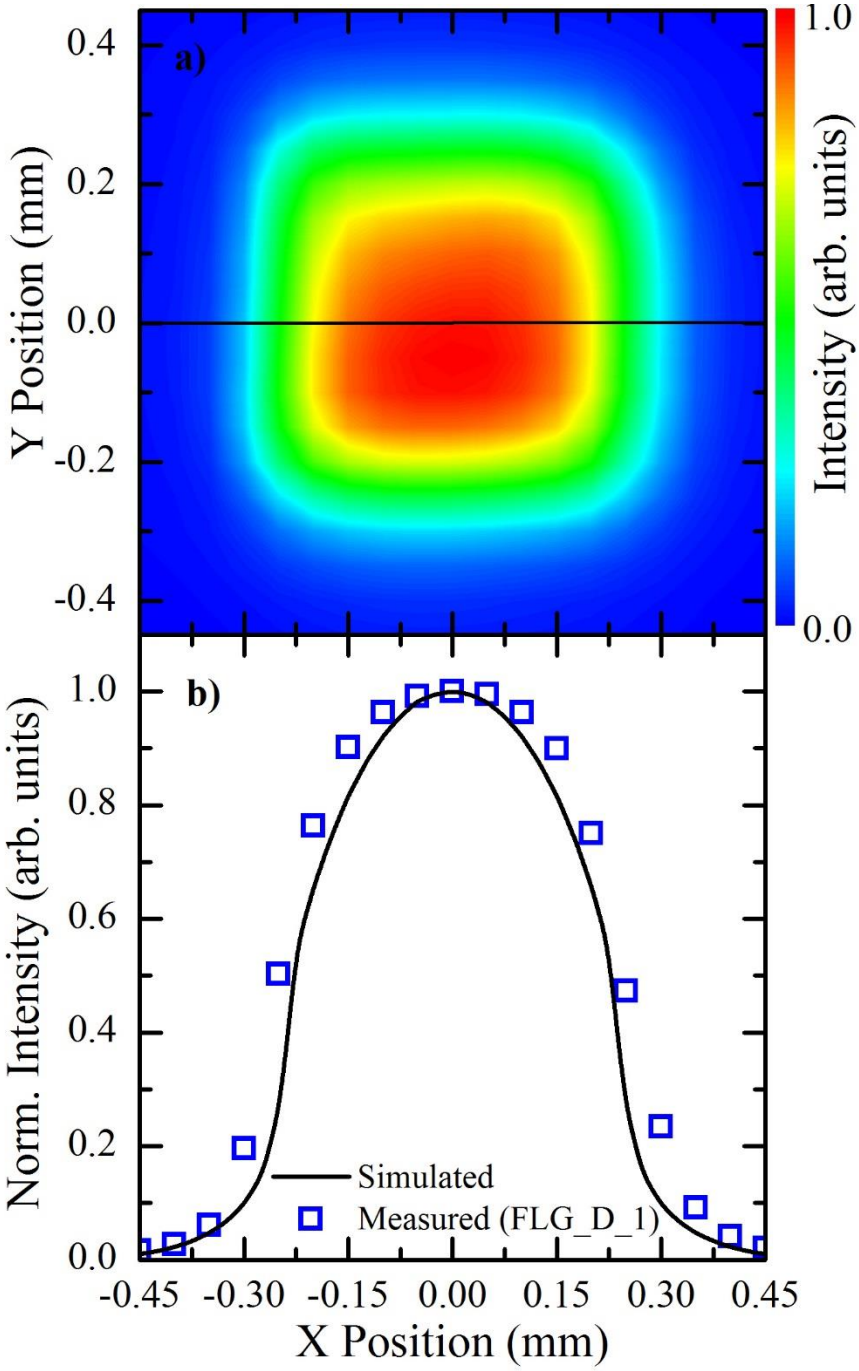

Figure 5.8 a) FLG_D_1 spatially resolved thermal emission map with the black line indicating the data taken for the 1D plot. b) Simulated normalised temperature profile along the surface of COMSOL model at 1 kHz compared with the normalised measured intensity across the centre of the few-layer device.

5.3 Modulation Characteristics

The modulation characteristics of an IR emitter are important for gas detection because higher modulation speeds allow for advanced signal processing techniques and improved sensor response. To investigate the modulation characteristics of graphene based emitters, the emission from three different devices is measured and simulated over a range of drive frequencies. The first two devices, SLG_D_2 and FLG_D_1, are the same square SLG and FLG devices discussed previously in this chapter. The third device, BN_D_1, is a device containing a large area few-layer graphene layer, encapsulated in few-layer hexagonal boron nitride (h-BN) on a SiO_2/Si substrate with an emitting area of 0.5 mm × 0.5 mm.

5.3.1 Single and Few-layer Graphene Devices

To gain insight into modulation frequencies at which the graphene emitters can be driven and how single-layer compared to few-layer, the emission intensities from SLG_D_2 and FLG_D_1 are measured and simulated as a function of drive frequency [17], from 1-100 kHz (the limit of the current source) at a consistent current density of 2.0×10^7 $A \cdot cm^{-2}$ and duty cycle (50%). For both the measurements and the simulations the emission intensity at each frequency is normalised to the measured/calculated intensity at 1 kHz and corrected for the frequency response of the measurement system. Figure 5.9 plots the normalised intensities of SLG_D_2 and FLG_D_1 as a function of drive frequency. The measured emission intensity drops of rapidly for both devices, with the emission

from SLG_D2 decreasing at a slower rate than the emission from FLG_D_1 above 20 kHz. Emission intensities were also calculated at various drive frequencies from COMSOL simulations of two different thin graphite thicknesses and are also plotted as a function of drive frequency in Figure 5.9. To calculate the emission intensities, the simulated temperatures of the thin graphite layer are extracted and assuming grey-body emission the intensities are calculated at each frequency by using the spectral response of the CMT detector. It is notable that the simulated emission intensities are 4-5 times greater than the measured emission values, however, it is more useful to look at the consequence of increasing the thermal mass of the thin graphite, opposed to comparing quantitative values. The calculated emission intensities are lower across the frequency range for the simulations with a thinner thickness of thin graphite layer, mirroring what was observed in the measurements. The qualitative agreement between the simulations and the measurements suggest that the larger emission intensities at higher frequencies for SLG_D_2 is due to the lower thermal mass of the single layer graphene compared to the few-layer graphene of FLG_D_1.

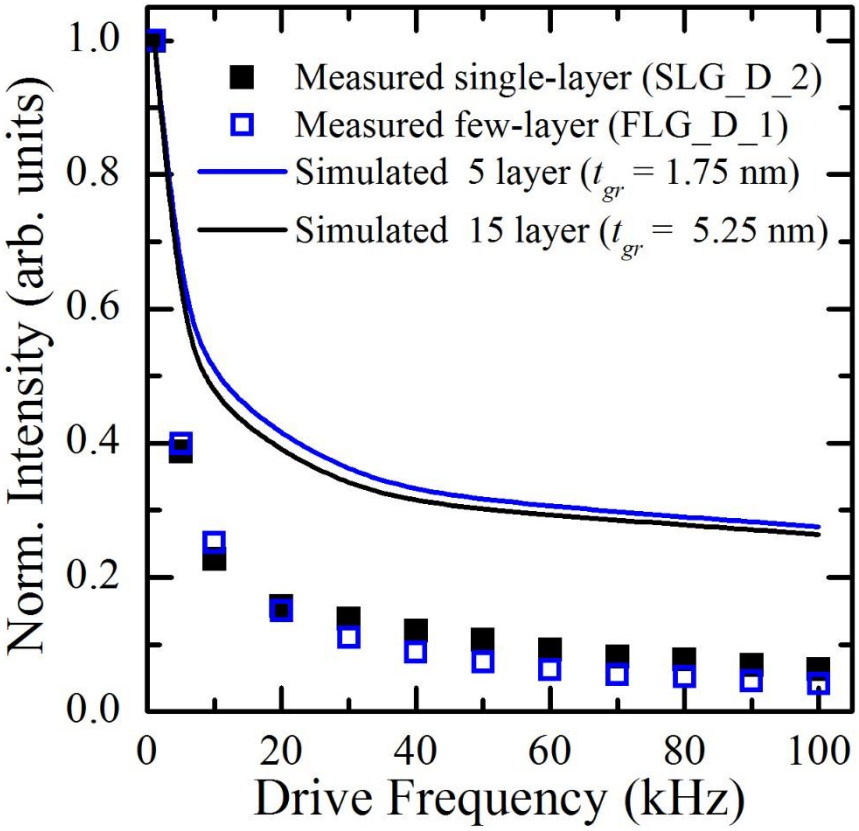

Figure 5.9 Simulated (lines) and measured (symbols) emission intensity as a function of drive frequency. Measurements are from a single-layer graphene device and a few-layer graphene device, while the simulations include two different thicknesses of thin graphite, t_{gr}.

5.3.2 Encapsulated Graphene Devices

Due to graphene's excellent intrinsic thermal properties the heat dissipation from graphene based devices is limited by the interface between graphene and the underlying substrate, contacts and surrounding materials [9]. For large devices, L and $W >> L_H$ and t_{ox} the heat dissipation is dominated by the graphene substrate interface and the underlying substrate [9], where L is the device length, W is the device width, L_H is the characteristic length and t_{ox} is the thickness of the underlying oxide layer. The characteristic length defines the exponential rise and

fall of the temperature profile across the device. Previously L_H has been shown to range from ~0.1–0.2 μm for exfoliated devices [139,149]. This suggests that for the large area devices studied here the dominant thermal path is down into the substrate. COMSOL simulations are performed for two different values of the interface thermal resistance, R_b, and drive frequencies ranging from 1-100 kHz. The temperatures in the centre of the thin graphite layer area are extracted from the COMSOL models at each drive frequency and plotted in Figure 5.10. For both thermal resistances, the highest on-temperature and the lowest off-temperature occurs for a 1 kHz drive frequency (pulse width = 0.5 ms). The on-temperatures decrease, and the off-temperatures increase, with increasing drive frequency. This suggests the time during one pulse becomes insufficient to both fully heat the graphene, when the current is on, and allow for the heat to fully dissipate, when the current is off, as the pulse width is reduced. The on-temperature is higher for the case of higher thermal resistance across the entire frequency range, as might be expected with the heat dissipation being made worse by the increase in the interface thermal resistance. In contrast the off-temperatures are higher across the frequency range for the case of lower thermal resistance. This may seem counter intuitive, however, this can be explained by the fact that the lower thermal resistance between graphene and SiO_2 leads to an overall increase in the background temperature of the substrate.

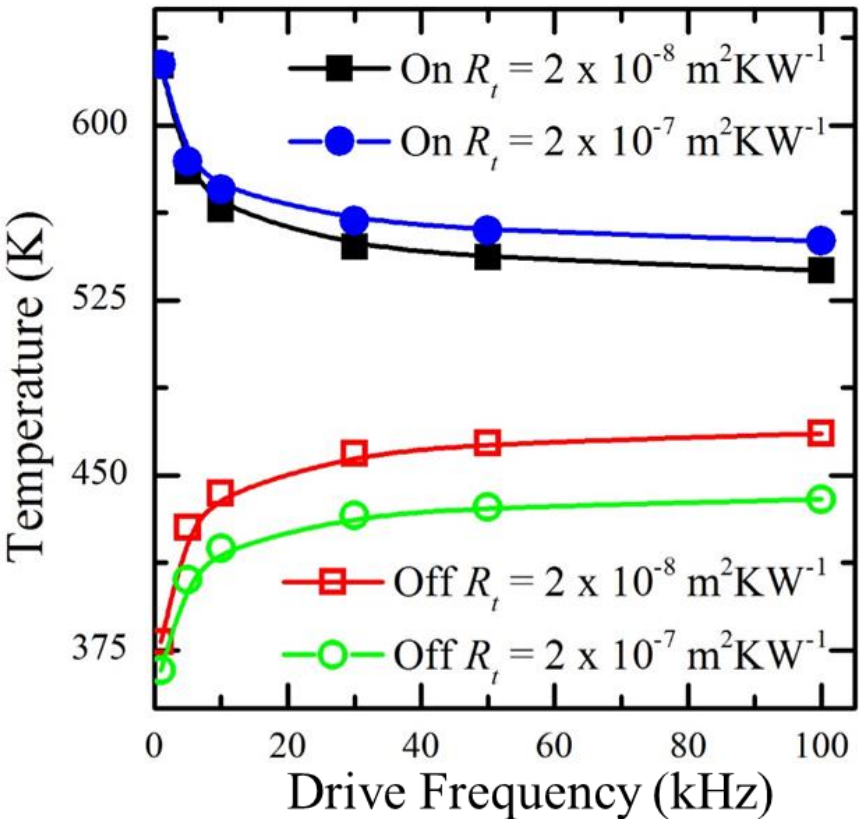

Figure 5.10 Simulated “on” and “off” temperatures at equilibrium for two different thermal resistances between the thin graphite layer and SiO_2 (lines are guides for the eye and not fitted curves).

Normalised emission intensities are calculated from the simulated temperatures, as discussed in the previous section 5.3.2, and plotted as a function of frequency in Figure 5.11. From the simulated intensities, it is clear that increasing the thermal resistance between the graphene and the underlying SiO_2 results in an increase in the calculated intensity, with an approximate increase of 1.5 above the frequency of 30 kHz for a theoretical thermal resistance increase $\Delta R_t = 1.8 \times 10^{-7}$ m^2KW^{-1} [17]. To investigate whether increasing the thermal resistance would have an impact on the modulation characteristics of the graphene devices, as suggested by the simulations, the emission intensities from FLG_D_1 and BN_D_1 were measured as a function of drive frequency, normalised to the 1 kHz measurements, and also plotted in Figure 5.11. From this plot it is clear that

the measured intensity drops rapidly as a function of frequency for both devices and is approximately 5-fold smaller than the calculated emission intensities across the frequency range. However, it is more informative not to compare the exact calculated and measured values but the difference between measured intensities obtained from the two different devices. A two fold increase can be observed in the normalised emission intensity above 30 kHz from the encapsulated device, BN_D_1 compared to the FLG_D_1. This can be explained by comparing the difference in the vertical thermal resistance, $\Delta R_{t,}$ of FLG_D_1 and BN_D_1 respectively, with ΔR_t being given by

$$\Delta R_t = R_{T(MLG)} - R_{t(BN)} \tag{5.2}$$

where $R_{T(FLG)}$ is the vertical thermal resistance of FLG_D_1 and $R_{T(BN)}$ is the vertical thermal resistance of BN_D_1. Assuming the thermal resistance of the underlying substrates (SiO_2 and Si for both) are the same in each case, these can be ignored and $\Delta R_t = (R_{BN}+R_{I1}+R_{I2}) – R_{I3}$. Taking the thickness of the bottom h-BN layer to be ~13 nm, $R_{BN} = 6.5 \times 10^{-9}$ m^2KW^{-1}, the c-axis thermal resistance per unit area of h-BN [150], $R_{I1} = 1.35 \times 10^{-7}$ m^2KW^{-1}, the interface thermal resistance of graphene and h-BN [149], $R_{I2} = 2.2 \times 10^{-8}$ m^2KW^{-1} , the interface thermal resistance of h-BN and SiO_2 [151], $R_{I3} = 2.0 \times 10^{-8}$ m^2KW^{-1}, the interface thermal resistance of graphene and SiO_2 [152] and $\Delta R_t = 1.4 \times 10^{-7}$ m^2KW^{-1}. By encapsulating the graphene in h-BN, the vertical thermal resistance is increased, and an increase in the measured intensity at high frequencies is observed. This is in good agreement, qualitatively, with the results of FEM simulations, where the value of the interface thermal resistance was increased by a similar amount, 1.8×10^{-7} m^2KW^{-1}.

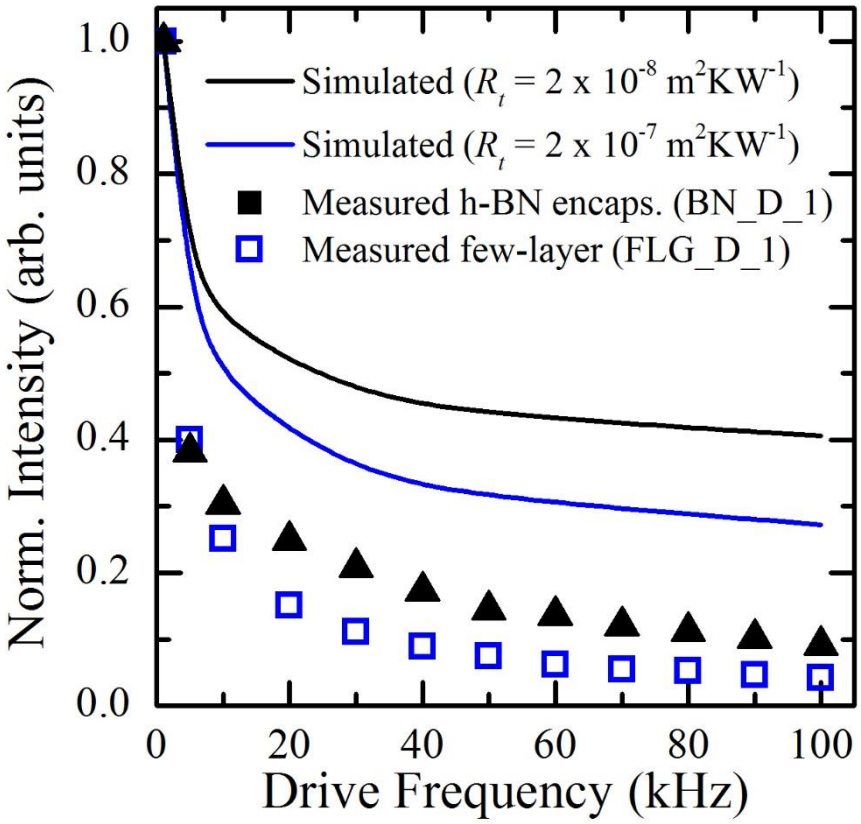

Figure 5.11 Simulated (lines) and measured (symbols) emission intensity as a function of drive frequency. Measurements are from a few-layer graphene device and a h-BN encapsulated few-layer graphene device, while the simulations include two different thermal resistances between thin graphite and SiO_2, R_t.

5.4 Summary

In summary, the thermal emission from devices comprised of single-layer and few-layer graphene was characterised spatially, using both measurements and simulations of the emission intensity as a function of position. It was demonstrated that in single-layer devices that the location of this hotspot can be moved along the graphene channel by applying various back gate voltages, resulting in the location of the CNP moving. This was previously seen for only small area, exfoliated graphene devices. Therefore, it can be concluded that the

observed thermal emission from these large area single-layer devices is qualitatively the same as the much smaller exfoliated ones. In contrast, the emission from the few-layer device was shown to be much more uniform along the channel, consistent with a uniform channel resistance and typical of a semi-metal filament supported by two thermal anchors. This was verified by the 2D COMSOL model of a five layer graphite device which both gave validity to the model and the assumption that few-layer devices can be thought of this way. Additionally, the modulation characteristics of these devices, as well as an h-BN encapsulated device, were also studied with measurements, and simulations, of the emission intensity over a range of drive frequencies (1-100 kHz). A measureable emission was achieved over the entire drive frequencies range, for all devices, with a large drop up off in emission intensity at higher frequencies. The emission intensity was larger at frequencies above 20 kHz for the single-layer device in comparison to the few-layer device. This is in qualitative agreement with the results of COMSOL simulations for two different thin graphite thicknesses, and is most likely due to the lower thermal mass of the single-layer device. Finally, an increase in emission intensities at high frequencies was observed in simulations with a greater thermal resistance between the graphene layer and the underlying substrate. An increase in the measured thermal emission as a function of drive frequency was also observed for a device with greater vertical thermal resistance (h-BN encapsulated few-layer graphene), compared to the few-layer device, confirming that the modulation speed of the graphene emitters can be improved by increasing the thermal resistance between the graphene layer and the substrate.

6. Spectral Control

6.1 Introduction

Generally, thermal emitters exhibit a broad emission spectrum defined by Planck's law. As many applications only utilise a narrow region of this spectrum, the ability to narrow the broad emission spectrum has recently attracted increasing attention due to its potential applications in areas such as gas sensing, thermophotovoltaics and thermal imaging [153–157]. In non-dispersive infrared sensing, for example, the absorption line width defines the spectral range required, often equivalent to a Q-factor greater than 50 [158]. Additionally, the power conversion efficiency of thermophotovoltaics could be improved by removing any part of the emitted spectra that has a lower energy than the band gap of the photovoltaic cell. There are multiple approaches to achieving the narrowing of the emission spectrum which include: utilising high absorptivity materials, such as rare earth oxides [159], metallic nanostructures based thermal emitters [160,161], and in more recent years, metamaterials in combination with a thin dielectric layer [162,163]. There are drawbacks to each approach with high absorptivity materials having no control over emission wavelength or band width, while thermal emitters based on metallic nano-structures are generally limited to near infrared applications with the Q factor of the emission peak limited to < 10 for both the metallic nanostructures as well as the metamaterials/dielectric approaches, due to the metals involved in both [164]. To narrow the spectra from the graphene based emitters a metamaterials/dielectric approach was utilised. For the metamaterial pairs of different sized gold (Au) rings are examined while hexagonal Boron Nitride is used as the dielectric. Finite Element Method (FEM) simulations performed by a colleague,

Mr. Cheng Shi, predict an electromagnetically induced transparency (EIT) analogous Fano resonance at certain frequencies, depending on the design of the ring resonators (RR) unit cell. Integrating this metamaterial/dielectric structure with few-layer graphene achieves an EIT-like Fano resonance at various frequencies of both the measured reflectance and emittance.

In this chapter the measured raw emission spectrum from both a single and few-layer graphene based emitter are presented in section 6.2.1, along with the corrected emission spectra from a blackbody calibration source. From these results values of the emissivity of the single-layer and few-layer graphene devices can be estimated along with the surface temperature of each device. In addition, these measurements clearly demonstrate that the emission spectra from graphene based devices is broadly grey-body in nature. The results from this section were adapted for publication in Prospective for graphene based thermal mid-infrared light emitting devices, AIP Advances 4, 087139 (2014). Section 6.3 goes on to further discuss the details of RR metamaterials with EIT-like Fano resonance. The following section, section 6.3.1 presents FEM simulations of the six RR unit cells on a 13 thick layer of h-BN, with each unit cell having different values for the pitch and radius of the rings. Continuing on from the simulation results in section 6.3.2 the measured results for the RR/h-BN structure implemented on top of few-layer graphene devices are shown. For these RR devices, the RR's were deposited on top of few-layer graphene encapsulated between two layers of 13 nm thick h-BN all on top of a SiO_2/Si substrate. The results of reflectance Fourier transform infrared (FTIR) spectroscopy measurements are presented from six different RR devices, with the same parameters for the RR's as was used in the FEM simulations, in section 6.4. This is followed by section 6.5, where both the measured raw emission and normalised

emission results, from four of the six RR devices, are presented and discussed. Initial results from split ring resonator devices designed to improve the peak transmittance percentage as well as the Q-factor are presented in section 6.6. Finally the chapter is concluded with a brief summary in section 6.7.

6.2 Spectroscopy

6.2.1 Single and Few-layer Graphene

The spectroscopy results of two single and few-layer graphene based devices are presented in the follow section. SLG_D_2 and FLG_D_1 are the same 0.5 mm × 0.5 mm graphene, single-layer graphene and few-layer graphene respectively, on SiO_2/Si devices first discussed in Chapter 5. A schematic diagram showing a typical single or few-layer graphene device is shown in Figure 6.1. For the spectroscopy measurements presented in section 6.2.2 a grating spectrometer was used along with a CMT detector connected to a lock-in amplifier for phase sensitive measurements. The experimental set-up is discussed in more details in section 4.3.1, while details on device fabrication are provided in Chapter 3.

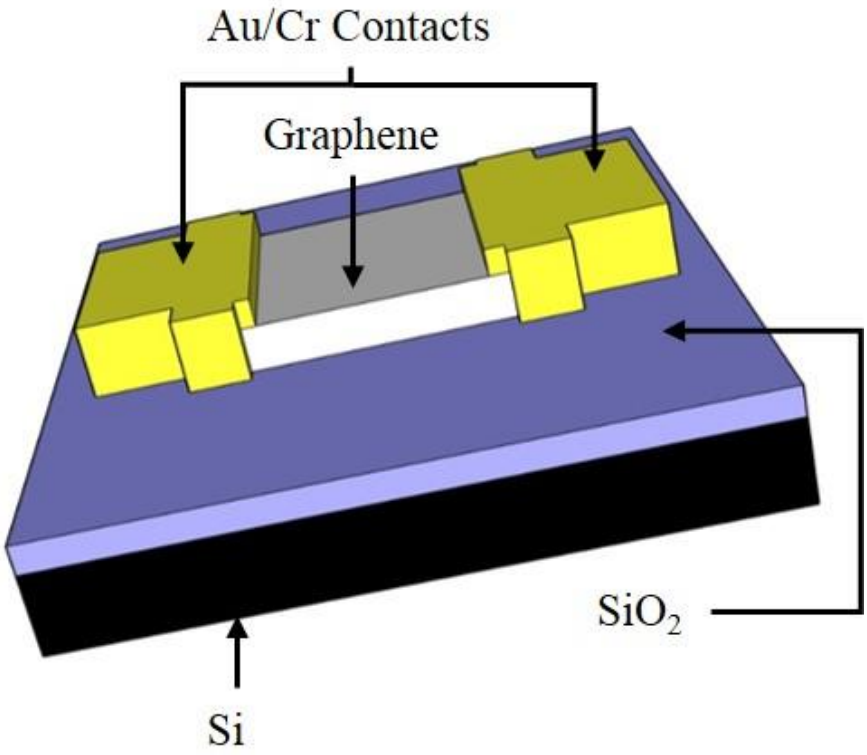

Figure 6.1 Schematic illustration of a typical graphene (either single or few-layer) device on a SiO_2/Si substrate.

6.2.2 Single and Few-layer Graphene Spectra

In Figure 6.2(a,b) the raw emission spectra is shown over the 50-150 THz region for the three devices. Each measured device spectra is plotted along with the measured spectra from a 673 K blackbody source, with the emission modulated at the same drive frequency as the devices by using a chopper. Savitzky-Golay smoothing is applied to the measured data. In all three cases the overall shape of the blackbody emission spectra is similar to the shape of the emission spectra from the devices, with FLG_D_1 showing the best fit, suggesting it is closest in temperature to the blackbody source. A maximum in the measured intensity of both the FLG_D_1 and the blackbody source is located at ~74 THz, while the

frequency corresponding to the maximum measured intensity of SLG_D_2 is ~71 THz. This similarity between the measured blackbody spectra and the spectra measured from the graphene devices suggests that the emission from graphene devices equates largely to grey-body emission and allows for an estimation of the emissivity of the devices [109]. Emissivity of single-layer graphene has previously been measured as 1.6 ± 0.8% [15], in good agreement with the measured absorbance of $\alpha = 2.3\%$ [44,45]. For few-layer graphene, as is seen with absorbance [165], the emissivity is predicted to increase linearly with the number of layers [44]. As the maximum intensity of the blackbody source emission being 32 times greater than the maximum intensity from FLG_D_1, the emissivity of FLG_D_1 can be estimated as 6%, assuming an emissivity of 95% for the blackbody source. The emissivity of SLG_D_2 can then be estimates as 2%, as the maximum intensity of emission from SLG_D_2 is 3 times smaller than FLG_D_1, consistent with the value obtained by Freitag *et al* [15]. Assuming a linear increase in the emissivity with the number of layers, it is estimated that FLG_D_1 consists of approximately three layers, which is consistent with the number of layers specified by the manufacturer (1-7 layers with an average of 4 layers).

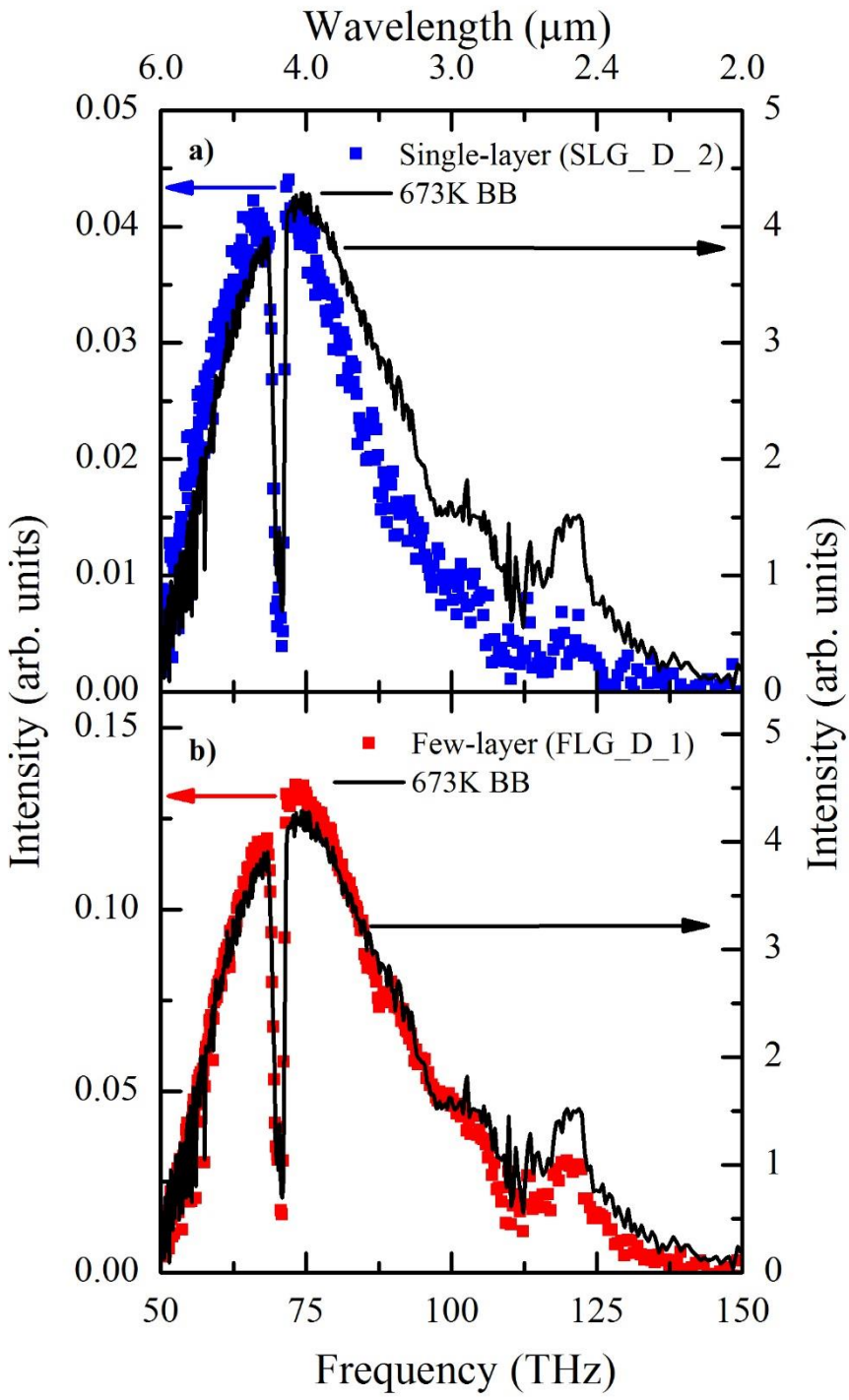

Figure 6.2 Measured raw emission spectrum from a 673 K blackbody source (black line) together with the emission spectra from a) SLG_D_2 and b) FLG_D_1.

As the measurements were performed in atmosphere the large intensity minimum seen across all of the emission spectra, at approximately 70 THz (4.3 μm), is

attributed to CO_2 absorption, as this corresponds to the frequency of a CO_2 absorption band. Additionally, water absorption is responsible for the broad dips in intensity above 100 THz (3.0 µm) and below 60 THz (3.0 µm). It is possible to correct for this as well as for the efficiency of the grating and the CMT detector response by using the blackbody source to calibrate the emission spectra. A calibration spectrum is generated by simulating a blackbody spectrum at 673 K and normalising it with the measured blackbody emission spectra. The raw spectra is then multiplied by the calibration spectra to generate the calibrated emission spectra plotted in Figure 6.3 (a,b), in conjunction with calculated spectra that gives the best qualitative fit to the calibrated emission spectra. The calculated spectra are generated by assuming the measured signal is the difference between two grey-bodies, discussed in more detail in section 4.3, the first being a grey-body at a higher temperature, corresponding to when the current is on, and the second, a grey-body at a lower temperature, corresponding to when the current is off. The emissivity of the grey-bodies are assumed to be 2% for the single-layer graphene case and 6% for the few-layer graphene case. This allows for an indication of the surface temperature of the devices to be made, yielding an estimated “on” and “off” temperature of 600 K and 350 K for SLG_D_2 and 620 K and 480 K for FLG_D_1

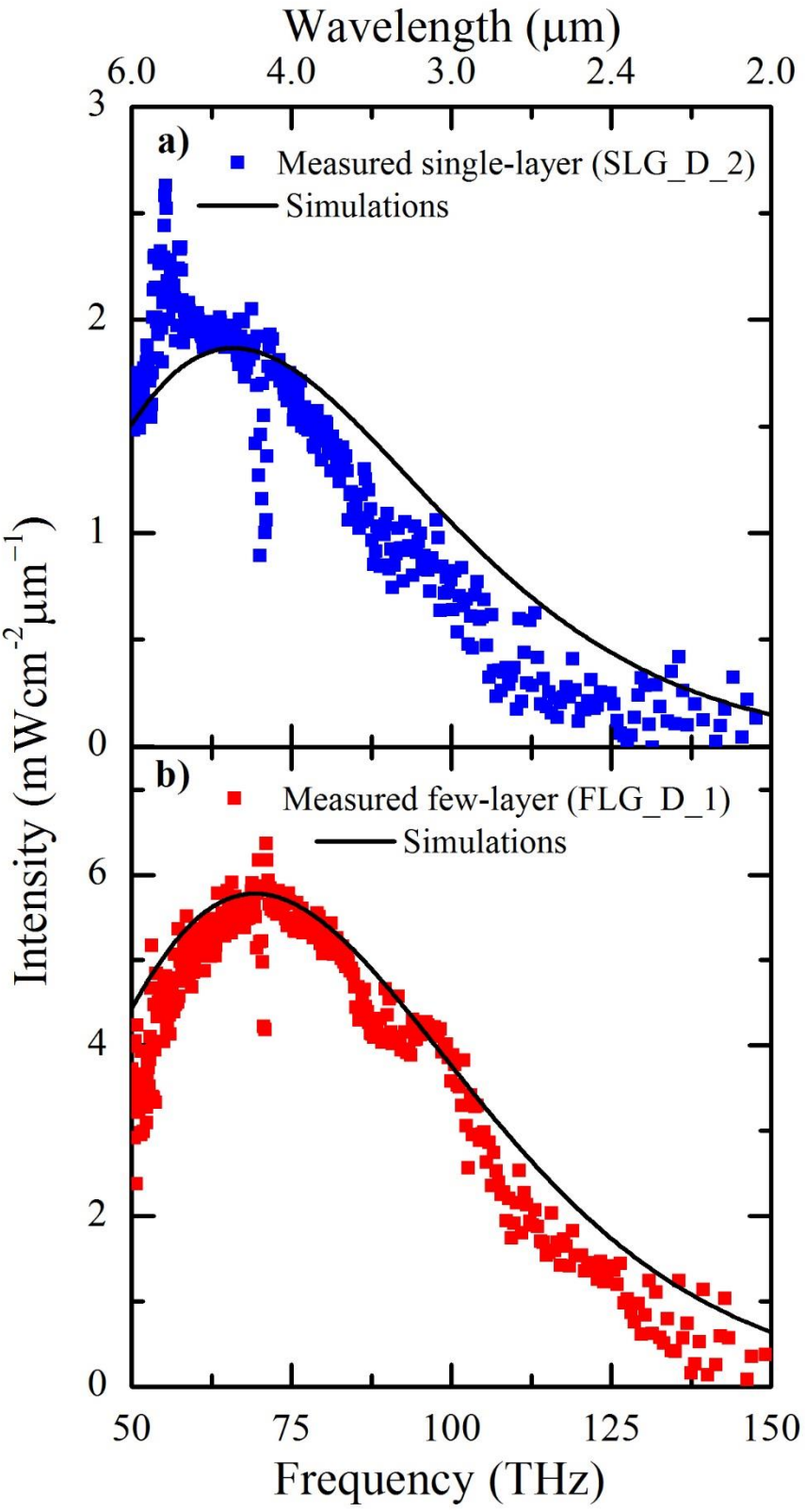

Figure 6.3 Calculated emission spectra (black lines) together calibrated emission spectra (symbols) from (a) SLG_D_2 (b) FLG_D_1.

6.3 Metamaterial Analog of Electromagnetically Induced Transparency

Electromagnetically induced transparency enhances transmittance over a narrow spectral region by reducing the absorption of coherent light through the quantum interference effect [166]. It was originally observed in atomic physics but has since been expanded to optical systems through metallic metamaterials [167–169] and other structures, such as photonic crystals [170] allowing for room temperature operation with incoherent light. Narrowing of a broadband spectrum has previously been achieved through various different ways [171–174]. The following sections focus on using RRs to narrow the emission spectra through the realisation of an EIT-like Fano resonance [175].

6.3.1 Initial Ring Resonator Designs

The first structures implemented to narrow the emission spectra from the graphene devices were Au RRs. The EIT-like Fano resonance is achieved through the strong coupling of a broadband (‘bright mode’) resonator with an incident excitation field interfering with a narrow band (‘dark mode’) resonator that is weakly coupled to that same excitation field. As a result of interference, a transmittance peak or reflectance dip is observed when both the resonance frequencies of the ‘dark mode’ and ‘bright mode’ are similar and their physical locations are close together [169]. For a RR the resonance frequency, $f_{r,}$ is given as [176]

$$f_r = \frac{cn}{2\pi r_{eff}\sqrt{\varepsilon_{eff}}} \quad (6.1)$$

where n is the mode number, 1 in this case, $r_{eff} = (r_{1,2}+0.5w)$ is the effective radius of the ring, c is the speed of light in a vacuum and ε_{eff} is effective permittivity of the metamaterial [177]. Drawbacks of narrowing the spectra in this way include the limitation of the Q-factor to typically less than 10 for metal based Fano resonance systems due to Ohmic damping resulting in non-radiative losses [178] and polarization sensitivity of the Fano resonance due to breaking of the symmetric metamaterial structure to achieve the Fano resonance [179]. To overcome the polarization dependence, the unit cells of the RRs are designed symmetrically, while the possibility to increase the Q-factor through implementation of a split ring resonator design is discussed in more detail in section 6.6.

To achieve transmittance peaks at various frequencies between 60 and 120 THz, where most gases have their specific absorption bands due to molecular vibrations, multiple RR designs were adapted using the finite element method software package COMSOL (by Mr. Cheng Shi) in order to determine the appropriate parameters of the RRs to achieve the peak in transmittance at each specified frequency. The unit cell of the RRs is shown in Figure 6.4(a) and is made of two pairs of rings with different radii, arranged periodically with the pair of rings with a smaller radius arranged in the diagonal direction and the pair of rings with the large radius arranged in the anti-diagonal direction.

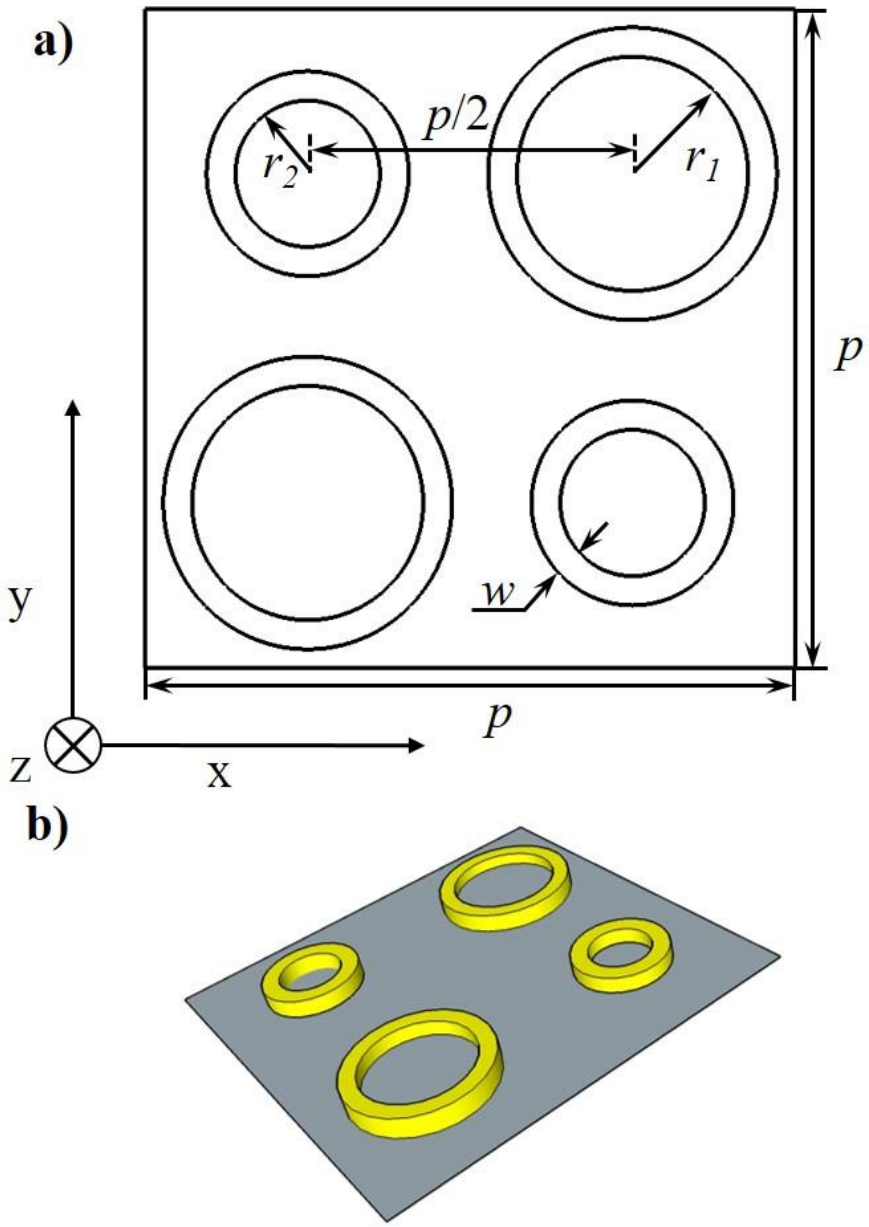

Figure 6.4 a) A 2D sketch of the unit cell of the RRs and b) a 3D schematic of RR unit cell.

For the simulations hexagon boron nitride is used as the substrate and is described as a 13 nm thick atomic layer with a permittivity of 4.1 [180]. The thickness and conductivity of the Au rings is set to 100 nm and 4.561×10^7 S/m respectively. Boundary conditions include a perfectly matched layer applied parallel to the RR plane both above the ring resonators and to the port which adheres to the bottom layer of h-BN substrate, while periodic boundary conditions

are applied to side boundaries perpendicular to the RR plane. The incident infrared wave is linearly polarised, with the field polarised either along the y-axis or x-axis, as defined in Figure 6.4(a). The simulated transmittance spectra, for six different designs of the RR unit cell, are shown below in Figure 6.5(a-f) with sharp transmittance peaks between 0.5 and 0.75 and an average Q-Factor of approximately 10. In these series of spectra, the dimensions of the unit cell including pitch, p, radius of the large ring, r_1, and small ring, r_2, increase from Figure 6.5(a) to Figure 6.5(f). The shape of the transmittance curves are all “W” shaped or dip, peak, dip, and by increasing the radii of the rings and pitch the transmittance dips and peak shift towards lower frequencies. The transmittance peaks are located at frequencies of 118 THz, 99.9 THz, 85 THz, 81.8 THz, 75 THz and 67.1 THz for the six different designs respectively. It is important to note that the underlying graphene/h-BN/SiO_2/Si that composes the rest of the fabricated RR devices was not included in the simulations. This could account for some of the differences that are observed between the simulations and the measurements.

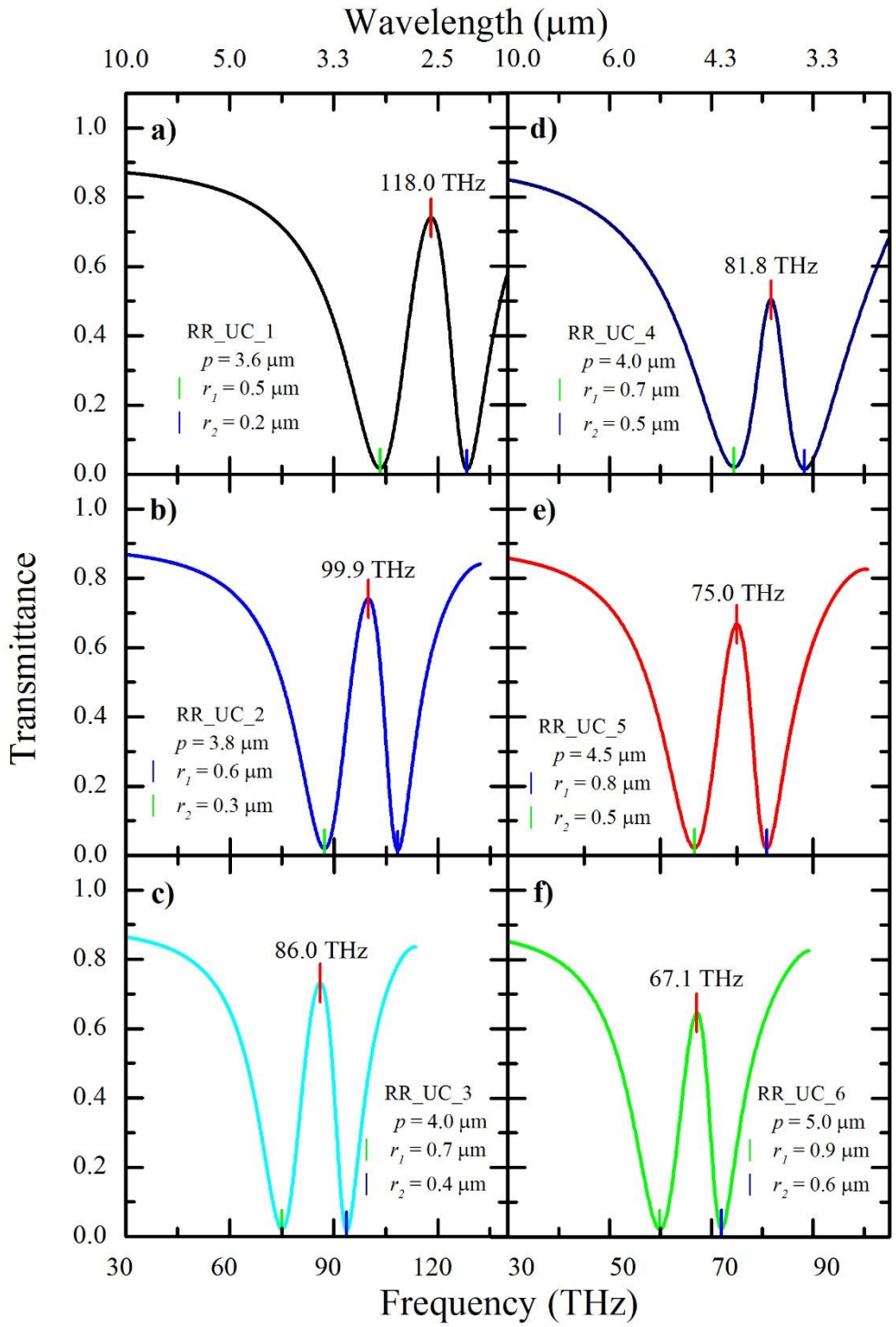

Figure 6.5 a-f) Simulated transmittance spectra for six different RR unit cell designs.

Figure 6.6(a) depicts the insensitivity of the RR_UC_5 design to the axis of polarisation, which was equally observed for the five other RR unit cell designs. The difference between the simulated transmittance spectra and the simulated

reflectance spectra can be observed in Figure 6.6(b), where the reflectance spectra is “M” shaped, or peak, dip, peak, the opposite of the W shaped transmittance spectra. This also holds true for reflectance simulations of the other five RR designs. Table 6.1 summarises the parameters of the six RR unit cells determined from the COMSOL. The RRs were investigated further using numerical simulations and the electric field and surface current distributions of RR_UC_5 are plotted in Figure 6.6(c-e) and Figure 6.6(f-h) respectively. From the electric field distribution it is clear that the broader dip at the lower frequency (f_1) is the result of the excitation of just the larger rings, while the smaller dip at higher frequency (f_3) is the result of excitation of just the smaller rings. At the frequency of the transmittance peak (f_2), the key feature, it can be observed from the electric field and surface current distributions that both the larger and smaller rings are equally excited, inducing out-of-phase surface currents on different groups of rings. This results in destructive interference of the transmittance modes, leading to the Fano resonance peak observed in the transmittance spectra.

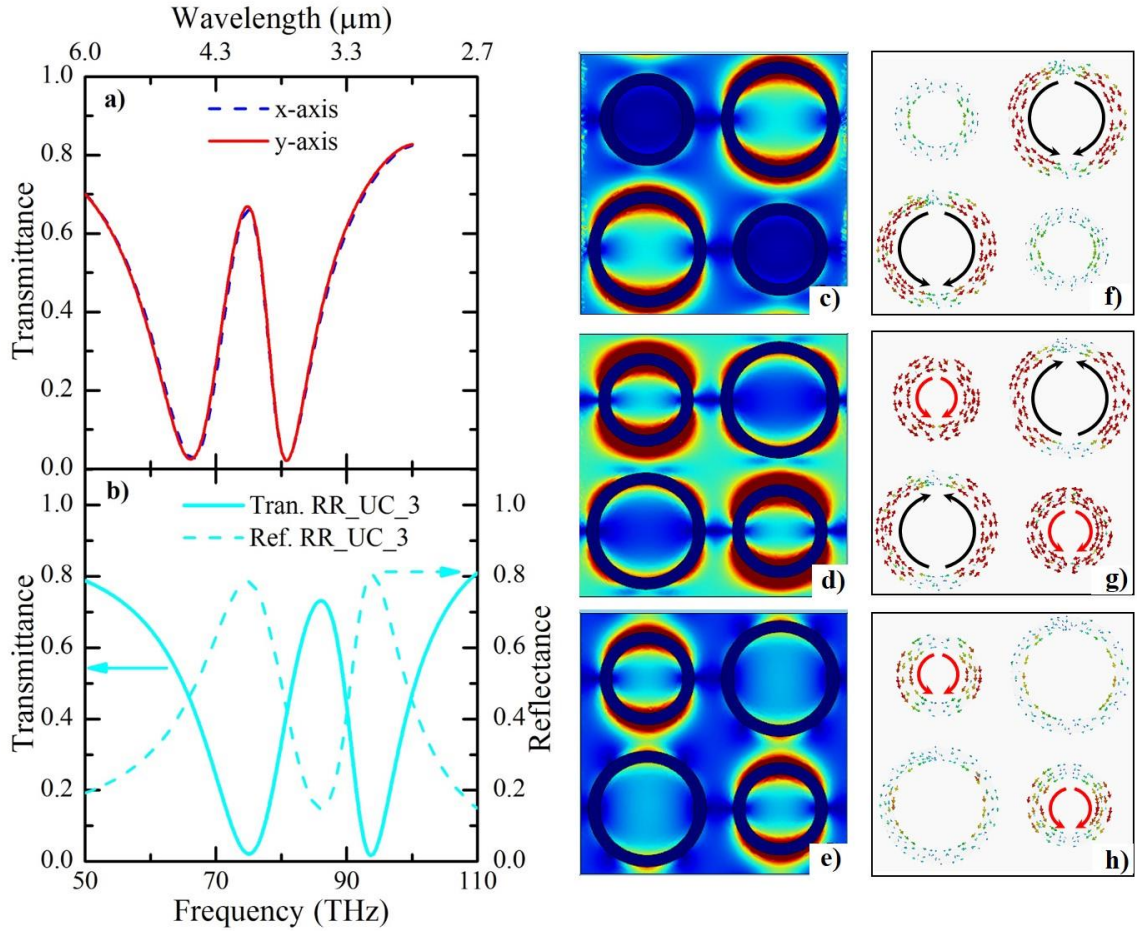

Figure 6.6 a) Simulated transmittance spectrum of RR_UC_5 (75 THz) for both the x-axis (blue dashed line) and y-axis (red line) linearly polarised incident waves. b) Simulated transmittance (line) and reflectance (dashed line) spectra from RR_UC_3 (86 THz), c-e) electric field distributions and f-h) surface current distributions at f_1 (66.5 THz), f_2 (75.0 THz) and f_3 (80.8 THz), respectively of RR_UC_5.

Table 6.1 Details of the dimensions of the different unit cell designs for the six different transmittance peaks.

Sample	r_1 (μm)	r_2 (μm)	p (μm)	w (μm)	Trans. Peak (THz)
RR_UC_1	0.5	0.2	3.6	0.2	118.0
RR_UC_2	0.6	0.3	3.8	0.2	99.9
RR_UC_3	0.7	0.4	4.0	0.2	86.0
RR_UC_4	0.7	0.5	4.0	0.2	81.8
RR_UC_5	0.8	0.5	4.5	0.2	75.0
RR_UC_6	0.9	0.6	5.0	0.2	67.1

6.3.2 Summary of Fabricated Devices

With the parameters of the six different RR designs obtained from COMSOL, the RR designs are incorporated into devices following the fabrication process described in Chapter 3. For each device, h-BN encapsulated graphene with an emitting area of 0.5 mm × 0.5 mm was divided into four 0.25 mm × 0.25 mm quadrants by arraying one of the six different RR unit cells designs over two 0.25 mm × 0.25 mm areas on the h-BN top layer in the diagonal direction. This leaves the remaining two 0.25 mm × 0.25 mm quadrants as h-BN encapsulated graphene without the RRs. This allows for the areas with RRs to be normalised to areas without RRs, on the same device. It also enables two spectra to be obtained from each device and compared. This is depicted schematically with a planar view in Figure 6.7(a) and a cross-section view in Figure 6.7(b). Pictures of a typical device are shown in Figure 6.7(c-d). Table 6.2 summarises the RR devices for which measurements are presented in the following sections. Multiple

RR devices are fabricated incorporating each unit cell design, in order to confirm reproducibility of spectral measurements. The measurement results presented in section 6.4 and 6.5 represent the average for each device.

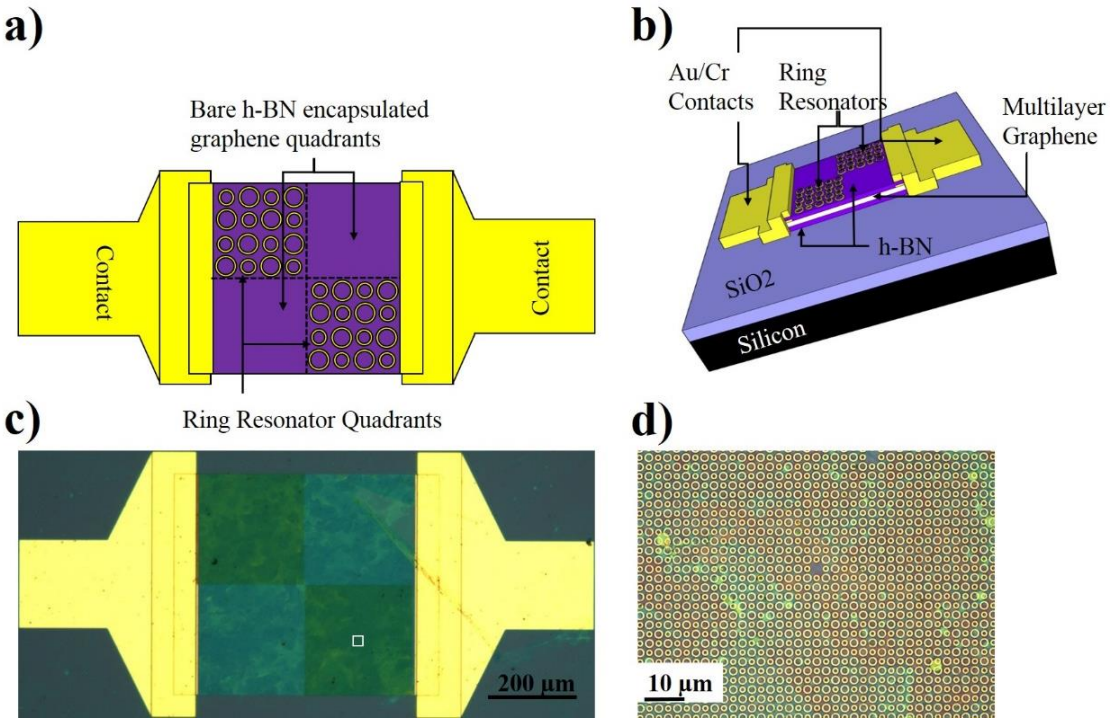

Figure 6.7 a) Planar schematic of a typical RR device, b) Cross-section schematic of a typical RR device, c) Micrograph taken at 5X magnification of RR_D_4, d) Microscope image with 100X magnification taken from within the white box shown in c).

Table 6.2 List of RR devices measured in this chapter.

Sample	Design	Refection Measurements	Emission Measurements	Area (mm^2)
RR_D_1	RR_UC_1	Figure 6.9(a) Figure 6.10(a)	Figure 6.13(a) Figure 6.14(a)	0.25
RR_D_2	RR_UC_2	Figure 6.9(b) Figure 6.10(b)	Figure 6.13(b) Figure 6.14(b)	0.25
RR_D_3	RR_UC_3	Figure 6.9(c) Figure 6.10(c)	None	0.25
RR_D_4	RR_UC_4	Figure 6.9(d) Figure 6.10(d)	None	0.25
RR_D_5	RR_UC_5	Figure 6.9(e) Figure 6.10(e)	Figure 6.13(c) Figure 6.14(c)	0.25
RR_D_6	RR_UC_6	Figure 6.9(f) Figure 6.10(f)	Figure 6.13(d) Figure 6.14(d)	0.25

6.4 Reflectance Measurements of RR Devices

In order to determine the physical location of the two quadrants with and the two quadrants without RRs a spatially resolved reflectance map was obtained by systematically scanning the microscope system over the surface of the sample and measuring the overall reflected signal at each point. For these experiments a mid-infrared laser (MIR) was passed through a microscope system on a motorised x-y stage and reflected at various points along the surface of the RR devices. The reflected beam was sent to an Infrared detector connected to a lock-in amplifier for phase sensitive measurements. The set-up for the reflectance mapping experiment is discussed in more detail in section 4.3. Figure 6.8(a) displays the reflectance map from a typical RR device while Figure 6.8(b) shows the same data plotted on a logarithmic scale. The areas with the largest overall measured intensity, the red regions at the top and bottom of the images, are the Au contacts. In the middle of the images, two distinct regions are clearly visible

pertaining to the two quadrants with RRs and the two quadrants without RRs. The quadrants are more distinct in Figure 6.8(b). The two green quadrants on the diagonal direction are the quadrants with RRs on top of the encapsulated graphene, whilst the two blue quadrants on the anti-diagonal direction, with approximately half the measured intensity compared to the green quadrants, are the two quadrants of encapsulated graphene without the RRs on top. The approximately double intensity from the quadrants with the RRs is to be expected due to the higher reflectivity of Au compared to bare h-BN encapsulated few-layer graphene.

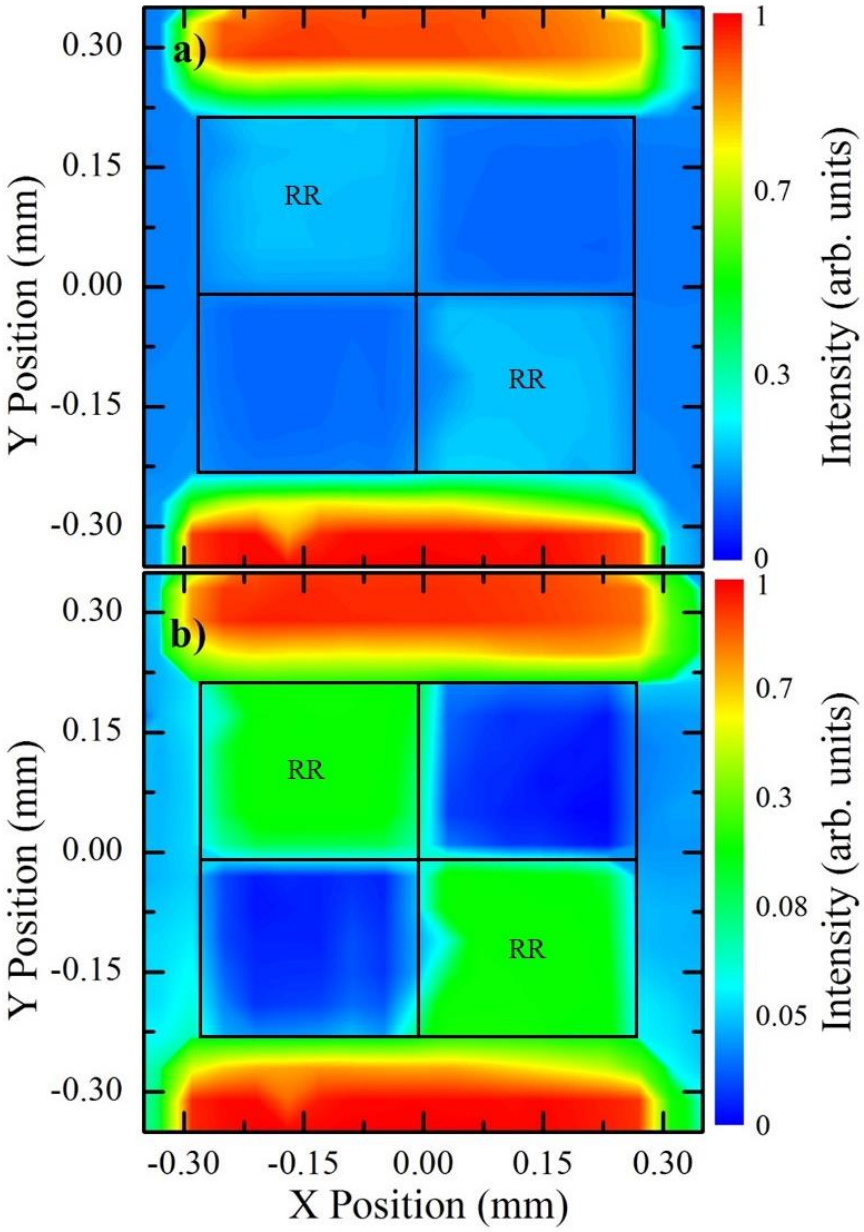

Figure 6.8 a) Spatially resolved reflectance map using a MIR laser from a typical RR device. b) Same data plotted on a logarithmic vertical scale.

After determining the location of each of the three different regions through spatially resolved reflectance measurements, FTIR rapid scans are performed, under atmospheric conditions, from the middle of each of the four quadrants and the Au contacts. The set-up for the reflectance FTIR measurements is described in section 4.5.2. This was repeated for each of the six different RR devices. Figure 6.9(a-f) displays the measured raw reflectance spectrum from 25 to 150 THz from

a quadrant with RRs, a quadrant without RRs and an Au contact, for the six different RR Devices. Due to the measurements being performed in atmosphere a large dip in intensity is observed at ~70 THz in all of reflectance measurements due to CO_2 absorption. There are also dips in intensity for all of the measurements from ~40-55 THz and from ~105-120 THz due to water absorption. Comparing the measured spectra from each location and device it is observed that the spectra from the quadrants without the RRs consistently has the lowest measured intensity over the frequency range while also showing a similar spectral response across each device. In comparison the Au contacts consistently has the largest measured intensity over the frequency range and also has a similar spectral response across each device. The similarity in spectral response from the quadrants without RRs and the Au contacts is to be expected while having the lowest and highest intensity over the frequency range respectively is consistent with the reflectance mapping measurements. In Figure 6.9 (a-f) the peak observed at ~41 THz in the reflectance spectrum from the RR quadrants is most likely due the h-BN optical phonon [83].

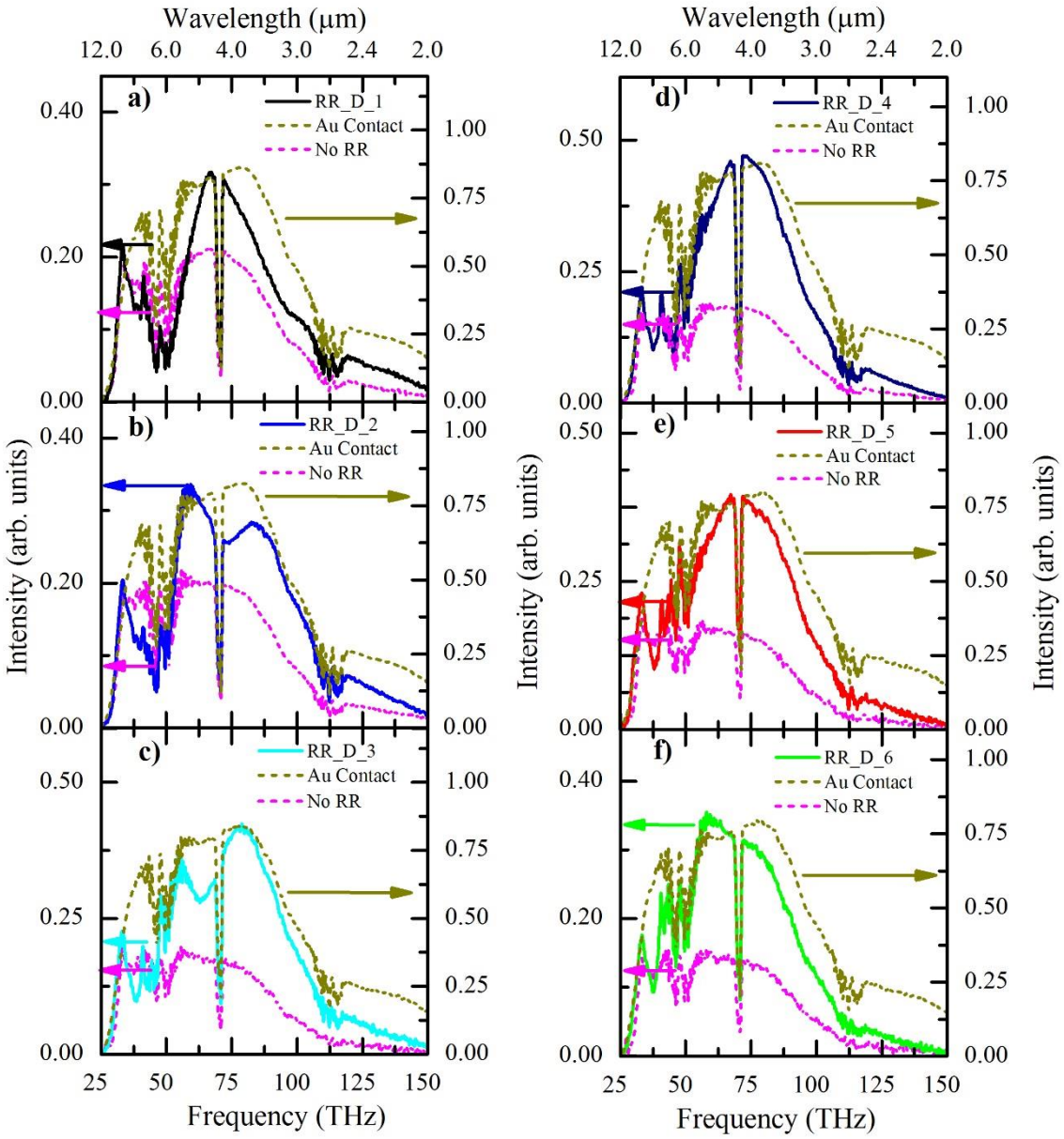

Figure 6.9 a-f) Measured values of reflectance intensity of a MIR broadband source as a function of frequency taken from a quadrant with RRs (solid lines), a quadrant without RRs (dashed magenta lines) and an Au contact (dashed green lines) for six different RR devices.

Importantly, it is clear from the raw reflectance measurements, without any normalization, that the spectral response obtained from the RR quadrants varies across the six devices. However, it is hard to draw any quantitative conclusions due to atmospheric absorption and the overall spectral response of the

measurement system. To correct for this the raw spectra from RR quadrants was normalised to the measured reflectance spectra from the Au contacts of each device, as the spectral response of Au is flat over the frequency range studied. This corrects for atmospheric absorption and the spectral response of the measurement system. The result of this normalization is displayed in Figure 6.10(a-f), which plots the reflectance percentage as a function of frequency for the six RR devices from quadrants with and without RRs. In Figure 6.10(b) CO_2 absorption is not fully corrected for, most likely due to small changes in the CO_2 concentration in the atmosphere between measurements.

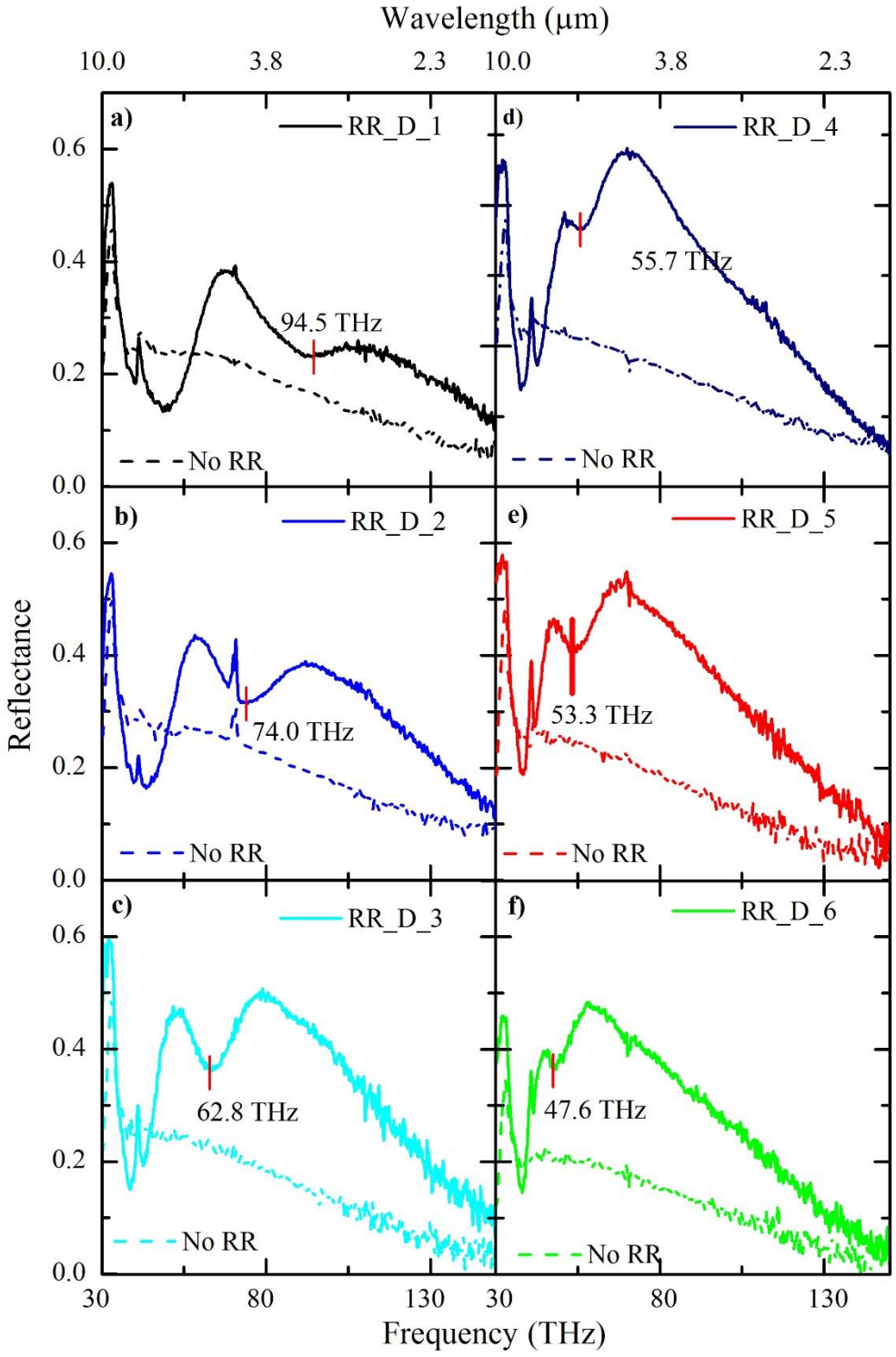

Figure 6.10 a-f) Measured reflectance as a function of frequency from quadrants with RRs (lines) and quadrants without RRs (dashes) normalised to Au contacts.

Away from the two peaks at 41 THz and 32 THz, each of the six reflectance spectra from the RR quadrants have the same “M” shaped spectral response that was predicted by the RR reflectance simulations, with it being most obvious in

Figure 6.10(b-c). The radii and pitch of the RR unit cells are smallest for the device spectra presented in Figure 6.10(a) and increase through to the largest for the device spectra 6.10(f). In each of the six spectra, a red line marks the centre frequency of the Fano resonance dip in reflectance. The frequency of each of the Fano resonance dips is plotted as a function of unit cell pitch, *p*, large ring radius, r_1 and small ring radius, r_2, in Figure 6.11(a). From this plot it is clear that the Fano resonance frequency decreases as both the pitch of the unit cell and radii of the 'bright' and 'dark' mode rings increases. This is consistent with the trend observed in the FEM simulations, suggesting that the "M" shaped region of the spectral response is due to the excitation of the RR structures and confirms that the frequency of the measured Fano resonance dip can be systematically controlled through the careful design of the RR unit cell. Figure 6.11(b) plots the calculated Q-factor for each of the six Fano resonance dips. It is can be observed that the Q-factor generally increases as the Fano resonance frequency decreases, though even the maximum Q-factor of 5.6 is still roughly half the theoretical limit of 10. To calculate the Q-factors the Breit-Wigner-Fano (BFW) line shape, given by

$$y = y_0 \frac{H\left(1 + \frac{x - x_c}{qw}\right)^2}{1 + \left(\frac{x - x_c}{w}\right)^2} \tag{6.2}$$

where *H* is the peak height, x_c is the centre frequency, *q* is the asymmetry factor, *w* is the width of the peak and y_0 is the baseline, was fit to the reflectance dips using the data analysis software Origin. After the fit converged, the Q-factor was then determined by dividing *w* on x_c . In each of the six reflectance spectra taken from RR quadrants the h-BN peak at 41 THz is more noticeable in comparison to

both the normalised spectra from the quadrants without RR and the raw reflectance spectra. As the resonance frequency of the RR modes decreases, the “bright” mode couples with the h-BN mode. This results in the “bright” mode increasingly narrowing with decreasing resonance frequency. Additionally, there is a large peak in reflectance that is present in all the spectra, including the quadrants without RRs, at ~32 THz. Due to the consistent frequency of this peak with changing RR designs and its presence in the measured spectra from quadrants without RRs, this peak is most likely due to the underlying SiO_2. A sharp change in refractive index at frequencies that are close to an absorption band of a transparent material is known as the Reststrahlen effect. This results in a large increase in reflectance of a narrow frequency range termed the Reststrahlen band and is specific to each material. The reflectance peak at 32 THz is close to a known absorption band of SiO_2 at ~33 THz, due to Si-O bond stretching, providing further evidence for this to be the case. Without the peaks at 32 and 41 THz, the measured spectra would better reflect the simulated spectra. Finally, while the simulations qualitatively agree with the measured results they do not quantitatively agree. The specific frequency of each of these RR modes are located at frequencies that are ~20-30% smaller than was predicted by the FEM simulations. This is possibly explained by the fact that simulations only take into account the top h-BN layer and the Au rings. The simulations do not account for the top h-BN layer, the few-layer graphene and the SiO_2/Si substrate.

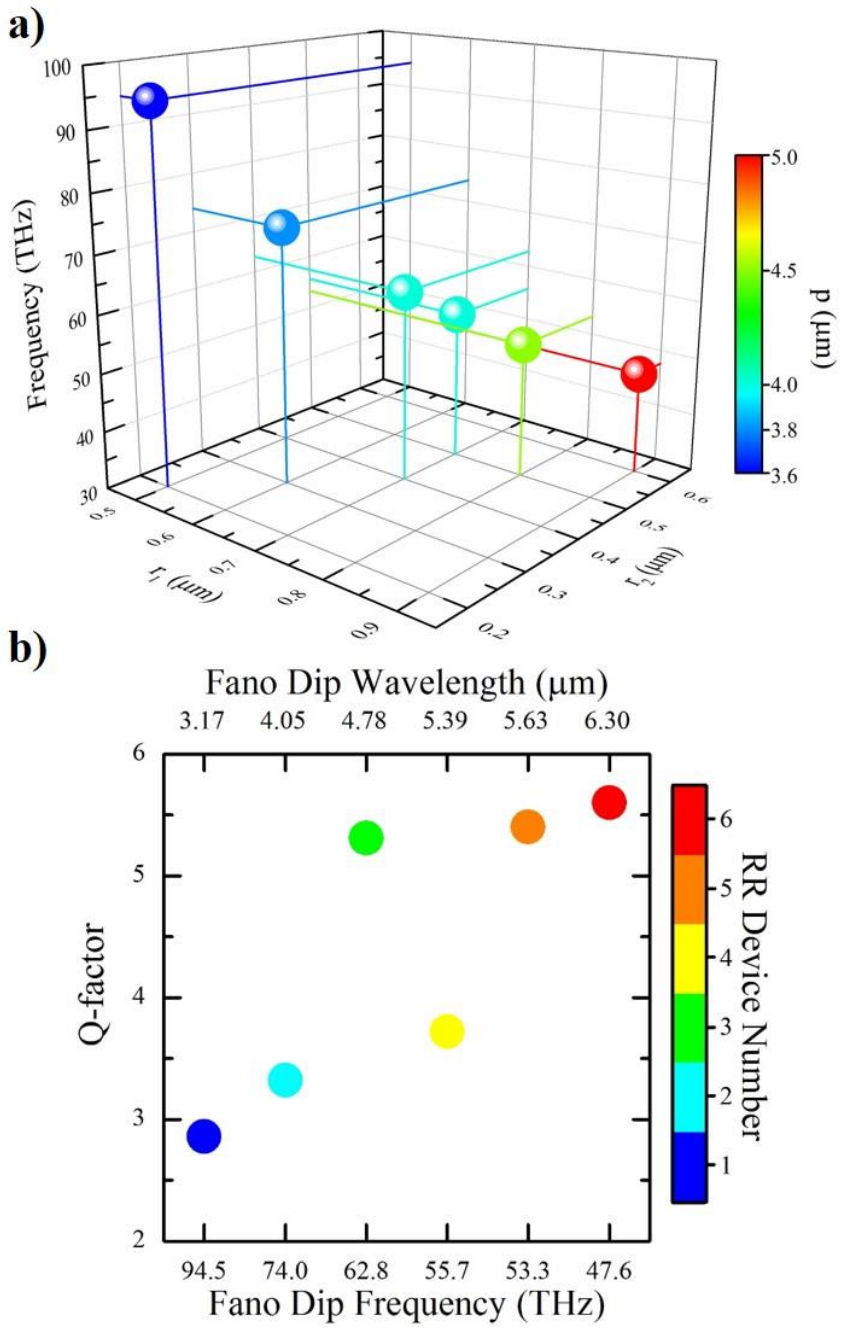

Figure 6.11 a) Frequency of Fano resonance dip as a function of large ring radius, r_1 (x-axis) small ring radius, r_2 (y-axis) and pitch, p (colour bar). b) Q-factor of the six Fano resonance dips and their corresponding frequency (x-axis) and device numbers (colour bar).

6.5 Emission Measurements of RR Devices

After the completion of the reflectance experiments the experimental set-up is reconfigured to allow for measurements of the emission spectra from the RR devices. As with the reflectance experiments, in order to locate the device in addition to determining the location of the quadrants with and without RRs, spatially resolved thermal emission mapping is performed prior to the measurements of any device emission spectra. To perform the thermal emission mapping the same microscope system mounted on a motorized x-y stage is used to collect the emitted light. The devices are driven with a 1 kHz square pulse wave with peak injection currents ranging from 60 mA to 80 mA. After the light is collected by the microscope system it is passed to a CMT detector connected to a lock-in amplifier for phase sensitive measurements. The experimental set-up for spatially resolved thermal emission mapping is discussed in more detail in section 4.3. A plot of the emission intensity as a function of xy position for RR_D_2 is shown in Figure 6.12. As was observed in the reflectance maps, four quadrants are visible and can be divided into two quadrant pairs, either with or without RRs. The maximum emission intensity is observed in the centre of the two quadrants without RRs. In comparison, the intensity from the centre of the two quadrants with RRs is ~30% less. This is the opposite of what was observed in the reflectance map and is to be expected if the RRs are narrowing the spectra as anticipated. The contacts are not visible in this image because they do not heat up and cool down on a sufficient time scale to be measureable by the measurement system. The results presented in this section are from devices with four of the six different RR device designs as none of the multiple devices fabricated with RR_D_4 and RR_D_5 were able to sustain a drive current.

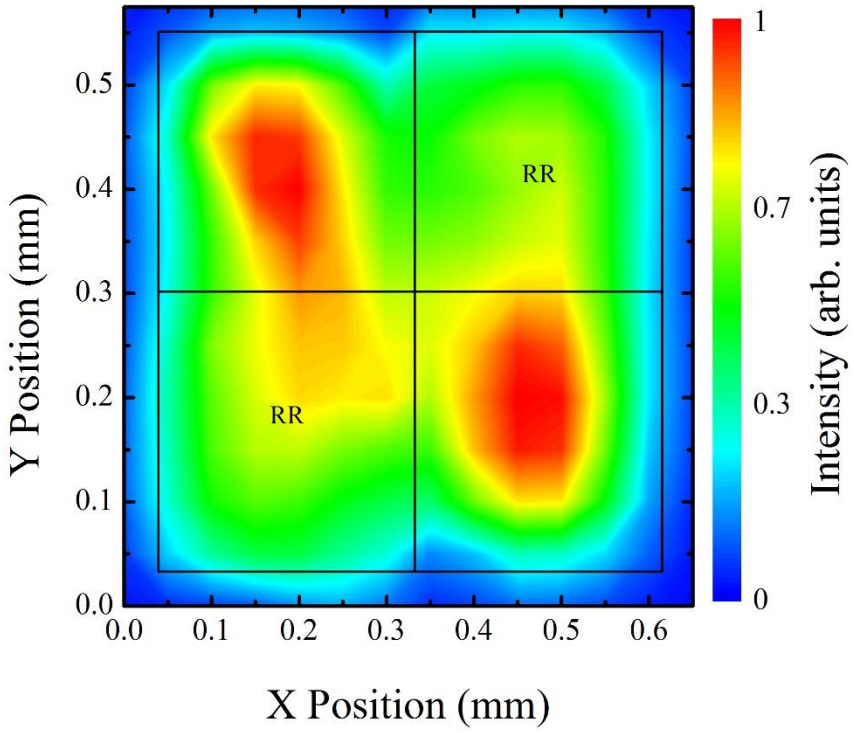

Figure 6.12 Spatially resolved thermal emission map of a typical RR device with a peak injection current of 80 mA.

With the location of the four different quadrants determined by the spatially resolved thermal emission mapping the system was set-up for emission FTIR measurements, as discussed in chapter 4 section 4.5. Multiple FTIR step scans are performed at various points in each of the four quadrants and averaged. This is done to reduce noise and to account for the fact the temperature of h-BN encapsulated graphene devices is not uniform across the surface, with the maximum temperature occurring in the middle [181]. The same procedure is performed on each RR device. The raw measured emission spectrum, from a quadrant with RRs and a quadrant without RR, is shown in Figure 6.13(a-d) for RR_D_1, RR_D_2, RR_D_5 and RR_D_6.

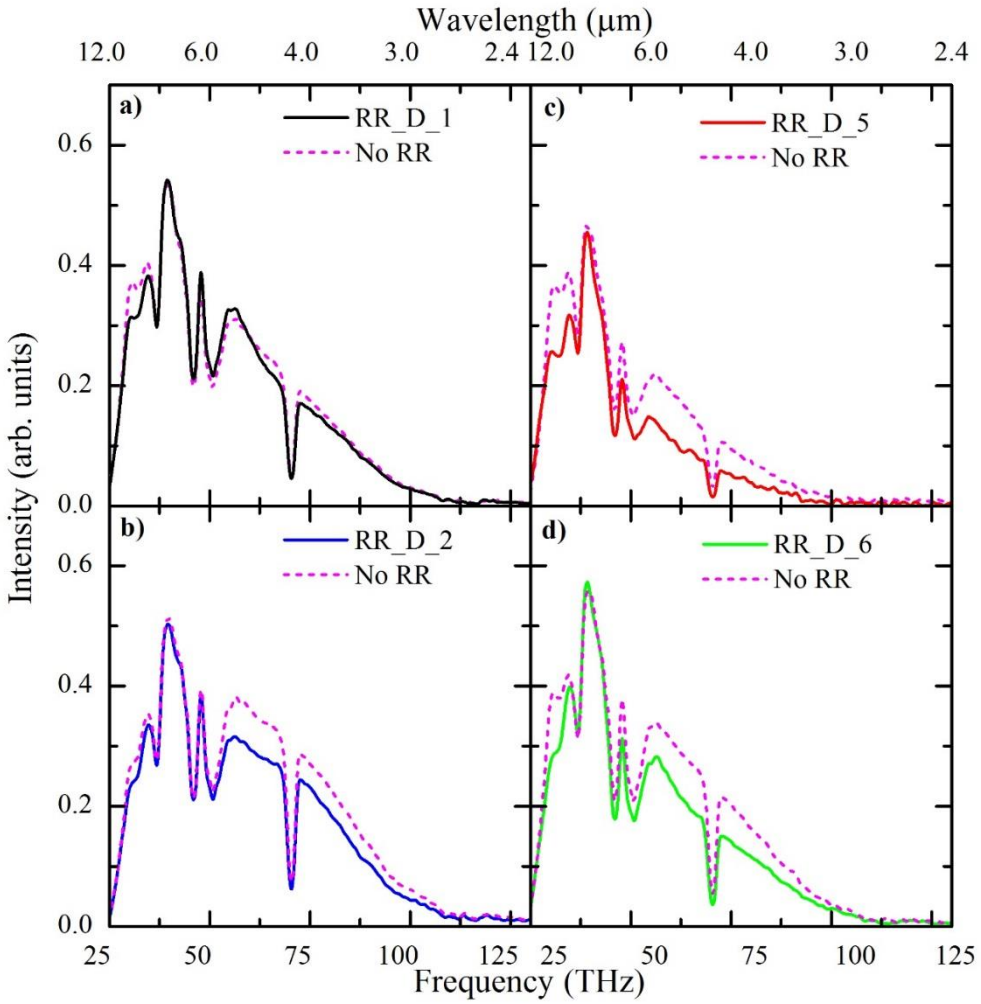

Figure 6.13 a-d) Averaged raw emission spectra from a quadrant with RRs (coloured lines) and a quadrant without RRs (purple dashes) for devices with four different RR designs.

The measurements are again performed under atmospheric conditions, resulting in atmospheric absorption accounting for the minimum in measured emission intensity at 70 THz, due to CO_2 absorption, and the two minima between 40-55 THz due to water absorption. In each of the four plots there is a qualitative difference in the shape of the emission spectra from quadrants with RRs compared to quadrants without RRs. The overall shape of the RR spectra changes across the four different devices, while the spectra from quadrants without RR stays relatively consistent, as expected. Additionally, in each of the

four plots the overall measured spectra from quadrants with RR is narrower than the spectra from regions without RR, with the integrated intensity of the quadrants without RRs increasing by an average of 20% when compared to the integrated intensity of the corresponding quadrants without RRs. This is consistent with what was observed in the spatially resolved thermal emission maps. In order to better examine the effect of the RRs on the emitted spectra of each device, the raw spectra from a RR quadrant is normalised to the raw spectra from a corresponding quadrant of encapsulated graphene without RRs, the results of which are shown in Figure 6.14(a-d). Along with normalisation, Savitzky-Golay smoothing was applied to the measured data.

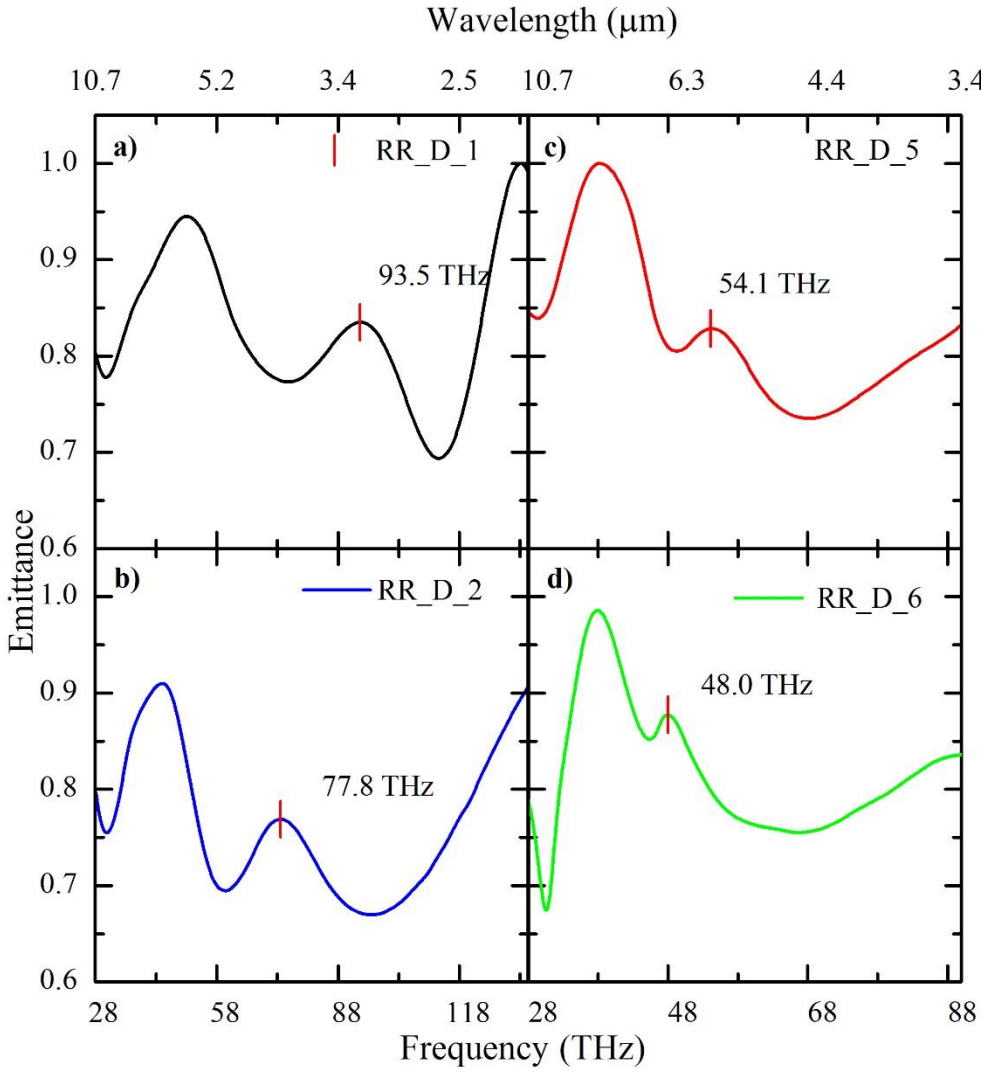

Figure 6.14 a-d) Measured emittance spectra of RR quadrants normalised to emission spectra from bare encapsulated graphene for four different RR devices.

Ignoring the minima that is present in all four of the normalised emission spectra at ~30 THz, a region in each of the four spectra can be described as dip, peak, dip or “W” shaped. This is in good agreement with the shape of the simulated transmittance spectra, as presented in previously in Figure 6.5(a-f). The “W” shaped section of the spectral response exhibits a shift to lower frequencies, with a red line marking the centre frequency of the EIT-like Fano resonance peak in each spectra, from the highest frequencies in Figure 6.14(a) through to lowest frequencies in Figure 6.14(d). Figure 6.15(a) plots the frequency of each of the

four red lines, the Fano resonance peaks, as a function of RR unit cell parameters: large ring radius, r_1, small ring radius, r_2, and unit cell pitch, p, whereas Figure 6.15(b) plots the Q-factors for the four resonance frequencies. The highest measured frequency of the Fano resonance peak is observed for the RR device with the smallest values of r_1, r_2 and p (RR_D_1). As all three of these values increase, the frequency of the measured Fano resonance peak decreases, relatively linearly, while the Q-factor of the peaks increases as the corresponding resonance frequency decreases. The values of the Q-factor are similar to those obtained from the reflectance measurements and they are all below the theoretical limit of 10. The minimum in the normalised emission spectra of the four devices at ~30 THz is most likely due to the underlying SiO_2. The frequency of this dip in emission approximately corresponds to the frequency of the reflectance maximum that is attributed to the Reststrahlen effect in section 6.4. This suggests that a portion of light that is emitted from the graphene down into the underlying substrate is being reflected back and transmitted from the ring resonator devices and is not being entirely normalised out.

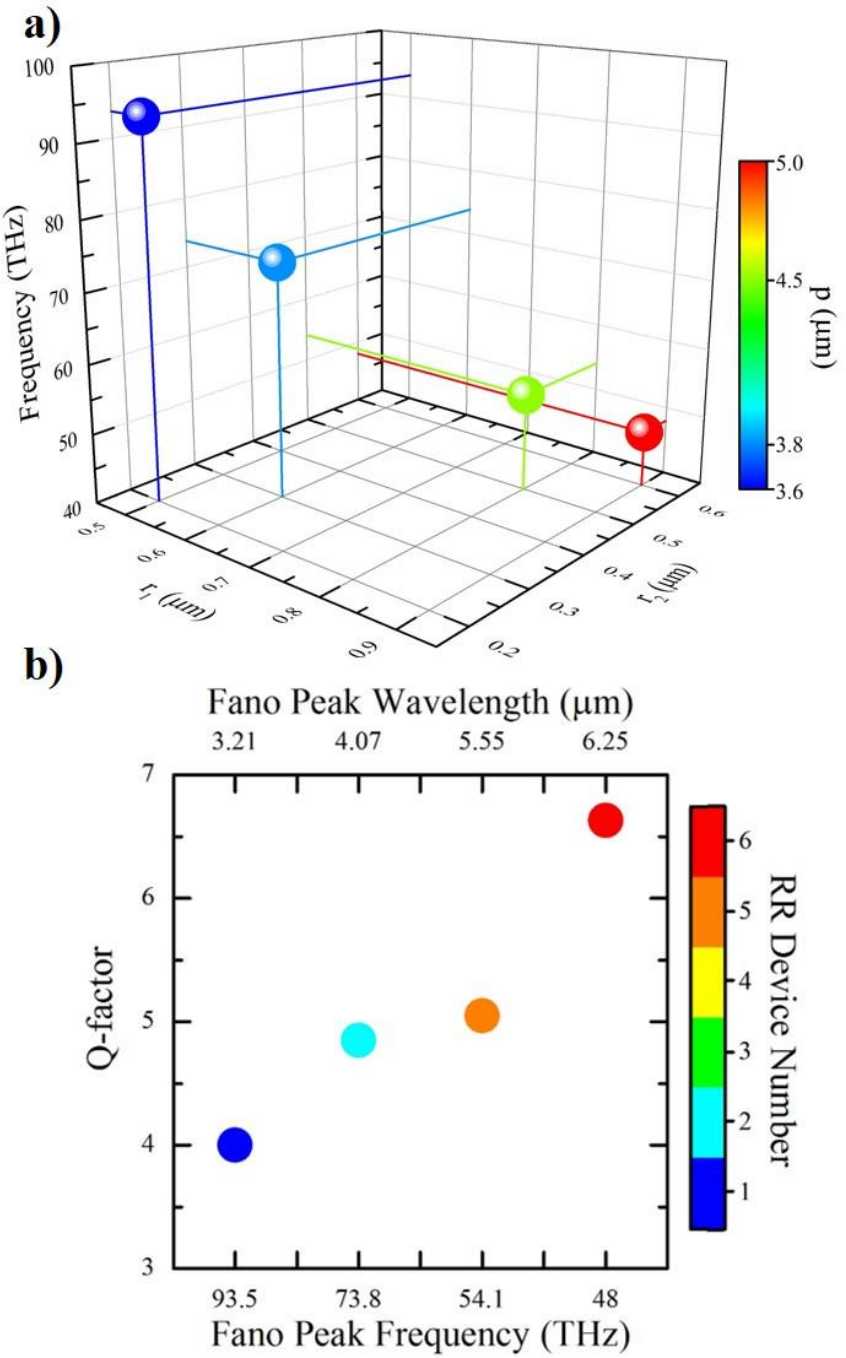

Figure 6.15 a) Frequency of Fano resonance peak as a function of large ring radius, r_1 (x-axis) small ring radius, r_2 (y-axis) and pitch, p (colour bar). b) Q-factor of the six Fano resonance peaks and their corresponding frequency (x-axis) and device number (colour bar).

A comparison of the results obtained from the transmittance simulations, the reflectance measurements and the emission measurements is made in Figure

6.16. Figure 6.16 plots the centre frequencies of the Fano resonances, obtained experimentally (from both reflectance and emission) and simulated, as a function of r_1, r_2 and p. Overall there is good qualitative agreement between the simulations and the experiments as all three data sets exhibit the same linear decrease in resonance frequencies with increasing r_1, r_2 and p. Additionally the quantitative agreement between the emission and reflectance measurements is good as the frequencies of the measured Fano resonances differ by at most ~1% between the devices with the same RR design. These results clearly demonstrate the ability to tune the broadband graphene emission spectra through the careful design of the RR unit cell. However, there is a consistent offset between the resonance frequencies predicted by the transmittance simulations and those observed in both the reflectance and emittance spectra. The measured resonance frequencies are consistently 25% lower than the simulation results. More measurements are required in order to determine the cause of this, though some possible explanations for this discrepancy include; a larger than expected thickness of h-BN, a larger than expected effective ring radii, over simplification of the simulations, or the large amount of scratches present on the surface of all of the devices that are either a result of the fabrication process or the general handling of the devices.

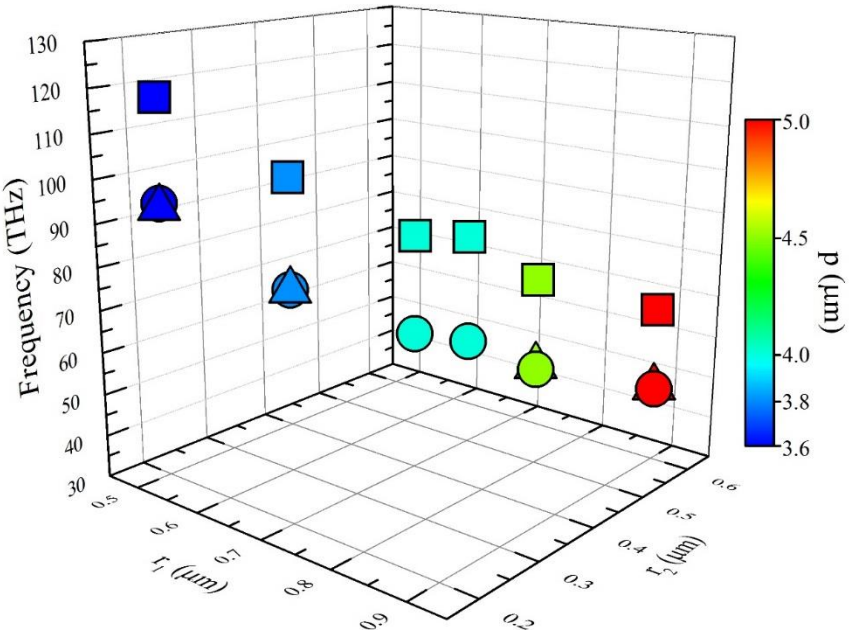

Figure 6.16 Four dimensional plot of Fano resonance frequency from emission measurements (circles), reflectance measurements (triangles) and transmittance simulations (squares) as a function of unit cell pitch, *p* (colour bar), large ring radius, r_1 (x-axis) and small ring radius, r_2 (y-axis).

Finally, a measurement of the polarization dependence of the emission from RR devices is studied by placing a linear polariser between the sample and the CMT detector. Emission spectra polarised along both the x-axis and y-axis is measured for RR_D_5. The raw emission spectrum is again normalised to the measured x-axis and y-axis polarised emission spectrum from bare h-BN encapsulated graphene. Figure 6.17 plots both polarisations on the same plot with no observable difference between the two spectra. This is consistent with the simulations, confirming the insensitivity of the RRs to the polarisation angle, due to the symmetric design of the unit cell.

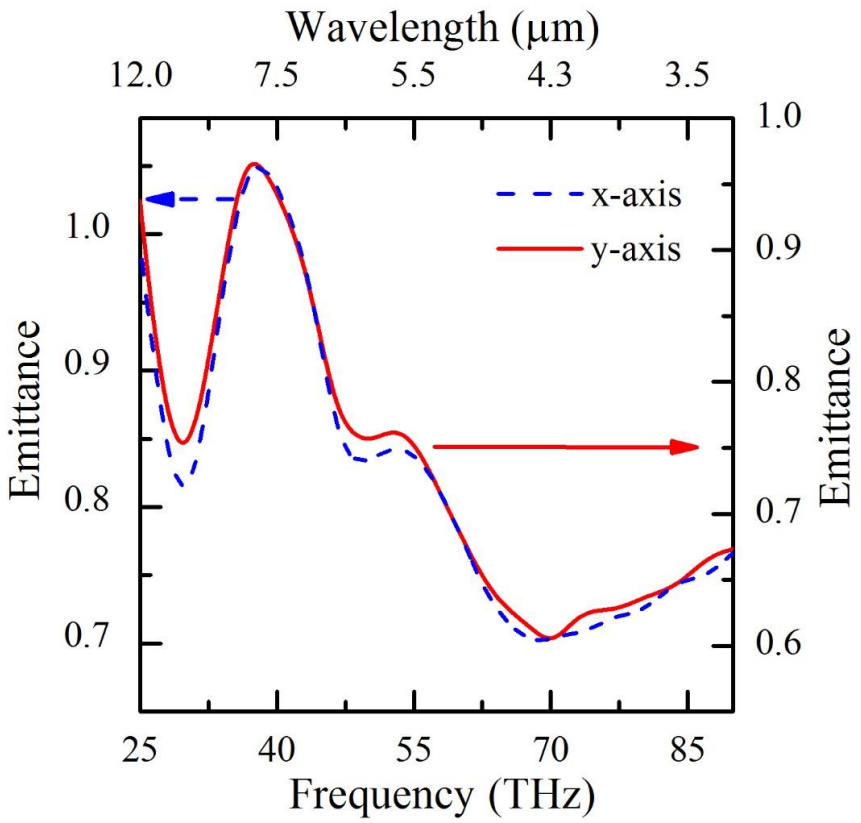

Figure 6.17 Measured normalised emittance spectra from RR_D_5 linearly polarised along the x-axis (blue dashed line) and y-axis (red line).

6.6 Initial Results on SRR Devices

In order to improve on the transmittance (~0.75) and relatively low Q-factors of the transmittance peaks predicted by the FEM simulations and dips/peaks observed in reflectance/emittance measurements an improved resonator design is implemented utilising split ring resonators (SRR) in place of the ring resonators. The splits in the rings are on a 45° angle to both the x-axis and y-axis, in order to maintain insensitivity to linear polarisations along either axis. A two dimensional sketch along with a three dimensional schematic of the SRR unit cell is displayed in Figure 6.18(a) and Figure 6.18(b) respectively. Three unit cells with different structural parameters were designed and simulated in COMSOL (by a colleague

Mr. Cheng Shi) in order to achieve transmittance peaks at 60 THz, 75 THz and 100 THz. Table 6.3 displays the different values of the structural parameters for the three different unit cell designs obtained from COMSOL that result in transmittance peaks at the requisite frequencies. The simulations showed that the transmittance peak of the improved designed increased to ~80% compared to the ~70% transmittance of the ring resonators, while the Q-factor of the transmittance peaks increased by approximately 70% compared to the RR.

Table 6.3 Details of the structural parameters for the three different unit cell designs.

Sample	r_1 (μm)	r_2 (μm)	l (μm)	p (μm)	w (um)	Trans. Peak (THz)
SRR_UC_1	0.6	0.2	1.32	4.0	0.2	100
SRR_UC_2	0.9	0.5	1.5	5.2	0.2	75
SRR_UC_3	1.2	0.8	1.68	6.4	0.2	60

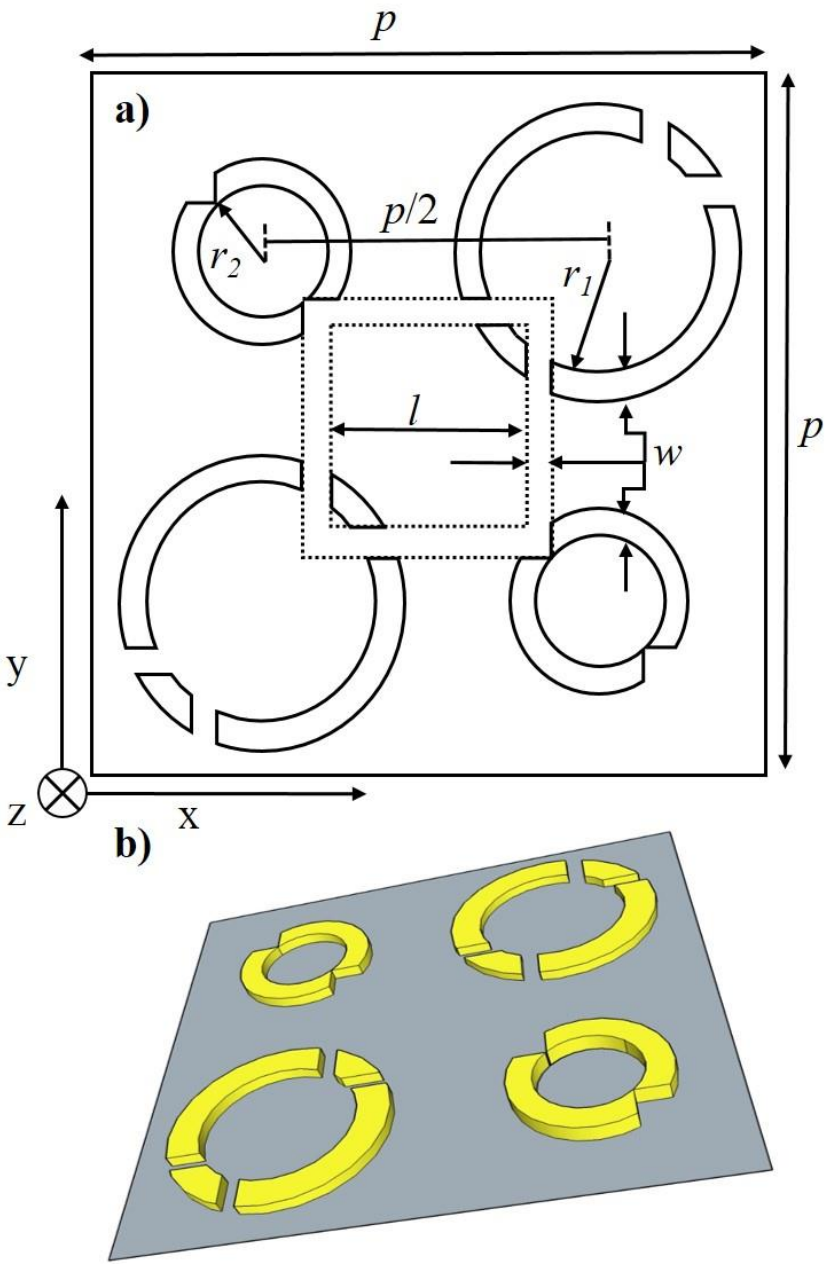

Figure 6.18 a) A 2D sketch of the unit cell of the SRRs and b) a 3D schematic of SRR unit cell.

The measurement results presented in this section are initial optical characterisation results from three different graphene encapsulated devices, SRR_D_1, SRR_D_2 and SRR_D_3, which are identical to the RR devices with the exception of the split rings replacing the ring resonators. The structural parameters of the SRRs of SSR_D_1, SRR_D_2 and SRR_D_3 corresponds to SRR_UC_1, SRR_UC_2 and SRR_UC_3 respectively. FTIR rapid scan

reflectance measurements are performed under atmospheric conditions from the quadrants with ring resonators for each of the three devices and the measured reflectance from the Au contacts. Figure 6.19 plots the normalised reflectance spectra (normalised to the Au contacts) of the split ring devices. The reflectance response of each of the devices shows the same “M” shaped reflectance response observed for the ring resonator devices, with the same Fano resonance dip that is the result of the induction of out-of-phase surface currents. Compared to the ring resonators the resonance frequencies of the Fano resonance dips are much closer to the Fano resonance transmittance peaks, a maximum of 3% different compared to the 25% of the RR devices, predicted by the simulations. Additionally there is the same trend of decreasing resonance frequency with increasing ring radius and pitch, while the Q-factor of the dips is not significantly larger than what was obtained from the measurement results of ring resonators. From Figure 6.19 it can be concluded that for unpolarised light, the split rings behave as standard ring resonators, with Fano resonance dip resulting from the induction of out-of-phase surface currents. It is expected that the reflectance response of the SRR would change if the incident beam were linearly polarised as the simulations predict a strong dependence on polarisation angle, due to the asymmetry of the split ring resonators, with the largest Q-factor of the transmittance peak obtained for either x-axis or y-axis polarisations.

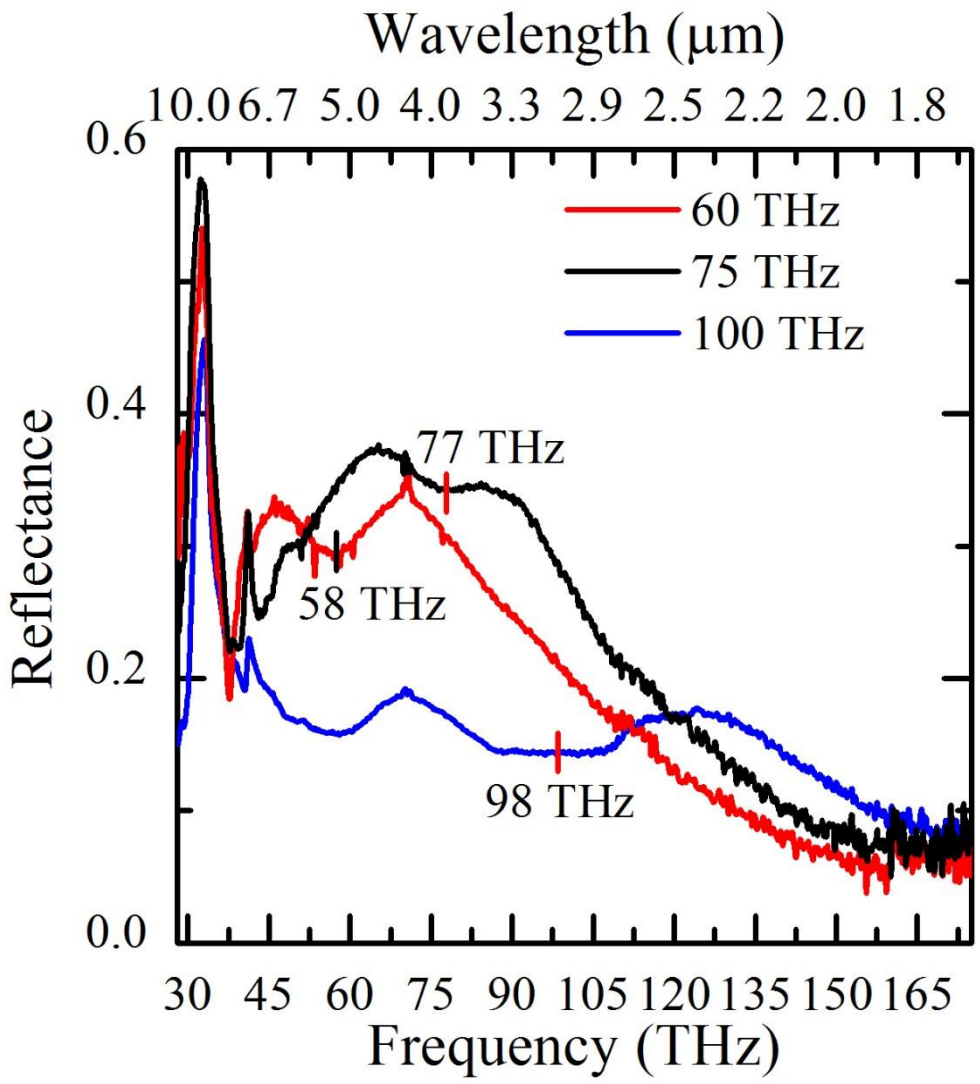

Figure 6.19 Measured reflectance spectra of SRR quadrants normalised to reflectance spectra from bare encapsulated graphene for SRR_D_1 (blue line), SRR_D_2 (black line) and SRR_D_3 (red line).

6.7 Summary

In summary, thermal emission spectroscopy measurements were performed on a single-layer graphene device, a few-layer graphene device, and a blackbody source and compared. The similarity between the blackbody spectrum and single-layer device suggests that emission from the single-layer graphene is

grey-body emission. Emissivities were estimated as 6% and 2% for single-layer and few-layer devices respectively. The corrected spectra of the graphene devices provide an estimate for the surface temperature of the graphene by comparing it to a calculated spectrum, providing values of on and off temperatures of 600 K and 350 K for the single-layer graphene device and 620 K and 480 K for few-layer graphene device

A pair of two different sized Au RRs in close proximity of each other, in the both spatial as well as frequency domains, were arrayed on top of h-BN encapsulated few-layer graphene in an aim to narrow the broad emission spectrum controllably. When placed on top of a dielectric they act as a metamaterial resonator analogue of the EIT effect. FEM modelling was used to generate six RR unit cell designs with a Fano resonance predicted to be located at various points between 60-120 THz. The simulations show a shift in the Fano resonance peak to lower frequencies with both an increase in ring radius size and pitch and an insensitivity to polarisation along the x-axis or y-axis. Optical characterisation measurements were performed on six RR devices, with unit cells matching the COMSOL generated designs. The initial measurements performed on the RR devices were FTIR reflectance measurements, with the normalised reflectance plots showing a clear shift in the Fano resonance dip to lower frequencies with increasing ring radius and pitch, analogous to what was predicted by the simulations. Emission FTIR measurements were performed on four of the six RR devices. Again a clear shift to lower frequencies is observed in the Fano resonance peak with increasing ring radius and pitch. A maximum difference of ~1% in Fano resonance frequency was observed comparing the reflectance spectra to the emission. Initial results from SRR devices show better agreement between simulations and measurements, with a maximum difference of approximately 3% observed for the

frequencies of the measured Fano reflectance dips compared to the transmittance peaks of the simulated spectra. From these results it can be concluded that RR and SRR can be utilised to predictably tune the graphene emission spectrum.

7 Patterned Substrates

7.1 Introduction

The primary motivations of investigating patterned substrates are to combine the thermal management aspects discussed in Chapter 5 with the spectral control discussed in Chapter 6. Patterned substrates have previously been shown to allow for the tuning of the emission spectra from small area, tens of μm^2, single-layer graphene (SLG) devices, by suspending the graphene over optical cavities of various depths [182]. Additionally, simulations and measurements of similarly suspended graphene devices [183] have shown an improvement on the low thermal radiation efficiency found for supported graphene devices [184], that is the consequence of heat dissipation into the substrate [141]. By suspending graphene on a patterned substrate the unwanted vertical heat dissipation is essentially eliminated, resulting in an increase in both efficiency and operating temperature [183].

Two different types of patterned substrates were considered for further investigation. Initial attempts were made to fabricate deeply etched hole arrays in SiO_2/Si. It was determined, after multiple attempts at fabrication with a dry etch process, that it would not be possible to fabricate the patterned SiO_2/Si substrates with the requisite dimensions, given the fabrication facilities available. The second type of patterned substrates considered were deeply etched, hexagonally arrayed, gallium nitride (GaN) nano-rods (NR) fabricated by collaborators at the University of Bath. They provide a high aspect ratio test bed for studying the

impact of patterned substrates in terms of both the thermal management and spectral response. A second advantage of GaN NR arrays is the possibility for the excitation of graphene plasmon modes, discussed in section 7.2. Although the samples used were designed for further processing into GaN NR LEDs [185], rather than for tuning infrared emission (IR), or facilitating the suspension of graphene and the subsequent fabrication into graphene based IR emitters, the advantages outweigh this shortcoming. Therefore the GaN NRs were chosen as the primary focus for investigation into graphene transferred on top of patterned substrates.

In this chapter, simulations of graphene on GaN NRs indicating the possibility of the excitation of various graphene plasmon modes are discussed in section 7.2. In section 7.3, the fabrication procedure for suspending the graphene on GaN NR arrays is presented. Section 7.4 then examines the optical characterisation of graphene suspended on two different GaN NRs substrates, utilising Fourier transform infrared spectroscopy (FTIR). This is followed by a brief summary of the chapter in section 7.5.

7.2 FDTD of Simulations of Graphene on GaN NRs

Finite difference time domain (FDTD) simulations, all of which were performed by a colleague, Mr. Bofeng Zhu at the University of Bristol, were utilised to predict the spectral response of single-layer graphene (SLG) on two different hexagonally arranged GaN NR substrates. The software employed for the simulations was Lumerical 2015B. The simulations were performed in order to determine if the graphene plasmons modes could be excited, if they can be

observed in the reflectance spectra and at what resonance frequencies they correspond to, and how they are affected by fundamental graphene properties, such as the chemical potential and scattering time. It is also possible that if the plasmon modes are observed in both the simulations and measurements of the reflectance spectra, a comparison between the two could be made in order to characterise some of the graphene properties. A 2D schematic of the simulated unit cell is displayed in Figure 7.1 below. Two different unit cells were studied using the FDTD simulations, with different values for pitch of the NRs, p, and diameter of the NRs, D. The unit cell dimensions are: D = 260 nm and p = 600 nm, UC_1, and D = 550 nm and p = 2000 nm, UC_2. The heights of the three different materials that make up the NRs are the same for both cases with, h_1 = 100 nm (etched Si), h_2 = 240 nm (AlN) and h_3 = 1640 nm (GaN), whilst the height of the silicon bottom layer was set to an infinite thickness for UC_1 and a finite thickness of 5 µm for UC_2. The dimensions of the simulated unit cells match the unit cell dimensions of the two different GaN NR arrays utilised as substrates for the samples studied in this chapter.

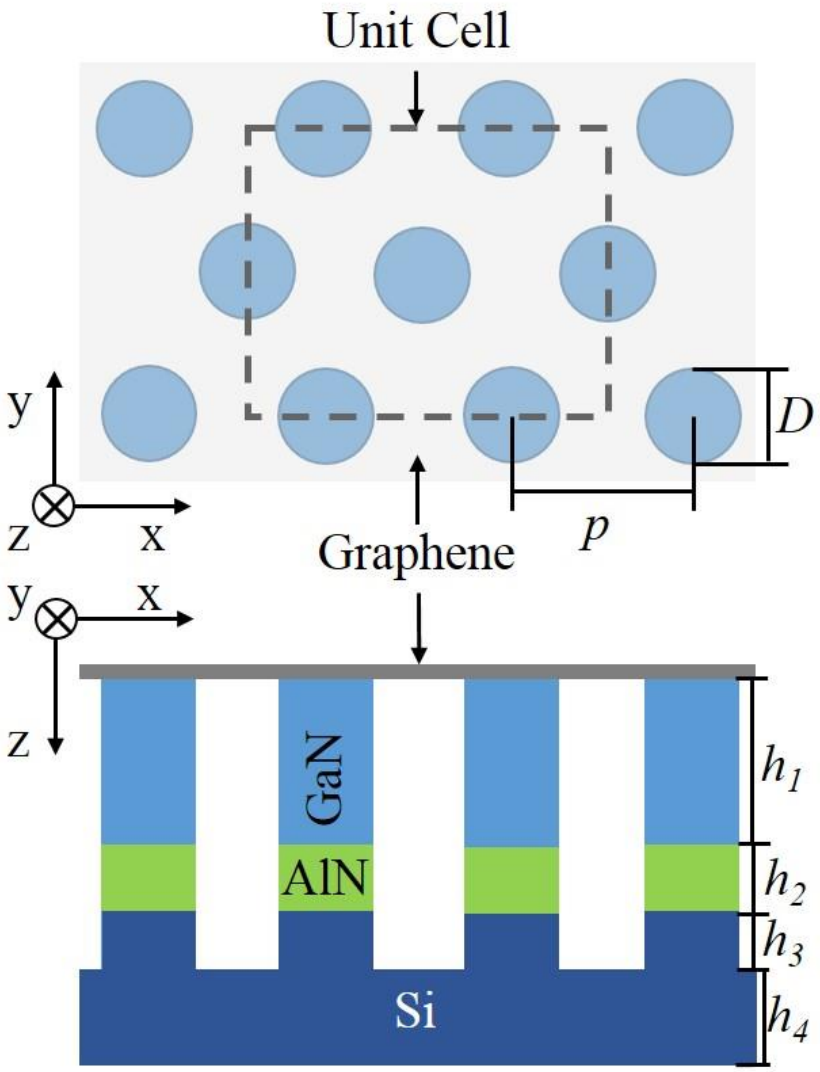

Figure 7.1 A 2D sketch of the SLG on GaN NR geometry and unit cell area used in the FDTD simulations (dashed line)

The simulation results presented in this section focus on UC_1, as no plasmon excitation was observed over the simulated spectral range for UC_2. Figure 7.2 (a) displays the calculated normalised reflectance spectra from UC_1, for a linearly polarised infrared wave, polarised along the y-axis of Figure 7.1. The normalisation is performed by dividing the calculated spectra from UC_1 by the same unit cell without graphene. A series of unevenly spaced (in terms of wavelength) reflectance minima can be observed in the calculated spectra. These can be attributed to various plasmon modes, with the order displayed

below the corresponding dip. The order of the plasmon resonance mode is determined by the number of plasmon wavelengths present on a single graphene topped NR, as shown in Figure 7.2 (b). The uneven spacing of the resonance modes is attributed to the indices of the graphene plasmon mode not being linearly dependent on wavelength. To gain a better understanding of how fundamental graphene properties affect both resonance frequency and the intensity of the graphene plasmons additional simulations are performed as a function of chemical potential and scattering time. Additional simulations of the dependence of the reflectance spectra on polarisation angle and rod diameter showed that plasmon modes shift to higher resonance frequencies for a smaller rod diameter but are essentially independent of linear polarisation angle.

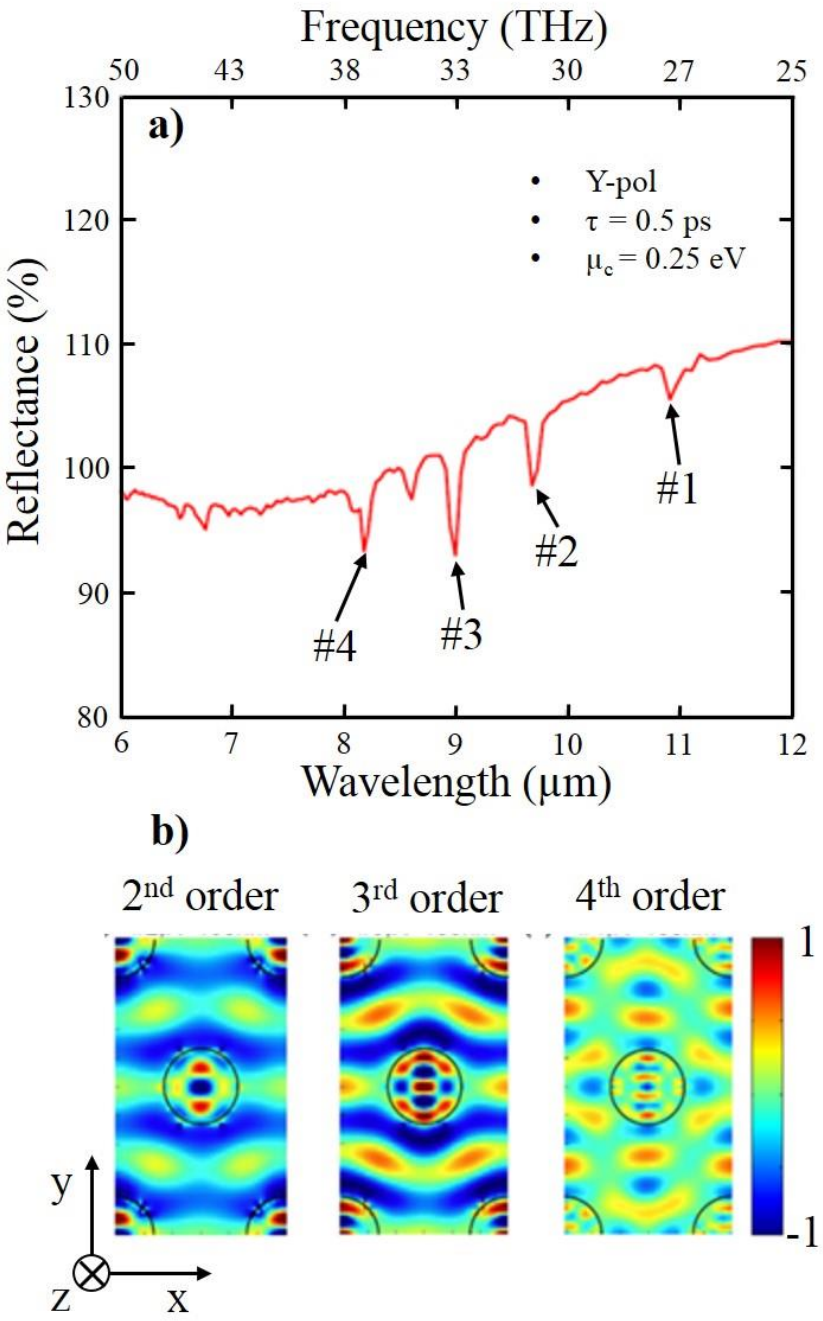

Figure 7.2 a) Normalised reflectance as a function of wavelength for SLG on top of UC_1. b) Normalised *Ey* field profiles from the 2nd order, 3rd order and 4th order resonance modes with the black circles representing the NRs

Undoped, pristine graphene has a chemical potential, μ_c, of zero at the Dirac point. The chemical potential depends on the carrier density [186] and as the carrier density increases, either chemically induced by dopants or electrically induced by

a back gate, the chemical potential increases. The plasmon frequency increases with the number of charge carries, scaling by approximately $n^{1/4}$ [187]. The chemical potential, μ_c, of chemical vapour deposition (CVD) single-layer graphene transferred onto a SiO_2/Si substrate has been shown to range from approximately 0.02 eV for lightly doped graphene, to 0.25 eV for highly doped graphene [188]. Figure 7.3 displays the calculated normalised reflectance spectra for a linearly polarised, along the y-axis, infrared wave, from UC1, for various values (0.2 eV, 0.25 eV and 0.3 eV) of the graphene chemical potential μ_c. For each spectrum the scattering time, τ, is set to 4.0 ps and the normalisation is performed by dividing the calculated spectra from SLG on top of the NR substrate by the spectra from the bare NR substrate. The large reflectance minima in the spectra can be attributed to the 2nd, 3rd and 4th order plasmon modes, with the order determined as discussed previously. As the chemical potential decreases from 0.3 eV to 0.2 eV, the resonance frequency and intensity of each of the resonance modes decrease. At μ_c = 0.2 eV the reflectance minima are no longer observed, due to increasing plasmon attenuation at lower chemical potentials. This suggests that an estimation of the amount of doping present in the highly doped SLG transferred on to GaN NRs can be made by comparing the measured reflectance spectra to the simulated spectra.

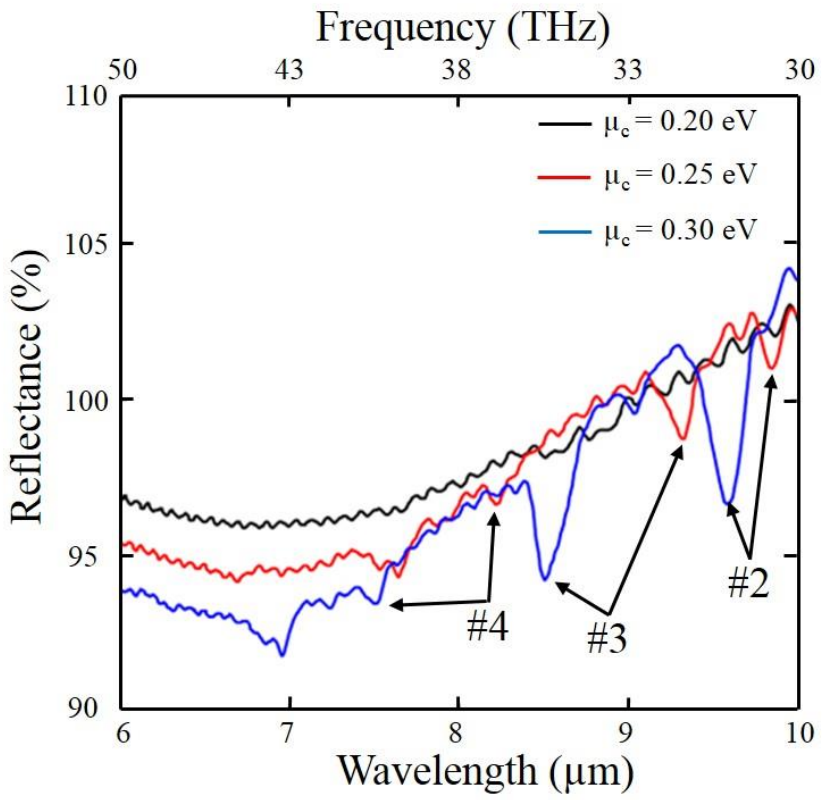

Figure 7.3 Simulated normalised reflectance spectrum for SLG on 600 nm pitch GaN NR substrate with an infinite thickness of Si and the graphene chemical potential set to 0.2 eV (black line), 0.25 eV (red line), 0.3 eV (blue line).

A second study performed with the FDTD simulations is the effect of the scattering time on the normalised reflectance spectra. For this, the spectra are calculated for three different values of the SLG scattering time (50 fs, 100 fs and 500 fs). The chemical potential of the graphene was set to a constant 0.25 eV while the incident wave was again linearly polarised along the y-axis for each of the three spectral calculations. The normalised reflectance from SLG with τ = 50 fs, τ = 100 fs and τ = 500 fs is presented in Figure 7.4. As the scattering time decreases from 500 fs to 50 fs the intensity of the plasmon resonance modes decreases while the resonance frequency increases slightly. At τ = 50 fs the reflectance minima corresponding to the plasmon resonances are no longer observed, due to the large plasmon attenuation at low scattering times . The

scattering time of CVD graphene has previously been measured through IR microscopy [189] and transport measurements [190] as ~50 fs for supported graphene. As the number of chemical adsorbates increases, due to the standard wet transfer process, the scattering time decreases slightly [189]. This, along with the dependence of the reflectance spectra on the chemical potential, suggests that dips in the measured reflectance due to the excitation of the graphene plasmons will only be observed in SLG on NR devices with a high amount of doping (μ_c > 0.2 eV) and higher mobility than is typically obtained for supported graphene samples (τ > 50 fs). This indicates there is a possibility to use the excitation of the plasmons as a method to characterise the quality of the graphene transfer. If dips are present in the measured reflectance spectra, that correspond to those observed in the FDTD simulations, it is suggests the quality of the graphene transfer is better than what is typically observed for CVD graphene transferred to flat substrates. If no dips can be attributed to the graphene plasmon modes, the chemical potential and scattering time are likely similar to CVD graphene on flat substrates.

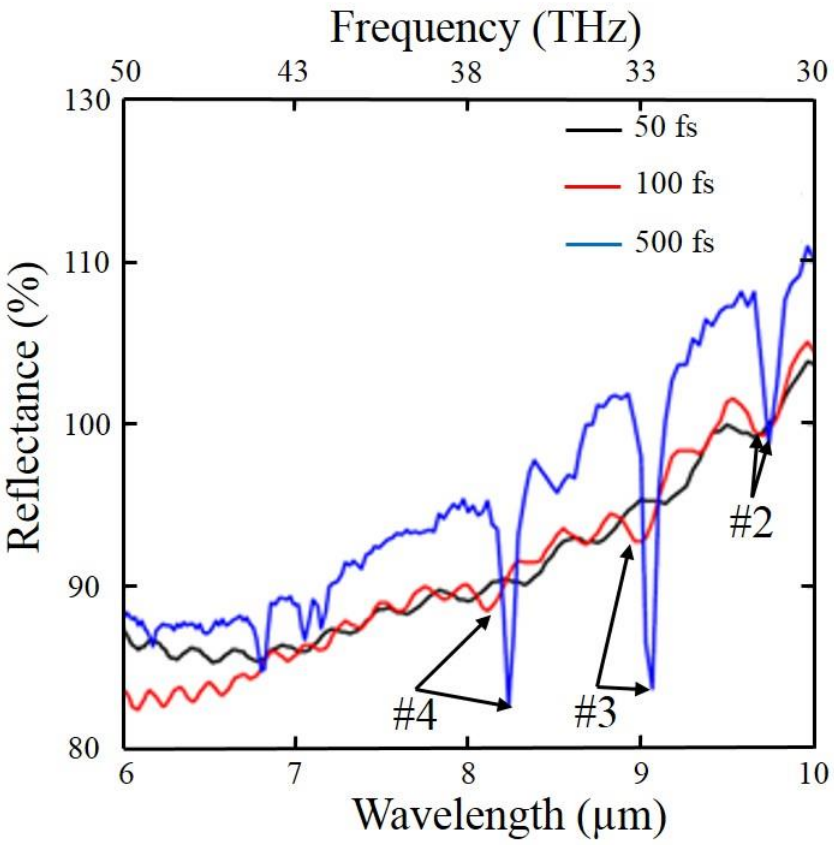

Figure 7.4 Normalised reflectance spectrum for graphene scattering times set to τ = 50 ps (black line), τ = 100 ps (red line) and τ = 500 ps (blue line).

7.3 Graphene/GaN NR Fabrication Process

7.3.1 Samples Used

Gallium nitride nano-rod arrays, with the same hexagonal design but different unit cell dimensions, were fabricated by a collaborator, Dr. Pierre-Marie Coulon at the University of Bath, and utilised as substrates for the experimental investigation into the effect of patterned substrates on graphene based emitters. All of the hexagonal NR arrays provided consist of GaN/AlN/Si NRs on a 500 μm Si substrate but they can be divided into two different arrays, NR_600 and

NR_2000, based on their respective unit cell dimensions. For NR_2000, the pitch of the nano-rods is 2.0 µm while the total height, h_t, of the nano-rods is ~1.94 µm, which is made up of ~1.60 µm of GaN (h_1), ~240 nm of AlN (h_2) and ~100 nm of Si (h_3). The diameter at the top of the rods is ~0.55 µm (D_T) and the diameter at the bottom of the nano-rods is ~0.64 µm (D_B). This difference in diameter at the top compared to the bottom is due to the top down fabrication process employed in the fabrication of the nano-rods. Figure 7.5(a) displays a cross-section scanning electron micrograph (SEMG), while Figure 7.5(b) shows a top down SEMG, of a typical NR_2000 substrate. The details for the NR_600 substrates are as follows: p = 0.6 µm, h_T ~1.99 µm, h_1 ~1.65 µm, h_2 ~240 nm and h_3 ~100 nm, D_T ~0.24 µm and D_B ~0.28 µm. A cross-section SEMG and a top-down SEMG, of a typical NR_600 substrate, are displayed in Figure7.5(c) and Figure 7.5(d) respectively.

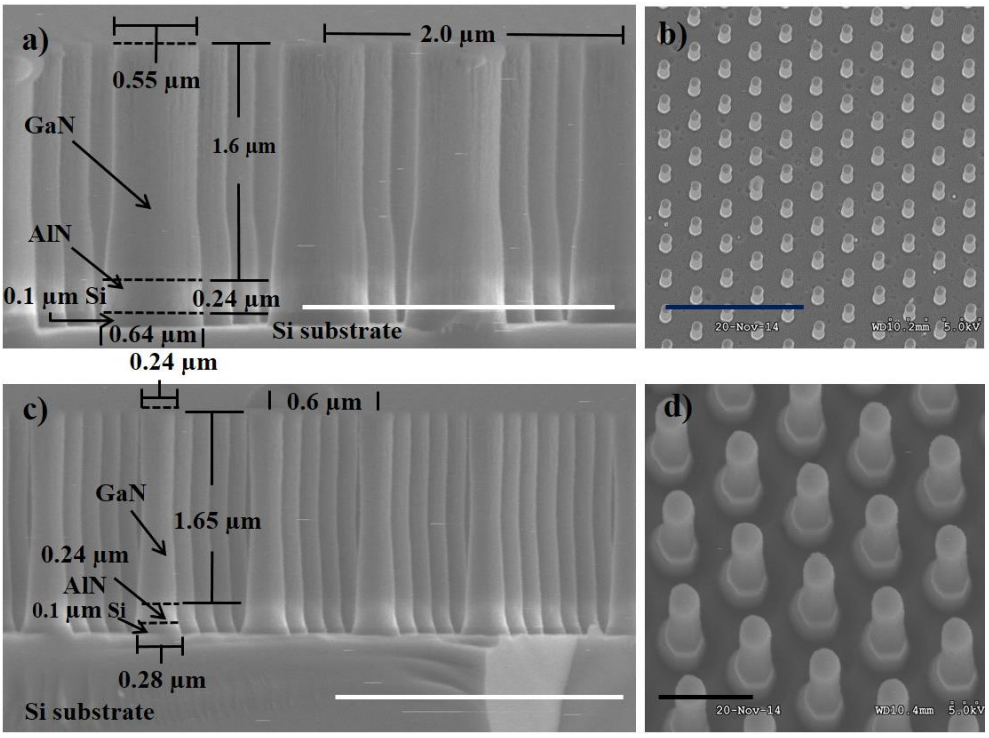

Figure 7.5 SEMG of the cross section and top down perspective for the a,b) 2000 nm pitch sample and c,d) 600 nm pitch samples. Scale bars are as follows: black = 1 µm, white = 2 µm and blue = 10 µm.

7.3.2 Standard Transfer Process

Using the standard polymethyl methacrylate (PMMA) assisted transfer technique described in section 3.3.1, to transfer CVD graphene on top of the GaN NR arrays resulted in samples with poor graphene coverage. Figure 7.6 shows a SEMG taken after using the standard transfer technique to transfer SLG on top of a NR_600 substrate. The thin dark regions are areas of graphene on top of NRs, the light grey regions, which make up the majority of the image, are regions of nano-rods with no graphene on top and the lightest areas are NRs that have been broken, by scratching the surface with tweezers or through general handling. This is an example of a particularly poor quality transfer illustrated by the low graphene

coverage. A possible explanation for this is the poor adhesion between GaN and graphene, discussed in more detail in section 3.4.1.

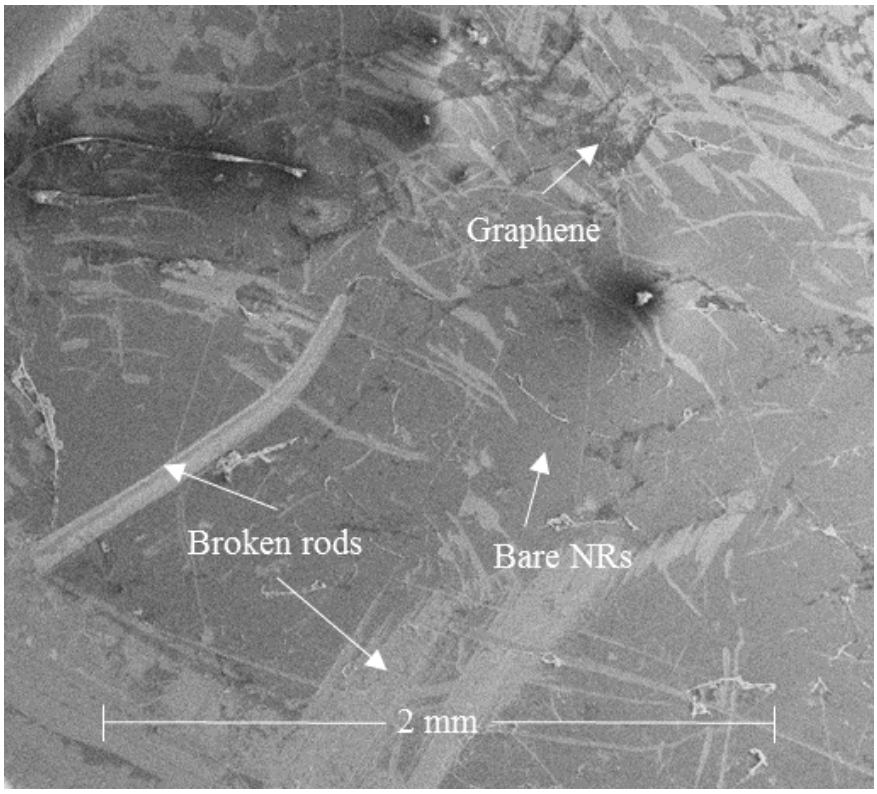

Figure 7.6 Scanning electron micrograph taken after transfer of SLG to a NR_600 substrate.

7.3.3 Modified Transfer Process

A modified wet transfer process, detailed in section 3.4.1, was developed in order to facilitate better graphene coverage on the GaN NR arrays. The key factors of the alternative transfer technique are: the implementation of a 30 minute post bake, prior to the removal of the PMMA support, and the utilisation of the critical point drier (CPD) to dry the sample, instead of blowing dry with nitrogen gas, after PMMA removal. The alternative method, however, did not always lead to satisfactory graphene coverage, though it was consistently better than the

coverage typically achieved with the standard process. One of the biggest issues with this technique was the inconsistency of the CPD. The majority of the time the CPD failed to reach the critical point, for which the only solution was to finish the process anyway. This often resulted in poor coverage of the graphene, similar to what is shown in Figure 7.6. When the critical point drying process was successfully completed, i.e. the critical point was reached, the amount of graphene left suspended on the nano-rods was typically much larger. SEMGs of SLG transferred onto a NR_600 array (GNR_600) using the modified wet transfer process are displayed in Figure 7.7(a,b). There were no issues with the CPD reaching the critical point for this transfer. Figure 7.7(a) shows ~0.25 mm^2 region with graphene successfully suspended over approximately 75% of the area, determined using the image processing programme ImageJ. The graphene coverage is clearly greater than the amount of graphene present in Figure 7.6 though less than the near complete coverage achieved by CVD transfer onto flat substrates [191]. Figure 7.7(b) displays an SEMG taken at a 52° angle from a boundary of graphene and no graphene. It is clear from this image that the graphene is suspended on top of the NRs. The bright white lines in the centre of the image are most likely from wrinkled up graphene are the result of the edge effect discussed in section 3.2.3. The coverage achieved from this transfer is typical for graphene transferred onto a NR_600 substrate following the modified wet transfer procedure with the CPD successfully reaching the critical point. Attempts were made to further improve the transfer process including: longer/short post bake times at higher/lower temperatures, thicker PMMA support layer (up to 2 µm thick), changing the cleaning procedure for the substrate, switching to a dry transfer technique (using transfer tape) and changing the method for how the substrate is initially brought into contact with the

graphene/PMMA layer. None of the aforementioned changes made any discernible impact to the graphene coverage. A possible explanation for not achieving better coverage is the relatively large aspect ratio, ~2.5, of suspended area (area where graphene is not supported by the nano-rods) to the supported area (area where graphene sits on top of the rods).

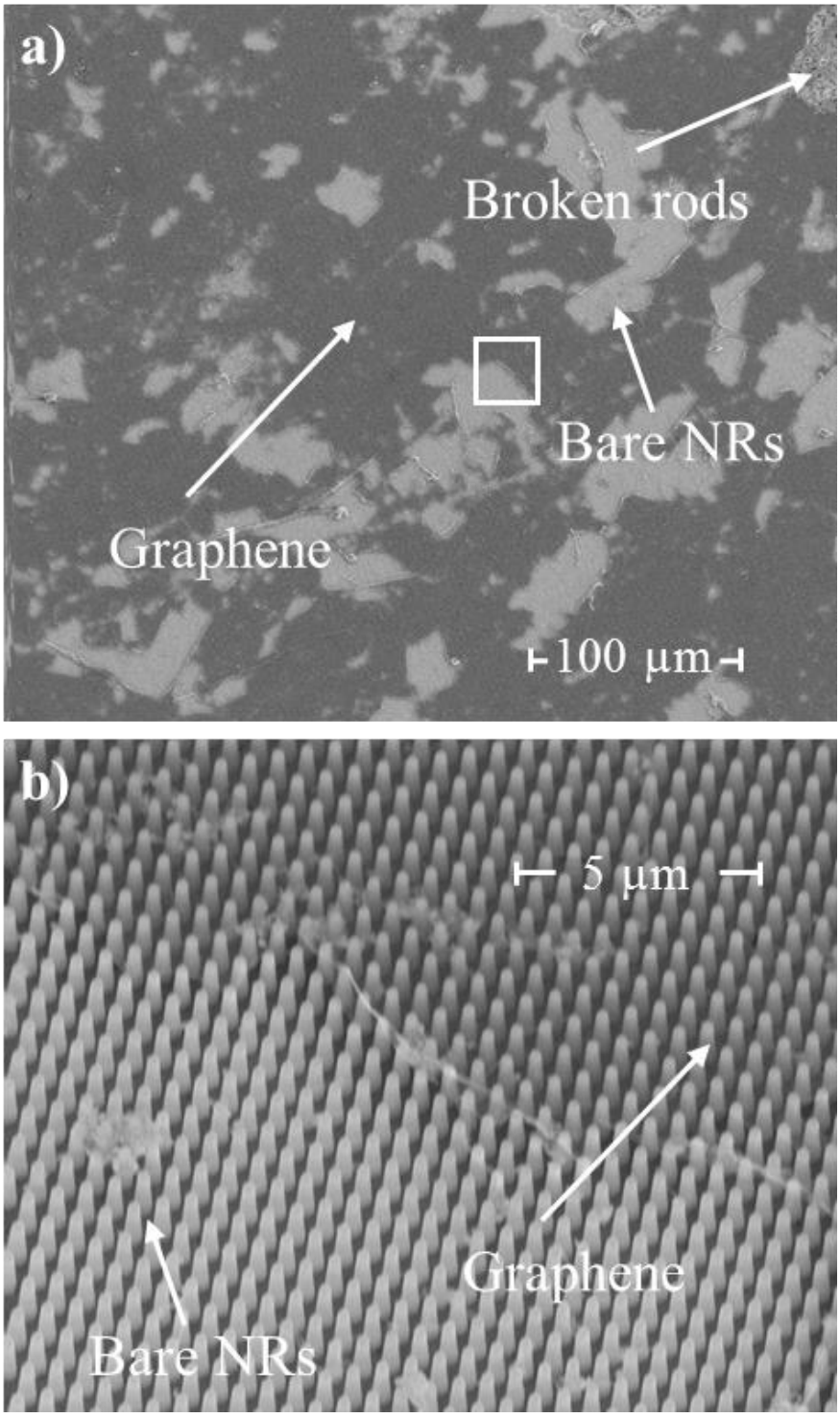

Figure 7.7 Scanning electron micrographs after the transfer of SLG to a NR_600 substrate at a) 650X magnification b) 3500X magnification from within the white square in (a) and at a 52° incident angle.

Raman spectroscopy, discussed in more detail in section 3.2.1, was performed on the sample pictured in Figure 7.7 in order to characterise the dark grey

regions, the areas believed to be suspended graphene, observed in the SEMG. Figure 7.8 shows a typical Raman spectrum, using a 532 nm green laser, taken from one of these regions, with clear peaks at 1578 cm^{-1} and 2693 cm^{-1} that correspond to the G and 2D bands respectively. As discussed in section 3.2.1, the presence of these peaks are a clear indication of graphene, while the D and D' peaks observed at 1346 and 1620 cm^{-1} are the disorder peaks, providing an indication of the amount of defects present. The 2D/G peak ratio of ~1 may indicate the presence of more than one layer of graphene in the area this spectrum was obtained from, but the symmetric nature of the 2D peak suggests it is likely to be single-layer graphene. The ratio was variable across the surface of the sample, with the lowest ratio observed in spectra taken from the wrinkled regions (brightest area in the middle of Figure 7.7(b)).

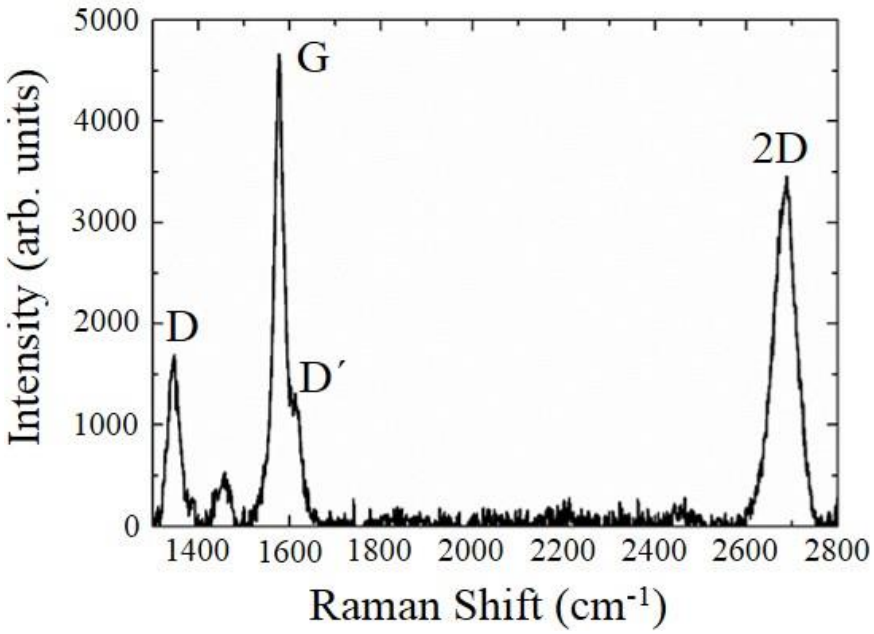

Figure 7.8 Raman spectrum of GNR_600.

As opposed of the transfer of graphene to NR_600, the transfer of graphene to NR_2000 was not significantly improved by the modified transfer technique. The graphene films transferred onto NR_2000 substrates were consistently

discontinuous, with a large amount of wrinkles and tears present in the regions where the graphene was successfully transferred on top of the nano-rods, and an overall coverage that was no greater than ~25%. Figure 7.9(a) shows a SEMG taken after the transfer of single-layer graphene to NR_2000, sample GNR_2000. It is clear that the coverage of graphene is significantly less when compared to GNR_600. The aspect ratio of suspended to supported graphene for GNR_2000 is ~17:1 or approximately 2X larger than the aspect ratio of GNR_600. This possibly explains the difference observed in the amount of graphene coverage. Figure 7.9(b) displays the Raman spectroscopy taken from the darker grey region in the middle of 7.9(a). The peaks are again indicative of graphene, with a 2D/G intensity ratio slightly greater than 1. Again, this is less than expected for SLG but the symmetric nature of the 2D peak suggests it is single-layer. It can be concluded that it is possible to transfer the graphene on top of these NR arrays, with varying degrees of success. Additionally, it is possible that by further modifying the transfer procedure or by reducing the suspended to supported ratio that the quality of the graphene transfer can be further improved.

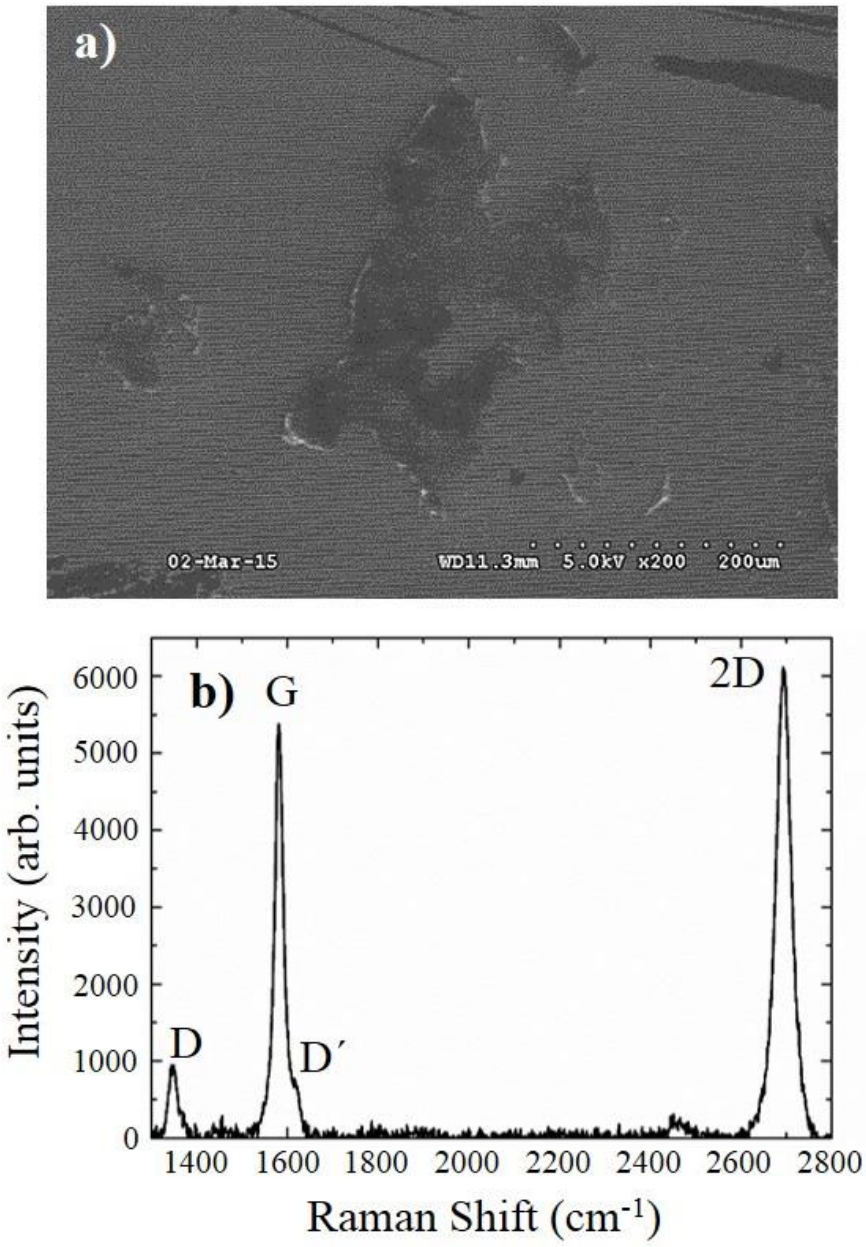

Figure 7.9 (a) SEM image of GNR_2000. (b) Raman spectra of GNR_2000

In contrast to the devices presented in Chapters 5 and 6, after the successful transfer of graphene to the NR substrates, further processing was not undertaken in order to fabricate graphene based emitters. The emitting areas were not defined and gold (Au)/chromium (Cr) contacts were not deposited. Neither of the arrays were designed with the intention of being fabricating into graphene based emitters. As both substrates are entirely composed of NRs, with no plateaus for contact deposition and bonding, it is possible that further processing would have

broken the NRs or damaged the graphene. Therefore, it was determined that optical characterisation of these samples would be performed without contacts. Without the deposition of contacts, it was not possible to apply a drive current and measure the emission, as was done for the other devices presented in this work. In the future, it is possible the arrays could be redesigned, with plateaus for contacts, if the reflectance measurements show promising results.

7.4 Optical Characterisation

To optically characterise GNR_600 and GNR_2000 FTIR spectroscopy was used in order to determine the effect of the nano-rod substrates and the graphene layer on the obtained spectra, in addition to whether the graphene plasmon can be excited and observed in the spectral response. Angled rapid scan FTIR reflectance measurements (described in more detail in section 4.5.2) were performed under atmospheric conditions for both samples, in addition to the bare NR arrays (NR_600 and NR_2000) and an Au mirror for comparison and normalisation.

7.4.1 Nano-rod Characterisation

The raw reflectance spectra of both devices and an Au mirror are plotted in Figure 7.10(a), while the reflectance spectra normalised to the Au mirror are plotted in Figure 7.10(b,c). The normalised spectra were obtained by dividing the raw spectra from the NR samples by the Au mirror spectrum. In the raw spectra, there is a clear CO_2 absorption band at 4.3 μm in all of the spectra, along with

noticeable dips in the spectra due to water absorption between 5-8 µm. The overall shape of the normalised spectra is sinusoidal, possibly due to the subwavelength size of the unit cell parameters. Therefore, the subwavelength structure acts as a homogenous thin film with an effective refractive index, $n_{eff,}$ leading to an interference effect that results from the optical path difference.

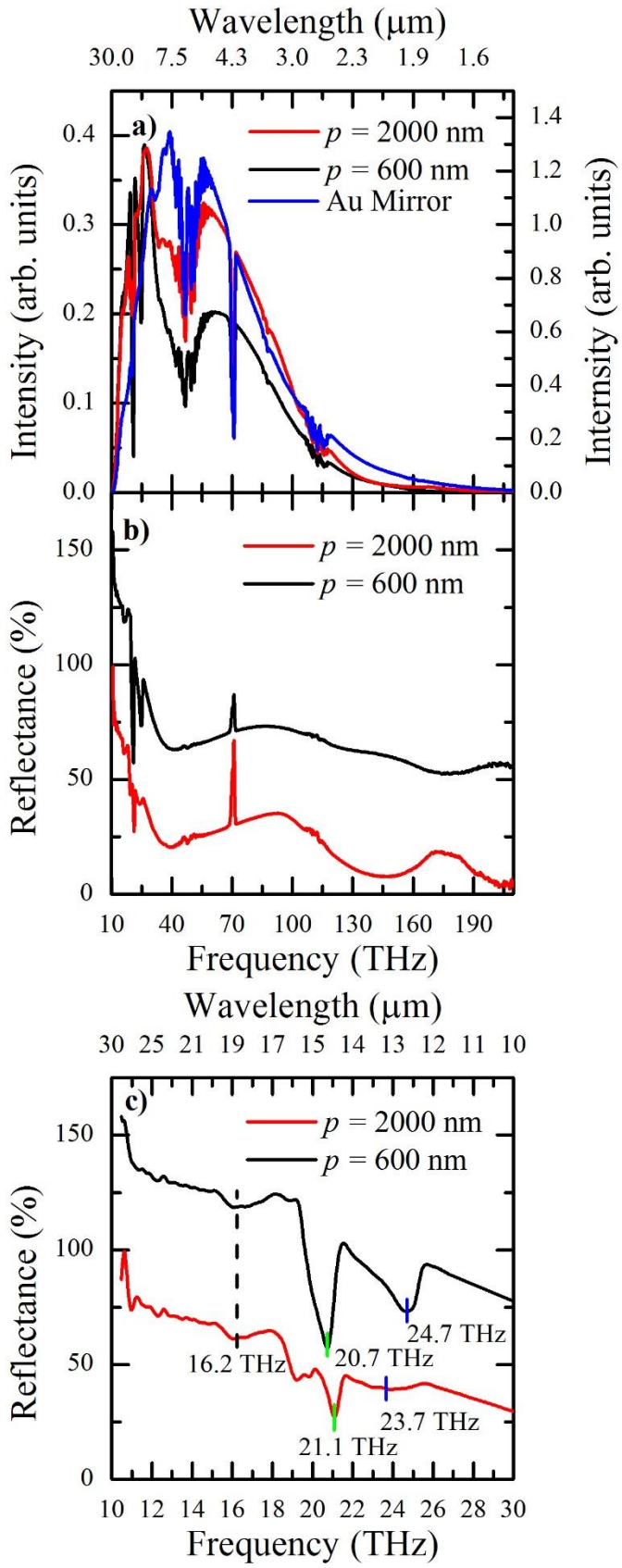

Figure 7.10 Measured a) raw reflectance spectra and b,c) normalised reflectance spectra from an Au mirror (blue line), *p* = 600 nm sample (black lines) and *p* = 2000 nm sample (red lines), black line is offset linearly in the y-direction by 50%.

A large increase can be observed in the reflectance at low frequencies due the Reststrahlen effect, with the Reststrahlen band of GaN occurring between ~12-26 THz [192]. However, as can be observed in Figure 7.10(c), there are large dips within the Reststrahlen band for both the p = 600 nm and p = 2000 nm samples. The dip marked by the black dashed line occurs at the same frequency,16.2 THz, for both samples and can be attributed to the excitation of the TO optical phonon mode of a GaN [193]. The other two dips within the Reststrahlen band, marked by green and blue lines can, possibly correspond to localised surface phonon polariton (SPhP) resonant modes. Caldwell *et al.* have demonstrated the use of silicon carbide (SiC) NRs, with similar unit cell parameters to the GaN NRs, for low-loss, sub-diffraction phonon confinement [194]. Measurements and simulations of SiC NRs showed the excitation of two SPhP resonant modes within the Reststrahlen band of SiC. These were attributed to a higher energy transverse dipole mode, and a lower energy monopole mode. The transverse dipole mode was shown to depend mostly on the NR diameter, with the resonance frequency of the transverse dipole mode shown to shift to higher frequencies as the diameter of the NRs increased. Alternatively, the monopole mode was observed to depend on both NR diameter and pitch, as well as the incident angle of the IR beam. The intensity of the monopole mode was shown to increase and the resonance frequency decrease with increasing diameter. The dependence of the monopole mode on pitch of the NRs was suggested to be the result of interpillar coupling. Additionally, the simulations showed that the monopole resonance mode will be sharper and deeper than the dipole mode.

From examining the peaks marked by the green and blue lines in Figure 7.10(c), it can be observed that the lower frequency peaks (green line) from both samples

are in fact sharper and more intense than the higher frequency peaks (blue lines). As the rod diameter of the GaN NRs is increased from 240 nm to 550 nm and the pitch from 600 nm to 2000 nm, the resonance frequency of the lower frequency mode increases from 20.7 THz to 21.1 THz, and the intensity decreases. This matches what was observed for the monopole resonance mode in the SiC NRs. The decrease in intensity is likely to be caused by a decrease in the coupling between the NRs [195]. Alternatively, the higher frequency mode shifts to lower frequencies as the pitch and rod diameter increase. This is also consistent with what was seen for the higher frequency transverse dipole mode of the SiC NRs. The intensity of this dip is also observed to decrease with increasing *p* and *d.* A possible explanation for this is the larger NR fill factor of the *p* = *600* nm sample. The similarity between these measurement results and what was observed by Caldwell *et al.* in SiC NRs suggests that these dips in the reflectance spectra are the result of localised SPhP resonances, with the higher frequency peak corresponding to a transverse dipole mode and lower frequency peak to a monopole mode. Further investigation is needed, including simulations and measurements such as Raman spectroscopy, in order to confirm that this is the case.

7.4.2 Modification by Graphene

The raw reflectance spectra of *p* = 600 nm and *p* = 2000 nm samples, both with and without graphene on top, are plotted in Figure 7.11(a,b). The important difference between the spectral responses of the samples with graphene on top, compared to their corresponding bare NR substrates, is that a lower measured

intensity across the entire spectral range is observed for the samples with graphene. This is to be expected as the graphene acts as an absorption layer that is wavelength independent [196], with the incident beam twice passing the graphene layer before being measured by the detector. The total integrated intensity of the spectra from the p = 600 nm sample with graphene is ~13% smaller than the integrated intensity from the bare 600 nm pitch substrate. This value is slightly larger than expected, given a theoretical single-layer graphene absorption of ~2.3% [44,45]. This is also the case when comparing the reflectance spectra from the p = 2000 nm samples, plotted in Figure 7.11(b). Compared to the p = 600 nm samples, the difference in measured intensity over the entire spectral range, caused by graphene absorption, is noticeably smaller, with just a 3.8% difference in the integrated intensity. This is slightly smaller than would be expected and can possibly be explained by the lower graphene coverage for the p = 2000 nm sample in comparison to the p = 600 nm sample. This suggests that the presence of graphene on top of patterned substrates can be confirmed by measuring the reflectance spectrum for patterned substrates with and without graphene on top.

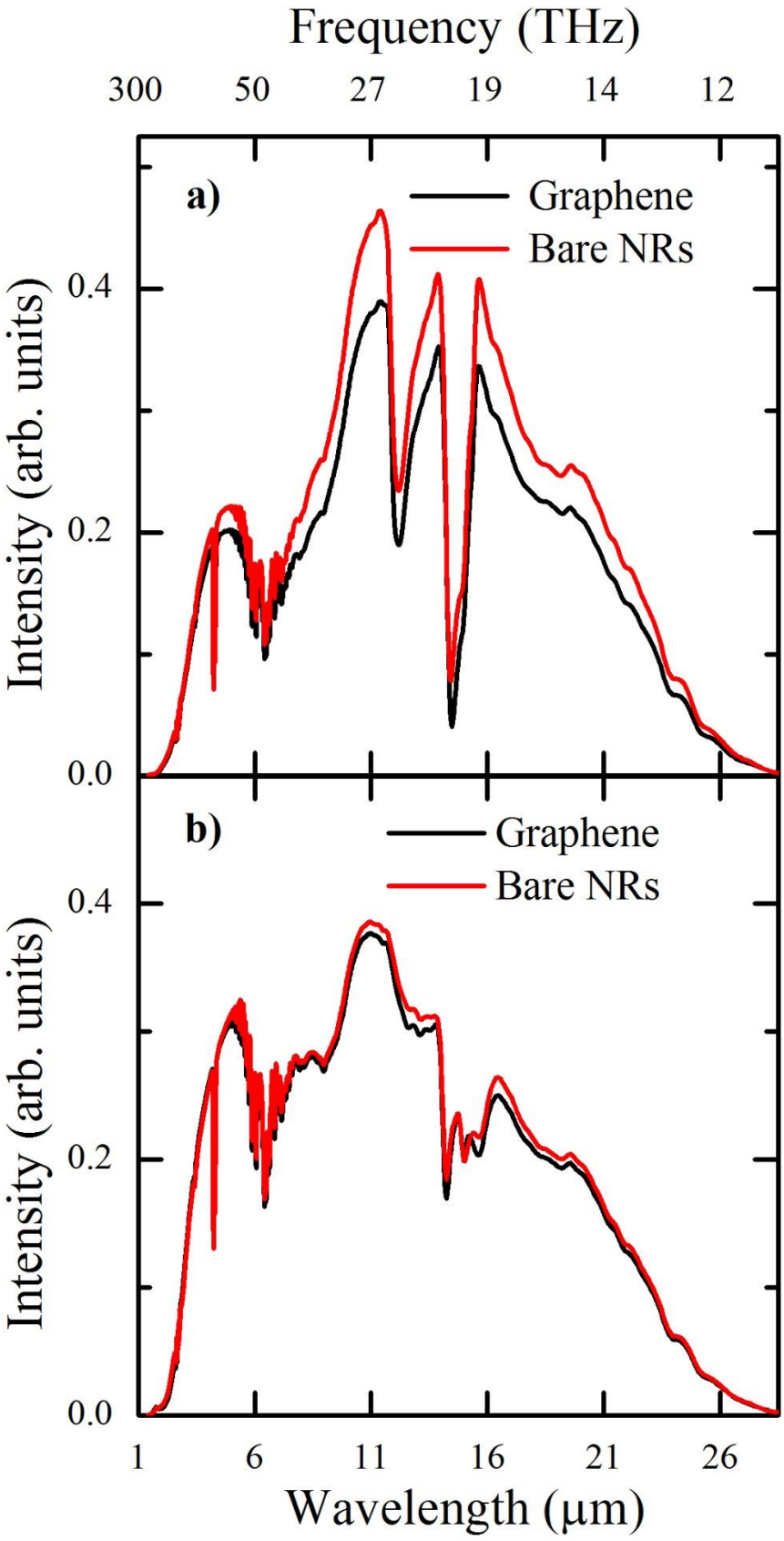

Figure 7.11 Measured raw reflectance spectra from NRs with (blacks lines) and without (red lines) graphene on top with a) p = 600 nm and b) p = 2000 nm.

To determine if the plasmon modes were excited as a result of the incident beam, the raw reflectance spectra were normalised by dividing the spectra from the samples with graphene by the spectra from the bare NR substrates, as was carried out for the FDTD results. This corrects for the detector response, atmospheric absorption and the spectral response of the underlying substrates. The resulting spectra are, therefore, the spectral response of the graphene on top of NRs. The normalised spectra is plotted in Figure 7.12 for GNR_600/NR_600 and GNR_2000/NR_2000. Both of the normalised spectra are largely flat over the plotted wavelength range, with the exception of Fano resonance observed at ~12 μm and ~14 μm in the normalised spectra for the *p* = 600 nm sample and ~14 μm for the *p* = 2000 nm sample. These Fano resonances are the result of a shift in wavelength of the resonance modes observed in the Reststrahlen band of the raw reflectance spectra. Graphene has previously been observed to cause a shift in the resonance frequency of Si photonic crystals, due to graphene's role as an absorbing layer on the Si photonic crystal samples [197–199]. Additionally, there are no dips in either of the normalised spectra that would indicate the excitation of the graphene plasmon. As discussed in section 7.2, reflectance minima corresponding to the excitation of plasmon modes were predicted to occur between 6-12 μm for UC_1, with unit cell parameters that match both NR_600 and GNR_600. However, no plasmon modes were observed in the simulated spectrum from UC_2, with unit cell parameters that match both NR_2000 and GNR_2000. As the excitation of the plasmon modes were only observed in simulations where scattering time and chemical potential of the graphene is set to higher values than what is typically measured in CVD graphene transferred to SiO_2/Si substrates, this is not unexpected and suggests electronic properties of

the graphene transferred onto the GaN substrates are similar to CVD graphene on more conventional substrates.

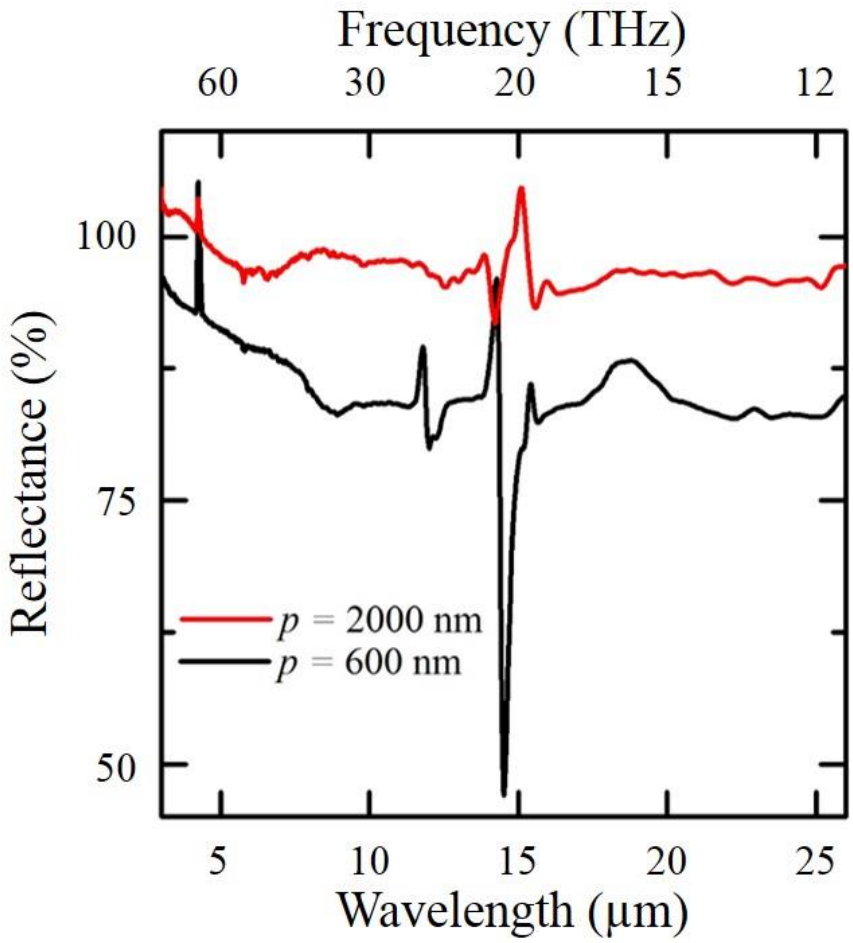

Figure 7.12 Normalised reflectance from graphene on a *p* = 600 nm substrate (red line) and a *p* = 2000 nm substrate (black line)

7.5 Summary

To summarise, FDTD simulations performed by Mr. Bofeng Zhu suggest the possibility of exciting the graphene plasmon in single-layer graphene suspended on GaN NR array devices. Comparing the measured reflectance spectra of the graphene to the simulated results could be a method of characterising the

graphene, as both the frequency and intensity of the dips in the simulated reflectance spectrum, which correspond to the excitation of graphene plasmon modes, show a dependence on graphene properties. Transferring graphene to the NR substrates using the standard transfer procedure resulted in extremely poor coverage of graphene on top. A modified wet transfer process utilising a critical point drier was implemented to improve the coverage. This resulted in a significant improvement to the graphene coverage for graphene transferred to *p* = 600 nm substrates and to a lesser degree the *p* = 2000 nm substrates. The reflectance spectra from NR substrates (both *p* = 600 nm and 2000 nm) with graphene on top was obtained using FTIR spectroscopy. Two dips in the reflectance spectra of the NR array were observed and attributed to localised surface photon polariton resonance modes, which can be described as transverse dipolar and monopolar. Additionally, it was concluded that the presence of graphene on top of the NRs can be determined by comparing the raw reflectance spectra for samples with and without graphene on top. Finally, normalised reflectance of the graphene was calculated by dividing the spectra from the bare NRs on the graphene devices. No dips were observed in the normalised spectra that would suggest excitation of the graphene plasmon. This suggests the properties of the CVD graphene are similar to that of CVD graphene transferred to more conventional substrates, such as SiO_2/Si. The results in this Chapter demonstrate that it is possible to transfer graphene to patterned substrates that contain features with an extreme aspect ratio. Ultimately, NR substrates could be used to improve the performance of graphene based infrared emitters by controlling both the spectral and thermal properties.

8 Conclusions and Future Work

The work presented in this thesis focuses on the development of graphene based devices as a new type of infrared (IR) emitter, to provide an alternative to the emitters that are currently on the market, for gas sensing applications. The three main types, incandescent micro-bulbs, incandescent thin membranes based on microelectromechanical systems (MEMS) and semiconductor LEDs all have significant disadvantages. There is, therefore, a continuing need for the development of a new type of emitter that is low cost, fast, efficient and robust. Although there has been some recent interest in the use of graphene based incandescent emitters that emit in the visible spectrum, to date relatively little work has been aimed at developing graphene based emitters that emit in the IR, with the infrared thermal emission primarily being employed in single-layer exfoliated devices to probe their electronic structure. This work addresses the suitability of graphene based emitters as next generation IR emitters. The graphene emitters were all fabricated in a cleanroom environment using standard electron beam lithography techniques. Spectral characterisation measurements of the devices were performed by both a Jobin-Yvon iHR550 grating spectrometer and a Bruker Fourier transform infrared spectrometer, with a Keithley source meter used for the application of a pulsed drive current. Additionally, spatial characterisation measurements were performed using an IR microscopy system with the devices mounted on a motorised xy-stage. A finite element software package, COMSOL, was utilised to model the graphene emitters and provide further insight into their operation. For the first time the operation of devices, composed of large area chemical vapour deposition (CVD) single layer graphene, under ambipolar conditions was demonstrated, while measurements and

simulations of the modulation characteristics of devices composed of single and few-layer graphene transferred onto SiO_2/Si provided insight into the high frequency operation of the devices and how the emission intensity at high frequencies can be improved through careful device design. Spectroscopy measurements of the devices demonstrated their broad spectrum, grey-body like emission. Spectral control of the broad emission spectra was demonstrated for devices containing few-layer graphene, encapsulated between two multilayer hexagonal boron nitride (h-BN) layers and integrated with metamaterial structures on the top h-BN layer. Finally, patterned substrates, specifically gallium nitride (GaN) nano-rods (NR), were investigated for the possibility of optically generating graphene plasmons, in addition to providing both spectral control of the emission, due to the periodicity of the NR arrays and improved high frequency operation.

The experimental results presented in this thesis are summarised in this chapter, along with suggestions for future investigations. Section 8.1 provides a summary of the spatially resolved thermal emission measurements for the single and few-layer graphene devices, in addition to conclusions of the modulation characteristic experiments. A summary of the investigation of spectral characteristics of the same single and few-layer graphene devices is presented in section 8.2. Conclusions from the experiments on encapsulated graphene devices integrated with metamaterial structures are also provided. Section 8.3 summarises the results for graphene on GaN NRs, including details of the modified transfer process implemented in the fabrication process of these devices. Finally, section 8.4 provides a brief discussion of the future work that could be undertaken on graphene IR emitters. The main conclusion from this work is that the thermal properties of the devices can be engineered, for example

to maximise the difference between the “on” and the “off” temperature by encapsulating the graphene in this way.

8.1 Thermal Control

The thermal emission from devices composed of either single or few-layer graphene on SiO_2/Si substrates was measured as a function of x and y position. A non-uniform thermal emission was observed for the single-layer devices, with a localised hot spot occurring a specific point along the graphene channel, due to resistance variation along the channel. The hotspot is located at the point of maximum resistance, the charge neutral point (CNP), due to the hot spots Joule heating nature. Measurements of the thermal emission at various back gate voltages (which modulates the carrier density) demonstrated the movement of the hotspot, and therefore the CNP, along the graphene channel, previously only observed in exfoliated devices. This demonstrates the operation of a large area CVD graphene device under ambipolar conditions and confirms that the emission for the single-layer CVD devices is qualitatively the same as much smaller, more pristine, exfoliated devices. Alternatively, a greater uniformity was observed in the emission map of the few-layer graphene device, suggesting a uniform channel resistance that is characteristic of a long semi-metal filaments. Good agreement was observed between the measured results and the simulation of the thermal emission of a 2D, five layer thick graphite device in COMSOL, suggesting that few-layer devices can be thought of as semi-metal filaments. Measurements and simulations of the emission intensity as a function of drive frequency (1-100 kHz) were also performed for these devices, in addition to a

device containing few-layer graphene, encapsulated in multilayer h-BN on a SiO_2/Si substrate. Comparing the single-layer device to the few-layer device, the emission intensity was approximately 1.5X larger for frequencies greater than 20 kHz, while a measureable emission was obtained across all drive frequencies for both devices. This was consistent with simulations performed in COMSOL for two different thin graphite thicknesses. A possible explanation for this is the lower thermal mass of the single-layer graphene. Additionally, COMSOL simulations suggest that the modulation speed of the graphene devices can be improved by increasing the thermal resistance between the graphene and the underlying substrate. An increase in the measured emission intensity at high frequencies was observed for the encapsulated few-layer graphene device compared to the un-encapsulated few-layer device, suggesting that encapsulating graphene in h-BN increases the thermal resistance.

8.2 Spectral Control

In addition to characterising the SiO_2/Si devices spatially, spectral characterisation measurements were also performed by measuring the emission intensity as a function of frequency with a grating spectrometer. The devices were determined to be grey-body emitters with emissivity values of 2%, for the single-layer device, and 6% for the few-layer device, by comparing the raw emission spectra to the measured emission spectrum from a 673 K blackbody source. Comparing the calculated spectra to the corrected spectra, the on/off surface temperature of the graphene was estimated as 620/480 K for the few-layer and 600/350 K for the single layer, similar values to what is seen in COMSOL.

FTIR spectroscopy measurements were utilised to characterise devices that contained few-layer graphene, encapsulated in h-BN, with metamaterial structures on top. The metamaterial structures included split ring resonators (SRR) and ring resonators (RR). COMSOL simulations were used to design six different RR unit cells and three SRR unit cells, with transmittance peaks between 60-120 THz. Transmittance simulations show an electro-magnetically induced transmittance (EIT) like spectral response, with a narrow transmittance peak that shifts to lower frequencies as ring radius and pitch of both the SRR and RR increases. Qualitative agreement with the simulations was observed in the measured reflectance spectra from six encapsulated graphene devices, each with a different RR unit cell arrayed on top. The same “M” shaped reflectance response from the COMSOL simulations was observed in the measurements of each of the six devices. Additionally, the Fano resonance frequency was shown to shift from higher to lower frequencies with increasing ring radius and pitch. Measurements of the emission spectra from four of the six devices also showed good qualitative agreement with the simulations. The same “W” shaped emission response was observed in both the transmittance simulations and the emission measurements. The shift in the Fano resonance to lower frequencies was also observed in the emission measurements as ring radius and pitch increased. While there was not good agreement between the simulations and the measurements on the specific frequency of the Fano resonances, there was a negligible difference (<1%) between the Fano resonance frequency of the reflectance measurements and the emission measurements. Initial results on SRR devices showed better quantitative agreement between the simulations and the measurements, however, more work is needed on this device. The key point

of this work is the demonstration of the predictable control of the graphene devices emission spectra.

8.3 Patterned Substrates

Two devices containing single-layer graphene suspended on GaN NR arrays, with different structural parameters, were fabricated with the intention to study both the thermal management properties and the spectral impact of patterned substrates. Additionally, FDTD simulations suggested that suspending single-layer graphene on the NR arrays may allow for the generation of graphene plasmons, observable as dips in in the spectral response of graphene. This could potentially be utilised to characterise properties of the graphene present, such as doping level and scattering time. A scanning electron microscope was used to determine if the graphene was successfully transferred on top of the NR arrays. Scanning electron micrographs (SEMG), taken after the transfer of graphene to the NR arrays using the standard wet transfer process, showed that there was a poor coverage of graphene suspended on the NRs. In order to improve the graphene coverage, the standard wet transfer process was modified to include additional steps, such as a 30 minute post bake and critical point drying. SEMGs of devices fabricated with the modified transfer process showed significantly better graphene coverage, particularly for the graphene transferred to the p = 600 nm substrate, possibly due to larger NR fill factor. The samples were optically characterised using FTIR reflectance measurements, in order to determine the impact of the NR substrates and graphene on the device's spectral response. This was performed by normalising the raw measured reflectance spectra to that

of a gold (Au) mirror and bare NR substrates respectively. From observing the spectra normalised to the Au mirror, it is evident that the NR substrates have a significant impact on the spectral response. The overall shape of the NR reflectance spectra was sinusoidal, a result of the interference brought on by the optical path difference. Within the high reflectance region, the Reststrahlen band, dips in the normalised spectra were observed. These are attributed to the excitation of localised surface phonon polaritons. After obtaining the spectral resonance of the graphene individually, by normalising the raw reflectance from the samples to bare NR arrays, there were no dips in the reflectance that would indicate generation of graphene plasmons. This suggests that partially suspending the graphene on either of the NR arrays results in graphene that has similar doping level and scatter times as CVD graphene transferred onto flat, oxidised, silicon substrates. These results demonstrate that; it is possible to transfer graphene to patterned substrates containing high aspect ratio features, allowing for the control of the devices spectral and thermal properties; suspending the graphene on the patterned substrates does not result in significant changes to the electrical properties of the graphene and finally; the presence of graphene on top of the patterned substrates can be determined through measurements of the reflectance response of the patterned substrates with and without graphene on top.

8.4 Future Work

The potential for a mid-IR incandescent emitter based on graphene for gas sensing applications is demonstrated by the work presented in this thesis. One

of the significant advantages of these devices is their theoretical ability to operate under atmospheric conditions, with Barnard *et al* demonstrating this for h-BN encapsulated devices [181]. However, the emission results presented in this thesis were all taken from measurements that were obtained from devices that were driven under vacuum. It could be interesting to investigate the performance of the devices presented here under atmospheric conditions, including how reliable they are and what the average life time is compared to devices operated under vacuum.

Furthermore, more work is required on characterising the impact of patterned substrates on the graphene based emitters. Emission measurements could not be performed on these samples, as the current design of the NR emitters prevented the fabrication of contacts on the graphene. Therefore, to characterise emission from these samples the NR arrays need to be redesigned with flat regions for contact deposition and wire bonding. Additionally, if the NR arrays are being redesigned to facilitate contacting and bonding, the ratio of suspended to supported graphene could also be reduced in order to facilitate better graphene coverage. Xu *et al.* have previously demonstrated coverage of graphene on GaN NRs, with an approximate suspended to supported ratio of 2:1, that is comparable to what has been observed for graphene transferred to flat unpatterned substrates [200]. Alternatively, the NR could be grown on top of the graphene [201] to eliminate the transfer process entirely.

While the results from the ring resonators and split ring resonators show that it is possible to control the spectral response of the graphene devices using an integrated metamaterial structure, there is room for improvement in the Q-factor of the resonance peaks. Additionally, it would be a significant advantage for the

graphene emitters if their emission spectrum could be actively controlled. Numerical simulations performed by Ding *et al.* have demonstrated single and multiple transparency windows in graphene based metamaterial structures that are actively tuneable by varying the Fermi energy [202]. The metamaterial structure is based on a quadrupole slot to achieve the single transparency window, while multiple transparency windows are achieved for the dolmen-like slot structure. To fabricate graphene emitters based on this metamaterial structure, single-layer graphene could be transferred directly on top of the h-BN top layer of the encapsulated devices. The Fermi level of the graphene metamaterial structure could then be shifted by utilising an ion-gel top gate [203].

Finally, graphene has been shown to be a promising material for the realisation of a tuneable plasmonic photodetector [204]. To achieve this, graphene on SiO_2/Si was patterned into nano-ribbons and the hybrid plasmon-phonon modes were excited with an s-polarised incident beam, resulting in the generation of an in-resonance photocurrent. The tuneability of the photodetectors was achieved by either altering the nano-ribbon width or by varying the Fermi level with the Si back gate. Luxmoore *et al.* have demonstrated that integrating a metamaterial with the graphene nano-ribbons leads to an enhancement in photodetector response [205]. The metamaterials utilised for this were dual metal (Au, Al) split ring resonators. With the demonstration of operational IR emitters and detectors based on graphene on SiO_2/Si, it would be interesting to design and test a fully integrated infrared sensor based on the graphene emitters presented in this work and graphene based photodetectors similar to the ones demonstrated by Luxmoore *et al.* It is possible that an actively tuneable emitter and detector could be integrated on the same chip, forming the basis of a spectrometer-on-a-chip.

Bibliography

[1] Yasuda T, Yonemura S and Tani A 2012 Comparison of the Characteristics of Small Commercial NDIR CO2 Sensor Models and Development of a Portable CO_2 Measurement Device *Sensors* **12** 3641–55

[2] Iseki T, Tai H and Kimura K 2000 A portable remote methane sensor using a tunable diode laser *Meas. Sci. Technol.* **11** 594-602

[3] Zhang Y, Gao W, Song Z, An Y, Li L, Song Z, Yu W W and Wang Y 2010 Design of a novel gas sensor structure based on mid-infrared absorption spectrum *Sens. Actuators B Chem.* **147** 5–9

[4] Brugger J, Briand D, Muda R, Lewis E, O'Keeffe S, Dooly G and Clifford J 2009 Proceedings of the Eurosensors XXIII conferenceA Compact Optical Fibre Based Mid- Infrared Sensor System for Detection of High Level Carbon Dioxide Emissions in Exhaust Automotive Applications *Procedia Chem.* **1** 593–6

[5] Ali S Z, Luca A D, Hopper R, Boual S, Gardner J and Udrea F 2015 A Low-Power, Low-Cost Infra-Red Emitter in CMOS Technology *IEEE Sens. J.* **15** 6775–82

[6] Zotova N V, Il'inskaya N D, Karandashev S A, Matveev B A, Remennyi M A and Stus' N M 2006 Flip-chip LEDs with deep mesa emitting at 4.2 μm *Semiconductors* **40** 697–703

[7] Novoselov K S, Geim A K, Morozov S V, Jiang D, Zhang Y, Dubonos S V, Grigorieva I V and Firsov A A 2004 Electric Field Effect in Atomically Thin Carbon Films *Science* **306** 666–9

[8] Neto A H C, Guinea F, Peres N M R, Novoselov K S and Geim A K 2009 The electronic properties of graphene *Rev. Mod. Phys.* **81** 109–62

[9] Pop E, Varshney V and Roy A K 2012 Thermal properties of graphene: Fundamentals and applications *MRS Bull.* **37** 1273–81

[10] Ovid'ko I A 2013 Mechanical Propertied of Graphene *Rev. Adv. Mater. Sci.* **34** 1–11

[11] Kim Y D, Kim H, Cho Y, Ryoo J H, Park C-H, Kim P, Kim Y S, Lee S, Li Y, Park S-N, Shim Y, Yoon D, Dorgan V E, Pop E, Heinz T F, Hone J, Chun S-H, Cheong H, Lee S W, Bae M-H and Park Y D 2015 Bright visible light emission from graphene *Nat. Nanotechnol.* **10** 676–81

[12] Lee K J, Chandrakasan A P and Kong J 2011 Breakdown Current Density of CVD-Grown Multilayer Graphene Interconnects *IEEE Electron Device Lett.* **32** 557–9

[13] Bae M-H, Ong Z-Y, Estrada D and Pop E 2010 Imaging, Simulation, and Electrostatic Control of Power Dissipation in Graphene Devices *Nano Lett.* **10** 4787–93

[14] Bae M-H, Islam S, Dorgan V E and Pop E 2011 Scaling of High-Field Transport and Localized Heating in Graphene Transistors *ACS Nano* **5** 7936–44

[15] Freitag M, Chiu H-Y, Steiner M, Perebeinos V and Avouris P 2010 Thermal infrared emission from biased graphene *Nat. Nanotechnol.* **5** 497–501

[16] Luxmoore I J, Adlem C, Poole T, Lawton L M, Mahlmeister N H and Nash G R 2013 Thermal emission from large area chemical vapor deposited graphene devices *Appl. Phys. Lett.* **103** 131906

[17] Mahlmeister N H, Lawton L M, Luxmoore I J and Nash G R 2016 Modulation characteristics of graphene-based thermal emitters *Appl. Phys. Express* **9** 12105

[18] Martin P E and Barker E F 1932 The Infrared Absorption Spectrum of Carbon Dioxide *Phys. Rev.* **41** 291–303

[19] Hodgkinson J and Tatam R P 2013 Optical gas sensing: a review *Meas. Sci. Technol.* **24** 12004

[20] Smith S D, Hardaway H R and Crowder J G 2002 Recent developments in the applications of mid-infrared lasers, LEDs, and other solid state sources to gas detection **4651** 157–72

[21] Dmitriev V D and Kholopov G K 1965 Radiant emissivity of tungsten in the infrared region of the spectrum *J. Appl. Spectrosc.* **2** 315–20

[22] MacIsaac D, Kanner G and Anderson G 1999 Basic physics of the incandescent lamp (lightbulb) *Phys. Teach.* **37** 520–5

[23] Puton J, Jasek K, Siodłowski B, Knap A and Wiśniewski K 2002 Optimisation of a pulsed IR source for NDIR gas analysers *Opto - Electron. Rev.* 97–103

[24] Weber M, Lerch P and Renaud P 1997 Improved design for fast modulating IR sources *J. Micromechanics Microengineering* **7** 210

[25] Mutschall D, Scheibe C and Obermeier E 1995 Basic Micro Module For Chemical Sensors With On Chip Heater And Buried Sensor Structure *The 8th International Conference on Solid-State Sensors and Actuators, 1995 and Eurosensors IX.. Transducers '95* **1** 256–9

[26] Parameswaran M, Robinson A M, Blackburn D L, Gaitan M and Geist J 1991 Micromachined thermal radiation emitter from a commercial CMOS process *IEEE Electron Device Lett.* **12** 57–9

[27] Bauer D, Heeger M, Gebhard M and Benecke W 1996 Design and fabrication of a thermal infrared emitter *Sens. Actuators Phys.* **55** 57–63

[28] Hildenbrand J, Peter C, Lamprecht F, Kürzinger A, Naumann F, Ebert M, Wehrspohn R, Korvink J G and Wöllenstein J 2010 Fast transient temperature operating micromachined emitter for mid-infrared optical gas sensing systems: design, fabrication, characterization and optimization *Microsyst. Technol.* **16** 745–54

[29] Alexandrov S E, Gavrilov G A, Kapralov A A, Karandashev S A, Matveev B A, Sotnikova G Y and Stus' N M 2002 Portable optoelectronic gas sensors operating in the mid-IR spectral range (λ=3 5 μm) **4680** 188–94

[30] Krier A and Sherstnev V V 2000 Powerful interface light emitting diodes for methane gas detection *J. Phys. Appl. Phys.* **33** 101

[31] Jung D, Yu L, Wasserman D and Larry Lee M 2015 Mid-infrared electroluminescence from InAs type-I quantum wells grown on InAsP/InP metamorphic buffers *J. Appl. Phys.* **118** 183101

[32] Ivanov-Omskii V I and Matveev B A 2007 Negative luminescence and devices based on this phenomenon *Semiconductors* **41** 247–58

[33] Das N C 2007 Increase in midwave infrared light emitting diode light output due to substrate thinning and texturing *Appl. Phys. Lett.* **90** 11111

[34] Das N C 2010 Infrared light emitting device with two color emission *Solid-State Electron.* **54** 1381–3

[35] Weik F, Steinmeyer G, Tomm J W, Glatthaar R, Vetter U, Nurnus J and Lambrecht A 2006 A room-temperature continuous-wave operating midinfrared light emitting device *J. Appl. Phys.* **99** 114506

[36] Smith S D, Vass A, Karpushko F, Hardaway H and Crowder J G 2001 The prospects of LEDs, diode detectors and negative luminescence in infrared sensing of gases and spectroscopy *Philos. Trans. R. Soc. Lond. Math. Phys. Eng. Sci.* **359** 621–34

[37] Gong X y., Kan H, Makino T, Watanabe K, Iida T, Suzuki H, Aoyama M and Yamaguchi T 2000 Light Emitting Diodes Fabricated from Liquid Phase Epitaxial InAs/$InAs_xP_{1-x-y}$Sby/$InAs_{x'}P_{1-x'-y'}Sb_{y'}$ and InAs/$InAs_{1-x}Sb_x$ Multi-Layers *Cryst. Res. Technol.* **35** 549–55

[38] Haigh M K, Nash G R, Smith S J, Buckle L, Emeny M T and Ashley T 2007 Mid-infrared $Al_xIn_{1-x}Sb$ light-emitting diodes *Appl. Phys. Lett.* **90** 231116

[39] Krier A, Yin M, Smirnov V, Batty P, Carrington P J, Solovev V and Sherstnev V 2008 The development of room temperature LEDs and lasers for the mid-infrared spectral range *Phys. Status Solidi A* **205** 129–43

[40] McNeal M P, Moelders N, Pralle M U, Puscasu I, Last L, Ho W, Greenwald A C, Daly J T, Johnson E A and George T 2002 Development of optical MEMS CO_2 sensors **4815** 30–5

[41] Massoud M 2005 *Engineering Thermofluids: Thermodynamics, Fluid Mechanics, and Heat Transfer* (Springer Science & Business Media)

[42] Faughn S and 1998 *College Physics: 5th (Fifth) Edition* (Cengage Learning)

[43] Das A and Melissinos A C 1986 *Quantum Mechanics: A Modern Introduction* (CRC Press)

[44] Nair R R, Blake P, Grigorenko A N, Novoselov K S, Booth T J, Stauber T, Peres N M R and Geim A K 2008 Fine Structure Constant Defines Visual Transparency of Graphene *Science* **320** 1308–1308

[45] Mak K F, Sfeir M Y, Wu Y, Lui C H, Misewich J A and Heinz T F 2008 Measurement of the Optical Conductivity of Graphene *Phys. Rev. Lett.* **101** 196405

[46] Bonaccorso F, Sun Z, Hasan T and Ferrari A C 2010 Graphene photonics and optoelectronics *Nat. Photonics* **4** 611–22

[47] Casiraghi C, Hartschuh A, Lidorikis E, Qian H, Harutyunyan H, Gokus T, Novoselov K S and Ferrari A C 2007 Rayleigh Imaging of Graphene and Graphene Layers *Nano Lett.* **7** 2711–7

[48] Riedl M J 2001 *Optical Design Fundamentals for Infrared Systems* (SPIE Press)

[49] Meier A von 2006 *Electric Power Systems: A Conceptual Introduction* (John Wiley & Sons)

[50] Lindefelt U 1994 Heat generation in semiconductor devices *J. Appl. Phys.* **75** 942–57

[51] Shirmohammadi D and Hong H W 1992 Reconfiguration of electric distribution networks for resistive life losses reduction *IEEE Trans. Power Deliv.* **v** 1492–8

[52] Miller D A B and Ozaktas H M 1997 Limit to the bit-rate capacity of electrical interconnects from the aspect ratio of the system architecture *J. Parallel Distrib. Comput.* **41** 42–52

[53] Hummelgård M, Zhang R, Carlberg T, Vengust D, Dvorsek D, Mihailovic D and Olin H 2010 Nanowire transformation and annealing by Joule heating *Nanotechnology* **21** 165704

[54] Sosnowchik B D, Lin L and Englander O 2010 Localized heating induced chemical vapor deposition for one-dimensional nanostructure synthesis *J. Appl. Phys.* **107** 51101

[55] Mak K F, Lee C, Hone J, Shan J and Heinz T F 2010 Atomically thin MoS_2: A new direct-gap semiconductor *Phys. Rev. Lett.* **105**

[56] Baugher B W H, Churchill H O H, Yang Y and Jarillo-Herrero P 2014 Optoelectronic devices based on electrically tunable p-n diodes in a monolayer dichalcogenide *Nat. Nanotechnol.* **9** 262–7

[57] Ci L, Song L, Jin C, Jariwala D, Wu D, Li Y, Srivastava A, Wang Z F, Storr K, Balicas L, Liu F and Ajayan P M 2010 Atomic layers of hybridized boron nitride and graphene domains *Nat. Mater.* **9** 430–5

[58] Liu H, Neal A T, Zhu Z, Luo Z, Xu X, Tománek D and Ye P D 2014 Phosphorene: An unexplored 2D semiconductor with a high hole mobility *ACS Nano* **8** 4033–41

[59] Lin Y-C, Dumcenco D O, Huang Y-S and Suenaga K 2014 Atomic mechanism of the semiconducting-to-metallic phase transition in single-layered MoS_2 *Nat. Nanotechnol.* **9** 391–6

[60] Mousavi H and Moradian R 2013 Metallic and semimetallic properties of doped graphene and boron nitride planes *Solid State Commun.* **153** 17–22

[61] Liu H, Du Y, Deng Y and Ye P D 2015 Semiconducting black phosphorus: synthesis, transport properties and electronic applications *Chem. Soc. Rev.* **44** 2732–43

[62] Britnell L, Gorbachev R V, Jalil R, Belle B D, Schedin F, Katsnelson M I, Eaves L, Morozov S V, Mayorov A S, Peres N M R, Castro Neto A H, Leist J, Geim A K, Ponomarenko L A and Novoselov K S 2012 Electron Tunneling through Ultrathin Boron Nitride Crystalline Barriers *Nano Lett.* **12** 1707–10

[63] Wehling T O, Katsnelson M I and Lichtenstein A I 2008 First-principles studies of water adsorption on graphene: The role of the substrate *Appl. Phys. Lett.* **93** 202110

[64] Zhan D, Sun L, Ni Z H, Liu L, Fan X F, Wang Y, Yu T, Lam Y M, Huang W and Shen Z X 2010 $FeCl_3$-Based Few-Layer Graphene Intercalation Compounds: Single Linear Dispersion Electronic Band Structure and Strong Charge Transfer Doping *Adv. Funct. Mater.* **20** 3504–3509

[65] Chen S, Cai W, Chen D, Ren Y, Li X, Zhu Y and Ruoff R S 2010 Adsorption/desorption and electrically controlled flipping of ammonia molecules on graphene *New J. Phys.* **12** 125011

[66] Chen J-H, Jang C, Adam S, Fuhrer M S, Williams E D and Ishigami M 2008 Charged-impurity scattering in graphene *Nat. Phys.* **4** 377–81

[67] Lohmann T, von Klitzing K and Smet J H 2009 Four-Terminal Magneto-Transport in Graphene p-n Junctions Created by Spatially Selective Doping *Nano Lett.* **9** 1973–9

[68] Watanabe K, Taniguchi T and Kanda H 2004 Direct-bandgap properties and evidence for ultraviolet lasing of hexagonal boron nitride single crystal *Nat. Mater.* **3** 404–9

[69] Kim K K, Hsu A, Jia X, Kim S M, Shi Y, Dresselhaus M, Palacios T and Kong J 2012 Synthesis and Characterization of Hexagonal Boron Nitride Film as a Dielectric Layer for Graphene Devices *ACS Nano* **6** 8583–90

[70] Dean C R, Young A F, Meric I, Lee C, Wang L, Sorgenfrei S, Watanabe K, Taniguchi T, Kim P, Shepard K L and Hone J 2010 Boron nitride substrates for high-quality graphene electronics *Nat. Nanotechnol.* **5** 722–6

[71] Wu Y H, Yu T and Shen Z X 2010 Two-dimensional carbon nanostructures: Fundamental properties, synthesis, characterization, and potential applications *J. Appl. Phys.* **108** 71301

[72] Lepri S, Livi R and Politi A 2003 Thermal conduction in classical low-dimensional lattices *Phys. Rep.* **377** 1–80

[73] Basile G, Bernardin C and Olla S 2006 Momentum Conserving Model with Anomalous Thermal Conductivity in Low Dimensional Systems *Phys. Rev. Lett.* **96** 204303

[74] Balandin A A, Ghosh S, Bao W, Calizo I, Teweldebrhan D, Miao F and Lau C N 2008 Superior Thermal Conductivity of Single-Layer Graphene *Nano Lett.* **8** 902–7

[75] Jo I, Pettes M T, Kim J, Watanabe K, Taniguchi T, Yao Z and Shi L 2013 Thermal Conductivity and Phonon Transport in Suspended Few-Layer Hexagonal Boron Nitride *Nano Lett.* **13** 550–4

[76] Srivastava G P 1990 *The Physics of Phonons* (CRC Press)

[77] Oshima C, Aizawa T, Souda R, Ishizawa Y and Sumiyoshi Y 1988 Surface phonon dispersion curves of graphite (0001) over the entire energy region *Solid State Commun.* **65** 1601–4

[78] Saito R, Dresselhaus G and Dresselhaus M S 1998 *Physical Properties of Carbon Nanotubes* (Imperial College Press)

[79] Mohr M, Maultzsch J, Dobardžić E, Reich S, Milošević I, Damnjanović M, Bosak A, Krisch M and Thomsen C 2007 Phonon dispersion of graphite by inelastic x-ray scattering *Phys. Rev. B* **76** 35439

[80] Pettes M T, Jo I, Yao Z and Shi L 2011 Influence of Polymeric Residue on the Thermal Conductivity of Suspended Bilayer Graphene *Nano Lett.* **11** 1195–200

[81] Constantinescu G, Kuc A and Heine T 2013 Stacking in Bulk and Bilayer Hexagonal Boron Nitride *Phys. Rev. Lett.* **111** 36104

[82] Lindsay L and Broido D A 2011 Enhanced thermal conductivity and isotope effect in single-layer hexagonal boron nitride *Phys. Rev. B* **84** 155421

[83] Michel K H and Verberck B 2011 Phonon dispersions and piezoelectricity in bulk and multilayers of hexagonal boron nitride *Phys. Rev. B* **83** 115328

[84] Jeong C, Datta S and Lundstrom M 2011 Full dispersion versus Debye model evaluation of lattice thermal conductivity with a Landauer approach *J. Appl. Phys.* **109** 73718

[85] Ghosh S, Calizo I, Teweldebrhan D, Pokatilov E P, Nika D L, Balandin A A, Bao W, Miao F and Lau C N 2008 Extremely high thermal conductivity of graphene:

Prospects for thermal management applications in nanoelectronic circuits *Appl. Phys. Lett.* **92** 151911

[86] Chen S, Moore A L, Cai W, Suk J W, An J, Mishra C, Amos C, Magnuson C W, Kang J, Shi L and Ruoff R S 2011 Raman Measurements of Thermal Transport in Suspended Monolayer Graphene of Variable Sizes in Vacuum and Gaseous Environments *ACS Nano* **5** 321–8

[87] Chen S, Wu Q, Mishra C, Kang J, Zhang H, Cho K, Cai W, Balandin A A and Ruoff R S 2012 Thermal conductivity of isotopically modified graphene *Nat. Mater.* **11** 203–7

[88] Ghosh S, Bao W, Nika D L, Subrina S, Pokatilov E P, Lau C N and Balandin A A 2010 Dimensional crossover of thermal transport in few-layer graphene *Nat. Mater.* **9** 555–8

[89] Balandin A A 2011 Thermal properties of graphene and nanostructured carbon materials *Nat. Mater.* **10** 569–81

[90] Levinshtein M E, Rumyantsev S L and Shur M S 2001 *Properties of Advanced Semiconductor Materials: GaN, AIN, InN, BN, SiC, SiGe* (John Wiley & Sons)

[91] Islam S, Li Z, Dorgan V E, Bae M H and Pop E 2013 Role of Joule Heating on Current Saturation and Transient Behavior of Graphene Transistors *IEEE Electron Device Lett.* **34** 166–8

[92] Benedict L X, Louie S G and Cohen M L 1996 Heat capacity of carbon nanotubes *Solid State Commun.* **100** 177–80

[93] Nihira T and Iwata T 2003 Temperature dependence of lattice vibrations and analysis of the specific heat of graphite *Phys. Rev. B* **68** 134305

[94] Tohei T, Kuwabara A, Oba F and Tanaka I 2006 Debye temperature and stiffness of carbon and boron nitride polymorphs from first principles calculations *Phys. Rev. B* **73** 64304

[95] Fried L E and Howard W M 2000 Explicit Gibbs free energy equation of state applied to the carbon phase diagram *Phys. Rev. B* **61** 8734–43

[96] Ong Z-Y and Pop E 2011 Effect of substrate modes on thermal transport in supported graphene *Phys. Rev. B* **84** 75471

[97] Thomas S, Ajith K M, Chandra S and Valsakumar M C 2015 Temperature dependent structural properties and bending rigidity of pristine and defective hexagonal boron nitride *J. Phys. Condens. Matter* **27** 315302

[98] Slack G A and Bartram S F 1975 Thermal expansion of some diamondlike crystals *J. Appl. Phys.* **46** 89–98

[99] Haynes W M 2015 *CRC Handbook of Chemistry and Physics, 96th Edition* (CRC Press)

[100] Seol J H, Jo I, Moore A L, Lindsay L, Aitken Z H, Pettes M T, Li X, Yao Z, Huang R, Broido D, Mingo N, Ruoff R S and Shi L 2010 Two-Dimensional Phonon Transport in Supported Graphene *Science* **328** 213–6

[101] Jang W, Chen Z, Bao W, Lau C N and Dames C 2010 Thickness-Dependent Thermal Conductivity of Encased Graphene and Ultrathin Graphite *Nano Lett.* **10** 3909–13

[102] Lindsay L, Broido D A and Mingo N 2010 Flexural phonons and thermal transport in graphene *Phys. Rev. B* **82** 115427

[103] Qiu B and Ruan X 2012 Reduction of spectral phonon relaxation times from suspended to supported graphene *Appl. Phys. Lett.* **100** 193101

[104] Liao A D, Wu J Z, Wang X, Tahy K, Jena D, Dai H and Pop E 2011 Thermally Limited Current Carrying Ability of Graphene Nanoribbons *Phys. Rev. Lett.* **106** 256801

[105] Barnard H R, Zossimova E, Mahlmeister N H, Lawton L M, Luxmoore I J and Nash G R 2016 Boron nitride encapsulated graphene infrared emitters *Appl. Phys. Lett.* **108** 131110

[106] Berciaud S, Han M Y, Mak K F, Brus L E, Kim P and Heinz T F 2010 Electron and Optical Phonon Temperatures in Electrically Biased Graphene *Phys. Rev. Lett.* **104** 227401

[107] Chae D-H, Krauss B, von Klitzing K and Smet J H 2010 Hot Phonons in an Electrically Biased Graphene Constriction *Nano Lett.* **10** 466–71

[108] Engel M, Steiner M, Lombardo A, Ferrari A C, Löhneysen H v, Avouris P and Krupke R 2012 Light–matter interaction in a microcavity-controlled graphene transistor *Nat. Commun.* **3** 906

[109] Lawton L M, Mahlmeister N H, Luxmoore I J and Nash G R 2014 Prospective for graphene based thermal mid-infrared light emitting devices *AIP Adv.* **4** 87139

[110] Pop E 2010 Energy dissipation and transport in nanoscale devices *Nano Res.* **3** 147–69

[111] Dorgan V E, Behnam A, Conley H J, Bolotin K I and Pop E 2013 High-Field Electrical and Thermal Transport in Suspended Graphene *Nano Lett.* **13** 4581–6

[112] Yi M and Shen Z 2015 A review on mechanical exfoliation for the scalable production of graphene *J. Mater. Chem. A* **3** 11700–15

[113] Tetlow H, Posthuma de Boer J, Ford I J, Vvedensky D D, Coraux J and Kantorovich L 2014 Growth of epitaxial graphene: Theory and experiment *Phys. Rep.* **542** 195–295

[114] Viculis L M, Mack J J, Mayer O M, Hahn H T and Kaner R B 2005 Intercalation and exfoliation routes to graphite nanoplatelets *J. Mater. Chem.* **15** 974–8

[115] Pei S and Cheng H-M 2012 The reduction of graphene oxide *Carbon* **50** 3210–28

[116] Stankovich S, Dikin D A, Dommett G H B, Kohlhaas K M, Zimney E J, Stach E A, Piner R D, Nguyen S T and Ruoff R S 2006 Graphene-based composite materials *Nature* **442** 282–6

[117] Xie L, Wang H, Jin C, Wang X, Jiao L, Suenaga K and Dai H 2011 Graphene Nanoribbons from Unzipped Carbon Nanotubes: Atomic Structures, Raman Spectroscopy, and Electrical Properties *J. Am. Chem. Soc.* **133** 10394–7

[118] Yu Q, Lian J, Siriponglert S, Li H, Chen Y P and Pei S-S 2008 Graphene segregated on Ni surfaces and transferred to insulators *Appl. Phys. Lett.* **93** 113103

[119] Li X, Cai W, An J, Kim S, Nah J, Yang D, Piner R, Velamakanni A, Jung I, Tutuc E, Banerjee S K, Colombo L and Ruoff R S 2009 Large-area synthesis of high-quality and uniform graphene films on copper foils *Science* **324** 1312–4

[120] Geim A K and Novoselov K S 2007 The rise of graphene *Nat. Mater.* **6** 183–91

[121] Blake P, Hill E W, Neto A H C, Novoselov K S, Jiang D, Yang R, Booth T J and Geim A K 2007 Making graphene visible *Appl. Phys. Lett.* **91** 63124

[122] Ferrari A C, Meyer J C, Scardaci V, Casiraghi C, Lazzeri M, Mauri F, Piscanec S, Jiang D, Novoselov K S, Roth S and Geim A K 2006 Raman Spectrum of Graphene and Graphene Layers *Phys. Rev. Lett.* **97** 187401

[123] Malard L M, Pimenta M A, Dresselhaus G and Dresselhaus M S 2009 Raman spectroscopy in graphene *Phys. Rep.* **473** 51–87

[124] Reina A, Jia X, Ho J, Nezich D, Son H, Bulovic V, Dresselhaus M S and Kong J 2009 Large Area, Few-Layer Graphene Films on Arbitrary Substrates by Chemical Vapor Deposition *Nano Lett.* **9** 30–5

[125] Graf D, Molitor F, Ensslin K, Stampfer C, Jungen A, Hierold C and Wirtz L 2007 Spatially Resolved Raman Spectroscopy of Single- and Few-Layer Graphene *Nano Lett.* **7** 238–42

[126] Beams R, Gustavo Cançado L and Novotny L 2015 Raman characterization of defects and dopants in graphene *J. Phys. Condens. Matter Inst. Phys. J.* **27** 83002

[127] Arenal R, Ferrari A C, Reich S, Wirtz L, Mevellec J-Y, Lefrant S, Rubio A and Loiseau A 2006 Raman Spectroscopy of Single-Wall Boron Nitride Nanotubes *Nano Lett.* **6** 1812–6

[128] Gorbachev R V, Riaz I, Nair R R, Jalil R, Britnell L, Belle B D, Hill E W, Novoselov K S, Watanabe K, Taniguchi T, Geim A K and Blake P 2011 Hunting for Monolayer Boron Nitride: Optical and Raman Signatures *Small* **7** 465–8

[129] Postek M T, Howard K S, Johnson A H and McMichael K L 1980 *Scanning Electron Microscopy: a Student's Handbook* (Ladd Research Industries)

[130] Suk J W, Kitt A, Magnuson C W, Hao Y, Ahmed S, An J, Swan A K, Goldberg B B and Ruoff R S 2011 Transfer of CVD-Grown Monolayer Graphene onto Arbitrary Substrates *ACS Nano* **5** 6916–24

[131] Lewins C J, Boulbar E D L, Lis S M, Edwards P R, Martin R W, Shields P A and Allsopp D W E 2014 Strong photonic crystal behavior in regular arrays of core-shell and quantum disc InGaN/GaN nanorod light-emitting diodes *J. Appl. Phys.* **116** 44305

[132] Koenig S P, Boddeti N G, Dunn M L and Bunch J S 2011 Ultrastrong adhesion of graphene membranes *Nat. Nanotechnol.* **6** 543–6

[133] Wang L, Liu W, Zhang Y, Zhang Z-H, Tiam Tan S, Yi X, Wang G, Sun X, Zhu H and Volkan Demir H 2015 Graphene-based transparent conductive electrodes for GaN-based light emitting diodes: Challenges and countermeasures *Nano Energy* **12** 419–36

[134] Youn D-H, Yu Y-J, Choi H, Kim S-H, Choi S-Y and Choi C-G 2013 Graphene transparent electrode for enhanced optical power and thermal stability in GaN light-emitting diodes *Nanotechnology* **24** 75202

[135] Velasco J, Zhao Z, Zhang H, Wang F, Wang Z, Kratz P, Jing L, Bao W, Shi J and Lau C N 2011 Suspension and measurement of graphene and Bi_2Se_3 thin crystals *Nanotechnology* **22** 285305

[136] Velasco Jr. J, Liu G, Bao W and Lau C N 2009 Electrical Transport in High Quality Graphene pnp Junctions *New J. Phys.* **11** 95008

[137] Tombros N, Veligura A, Junesch J, Berg J J van den, Zomer P J, Wojtaszek M, Marun I J V, Jonkman H T and Wees B J van 2011 Large yield production of high

mobility freely suspended graphene electronic devices on a polydimethylglutarimide based organic polymer *J. Appl. Phys.* **109** 93702

[138] Li X, Zhu Y, Cai W, Borysiak M, Han B, Chen D, Piner R D, Colombo L and Ruoff R S 2009 Transfer of large-area graphene films for high-performance transparent conductive electrodes *Nano Lett.* **9** 4359–63

[139] Bae M-H, Ong Z-Y, Estrada D and Pop E 2010 Imaging, Simulation, and Electrostatic Control of Power Dissipation in Graphene Devices *Nano Lett.* **10** 4787–93

[140] Grosse K L, Bae M-H, Lian F, Pop E and King W P 2011 Nanoscale Joule heating, Peltier cooling and current crowding at graphene-metal contacts *Nat. Nanotechnol.* **6** 287–90

[141] Pop E 2010 Energy dissipation and transport in nanoscale devices *Nano Res.* **3** 147–69

[142] Balandin A A, Ghosh S, Bao W, Calizo I, Teweldebrhan D, Miao F and Lau C N 2008 Superior Thermal Conductivity of Single-Layer Graphene *Nano Lett.* **8** 902–7

[143] Freitag M, Steiner M, Martin Y, Perebeinos V, Chen Z, Tsang J C and Avouris P 2009 Energy Dissipation in Graphene Field-Effect Transistors *Nano Lett.* **9** 1883–8

[144] Subrina S and Kotchetkov D 2008 Simulation of Heat Conduction in Suspended Graphene Flakes of Variable Shapes *J. Nanoelectron. Optoelectron.* **3** 249–69

[145] Subrina S 2012 Heat Transport in Graphene Interconnect Networks With Graphene Lateral Heat Spreaders *IEEE Trans. Nanotechnol.* **11** 777–81

[146] Balandin A A 2011 Thermal properties of graphene and nanostructured carbon materials *Nat. Mater.* **10** 569–81

[147] Chen S, Moore A L, Cai W, Suk J W, An J, Mishra C, Amos C, Magnuson C W, Kang J, Shi L and Ruoff R S 2011 Raman Measurements of Thermal Transport in Suspended Monolayer Graphene of Variable Sizes in Vacuum and Gaseous Environments *ACS Nano* **5** 321–8

[148] Mak K F, Lui C H and Heinz T F 2010 Measurement of the thermal conductance of the graphene/SiO_2 interface *Appl. Phys. Lett.* **97** 221904

[149] Chen C-C, Li Z, Shi L and Cronin S B 2014 Thermal interface conductance across a graphene/hexagonal boron nitride heterojunction *Appl. Phys. Lett.* **104** 81908

[150] Simpson A and Stuckes A D 1971 The thermal conductivity of highly oriented pyrolytic boron nitride *J. Phys. C Solid State Phys.* **4** 1710

[151] Yuxiang Ni J J 2015 Thermal transport across few-layer boron nitride encased by silica *Appl. Phys. Lett.* **107** 31603

[152] Chen Z, Jang W, Bao W, Lau C N and Dames C 2009 Thermal contact resistance between graphene and silicon dioxide *Appl. Phys. Lett.* **95** 161910

[153] Tong J K, Hsu W-C, Huang Y, Boriskina S V and Chen G 2015 Thin-film "Thermal Well" Emitters and Absorbers for High-Efficiency Thermophotovoltaics *Sci. Rep.* **5** 10661

[154] Hanamura K and Kameya Y 2008 Spectral Control of Thermal Radiation using Rectangular Micro-Cavities on Emitter-Surface for Thermophotovoltaic Generation of Electricity *J. Therm. Sci. Technol.* **3** 33–44

[155] Rinnerbauer V, Lenert A, Bierman D M, Yeng Y X, Chan W R, Geil R D, Senkevich J J, Joannopoulos J D, Wang E N, Soljačić M and Celanovic I 2014 Metallic Photonic Crystal Absorber-Emitter for Efficient Spectral Control in High-Temperature Solar Thermophotovoltaics *Adv. Energy Mater.* **4** 1400334

[156] Ueba Y and Takahara J 2012 Spectral Control of Thermal Radiation by Metasurface with Split-Ring Resonator *Appl. Phys. Express* **5** 122001

[157] Inoue T, De Zoysa M, Asano T and Noda S 2015 Realization of narrowband thermal emission with optical nanostructures *Optica* **2** 27-35

[158] Rothman L S, Gordon I E, Barbe A, Benner D C, Bernath P F, Birk M, Boudon V, Brown L R, Campargue A, Champion J-P, Chance K, Coudert L H, Dana V, Devi V M, Fally S, Flaud J-M, Gamache R R, Goldman A, Jacquemart D, Kleiner I, Lacome N, Lafferty W J, Mandin J-Y, Massie S T, Mikhailenko S N, Miller C E, Moazzen-Ahmadi N, Naumenko O V, Nikitin A V, Orphal J, Perevalov V I, Perrin A, Predoi-Cross A, Rinsland C P, Rotger M, Šimečková M, Smith M A H, Sung K, Tashkun S A, Tennyson J, Toth R A, Vandaele A C and Vander Auwera J 2009 The HITRAN 2008 molecular spectroscopic database *J. Quant. Spectrosc. Radiat. Transf.* **110** 533–72

[159] Bitnar B, Durisch W, Mayor J-C, Sigg H and Tschudi H R 2002 Characterisation of rare earth selective emitters for thermophotovoltaic applications *Sol. Energy Mater. Sol. Cells* **73** 221–34

[160] Lin S-Y, Fleming J G and El-Kady I 2003 Three-dimensional photonic-crystal emission through thermal excitation *Opt. Lett.* **28** 1909–11

[161] Sai H and Yugami H 2004 Thermophotovoltaic generation with selective radiators based on tungsten surface gratings *Appl. Phys. Lett.* **85** 3399–401

[162] Puscasu I and Schaich W L 2008 Narrow-band, tunable infrared emission from arrays of microstrip patches *Appl. Phys. Lett.* **92** 233102

[163] Mason J A, Smith S and Wasserman D 2011 Strong absorption and selective thermal emission from a midinfrared metamaterial *Appl. Phys. Lett.* **98** 241105

[164] Yang Y, Kravchenko I I, Briggs D P and Valentine J 2014 All-dielectric metasurface analogue of electromagnetically induced transparency *Nat. Commun.* **5** 5753

[165] Bao Q, Zhang H, Wang Y, Ni Z, Yan Y, Shen Z X, Loh K P and Tang D Y 2009 Atomic-Layer Graphene as a Saturable Absorber for Ultrafast Pulsed Lasers *Adv. Funct. Mater.* **19** 3077–83

[166] Boller K-J, Imamoğlu A and Harris S E 1991 Observation of electromagnetically induced transparency *Phys. Rev. Lett.* **66** 2593–6

[167] Zhang S, Genov D A, Wang Y, Liu M and Zhang X 2008 Plasmon-Induced Transparency in Metamaterials *Phys. Rev. Lett.* **101** 47401

[168] Xu Q, Sandhu S, Povinelli M L, Shakya J, Fan S and Lipson M 2006 Experimental Realization of an On-Chip All-Optical Analogue to Electromagnetically Induced Transparency *Phys. Rev. Lett.* **96** 123901

[169] Papasimakis N, Fedotov V A, Zheludev N I and Prosvirnin S L 2008 Metamaterial Analog of Electromagnetically Induced Transparency *Phys. Rev. Lett.* **101** 253903

[170] Yang X, Yu M, Kwong D-L and Wong C W 2009 All-Optical Analog to Electromagnetically Induced Transparency in Multiple Coupled Photonic Crystal Cavities *Phys. Rev. Lett.* **102** 173902

[171] Dhouibi A, Nawaz B, Lupu A, De L and Priou A 2013 Excitation of trapped modes from a metasurface composed of only Z-shaped meta-atoms *Appl. Phys. Lett.* **103**

[172] Singh R, Cao W, Al-Naib I, Cong L, Withayachumnankul W and Zhang W 2014 Ultrasensitive terahertz sensing with high-Q Fano resonances in metasurfaces *Appl. Phys. Lett.* **105** 171101

[173] Shekhar P, Atkinson J and Jacob Z 2014 Hyperbolic metamaterials: fundamentals and applications *Nano Converg.* **1** 1-17

[174] Zhang H, Demir H V and Govorov A O 2014 Plasmonic Metamaterials and Nanocomposites with the Narrow Transparency Window Effect in Broad Extinction Spectra *ACS Photonics* **1** 822–32

[175] Lukin M D and Imamoğlu A 2001 Controlling photons using electromagnetically induced transparency *Nature* **413** 273–6

[176] Hsieh L-H and Chang K 2002 Equivalent lumped elements G, L, C, and unloaded Q's of closed- and open-loop ring resonators *IEEE Trans. Microw. Theory Tech.* **50** 453–60

[177] Smith D R, Vier D C, Koschny T and Soukoulis C M 2005 Electromagnetic parameter retrieval from inhomogeneous metamaterials *Phys. Rev. E* **71** 36617

[178] Luk'yanchuk B, Zheludev N I, Maier S A, Halas N J, Nordlander P, Giessen H and Chong C T 2010 The Fano resonance in plasmonic nanostructures and metamaterials *Nat. Mater.* **9** 707–15

[179] Liu N, Langguth L, Weiss T, Kästel J, Fleischhauer M, Pfau T and Giessen H 2009 Plasmonic analogue of electromagnetically induced transparency at the Drude damping limit *Nat. Mater.* **8** 758–62

[180] Madelung O, Rössler U and Schulz M 2001 *Group IV Elements, IV-IV and III-V Compounds. Part a - Lattice Properties. a* (Springer-Verlag)

[181] Barnard H R, Zossimova E, Mahlmeister N H, Lawton L M, Luxmoore I J and Nash G R 2016 Boron nitride encapsulated graphene infrared emitters *Appl. Phys. Lett.* **108** 131110

[182] Kim Y D, Kim H, Cho Y, Ryoo J H, Park C-H, Kim P, Kim Y S, Lee S, Li Y, Park S-N, Shim Yoo Y, Yoon D, Dorgan V E, Pop E, Heinz T F, Hone J, Chun S-H, Cheong H, Lee S W, Bae M-H and Park Y D 2015 Bright visible light emission from graphene *Nat. Nanotechnol.* **10** 676–81

[183] Dorgan V E, Behnam A, Conley H J, Bolotin K I and Pop E 2013 High-Field Electrical and Thermal Transport in Suspended Graphene *Nano Lett.* **13** 4581–6

[184] Berciaud S, Han M Y, Mak K F, Brus L E, Kim P and Heinz T F 2010 Electron and Optical Phonon Temperatures in Electrically Biased Graphene *Phys. Rev. Lett.* **104** 227401

[185] Boulbar E D L, Gîrgel I, Lewins C J, Edwards P R, Martin R W, Šatka A, Allsopp D W E and Shields P A 2013 Facet recovery and light emission from GaN/InGaN/GaN core-shell structures grown by metal organic vapour phase epitaxy on etched GaN nanorod arrays *J. Appl. Phys.* **114** 94302

[186] Vakil A and Engheta N 2011 Transformation Optics Using Graphene *Science* **332** 1291–4

[187] Grigorenko A N, Polini M and Novoselov K S 2012 Graphene plasmonics *Nat. Photonics* **6** 749–58

[188] Hajaj E M, Shtempluk O, Kochetkov V, Razin A and Yaish Y E 2013 Chemical potential of inhomogeneous single-layer graphene *Phys. Rev. B* **88** 45128

[189] Yan H, Xia F, Zhu W, Freitag M, Dimitrakopoulos C, Bol A A, Tulevski G and Avouris P 2011 Infrared Spectroscopy of Wafer-Scale Graphene *ACS Nano* **5** 9854–60

[190] Hong X, Zou K and Zhu J 2009 Quantum scattering time and its implications on scattering sources in graphene *Phys. Rev. B* **80** 241415

[191] Deokar G, Avila J, Razado-Colambo I, Codron J-L, Boyaval C, Galopin E, Asensio M-C and Vignaud D 2015 Towards high quality CVD graphene growth and transfer *Carbon* **89** 82–92

[192] Ng S S, Hassan Z, Hashim M R, Kordesch M E, Halverson W and Colter P C 2002 Infrared characterization of GaN/Si grown at different temperatures by MOCVD *IEEE International Conference on Semiconductor Electronics, 2002. Proceedings. ICSE 2002* 209–12

[193] Ibáñez J, Hernández S, Alarcón-Lladó E, Cuscó R, Artús L, Novikov S V, Foxon C T and Calleja E 2008 Far-infrared transmission in GaN, AlN, and AlGaN thin films grown by molecular beam epitaxy *J. Appl. Phys.* **104** 33544

[194] Caldwell J D, Glembocki O J, Francescato Y, Sharac N, Giannini V, Bezares F J, Long J P, Owrutsky J C, Vurgaftman I, Tischler J G, Wheeler V D, Bassim N D, Shirey L M, Kasica R and Maier S A 2013 Low-Loss, Extreme Subdiffraction Photon Confinement via Silicon Carbide Localized Surface Phonon Polariton Resonators *Nano Lett.* **13** 3690–7

[195] Simpkins B S, Long J P, Glembocki O J, Guo J, Caldwell J D and Owrutsky J C 2012 Pitch-dependent resonances and near-field coupling in infrared nanoantenna arrays *Opt. Express* **20** 27725

[196] Dawlaty J M, Shivaraman S, Strait J, George P, Chandrashekhar M, Rana F, Spencer M G, Veksler D and Chen Y 2008 Measurement of the optical absorption spectra of epitaxial graphene from terahertz to visible *Appl. Phys. Lett.* **93** 131905

[197] Gan X, Mak K F, Gao Y, You Y, Hatami F, Hone J, Heinz T F and Englund D 2012 Strong Enhancement of Light–Matter Interaction in Graphene Coupled to a Photonic Crystal Nanocavity *Nano Lett.* **12** 5626–31

[198] Majumdar A, Kim J, Vuckovic J and Wang F 2013 Electrical Control of Silicon Photonic Crystal Cavity by Graphene *Nano Lett.* **13** 515–8

[199] Gan X, Shiue R-J, Gao Y, Mak K F, Yao X, Li L, Szep A, Walker D, Hone J, Heinz T F and Englund D 2013 High-Contrast Electrooptic Modulation of a Photonic Crystal Nanocavity by Electrical Gating of Graphene *Nano Lett.* **13** 691–6

[200] Xu K, Xu C, Xie Y, Deng J, Zhu Y, Guo W, Mao M, Xun M, Chen M, Zheng L and Sun J 2013 GaN nanorod light emitting diodes with suspended graphene transparent electrodes grown by rapid chemical vapor deposition *Appl. Phys. Lett.* **103** 222105

[201] Mazid Munshi A and Weman H 2013 Advances in semiconductor nanowire growth on graphene *Phys. Status Solidi RRL – Rapid Res. Lett.* **7** 713–26

[202] Ding J, Arigong B, Ren H, Zhou M, Shao J, Lu M, Chai Y, Lin Y and Zhang H 2014 Tuneable complementary metamaterial structures based on graphene for single and multiple transparency windows *Sci. Rep.* **4** 6128

[203] Liu J, Qian Q, Zou Y, Li G, Jin Y, Jiang K, Fan S and Li Q 2014 Enhanced performance of graphene transistor with ion-gel top gate *Carbon* **68** 480–6

[204] Freitag M, Low T, Zhu W, Yan H, Xia F and Avouris P 2013 Photocurrent in graphene harnessed by tunable intrinsic plasmons *Nat. Commun.* **4** 1951

[205] Luxmoore I J, Liu P Q, Li P, Faist J and Nash G R 2016 Graphene–Metamaterial Photodetectors for Integrated Infrared Sensing *ACS Photonics* **3** 936–41